Secondary Flows In Centrifugal Compresser Impellers

Dissertation submitted to the
University of Cambridge in
Candidature for the Degree
of Doctor of Philosophy,
June 1979

Mark Wyatt Johnson

Clare College

SECONDARY FLOWS IN CENTRIFUGAL COMPRESSOR IMPELLERS

Preface

This thesis, which I am submitting for the PhD degree, is the result of my own work, however some sections have already been published in co-authorship with my research supervisor, Dr. John Moore, in the following papers

1. MOORE,J., MOORE,J.G., JOHNSON,M.W., 'On Three-Dimensional Flow in Centrifugal Impellers', Aeronautical Research Council, CP No.1384, 1977.
2. JOHNSON,M.W., 'Secondary Flow in Rotating Bends', ASME J. of Eng. for Power, Vol.100, No.4, Oct 1978, p553-560.
3. JOHNSON,M.W. and MOORE,J., 'The Development of Wake Flow in a Centrifugal Impeller', ASME Paper No. 79-GT-152, March 1979.
4. JOHNSON,M.W. and MOORE,J., 'Wake Flows in a Centrifugal Impeller', to be published.

I should like to thank John Moore, for his stimulating ideas throughout this project and in particular, for his encouragement and aid in the preparation of the results for publication. I also thank Peter Timmis of Rolls Royce (1971) Ltd., for his helpful discussion on research in Centrifugal Compressors as viewed by the Gas Turbine Industry. I am also grateful to Rolls Royce for their financial support for this project and to the Science Research Council for my research grant.

Mark W. Johnson. May 1979.

Clare College.

This dissertation is the result of my own work and includes nothing which is the outcome of work done in collaboration.

Mark W Johnson.

SECONDARY FLOWS IN CENTRIFUGAL COMPRESSOR IMPELLERS - Mark W. Johnson

Detailed flow measurements made in a 1 metre diameter, shrouded, centrifugal (Ghost) impeller running at 500 rpm are presented. Relative velocities and rotary stagnation pressures ($p^*=p-\frac{1}{2}\rho\omega^2r^2+\frac{1}{2}\rho W^2$) were measured on five cross-sectional planes between the impeller inlet and the outlet, using probes which were traversed within the rotating impeller passage. The reduced static pressures ($p_r=p-\frac{1}{2}\rho\omega^2r^2$), calculated from the flow measurements, are also presented.

Measurements were made in a 'design' flow (approximately zero incidence at the blade leading edge), a 'below design' flow and an 'above design' flow. A wake flow was observed in all three flows and there were two major sources of the wake fluid. Firstly, from the separation of the shroud boundary layer and secondly, from the accumulation of low p^* fluid from the other boundary layers by secondary flows. The results showed that the wake's position at the outlet moved from the suction side in the 'below design' flow, to the suction-side/shroud corner region in the 'design' flow and to the shroud in the 'above design' flow, because of the change in the relative strengths of the secondary flows generated by rotation and curvature. The modifications to turbulent mixing, by curvature and rotation, probably influenced the wake size.

In order to predict the wake's location at the impeller discharge, a simple secondary flow model, which represented the impeller as a pipe bend, was devised. This model was successfully tested on two analytically soluble flows, in a stationary bend and in a rotating straight pipe. The model was then used for the more complex flows in a rotating axial-to-radial bend and in the Ghost and Eckardt's centrifugal impellers. The theoretical results for these impellers showed several of the features observed in the flow measurements.

CONTENTS

NOMENCLATURE

a,b,d	constants in Equation A1.1
D	duct diameter
$\dot{m}$	mass flow rate for 1 impeller passage
p	static pressure
p_r	reduced static pressure, $p_r=p-\frac{1}{2}\rho\omega^2r^2$
p^*	rotary stagnation pressure, $p^*=p+\frac{1}{2}\rho W^2-\frac{1}{2}\rho\omega^2r^2$
P	dimensionless static pressure, Equation 2.1
P_r	dimensionless reduced static pressure, Equation 2.2
P^*	dimensionless rotary stagnation pressure, Equation 2.3
r,θ,z'	cylindrical polar co-ordinates
r_o,R,z''_o	constants in Equation A1.3
R_n	radius of curvature of streamline
Ro	Rossby Number
s,n,b	streamwise, normal and binormal directions - streamwise co-ordinates
s^*	linear period of oscillation
St	rotary stagnation pressure gradient strength, Equation 6.19
t	time
T	Temperature
U	absolute axial velocity
V	absolute velocity
W	relative velocity
x/x_o	meridional inlet-to-outlet co-ordinate, measured along the shroud
y/y_o	pressure side to suction side co-ordinate
z/z_o	hub-to-shroud co-ordinate
z'	direction of axis of rotation
z''	axial distance upstream of the impeller hub at the outlet
γ	blade angle, Appendix 1
ω	angular velocity of passage rotation
Ω	absolute vorticity

ρ	fluid density
$\underline{\nabla}$	Del vector operator
Δ	Finite difference
θ_1, θ_2	probe angles, Section 2.4
ϕ	flow angle, Chapter 6
ϕ^*	angular period of oscillation

Subscripts

i	inlet value
m	meridional value
min	minimum value
max	maximum value
o	outlet value
s	component in streamwise direction
x,y,z	components in x,y,z directions

Superscripts

$\bar{}$	average value (or mass-averaged value, where appropriate)
$\hat{}$	unit vector

CHAPTER 1

A REVIEW OF PREVIOUS WORK ON CENTRIFUGAL COMPRESSORS

1.1 Introduction

The centrifugal compressor has many applications in turbomachines where a high pressure ratio per stage (up to 15:1) is required, but the mass flow rate is relatively low. The commonest applications of the centrifugal compressor are in small gas turbines and in turbochargers. The efficiency of the compressor used in a gas turbine is critical, as every 1% lost in compressor efficiency increases the specific fuel consumption of the gas turbine by about 3%. In 1968, Dean [1] found that although compressor efficiencies of about 90% were not uncommon at low pressure ratios (less than 2:1), the efficiency decreased dramatically with increased pressure ratio and an efficiency for a 10:1 pressure ratio machine was typically only about 75%.

The compact nature of the centrifugal compressor has led to its widespread application in small gas turbines in ships, small aircraft and power generating plant, where its simplicity, light-weight and relatively low cost make it economically viable, despite its relatively low efficiency. The small gas turbine is also often used in place of large reciprocating engines, particularly in situations where light-weight and reliability are of paramount importance, for instance in helicopters and small aircraft. This market has recently been researched by Smith and Benstein [2], who predict an increase in the use of small gas turbines within the next ten years.

The future of the centrifugal compressor therefore looks fairly bright, particularly as many workers in the field (e.g. Dean [1]) believe that the relatively low efficiency is not inherent and better understanding of flow phenomena experienced in the centrifugal compressor could improve their design, such that their

efficiency is increased to perhaps 90% at pressure ratios as high as 8:1.

The aim of this chapter is to look at the development of the centrifugal compressor geometry, together with the observations made of the flow phenomena within the impeller channels and the attempts made at theoretical prediction of these phenomena.

1.2 The basic fluid mechanics of the centrifugal compressor

The simplest analysis available to the theoretician, which can only be applied to inviscid flows, is essentially based on Euler's equation, which can be expressed along a relative streamline within a rotor as

$$dp - \rho\omega^2 r dr + \rho W dW = 0 \qquad -1.1$$

From this equation the change in static pressure through a rotor is given by

$$\Delta p = \underbrace{\int_{\text{Inlet}}^{\text{Outlet}} \rho d(\tfrac{1}{2}\omega^2 r^2)}_{\text{Centrifugal Term.}} - \underbrace{\int_{\text{Inlet}}^{\text{Outlet}} \rho d(\tfrac{1}{2}W^2)}_{\text{Diffusion Term.}} \qquad -1.2$$

The first term is the centrifugal pressure rise, which will be achieved almost independently of the internal flow through the rotor. The second term gives the pressure rise due to the diffusion of the relative flow.

Based on this equation, the designer wishing to achieve the maximum pressure rise conceives an impeller with a high ratio between the outlet and inlet radii and with impeller passages which increase in area between the inlet and outlet. This flow model, however, poorly represents the true state of affairs, as the velocity profile at the exit of a centrifugal impeller passage is always found experimentally to be very non-uniform.

1.3 Early experimental and theoretical work

It was suggested as early as 1902 by J.A.Smith [3](reported by Gibson [4]) that "under certain conditions the flow tends to leave

the leading face (suction side) of a centrifugal pump impeller passage. The flow then passes along the trailing face (pressure side) and there is a region of 'dead' fluid on the leading face." Carrard [5,6] in 1923, made pressure measurements within a 2-dimensional radial flow impeller. His results showed regions of 'dead' fluid (subsequently referred to as 'wake' fluid) originating at the leading edge of the blades on either the suction side at low flow rates or on the pressure side at high flow rates. But, more significantly, he observed that at certain intermediate flow rates, the wake region started on the suction surface, but away from the impeller inlet. Similar results have since been obtained by other authors in rotating diffusers (e.g. Moore [7]).

Carrard also calculated the velocity distribution in the jet using Flugel's [8] streamline curvature method assuming a zero velocity for the fluid in the wake. This streamline curvature method equated the centrifugal and Coriolis accelerations ($-\omega^2 r$ and $2\omega W$ respectively) with the relative accelerations of the fluid particle (dW/dt and $-W^2/R_n$). Carrard considered this equilibrium only in the blade-to-blade plane as his impeller was 2-dimensional and he used an expression, similar to Equation 1.1, in the streamwise direction

$$\frac{dp}{ds} = -\rho W\frac{dW}{ds} + \rho\omega^2 r\frac{dr}{ds} \qquad -1.3$$

and in the normal direction he obtained

$$\frac{dp}{dn} = \frac{\rho W^2}{R_n} - 2\rho\omega W + \rho\omega^2 r\frac{dr}{dn} \qquad -1.4$$

These equations were then used together to eliminate the pressure p

$$2\omega - \frac{dW}{dn} - \frac{W}{R_n} = 0 \qquad -1.5$$

and this equation was integrated assuming R_n to be constant to obtain an expression for the relative velocity in the jet. Carrard was also able to model the separated flow assuming that the relative velocity was zero within the wake and that no diffusion occurred in the jet

after the wake had formed.

This method gave remarkably good agreement with Carrard's experimental results and this two dimensional flow analysis was used to explain observed 'jet-wake' flow patterns for many years [9,10].

The result of separation of the flow from the suction surface of the blade and the development of the wake is to, in effect, block off a considerable proportion of the passage's cross-sectional area. This reduction in the passage's effective outlet area reduces the relative diffusion of the flow and hence reduces the static pressure rise achieved by the impeller.

1.4 The first observations of 3-dimensional flow phenomena

In the 1950's, NACA undertook a major programme of research, which was described by Hamrick et al. [11,12]. The results presented by Hamrick of velocities, static pressures and stagnation pressures were from measurements in an almost 2-dimensional radial flow impeller. Hamrick observed separated flow regions similar to Carrard's, but even though Hamrick's impeller had only a fairly weak curvature in the meridional plane, the flow exhibited large non-uniformities in the hub-to-shroud direction. Tip leakage at the shroud was probably responsible for some of these 3-dimensional features of the flow, particularly close to the discharge of the impeller, but it was concluded by Moore, Moore and Johnson [13] that some of the 3-dimensional flow features, which Hamrick observed, were due to the curvature in the meridional plane.

More recent results for 2-dimensional or almost 2-dimensional impellers have been presented by Fujie [14], Fowler [15], Lennemann and Howard [16,17,18] and most recently by Olivari and Salaspini [19]. In each study the discharge velocities clearly show a wake flow and in many cases non-uniformities are present in the hub-to-shroud direction as well as in the blade-to-blade direction.

By the late 1940's, the 2-dimensional radial compressor was

being superceded by the machine which received an axial flow at the inlet. The impellers of these machines had an inducer to turn the relative velocity, which had a substantial circumferential component, to the axial direction and an axial-to-radial bend to turn the flow into the radial section of the impeller. It was therefore becoming necessary to analyse the flow in the meridional plane as well as in the blade-to-blade plane.

1.5 Flow theory for a 3-dimensional impeller

Let us consider a flow in an impeller with passage curvature in the blade-to-blade and meridional directions. The streamline curvature methods used by Carrard can still be applied, but we must write the equations in a more general, 3-dimensional form.

The general equation of motion, in vector notation, is, for an inviscid fluid,

$$\frac{1}{\rho}\underline{\nabla}p = -(\underline{W}.\underline{\nabla})\underline{W} - 2\underline{\omega}x\underline{W} - \underline{\omega}x(\underline{\omega}x\underline{r}) \qquad -1.6$$

which is a statement of Equations 1.3 and 1.4 in vector form.
We now also need the continuity equation

$$\underline{\nabla}.(\rho\underline{W}) = 0 \qquad -1.7$$

but although these two vector equations (1.6 and 1.7) are sufficient to solve for p and $\underline{W}$ in an incompressible flow, we need a further thermodynamic relation between the fluid properties p and ρ for an inviscid, compressible flow. The normal further assumption is that the flow is not only frictionless, and hence reversible, but is also adiabatic. This means the flow is isentropic and so

$$\frac{p}{\rho^{\gamma}} = \text{Constant} \qquad -1.8$$

Sometimes, it is more appropriate to assume that the flow is isothermal, which assuming also that the fluid is a perfect gas, we can use the relation

$$\frac{p}{\rho} = RT = \text{Constant} \qquad -1.9$$

It is therefore possible to solve equations 1.6, 1.7 and 1.8 or 1.9

to obtain the distributions of pressure and relative velocity throughout the impeller.

Now, in an incompressible flow, by writing the reduced static pressure $p_r = p - \frac{1}{2}\rho\omega^2 r^2$, Equation 1.6 becomes

$$\frac{1}{\rho}\underline{\nabla} p_r = -(\underline{W}.\underline{\nabla})\underline{W} \quad - \quad 2\underline{\omega}x\underline{W} \qquad -1.10$$

Streamline Curvature. Coriolis.

We can see from this equation that gradients of reduced static pressure will result because of curvature or because of rotation. This equation can be integrated to obtain Bernoulli's equation in a rotating co-ordinate frame

$$p^* = p_r + \frac{1}{2}\rho W^2 \qquad -1.11$$

Let us now consider the effects that the curvature and rotation are to have on an inviscid, incompressible (i.e. potential*) flow through the impeller.

At the impeller inlet the static pressure p and the axial velocity U are assumed to be uniform. In the rotating co-ordinate frame however, the circumferential velocity component (ωr) is higher on the shroud than on the hub and therefore a higher relative velocity and lower reduced static pressure (Equation 1.11) will result at the shroud. As the blades load through the inducer bend, a blade-to-blade pressure gradient will be induced and so the velocity on the suction side will be higher than on the pressure side. The magnitude of the blade-to-blade pressure difference can be calculated from the radius of curvature of the inducer bend using the first term on the right hand side of the streamline curvature equation 1.4.

The fluid then flows around the axial-to-radial bend, the blade-to-blade pressure gradient due to the inducer bend is gradually replaced by the blade-to-blade pressure gradient induced by the Coriolis forces. This loading of the blades by the Coriolis forces

*where the absolute velocity is irrotational

is calculated from the second term on the right hand side of Equation 1.4. The hub-to-shroud pressure gradient, which turns the flow around the axial-to-radial bend, is again calculated according to the streamline curvature term (first term on the right hand side) in Equation 1.4.

Finally, the hub-to-shroud pressure gradient disappears as the passage becomes radial, leaving just the blade-to-blade pressure gradient due to the passage rotation. Potential flow theory then predicts a flow of low relative velocity on the pressure side and high relative velocity on the suction side of the passage. As the fluid gets to the outlet, the blades will unload and the flow will once more become uniform in relative velocity and reduced static pressure.

1.6 Three-dimensional flow phenomena

Several authors [20,21,22,23] have recently presented papers showing observations of relative velocity over the outlet plane of 3-dimensional impellers. In all these studies wakes were observed in the outlet plane and in most cases the flow velocities were neither uniform in the blade-to-blade nor the hub-to-shroud directions. A potential flow model therefore is not sufficient to model the outlet flow even approximately.

The flow prediction techniques adopted in the 1960's were essentially potential flow streamline curvature calculations, only a proportion of the impeller outlet area was assumed to be blocked by the wake fluid. The value of this blockage factor was determined empirically. This type of calculation was usually performed in either the meridional plane (e.g. Wood and Marlow [24] and Hamrick et al. [25]) or in the blade-to-blade plane (e.g. Katsanis [26]), and so was only a 2-dimensional flow model. These techniques worked reasonably well in operating zones in which designers were experienced, but as pressure ratios and operating speeds increased in order

to improve the overall performance of the gas turbine, new compressors often fell short of their predicted performance, as noted by Dean [1].

The main drawback of these prediction techniques was that designers could not predict where the wake might first develop, what position the wake would adopt in the outlet plane and how much blockage the wake would present to the outlet flow. Fortunately, some light was being thrown on these 3-dimensional aspects of the flow by theoreticians working on secondary flow.

1.7 Secondary flow theory

In a potential flow, the rotary stagnation pressure p^* is uniform throughout the flow field. However, in a real viscid flow, the rotary stagnation pressure may be uniform at the inlet, but either because of a subsequent separation of the flow or just by viscous losses occurring in the boundary layers, areas of low p^* fluid will develop.

In the 1950's, various authors [27,28,29] published papers, which described how a streamwise component of vorticity would be generated, whenever fluid with a gradient of p^* was present in a curved or rotating passage. Their analyses were extended, in 1973 by Lakshminarayana and Horlock [30], to compressible, viscid flows, but here, in this thesis, we only consider how gradients of p^*, already present in the flow field, would be convected along a streamline, without considering the modification of the p^* gradient by the viscous forces present.

The equation governing generation of absolute streamwise vorticity was presented recently by Hawthorne [31] in the simple form

$$\frac{\partial}{\partial s}\left(\frac{\Omega_s}{W}\right) = \frac{2}{\rho W^2}\left(\underbrace{\frac{1}{R_n}\frac{\partial p^*}{\partial b}}_{\text{Curvature Term.}} + \underbrace{\frac{\omega}{W}\frac{\partial p^*}{\partial z'}}_{\text{Rotation Term.}}\right) \qquad -1.12$$

In the Equation 1.12, $p^*=p+\frac{1}{2}\rho(W^2-\omega^2r^2)$ is the rotary stagnation pressure, W is the fluid velocity relative to the rotor and ωr is the rotor circumferential velocity. The equation is expressed in streamwise co-ordinates where, s is the streamwise direction, n is the normal direction and b is the binormal direction. The two terms contributing to the generation of streamwise vorticity are due to, (1) the centrifugal forces due to the curvature of the relative streamline with a radius R_n and (2) the Coriolis forces due to the passage rotation with angular velocity ω, about the axis of rotation z'. These two terms are associated with gradients of p* in the binormal and axial directions respectively.

Let us consider the fluid flow through a pipe bend. Boundary layers will develop on the pipe walls and the gradients of p* in these boundary layers will result in the generation of streamwise vorticity. The effect of this vorticity is to induce secondary flow in the boundary layer, which convects low p* fluid towards the inside of the pipe bend. There are two points, one on the inside and one on the outside of the bend, where the gradient of p* is in the normal direction and hence the value of $\frac{\partial}{\partial s}\left(\frac{r_s}{W}\right)$ is zero and therefore at these points no streamwise vorticity is generated. If a particle of low p* fluid is displaced slightly from the point on the outside of the bend though, it will flow around the pipe wall towards the inside of the bend. However, a low p* fluid particle displaced from the inside of the bend, will simply return to the same position.

1.8 Stable location of low p* fluid

The stable location of low p* fluid is defined, by the author, as the point on the wall of a stationary or rotating passage, where a gradient of p* in the boundary layer can exist without any net generation of streamwise vorticity, and if the orientation of fluid with this gradient of p* suffers a small disturbance, it will tend to return to its original orientation. There are several important

consequences that follow from this definition:

(1) As the value of $\frac{\partial}{\partial s}\left(\frac{r_s}{W}\right)$ is zero at the stable location for low p* fluid, either the gradient of p* at this point is in a direction perpendicular to both the binormal and axial directions or the two terms on the right hand side of Equation 1.12 are equal in magnitude, but opposite in sign.

(2) The stable location for low p* fluid is also the point to which all low p* fluid in the passage will tend to move.

(3) The stable location for low p* fluid is coincident with the position of the minimum reduced static pressure ($p_r=p-\frac{1}{2}\rho\omega^2r^2$). This can be shown by considering the boundary layer on the wall close to the point of lowest p_r. The lowest p* fluid in the boundary layer will be the fluid with the lowest relative velocity and will therefore be found very close to the wall. This fluid will not experience accelerations due to either curvature or rotation, as its relative velocity is approximately zero, and it will therefore under the influence of the p_r gradients, accelerate towards the region of minimum p_r. It is clear therefore that the point of minimum p_r is also the stable location for the lowest p* fluid.

1.9 Secondary flow in the centrifugal impeller

In the centrifugal compressor impeller, with radially ending blades, there are two bends, the inducer and the axial-to-radial bend, which will both lead to secondary flow in the boundary layers; in addition, there will be secondary flow generated due to the passage rotation.

1.9.1 The inducer bend

Firstly, let us consider the inducer bend, which reduces the circumferential component of the relative velocity. There will be secondary flows generated by the Coriolis forces, which tend to move low p* fluid up towards the shroud and there will also be secondary flows generated by the inducer's curvature which will convect low

p* fluid towards the suction surface (i.e. the inside of the inducer bend). The stable location for low p* fluid will therefore be somewhere between the centres of the suction surface and the shroud, the exact position being dependent on the relative strengths of the two contributions to secondary flow.

The relative magnitudes of these contributions to secondary flow, due to curvature and due to rotation, can be compared by evaluating the Rossby Number ($Ro=W/\omega R_n$). As can be seen from the streamwise vorticity Equation 1.12, if the Rossby Number is large, the flow will be dominated by curvature and if it is small, the flow will be dominated by the rotational effects. The Rossby Number for the inducer bend is about 0.25 for most impellers (Reference Lakshminarayana and Horlock [30]) and hence passage rotation will have a more dominant effect than the inducer bend's curvature on the development of secondary flow in the inducer. It is therefore reasonable to predict that the stable location for low p* fluid, in the inducer bend, will be closer to the centre of the shroud than the centre of the suction surface. A flow similar to the flow in the inducer has been studied recently by Anand and Lakshminarayana [32].

1.9.2 The axial-to-radial bend

The axial-to-radial bend has its curvature orientated at 90 degrees to the curvature of the inducer bend. The curvature of this bend induces secondary flows which tend to move low p* fluid in the boundary layers, towards the shroud. The secondary flows induced by the passage rotation are due to the Coriolis acceleration ($2\underline{\omega}x\underline{W}$) and therefore the generation of streamwise vorticity is proportional to the component of relative velocity in a plane perpendicular to the axis of rotation. This velocity component will get larger through the axial-to-radial bend, reaching a maximum in the final radial section of the impeller. The Coriolis forces generate secondary flows which tend to move low p* fluid in the boundary layers towards

the suction surface.

The Rossby Number associated with the axial-to-radial bend is close to unity (e.g. Eckardt's impeller Ro=0.7), so close to the end of the axial-to-radial bend the secondary flows generated because of the bend's curvature are likely to be as significant as those generated because of the passage rotation.

This secondary flow theory tells the designer how low p* fluid will be convected and where it is likely to accumulate in his impeller. However, it does not tell him how much low p* fluid he can expect in his discharge flow or what the distribution of values of p* will be in the wake. In order to predict this, it is necessary to add loss mechanisms to the theoretical model and then the secondary flow model will convect this low p* fluid as it is produced.

1.10 Losses in the impeller

Dean [1] divides the losses in the impeller into four main areas: (1) Wall friction, (2) leakage, (3) mixing and (4) secondary flow.

1.10.1 Wall friction and leakage

The wall friction is usually modelled by a 2-dimensional turbulent boundary layer model. However, this model takes no account of any 3-dimensional effects. Tip leakage is usually modelled as flow through a simple gap, taking no account of the moving blades and the stationary shroud. Dean [1] concludes however, that there is little justification for improving these models as the p* losses they initiate are fairly small anyway, for most impellers.

1.10.2 Mixing

Johnston [33,34,35,36] and Bradshaw [37,38] have studied the influences of curvature and rotation on turbulent mixing in rotating passages. Mixing can be modelled as a transfer of momentum between fluid particles travelling at different velocities. If we consider a shear layer, we can model the mixing in the layer, by allowing an

exchange of fluid from one level of the shear layer to a neighbouring level of the shear layer and then by momentum and energy considerations, we can calculate the change in velocity for each level of the shear layer. Mixing models of this type have been used for stationary, straight ducts for many years. However, associated with a shear layer there will be a gradient of p*, so if the shear layer experiences curvature or Coriolis acceleration, secondary flows can develop, which can either assist or resist the exchange of fluid between the levels of the shear layer. It is therefore apparent that low p* regions, close to the stable location for low p* fluid, will tend to mix out slowly, whereas low p* fluid in other locations will mix out more rapidly.

In a centrifugal impeller, mixing is suppressed only weakly in the inducer and so mixing models, which are used for simple pipe flows, are often used. In the axial-to-radial bend however, mixing is strongly suppressed on the shroud, which is the usual location for the appearance and development of a separated flow region. In the final radial section of the impeller, Coriolis forces will suppress mixing close to the suction surface, which is often the location of the wake, but should the wake be on the shroud, more rapid mixing out may be expected.

1.10.3 Secondary flow

Dean [1] considered the kinetic energy of secondary flows as being a loss and he concluded that this kinetic energy was fairly small as this has been shown to be the case for axial machines by Lakshminarayana and Horlock [39]. However, it is clear that secondary flow will have a strong influence on wall friction losses, the separation which leads to the formation of the wake and the mixing losses which occur between the fluid in the wake and in the jet.

1.11 The diffuser

The efficiency of the centrifugal compressor is, of course,

dependent not only on the flow in the impeller, but also on the losses in the diffuser. There are two contributions to the loss in stagnation pressure in the diffuser; firstly, the wall friction which, as for the impeller, is fairly small and secondly, the main loss, due to the mixing out of the impeller discharge flow.

The diffuser's performance therefore, is to a large extent dictated by the flow which is delivered to it. As experimental results [20,21,22,23] have shown, this flow is usually highly non-uniform with an extensive wake region residing on the suction surface or on the shroud.

In 1960, Dean and Senoo [40] presented a 2-dimensional analysis of the flow through a vaneless diffuser. Their analysis was made in the blade-to-blade plane, assuming uniformity in the hub-to-shroud direction, and was therefore only applicable where the wake was on the suction surface in the discharge flow from the impeller. Comparisons of experimental results and this flow model showed good agreement and also that the non-uniform flow from the impeller outlet very rapidly mixed out into a uniform flow in the diffuser. This rapid mixing occurs because the strong gradients of p* present within the impeller are no longer protected by Coriolis forces when they reach the diffuser.

The flow model of Dean and Senoo was simplified by Johnston and Dean in 1966 [41], by assuming that the mixing between the jet and the wake fluid occurred instantaneously. This model was compared with the original Dean and Senoo variant by Senoo and Ishida in 1975 [42] and they concluded that for even the most distorted impeller flows, Dean and Senoo's model would be more accurate by a maximum of only about 1% of stage efficiency. It therefore appears that Johnston and Dean's simple flow model will be sufficiently accurate for most diffusers.

Rebernik [43] presented a flow model for a vaneless diffuser in

1972. He assumed the flow to be axisymmetric, incompressible and inviscid and therefore did not include mixing losses. When he compared his calculated streamlines with his experimental results, which showed considerable hub-to-shroud variations, he obtained good agreement. So it appears that, mixing does not have a dominant influence on the flow pattern in the hub-to-shroud plane. It is concluded therefore, as Dean [1] concluded, that mixing in the hub-to-shroud direction proceeds at a much slower rate than in the blade-to-blade direction, in a vaneless diffuser. Further work on vaneless diffusers has been performed by Johnston [44] and Jansen [45,46].

Dean [1] recognised that to improve the diffuser's own efficiency, the lower the absolute velocity of the fluid entering the diffuser, the better. This led many designers to the use of impellers with backward swept blades, the fluid discharging in an almost tangential direction, so that the absolute velocity was approximately the difference between the tangential velocity of the impeller and the relative velocity of the flow. However, in most impellers with radially ending blades, improving internal diffusion decreases both the relative and absolute velocities. This improvement in diffusion therefore, not only improves the impeller's performance, but also improves the efficiency of the diffuser and hence greatly benefits the whole machine.

A chief aim of the impeller designer must therefore be to improve the internal diffusion by increasing the uniformity of the impeller discharge flow and, in order to achieve this, a better prediction of the secondary flows and the effects of the rotation and curvature on turbulent mixing is required.

1.12 Three-dimensional flow models

At the time of writing, various workers are attempting to produce flow models which take into account not only the potential

flow aspects, but also the secondary flows and the viscous losses due to tip leakage, the boundary layer development and mixing. Previously, authors have preferred to calculate the jet and the wake regions separately. The jet region has been calculated as a potential flow [24,25,26,47] and the size of the wake has been predicted by 2-dimensional turbulent boundary layer models and tip leakage models which ignore the passage rotation. Today, authors [13,48,49] prefer to start their calculations from the three momentum equations, derived directly from the Navier-Stokes equation, which takes account of the potential flow, viscosity and the secondary flows, but additional models for the development of the turbulent boundary layers and the mixing, which occurs within the boundary layers, have to be added.

In the next few years, it seems very likely that fairly accurate prediction of the formation and development of the wake within the centrifugal compressor impeller will become possible.

1.13 Recent three-dimensional flow observations

Perhaps the most detailed measurements made within a centrifugal compressor impeller in recent years are those of Eckardt [50,51,52, 53]. Eckardt used a laser-2-focus velocimeter to measure statistically averaged mean values of a flow velocity and a flow angle and he hence obtained two velocity components (approximately in the meridional and circumferential directions) in his impeller flow. These two velocity components are perpendicular to the optical axis of the laser beams, but it was impossible for Eckardt to obtain any information on the third component of velocity in the hub-to-shroud direction, which is parallel to the optical axis. However, Eckardt obtained a remarkably complete picture of the meridional component of velocity at five cross-sectional planes between the inlet and outlet of his impeller, together with the circumferential components of cross velocity which provided an incomplete, but nevertheless

flow aspects, but also the secondary flows and the viscous losses due to tip leakage, the boundary layer development and mixing. Previously, authors have preferred to calculate the jet and the wake regions separately. The jet region has been calculated as a potential flow [24,25,26,47] and the size of the wake has been predicted by 2-dimensional turbulent boundary layer models and tip leakage models which ignore the passage rotation. Today, authors [13,48,49] prefer to start their calculations from the three momentum equations, derived directly from the Navier-Stokes equation, which takes account of the potential flow, viscosity and the secondary flows, but additional models for the development of the turbulent boundary layers and the mixing, which occurs within the boundary layers, have to be added.

In the next few years, it seems very likely that fairly accurate prediction of the formation and development of the wake within the centrifugal compressor impeller will become possible.

1.13 Recent three-dimensional flow observations

Perhaps the most detailed measurements made within a centrifugal compressor impeller in recent years are those of Eckardt [50,51,52, 53]. Eckardt used a laser-2-focus velocimeter to measure statistically averaged mean values of a flow velocity and a flow angle and he hence obtained two velocity components (approximately in the meridional and circumferential directions) in his impeller flow. These two velocity components are perpendicular to the optical axis of the laser beams, but it was impossible for Eckardt to obtain any information on the third component of velocity in the hub-to-shroud direction, which is parallel to the optical axis. However, Eckardt obtained a remarkably complete picture of the meridional component of velocity at five cross-sectional planes between the inlet and outlet of his impeller, together with the circumferential components of cross velocity which provided an incomplete, but nevertheless

informative picture of the 3-dimensional aspects of the flow.

Eckardt's results of the meridional velocity showed the formation of a wake which first appeared at his Station 3, which was situated in the axial-to-radial bend about halfway through his impeller passage. Eckardt observed that the blade-to-blade velocities were still relatively weak at Station 3, which is what might be expected as the secondary flows in this direction are generated by the Coriolis forces, which are fairly weak until the flow has turned to a predominantly radial direction. He was therefore unable to conclude that the formation of the wake was a direct result of the convection of low momentum fluid by the secondary flows. However, it is interesting to speculate whether the formation of the wake, which was observed to occur in a region of high meridional curvature, could have resulted from the convection of low momentum fluid from the suction surface boundary layer by a secondary flow in the hub-to-shroud direction. The Rossby Number for the axial-to-radial bend is close to unity and therefore the secondary flow along the suction surface, generated by the curvature of the axial-to-radial bend, can be expected to be at least as strong as the secondary flow along the shroud, generated by the Coriolis forces in the radial section of the passage. Eckardt observed a strong secondary flow along the shroud in the radial portion of his impeller and therefore it may be presumed that the secondary flow across the suction surface in the axial-to-radial bend may have had a dominant influence on the formation of the wake.

1.14 Contribution of this thesis

Clearly, as Eckardt concluded, further measurements are necessary to improve the understanding of the wake flow in a centrifugal compressor impeller channel. Therefore in this work, in order to gain a complete picture of the steady, 3-dimensional aspects of the impeller flow, all three mutually perpendicular velocity

components were measured. It was also felt to be important to take measurements of the rotary stagnation pressure p* of the fluid, so that the gradients of p* could be observed and hence the generation of secondary velocities predicted and also so that the subsequent movement of low p* fluid could be traced.

In order to allow detailed measurements to be made in this study, a large impeller (Outlet diameter=1metre) was chosen, so that a large number of measurements could be made in the impeller passages. The geometry of the impeller is similar to that of Eckardt's impeller as described by Moore [54] and in particular the Rossby Numbers associated with the two impeller flows are both close to unity.

It is also hoped that the experimental results presented in this thesis are sufficiently detailed that flow modellers will be able to use the data for assessing the accuracy of their flow prediction programs. However, the flow velocities in the experimental work were very low (less than 25m/s) and so the impeller flow must be considered as incompressible. For this reason, little discussion is presented of the effects of compressibility or shock waves. There is also no discussion in this work, of unsteady phenomena such as rotating stall or surge, as although these aspects of the internal flow in modern centrifugal compressors are clearly important, the author felt that they lay outside the scope of this thesis.

CHAPTER 2

THE EXPERIMENTAL RIG AND PROCEDURE

2.1 The Test Rig

The Centrifugal Compressor Rig is shown in a schematic diagram (Figure 2.1) and in a photograph (Figure 2.2). The impeller is from a De Havilland Ghost engine and details of the impeller geometry are given in Appendix 1. A glass fibre shroud, of about 3mm. thickness is bolted to, and therefore rotates with, the impeller, which is driven by an 11 hp,dc electric motor; the running speed of 500 rpm is controlled by a Ward Leonard set. A disc with 60 holes drilled around a diameter is attached to the impeller shaft. A light-sensitive diode and a lamp are mounted either side of the disc, so that a pulse is emitted from the diode whenever a hole passes. These pulses are amplified and transmitted to a frequency counter, which counts for periods of 10 seconds and hence gives the impeller's rotational speed to $\pm$0.1 rpm. The air flow is delivered to the impeller through a duct, containing several wire mesh screens and a honeycomb, which ensure a uniform inlet flow without swirl. The boundary layers are tripped by emery paper on the passage walls at the impeller inlet to ensure that they are turbulent. A rubber seal attached to the inlet duct and running on the outside of the shroud prevents air leakage at the impeller inlet. The flow rate is regulated by the number and mesh-size of the screens and these also produce a total pressure drop, the impeller producing a corresponding increase to bring the fluid's pressure back to atmospheric. No diffuser is fitted so the impeller exhausts directly.

2.2 Traversing Gear

A traversing gear (see Figures 2.4 and 2.5) is driven by a small electric motor, which when supplied with power through slip-rings, moves a measuring probe across one of the 19 impeller passages, which was chosen for detailed flow measurements. The position of the five

measurement stations are shown in Figure 2.6 and are also given numerically in Appendix 2.

The traversing gear has to withstand centrifugal loadings of up to 130 'g', so the motor is mounted with its axis tangential to the impeller's axis of rotation, so that the weight of the armature is taken by the motor's bearings. The motor has a gearbox, the shafts of which are parallel to the motor's axis, so the weight of the gearwheels is also taken by their bearings. The gearbox reduces the shaft speed in the ratio 141:1, which gives an output shaft speed of 60-100 rpm under load. This output shaft turns the leadscrew through a pair of bevel gears.

A microswitch is mounted adjacent to one of two cams, one on the motor shaft and one on the leadscrew. The cam is chosen so that the 'g' loadings are most favourable to the microswitch's operation. The microswitch switches a voltage, supplied to it through slip-rings, once for every revolution of the leadscrew and the number of these electrical pulses is counted by a frequency counter. One revolution of the leadscrew moves the carriage and measurement probe 1 mm, so this gives the probe's position within ± 1 mm.

This traversing gear can be mounted at several positions at each of the first 4 stations (see Figure 2.7), so that the entire cross section at each station can be covered by probe traverses at less than 1 cm intervals. The probe is mounted on the carriage so that the probe passes through a hole in the shroud (see Figure 2.8) such that it can be traversed in the hub-to-shroud direction.

A second traversing gear (Figure 2.9) similar in design to the above one , is used at Station 5, where traverses are made in the suction side to pressure side direction. This traversing gear has the motor axis parallel to the leadscrew, using a dog clutch instead of the bevel gears, and the probe stem is perpendicular to the leadscrew. The depth of the probe tip below the shroud is altered

between successive traverses.

2.3 Pressure measurement

The differential pressures from the measurement probe are converted to electrical signals by 3 sensitive pressure transducers, which are mounted on the impeller flange at a radius of 50 mm (14'g') and with their diaphragms perpendicular to the axis of rotation to minimise the effects of this 'g' loading. The pressure transducers have a calibrated range of $\pm$10 cm H_2O ($\pm$981 N/m^2). They are operated with 5 volt excitation supplied from a uA 7805 voltage regulator. The signals from the pressure transducers are amplified by '725' integrated circuit amplifiers (Circuit diagram-Figure 2.10), which are mounted on a circuit board bolted to the impeller flange. The amplifier voltage gains are about 1000, which gives a sensitivity, for a pressure transducer and amplifier together, of about 1.5 mV per N/m^2. The pressure transducers, voltage regulator and amplifiers are covered with polystyrene to reduce temperature effects when the impeller is rotating.

The amplifiers and voltage regulator are supplied with $\pm$12 volts through slip-rings from a stabilised power supply, the supply being smoothed by capacitors mounted on the impeller flange. The signals from the amplifiers pass through slip-rings and a resistor-capacitor smoothing circuit (time constant=2 seconds) to a digital voltmeter where the voltage can be read to $\pm$0.1 mV (equivalent to $\pm$0.07 N/m^2).

The typical drift of the zero pressure voltage reading of a pressure transducer and amplifier during a traverse (about 30 mins) is $\pm$3 mV ($\pm$2 N/m^2) in a typical reading of 150 mV (100N/m^2). The difference in the zero pressure reading when the impeller is stationary and when it is rotating (due to the distortion of the diaphragm and any cooling of the pressure transducers and amplifiers due to air flow across them) is about $\pm$1 mV ($\pm$0.7 N/m^2).

2.4 Velocity measurements

2.4.1 5-Hole probe

A 5-hole probe constructed from 5 lengths of 0.7 mm outside diameter by 0.4 mm inside diameter hypo dermic tubing soldered into a 300 mm length of 3 mm outside diameter hypo dermic is shown in Figure 2.11. The centre tube (No. 1) is filed perpendicular to its axis and the ends of the surrounding 4 tubes are filed at 45 degrees to their axes. The ends of the tubes are cleaned out with a 0.4 mm drill.

The 5 holes are connected to the pressure transducers so that they measure p_1-p_2, p_1-p_3 and p_4-p_5, the subscript numbers are those of the 5 holes defined in Figure 2.11. The probe is then calibrated in a duct with air travelling at V≐15 m/s (measured by a Pitot-static tube alongside the 5-hole probe) for θ_1 and θ_2 as defined in Figure 2.11 and 3 sets of calibration curves are plotted.

Set A

$$\frac{p_1-p_3}{p_1-p_2} = f(\theta_1) \qquad \text{For } \theta_1 \leq 0$$

$$\frac{p_1-p_2}{p_1-p_3} = f(\theta_1) \qquad \text{For } \theta_1 \geq 0$$

For each value of θ_2

Set B

$$\frac{p_4-p_5}{p_1-p_2} = f(\theta_2) \qquad \text{For } \theta_2 \leq 0$$

$$\frac{p_4-p_5}{p_1-p_3} = f(\theta_2) \qquad \text{For } \theta_2 \geq 0$$

For each value of θ_1

Set C

$$\frac{p_1-p_2}{\frac{1}{2}\rho V^2} = f(\theta_1) \qquad \text{For } \theta_1 \leq 0$$

$$\frac{p_1-p_3}{\frac{1}{2}\rho V^2} = f(\theta_1) \qquad \text{For } \theta_1 \geq 0$$

For each value of θ_2

Where ρ is the atmospheric air density.

The denominator needs to be changed from p_1-p_2 to p_1-p_3 for sets A and B as $p_1-p_2=0$ for $\theta_1 \doteq 22.5$degrees and $p_1-p_3=0$ for $\theta_1 \doteq -22.5$degrees.

These calibration results are shown for the 5-hole probe used in Figures 2.12 to 2.17.

A computer is used to find the best fit cubics for each calibration curve and the coefficients of these cubics are stored on disc.

2.4.2 Velocity measurements in the impeller

All the readings taken during an experimental run are recorded directly onto paper tape, so that they can be transferred to the computer quickly and accurately.

Before a run commences, the 5-hole probe is fitted with a cap, so that the 5 holes are connected to each other, but not to the surrounding air. The impeller is then rotated at the operating speed and the pressure readings for each pressure transducer compared with the reading when the impeller was stationary. If there is a significant difference between the two readings for any of the transducers, there is a leak in one of the pressure lines.

When it has been established that there are no leaks the probe is uncapped and the probe adjusted so that it just touches the shroud when the traversing gear carriage is on its stop and the probe nose is pointing in approximately the relative streamline direction. Atmospheric pressure and temperature, the angle of the probe in the traversing gear (see Figure 2.18) and the zero pressure readings are measured and recorded. The impeller is now run up to speed and the actual running speed is recorded from the frequency counter. The number of leadscrew turns and the 3 pressure transducer readings are now recorded at each measurement point, the traversing motor being switched on to move the probe from one point to the next. At the end of a traverse, the impeller's running speed is recorded again and finally when the impeller is stationary, a second set of zero pressure readings are taken.

2.4.3 Velocity calculation

The computer uses the zero pressure readings before and after the traverse to calculate the drift of the zero pressure readings. It assumes that this drift occurs linearly with the number of readings taken and corrects each pressure reading accordingly. The pressure relations $\frac{p_1-p_2}{p_1-p_3}$; $\frac{p_4-p_5}{p_1-p_2}$ and $\frac{p_4-p_5}{p_1-p_3}$ are then calculated for each measurement point.

For each point the computer ini tially sets θ_2 to zero and uses the 'A' curves (Figures 2.12 and 2.13) to calculate θ_1. It then evaluates θ_2 from the 'B' curves (Figure 2.14 and 2.15) and can then return to the 'A' curves to improve its estimate of θ_1 and so on until θ_1 and θ_2 do not vary significantly with further computation. These values of θ_1 and θ_2 are then used with the 'C' curves (Figures 2.16 and 2.17) to calculate the value of $\frac{p_1-p_2}{\frac{1}{2}\rho V^2}$ or $\frac{p_1-p_3}{\frac{1}{2}\rho V^2}$ which were obtained during the calibration. These curves essentially give the proportion of the velocity head ($\frac{1}{2}\rho V^2$) which is obtained between holes 1 and 2 (or 1 and 3) on the 5-hole probe for the calculated values of θ_1 and θ_2. Therefore, from the value of p_1-p_2 (or p_1-p_3) obtained in the experiment , the relative velocity head ($\frac{1}{2}\rho W^2$), where ρ is the air density calculated from the atmospheric pressure and temperature at the time of the experiment, and hence W, the relative velocity of the air, can be calculated. The relative velocity is then corrected for the actual impeller running speed, assuming that this drifts in the same way as the zero pressure reading i.e. between the 2 readings taken and assuming that the relative velocity of the air is proportional to the running speed. The velocity of the air, along with its direction, has therefore been measured with an estimated accuracy of $\pm$1 m/s, in a relative velocity of 10 m/s, and $\pm$5 degrees in flow direction.

2.5 Rotary Stagnation Pressure measurements

The rotary stagnation pressure $p^*=p+\frac{1}{2}\rho(W^2-\omega^2r^2)$ is the pressure which is measured by a total pressure probe in a rotating passage.

2.5.1 Kiel probe

The Kiel probe used has the dimensions shown in Figure 2.19. One pressure transducer is used between the probe and a tapping on the impeller shaft which, because the shaft is hollow and is open at the opposite end to the impeller, connects the pressure transducer to atmospheric pressure. The procedure for measurements of p^* is very similar to that for the velocities except no calibration is required, the Kiel probe being fairly insensitive to flow direction (see Figure 2.20). The readings are corrected for the impeller running speed, assuming that p^* relative to atmospheric pressure is proportional to the impeller running speed squared. The estimated accuracy of the p^* measurements is ± 10 N/m^2.

2.5.2 Reduced Static Pressure

The reduced static pressure $p_r=p-\frac{1}{2}\rho\omega^2r^2$ is calculated from the measured values of p^* and relative velocity and the estimated accuracy of p_r is ± 40 N/m^2 in regions of high shear and ± 20 N/m^2 elsewhere.

2.5.3 Characteristic values of p*

The screens and honeycomb reduce the stagnation pressure of the air to a value below atmospheric pressure, but ensure that the stagnation pressure is uniform over the inlet cross section. This uniform stagnation pressure at the inlet will subsequently be referred to as p^*_{max}. p^*_{max} is the highest value of p^* that will be found throughout the impeller flow.

The fluid with the lowest values of p^* (p^*_{min}) in the impeller inlet is fluid with low relative velocity in regions of low reduced static pressure $p_r=p-\frac{1}{2}\rho\omega^2r^2$. The regions of lowest p_r are found in the inlet plane near the shroud and usually on the suction side of

the blades, if the blades are correctly loaded and the lowest relative velocity is clearly zero in the boundary layer at the passage wall.

$p^*_{max}-p^*_{min}$ corresponds to the maximum dynamic pressure of the potential flow, which is often used to estimate the pressure recovery in centrifugal impellers.

2.5.4 Dimensionless Pressures

The dimensionless rotary stagnation pressure P*, reduced static pressure P_r and static pressure P are defined as

$$P^* = \frac{p^* - p^*_{min}}{p^*_{max}-p^*_{min}} \qquad -2.1$$

$$P_r = \frac{p_r - p^*_{min}}{p^*_{max}-p^*_{min}} \qquad -2.2$$

$$P = \frac{p - p^*_{min}}{p^*_{max}-p^*_{min}} \qquad -2.3$$

P* clearly varies between zero and one, a value of 1 corresponding to the potential flow (regions where viscosity has had no influence) and a value of 0 corresponding to the regions of p^*_{min} mentioned earlier.

P_r can also vary between 0 and 1. The value zero again corresponding to the p^*_{min} regions and the value of 1 is found in regions where all the dynamic pressure has been recovered as the fluid comes to rest due to diffusion of the flow.

P can take any positive value.

2.6 Presentation of the results

2.6.1 Relative velocities

The relative velocities are presented for each measurement station as contours representing the velocity component perpendicular to the measurement plane and the remaining velocity component, in the measurement plane, is represented by an arrow at each measurement

point.

The measurement planes are not perpendicular to the passage walls, particularly noticeably in the inducer bend where therefore, there is always a velocity component from the suction side to the pressure side of the passage. In the impeller, the suction and pressure surfaces diverge while the hub and shroud surfaces converge, so in the diagrams there are components of velocity in the measurement plane close to the walls in a direction perpendicular to them. As measurements of velocity could not be made very close to the passage walls, because of the size of the probe used, the velocities in the diagrams are not zero at the walls.

2.6.2 Mass Flow Rates

The measured relative velocities, at the measurement points, are extrapolated onto a 50 by 50 grid covering each measurement plane and these extrapolated values are integrated to calculate the mass flow rates, which are estimated to be accurate within $\pm$6%.

2.6.3 Rotary stagnation pressure P*

These measurements are presented in dimensionless form as P*. Again as measurements could not be made close to the walls, the strong gradients of p* in the boundary layers on the passage walls do not appear in the results.

2.6.4 Dimensionless reduced static pressure

The experimental results for the relative velocity and p* are extrapolated onto a 50 by 50 grid covering the measurement plane. These extrapolated values at the grid points are used to calculate $P_r = P^* - \frac{\frac{1}{2}\rho W^2}{p^*_{max} - p^*_{min}}$.

As P_r is almost constant, in a direction perpendicular to a wall, through the boundary layer, the values of P_r at the passage walls in the figures will be approximately the values which would have been obtained from static pressure tappings.

CHAPTER 3

EXPERIMENTAL RESULTS FOR A DESIGN FLOW

3.1 Introduction

The details of a 'design' flow, with approximately zero incidence at the blade leading edge, are presented in this chapter.

3.2 Inlet flow

The stagnation pressures measured in the inlet duct, shown in Figure 3.1, indicate that the inlet flow has a uniform value of $p^*=-270N/m^2$ gauge ($\pm 10N/m^2$). This value of p^* is therefore chosen as p^*_{max}.

The velocity diagram (Figure 3.2) shows that the axial velocity is fairly uniform across the duct's cross-section with an average value of 6.9m/s ($\pm$1.2m/s). The circumferential velocity component (=-0.5m/s) shows that a slight swirl exists,particularly close to the hub due to the rotation of the impeller nose. The hub-to-shroud or radial component of velocity is attributable to the blockage presented by the nose, which induces an elliptical flow in the meridional plane.

The axial velocities are numerically integrated over the duct's cross-sectional area to obtain a total flow rate of 2.0 ($\pm$0.3)kg/s. The equivalent average flow rate through one impeller passage must therefore be 0.10 ($\pm$0.02)kg/s.However, as seen from Appendix 3, the flow rate through the particular passage chosen is 0.14 ($\pm$0.01) kg/s, which is 40% above the average and it must therefore be concluded that the flow rates through each of the 19 impeller passages differ considerably.

3.3 Station 1

The passage flow rate of 0.14 ($\pm$0.01)kg/s is only slightly higher than the flow rate of 0.13kg/s, which is calculated from the inlet velocity triangles to give zero incidence angles at the blade leading edge. Indeed, the incidence angles at Station 1 (approx-

imately 6mm downstream of the leading edge) presented in Figure 3.3, show that the incidence is relatively small. The blade leading edges present a blockage for the inlet flow, which varies from 46% at the hub to 1% at the tip. This blockage induces an elliptical flow around the blade leading edges, in the blade-to-blade plane and therefore the incidence angles relative to the blade camber line are positive on the suction side and predominantly negative on the pressure side.

The variation in inlet velocity between the hub and the shroud, which is observed in Figure 3.5, is also associated with the leading edge blockage. The velocity contours in Figure 3.5, represent contours of the axial component of velocity at Station 1. These show that the fluid near the shroud has accelerated in the axial direction, as it enters the passage and therefore fluid from the lower half of the passage is moving in the hub-to-shroud direction to make up the increased flow. The maximum relative velocity (=22.6m/s) at Station 1 was measured close to the suction-side/shroud corner and the lowest value of p^*, p^*_{min}, will therefore be found on the wall close to this measurement point. The estimated value of p^*_{min} is $-585 N/m^2$ gauge.

The reduced static pressure diagram (Figure 3.6) shows the gradient of p_r in the hub-to-shroud direction due to the centrifugal acceleration. The pressure is also slightly higher on the pressure side than on the suction side, so the blades are lightly loaded. The minimum p_r occurs in the shroud/suction-side corner region ($P_r < 0.05$ at $y/y_0 = 0.75; z/z_0 = 1.0$). Within this region at the wall, fluid with the lowest p^* ($P^* < 0.05$) at Station 1, will occur, however this doesn't appear on the p^* diagram (Figure 3.4), as the Kiel probe could not be brought close enough to the passage wall to measure p^* within the thin boundary layer. Figure 3.4 also shows that little or no losses have occurred and the flow is therefore

essentially a potential flow.

3.4 Station 2

Close to the shroud there is a large adverse gradient of reduced static pressure, particularly between Station 2 and 3, as shown by the minimum values of P_r, -0.03 and 0.29 respectively, in the two reduced static pressure diagrams (Figures 3.9 and 3.12 respectively). This pressure rise occurs as the fluid reduces its tangential velocity, and hence its relative velocity, as it turns through the inducer bend. In this region near the shroud, at both Stations 2 and 3, the measured pressures were observed to be very unsteady and the flow probably exhibited reversed flow and large scale turbulence. This turbulence would enhance mixing, which could well explain the substantial increase in the amount of low p* fluid, which occurred in the suction-side/shroud corner region between Stations 1 and 2 (see Figure 3.7). However, there then appears to be a smaller increase in the amount of low p* fluid between Stations 2 and 3 (see Figure 3.10). This difference could be explained by modifications to the turbulence intensities by rotation and curvature.

The shroud boundary layer will be stabilised by Coriolis forces ($2\rho\underline{\omega}x\underline{W}$) in the early part of the inducer, but once the relative velocity has turned to the axial direction, these stabilising forces vanish. The curvature of the axial-to-radial bend also stabilises the shroud boundary layer and as this stabilisation is relatively stronger than the Coriolis stabilisation of this boundary layer, it is concluded that it is curvature which reduces the turbulent mixing close to the shroud and prevents a further large loss in p* between Stations 2 and 3.

On the hub surface, the boundary layer does not tend to separate as there is little or no pressure rise in the streamwise direction near the hub. In addition, secondary flows cause boundary

layer fluid to move from the hub wall onto the suction and pressure surfaces as shown in Figures 3.8 and 3.11. The region of low p* fluid observed on the suction side wall in Figure 3.7 is due to the thickening of the boundary layer caused by these secondary flows. Figure 3.8 shows that this low p* fluid is moving up the suction side wall to a point at approximately $z/z_0=0.6$. The stable location for this low p* fluid is in the suction-side/shroud corner, where the reduced static pressure is lowest. However, as P_r is increasing in the streamwise direction in this corner region, the flow here is decelerating and diverging. Hence cross velocities are induced, away from the corner, which oppose the secondary flow up the suction surface and so prevent the low p* fluid from reaching the corner region.

It is interesting that the large change in the distribution of P* between Stations 1 and 2 is not reflected in a similar change in the velocity distributions in Figures 3.5 and 3.8. The P* contours therefore offer an early indication of the development of a wake, which the velocities alone would not provide.

The blade-to-blade pressure gradient for the inducer bend at Station 2 can be approximately modelled by the streamline curvature equation

$$\frac{\partial p_r}{\partial r} = \frac{\rho W^2}{R_n} \qquad -3.1$$

Taking R_n for the inducer bend at Station 2 as 200mm and $\overline{W}$=12m/s, the calculated value for the blade-to-blade pressure gradient at about mid-height is $\Delta P_r=0.17$, which is of the same magnitude as the measured value. This pressure difference is larger near the shroud, where the relative velocities are higher ($\overline{W}$=17m/s) and the blade-to-blade distance is larger. The calculated value is $\Delta P_r=0.50$, which again compares well with the measured value.

3.5 Station 3

Station 3 is approximately halfway along the passage and the flow has turned through 58degrees of the axial-to-radial bend.

The reduced static pressure gradient required to turn the flow around the axial-to-radial bend can again be calculated from the streamline curvature equation 3.1. For the axial-to-radial bend, R_n=200mm and $\overline{W}$=12m/s, which gives a calculated hub-to-shroud pressure difference of ΔP_r=0.35, which is close to the measured value in most of the potential flow region (see Figure 3.12).

The velocity diagram (Figure 3.11) shows that the axial-to-radial bend is dominating the secondary flow pattern. The passage is occupied by two opposing vortices; an anticlockwise vortex on the suction side and a second, weaker, clockwise vortex on the pressure side of the passage. This is the pattern which is characteristic of a stationary axial-to-radial bend, but here there is evidence of a secondary flow along the shroud towards the suction side corner, which is generated by Coriolis forces due to the passage rotation. This flow along the shroud, together with the flow up the suction side, has convected the low p* fluid on these two walls at Station 2 into the shroud/suction-side corner region, as shown in Figure 3.10.

3.6 Station 4

At Station 4 , the passage is almost radial. The reduced static pressure distribution is therefore dominated by the tangential, blade-to-blade, gradient of pressure due to the Coriolis acceleration. This is seen in Figure 3.15, where the static pressure falls almost linearly from the pressure side to the suction side near the hub. Near the shroud however, the pattern is broken by a uniform pressure region in the wake.

This pressure gradient can be modelled fairly simply as due to

a radial flow with a mean velocity $\overline{W}$=12m/s. The tangential pressure gradient is then given by the simple expression

$$\frac{1}{r}\frac{\partial p_r}{\partial \theta} = -2\rho\omega W \qquad -3.2$$

In the impeller at Station 4, the tangential distance between the suction and pressure side walls is about 0.11m, hence we obtain a simple estimate for the pressure difference between the blade surfaces of 0.54. This agrees well with the measured static pressure difference of about 0.50.

The stable location for low p* fluid in the radial section of the passage is the suction side, which is also the position of the lowest reduced static pressure (see Figure 3.15), as would be predicted for a straight rotating channel. However, although the axial-to-radial bend has but a small influence on the p_r distribution, its influence remains in the inertia of the secondary flow vortices observed at Station 3 (see Figure 3.14). The flow up the suction and pressure surfaces to the shroud has weakened considerably, but low p* fluid is still being convected up the suction surface to the shroud. As illustrated by the velocities (Figure 3.14) and the p* contours (Figure 3.13), the wake has moved further along the shroud, its core now being at y/y_0=0.7, even though the stable location for low p* fluid has moved the other way. This movement must be attributed to the inertia of the anticlockwise vortex on the suction side of the passage. The second vortex, the clockwise one on the pressure side of the passage, has been greatly augmented along the shroud, by the action of Coriolis forces. The low p* fluid in the secondary flow up the suction side and in the secondary flow along the shroud collide on the shroud at y/y_0=0.7 and this causes low energy fluid to move away from the wall.

In the shear layer between the wake and the potential flow

region at Station 4 turbulent mixing is suppressed by the action of curvature and Coriolis forces.

3.7 Station 5

Station 5 is close to the impeller exit and the passage is still radial as shown in Figure 2.6.

The p* contours (Figure 3.16) show that the wake area has increased considerably between Stations 4 and 5 and that the minimum value of P*=0.52 observed at Station 5 is higher than the minimum value of P*=0.44 obtained at Station 4. The only flow mechanism by which the rotary stagnation pressure p* of a fluid particle can increase along a streamline is by mixing with neighbouring fluid particles which have higher values of p*. So, the lowest p* fluid observed at Station 4 must have mixed out with higher p* fluid between Stations 4 and 5. Turbulent mixing was suppressed at Station 4 by the strength of the pressure gradients but, as can be seen from the p_r diagram (Figure 3.18), these static pressure gradients have weakened because the passage is virtually straight and the blades are unloading close to the impeller discharge. The reduced static pressure on the suction side has risen while that on the pressure side has dropped only slightly. The pressure rise in the wake region is associated with the p* rise achieved by mixing, as no pressure rise can be achieved by diffusion because of the very low momentum of the wake fluid. However, the fluid in the suction-side/hub quarter of the passage has diffused considerably, decelerating from 18 to 13m/s, while the fluid in the pressure-side/shroud corner region has accelerated in order to accommodate the fluid which has diffused from the suction side.

The secondary velocities (Figure 3.17) show the divergence of the highest velocity fluid and this high momentum fluid is the most likely source of potential flow fluid required to mix out with the

wake flow. The cross velocities also show that the secondary flow up the suction side is carrying this high p* fluid into the wake region and a flow from the centre of the high velocity zone at y/y_0=0.75; z/z_0=0.25 is carrying similar fluid to the other side of the wake (y/y_0=0.4; z/z_0=0.9). The general trend in the cross velocities from the suction to the pressure side of the passage is due to the slip of the flow near the outlet. This is most marked on the pressure side of the passage. There is also still some evidence of the secondary flow along the shroud, due to the Coriolis forces, which has not been entirely effaced by the slip.

The wake has moved closer to the suction-side/shroud corner, so the secondary flow along the shroud must have overpowered the opposing secondary flow up the suction surface between Stations 4 and 5. However, the core of the wake is still a long way from its stable location on the suction side of the passage.

The dimensionless reduced static pressure P_r corresponds to the pressure coefficient of potential flow fluid, which has diffused from the maximum relative velocity in the inducer. This pressure coefficient is used by many designers as a simple criterion for 2-dimensional boundary layer growth in a diffusing impeller flow. Clearly, the boundary layer flow in this study is not 2-dimensional, but nevertheless, it is interesting that the value of 0.5 for the wake, is representative of the magnitude of pressure coefficient necessary to cause the separation of a 2-dimensional boundary layer.

3.8 Mass-averaged Pressures

The distributions of reduced static pressure and rotary stagnation pressure can be integrated to evaluate the mass-averaged pressures at each of the five stations. These are presented in Figure 3.19.

The mass-averaged P* shows that the main loss occurs between Stations 1 and 2, where most of the fluid which was close to the

shroud experienced an adverse pressure gradient and vigorous turbulent mixing between the separated boundary layer fluid and the potential flow occurred. There is very little further loss through the impeller.

The mass-averaged P_r shows an increase through the impeller. This represents only part of the static pressure rise through the impeller as, in addition, there is the centrifugal pressure rise $\frac{\Delta(\frac{1}{2}\rho\omega^2 r^2)}{p^*_{max}-p^*_{min}} = 0.72$ compared with the P_r achieved by diffusion of only 0.24.

3.9 Flow property spectra

The passage cross-sectional areas at each of the stations are almost equal. This means that the average velocity component along the passage is also approximately constant as the flow is essentially incompressible. However, because of the large cross velocities at the inlet, the relative velocities do decrease in the inducer bend and this diffusion results in a rise in $\overline{p}_r$. The spectrum of relative velocities (Figure 3.21) shows this reduction in the relative velocities between Stations 1 and 2 and to a lesser extent between Stations 2 and 3. At the same time, the appearance of the wake is illustrated by the ranges of very low relative velocities at Station 3 and it is interesting that although the wake occupies quite a significant proportion of the passage cross-section at Station 3 it contributes very little to the total flow rate there.

The P_r spectrum (Figure 3.22) illustrates the increase in p_r between Stations 1 and 2, but it also shows the drop in the minimum value of p_r present, because of the acceleration which occurred in the suction-side/shroud corner region as the blades loaded. Between Stations 2 and 3, this fluid decelerates again because of the adverse pressure gradient. The loss induced by the shroud boundary layer separation, which resulted from the adverse pressure gradient,

is clearly illustrated by the p* spectra for Stations 1, 2 and 3 (see Figure 3.20).

The relative velocities do not diffuse between Stations 3 and 4, so the reduced static pressure remains almost constant. However beyond Station 4, the blades are unloading and therefore, the p_r and relative velocities become more uniform and this produces a rise in the mass-averaged P_r. This increased uniformity is clearly illustrated in the p_r spectrum. The rise in the flow rates in the ranges (P_r=0.25 to 0.45) between Stations 4 and 5, which is due to mixing in the wake region, is particularly noticeable. This mixing also alters the P* spectrum, the fluid with P*=0.3 to 0.4 at Station 3 mixing out to P*=0.4 to 0.5 at Station 4, which in turn mixes out to increase the flow in the ranges of P*=0.5 to 0.65 at Station 5. The relative velocity spectra show how the most rapidly moving fluid, in the hub/suction-side corner region, decelerates considerably between Stations 4 and 5, because of the reduction in the strength of the tangential gradient of reduced static pressure, due to the unloading of the blades.

CHAPTER 4

EXPERIMENTAL RESULTS FOR BELOW AND ABOVE DESIGN FLOWS

4.1 Introduction

In the previous chapter, the details of the flow through the impeller at the 'design' flow rate have been discussed. It is of interest however, to discover how the secondary flow pattern through the impeller alters with a change of Rossby Number ($Ro=W/\omega R_n$).

In order to alter the Rossby Number, it is possible to change either the relative velocity W, or the rotational speed ω. In this study, it was considered most convenient to keep the rotational speed the same, as the 'g' loading at 500rpm was close to the maximum permissible in the design of the traversing gear and any reduction in rotational speed would decrease the relative velocities and hence the accuracy with which the relative velocities could be measured. Therefore, the Rossby Number was varied by changing the flow rate, which was achieved by altering the number and mesh-size of the screens in the inlet duct. Reference was made to the work of Elder [55] and Taylor and Bachelor [56] when the screens were chosen.

4.2 The 'Below design' flow

The flow discussed below is for a passage flow rate of 0.12 $\pm$0.01kg/s which is equivalent to 2.3kg/s for the whole impeller, which gives a Rossby Number 15% smaller than for the flow discussed in the previous chapter. The flow rates calculated at each measurement station and the characteristic values of p* are given in Appendix 3.

4.3 Station 1

The incidence angles (Figure 4.1), as would be expected for a lower flow rate, are larger than in the previous 'design' flow. The increase in incidence angle is consistently between 2 and 5 degrees over the cross-section at Station 1, which compares well

with the predicted change of 4 degrees calculated from the inlet velocity triangle. The angles are also now predominantly positive, which is typical of a 'below design' flow rate.

The p* contours (Figure 4.2) show that a considerable loss in stagnation pressure has occurred already. This is attributable to the adverse gradient of reduced static pressure on the shroud, where P_r changes from 0.0 to 0.14, between Stations 1 and 2. This adverse pressure gradient induces the shroud boundary layer separation as discussed previously for the 'design' flow rate. The separation at this flow rate is considerably more severe as shown by the large region of low p* fluid in Figure 4.2.

The reduced static pressure diagram (Figure 4.4) shows a very similar pattern to the 'design' flow (see Figure 3.6), except that the pressure surface is slightly more heavily loaded, because of the higher incidence angles.

The velocity contours (Figure 4.3) show that the axial velocity is lower than for the 'design' flow over most of the passage cross-section.

4.4 Station 2

There is a further substantial loss in p* between Stations 1 and 2 as illustrated by the contours at Station 2 (Figure 4.5). This loss is again attributed to the shroud boundary layer separation. As the velocity contours at Station 3 (Figure 4.9) indicate, there is a large amount of fluid, in the suction-side/shroud corner region, with a very low momentum. There is also a further pressure rise in this corner region, as the minimum value of P_r at Station 3 (see Figure 4.7) is 0.24, compared with P_r=0.14 at Station 2 (Figure 4.4). This may well mean that this large zone of low momentum fluid will tend to flow in a backward direction, relative to the potential flow. Such a substantial area of reverse flow would disrupt the main flow along the passage considerably and cause

large-scale turbulent mixing and so produce the very large region of low p* fluid observed at Station 2. Unsteadiness in the readings in this region was experienced during the experiments.

The p* contours (Figure 4.5) also show the thickening of the suction side boundary layer and the secondary flows convecting this fluid along the suction side, to a point at approximately $z/z_0=0.5$, can be observed in Figure 4.6. The stable location for this low p* fluid, at Station 2, is closer to the shroud corner, but the divergence of the flow in the suction-side/shroud corner region prevents the low p* fluid from reaching this location.

The velocity diagram also illustrates that in order to dedicate such a large proportion of the passage to the low p* fluid, the potential flow has had to accelerate slightly and the associated drop in reduced static pressure in the potential flow region is shown in Figure 4.7.

4.5 Station 3

The reduced static pressure contours (Figure 4.10) show the increase in pressure which promotes the separation of the shroud boundary layer. As this figure depicts, the pressure gradient due to curvature is now much stronger and this will therefore tend to suppress further turbulent mixing between the low momentum or wake fluid and the potential flow.

The twin passage vortices, which dominate the secondary flow pattern are now well established (see Figure 4.9), however they are weaker, than in the previous flow (see Figure 3.11), because of the lower relative velocities. The secondary flow up the suction surface (see Figure 4.9) has carried the low p* fluid from the thickened suction side boundary layer towards the wake, but it does not carry the fluid as close to the corner as in the 'design' flow (see Figure 3.11). This is probably due to the combined effect of the reduced inertia of the passage vortex and the gradient of p* in the suction

surface boundary layer not being so strong in the region z/z_0=0.4 to 0.8. The influence of the Coriolis generated secondary flow along the shroud towards the low p* region is now detectable in Figure 4.9.

The minimum reduced static pressure is observed on the suction surface (Figure 4.10), which implies that, although the flow is only two-thirds of the way around the axial-to-radial bend, the stable location for low p* fluid is already on the suction surface, the position which would be expected for a flow dominated by the passage rotation (i.e. with a low Rossby number).

4.6 Station 4

The strength of the gradient of reduced static pressure remains about the same as at Station 3 (see Figure 4.13), but with the relaxation of the axial-to-radial bend, the orientation has altered and the gradient is now essentially between the blades. This means that the pressure in the wake region has increased and as the wake fluid has virtually no momentum at Station 3, it is necessary for it to mix out to some extent in order for it to achieve this higher pressure. This mixing has raised the minimum value of P* present in the wake region from P*=0.29 to 0.40 between Stations 3 and 4 as can be seen from Figure 4.11. This mixing has been achieved with higher p* fluid supplied by the two major secondary flows; the first up the suction surface and the second across the shroud, as depicted by the cross velocities in Figure 4.12.

This velocity diagram also shows how the Coriolis generated secondary flows along the shroud have become much stronger and have greatly boosted the strength of the clockwise vortex on the pressure side of the passage. In the wake region (y/y_0=0.4 to 1.0; z/z_0=0.0 to 0.2), the two secondary flows appear to evade each other, one running over the other. This produces the rather elongated wake region illustrated in Figures 4.11 and 4.12. The wake's location

has moved slightly closer to the suction surface, so it must be concluded that the inertia of the anticlockwise vortex on the suction side of the passage is being overcome by the strength of the Coriolis generated secondary flow along the shroud. The wake's core is therefore much closer to the suction-side/shroud corner than at the 'design' flow condition.

The drop in pressure on the suction side (Figure 4.13) has caused a considerable acceleration of the potential flow near the suction-side/hub corner and a corresponding deceleration has occurred in the pressure-side/shroud corner region.

4.7 Station 5

Between Stations 4 and 5, the blades unload, reducing the blade-to-blade pressure gradient considerably (see Figure 4.16). This results in a rapid diffusion in the high velocity regions, which is depicted by the diverging arrows in Figure 4.15. The wake fluid also has to mix out further in order to reach the higher pressure at Station 5. This is accomplished by mixing with higher p* fluid supplied by the secondary flows or by direct mixing with fluid from the potential flow region. More mixing out of the potential flow region takes place at this flow condition than previously because,with the lower passage velocities, the mixing is not suppressed so strongly by the curvature and rotation and there is relatively more time for the mixing to occur.

The cross velocity arrows in Figure 4.15 show the dominance of the slip, but there is also still evidence of the secondary flow along the shroud and up the suction surface towards the wake's present position on the suction side of the passage (see Figure 4.14). This is the position which is expected for the wake in a flow with low Rossby Number, i.e. one dominated by the passage rotation. In this flow, the wake is close to the stable location for low p* fluid which, at the outlet, is still on the suction surface. The

inertia of the secondary flows therefore, are less important in determining the wake's position at the outlet in this 'below design' flow.

4.8 Mass-averaged pressures

The losses at this flow condition are significantly larger than at the 'design' condition, as illustrated by the mass-averaged P* values in Figure 4.17. This is not surprising, since a similar pressure rise is being demanded from the impeller, but the pressure rise achieved by diffusion is less significant in this flow, because of the lower relative velocities.

The mass-averaged P* shows a very substantial loss between the inlet and Station 2, which as described previously, is due to the separation and possible backflow of the shroud boundary layer fluid, which causes large-scale turbulent mixing in the inducer. Beyond Station 2, there is very little further loss until the blades unload between Stations 4 and 5 and this then results in mixing between the wake and the potential flow and hence a further loss in P*.

The mass-averaged reduced static pressure shows a steady rise through the impeller. This pressure rise is not as great as achieved in the 'design' flow, however the diffusion ratio (=Average relative velocity at the inlet divided by the average relative velocity at the outlet) is 1.64 $\pm$0.2 for this 'below design' flow compared with only 1.56 $\pm$0.2 for the 'design' flow. This suggests that the diffusion is greater at the lower flow rate, but the lower relative velocities result in a lower pressure rise.

4.9 Flow property spectra

The relative velocity spectra (Figure 4.19) indicate that, at Station 1, a very high proportion of the flow rate is made up of fluid with a high relative velocity, compared with the much more even distribution of relative velocity at the 'design' flow rate (see Figure 3.21). This is because of the higher incidence angles,

which mean that the fluid has to accelerate more around the blade leading edges. These velocity spectra also illustrate the rapid deceleration that occurs near the shroud, between Stations 1 and 2, because of the adverse pressure gradient. The associated separation of the shroud boundary layer causes the widespread loss of p* which dominates the p* spectra (Figure 4.18). Beyond Station 2, the distribution of p* and relative velocities remain much the same in the upper ranges, the further diffusion of the wake fluid is depicted by the appearance of the very low velocities present in the spectrum at Station 3. The subsequent mixing between Stations 3 and 4 is illustrated by the increase in the minimum observed value of P*. Between Stations 4 and 5, there is further mixing, which is to the detriment of the mass-averaged stagnation pressure of the fluid and results in the increase of the flow rate in the majority of the low ranges of the P* spectrum for Station 5.

4.10 The 'Above design' flow

The third and final flow discussed is for an 'above design' flow rate of 0.17 $\pm$0.01kg/s through the passage, which is equivalent to a flow through the impeller of 3.3kg/s. The flow rate and Rossby Number are therefore about 21% larger than for the 'design' flow. The main flow parameters are given in Appendix 3.

4.11 Station 1

Predictably, the incidence angles at the inlet (Figure 4.20), for this 'above design' flow rate are predominantly negative; the smallest angle of -20.2 degrees, achieved on the pressure surface near the shroud, is the largest magnitude of incidence angle in all of the three flows.

The p* contours (Figure 4.21) show a distribution which is uniform (P*=1.0 $\pm$0.02), except very close to the corners, where some loss of stagnation pressure has occurred, most noticeably near the shroud/pressure-side corner where the flow could be separated locally at the leading edge.

The reduced static pressure contours (Figure 4.23) illuminate the fact that the blades are unloaded to about 60% of their height and the rest of the blade (z/z_0=0.6 to 1.0) is actually negatively loaded. The velocity distribution (Figure 4.22) shows how the air accelerates to an axial velocity of up to 20m/s, about twice the magnitude of the axial velocity in the inlet duct, as it goes around the blade leading edge in this low pressure region. The gradient of axial velocity in the hub-to-shroud direction is considerably higher than in the previous flows, which is due to the blockage presented by the blade leading edges, which has a greater influence at this flow rate because of the higher relative velocities. This also means that the hub-to-shroud velocity component is stronger, as fluid from the lower half of the passage moves up to increase the flow rate in the top half.

4.12 Station 2

Between Station 1 and Station 2, the blades load so, at Station 2, the pressure on the pressure surface is higher than on the suction surface (see Figure 4.26). This complete reversal of the blade-to-blade pressure gradient also precipitates a reversal in the velocity gradient (see Figure 4.25). The flow in the suction-side/shroud corner region accelerates, while the flow in the opposite corner (y/y_0=0.0 to 0.2; z/z_0=0.5 to 1.0) decelerates. The adverse pressure gradient in the pressure-side/shroud corner region may cause a local separation of the boundary layer and hence the observed loss in p*.

The p* diagram (Figure 4.24), also shows the thickening of the suction side boundary layer. The velocity diagram (Figure 4.25) suggests that this fluid with reduced stagnation pressure (P*= 0.85 to 0.95) is being convected from the corners to the centre of the wall. The third region of reduced p* fluid, in the suction-side/shroud corner region, is probably also associated with the incidence at the blade leading edge.

A large loss in p* has therefore been avoided between Stations 1 and 2 at this flow condition, because a significant rise in reduced static pressure on the shroud has not yet occurred and therefore there has been little tendency for the shroud boundary layer to separate.

4.13 Station 3

The velocity measurements (Figure 4.28) indicate that the axial-to-radial bend is strongly influencing the secondary flow pattern. The secondary flow is dominated by the two opposing passage vortices, similar to those which resulted from the axial-to-radial bend's curvature in the previous two flows. The suction side vortex carries the low p* fluid, in the suction side boundary layer, up towards the shroud. The Coriolis forces have also induced a

secondary flow across the shroud, which is stronger at this point than previously achieved in the other two flows. This is probably because the gradient of p* is steeper near the shroud as the shroud boundary layer is relatively thin (see Figure 4.27) for a large proportion of the shroud's width (y/y_0=0.0 to 0.5). The p* diagram also shows that the secondary flows have convected the low p* fluid from both the shroud/pressure-side corner region and the suction side boundary layer into the wake region, which is now becoming fairly extensive.

The velocities in the potential flow region have altered very little between Stations 2 and 3 and the strength of the gradient of reduced static pressure (see Figure 4.29) has remained almost the same, although its orientation is now slightly more in the blade-to-blade direction. The lowest static pressure, and hence the stable location for low p* fluid, is still in the shroud/suction-side corner region and at present the secondary flow seems to be carrying further low p* fluid to this area.

4.14 Station 4

The static pressure contours (Figure 4.32) bring to light two changes between Stations 3 and 4. The first change is the continued re-orientation of the pressure gradient which, as would be predicted close to the end of the axial-to-radial bend, is in the blade-to-blade direction, the stable location for low p* fluid being established on the suction surface. The second change is that the lowest value of reduced static pressure has increased from P_r=0.05 to 0.22. This alteration has not affected the flow in the suction-side/shroud corner region significantly, as in this region P_r=0.25 at Station 3. However, the wake, as illustrated in Figure 4.30, has moved further along the shroud, as it did at the 'design' flow rate, because of the inertia of the suction side passage vortex. This has placed the low p* fluid of the wake in a region of P_r=0.45, so the

wake fluid has had to endure a very substantial increase in pressure. Figure 4.31, the velocity diagram, illustrates that the size of the wake's core has increased considerably.

The cross velocities in Figure 4.31, show that the suction side passage vortex is still very strong and still pumps fluid up the suction surface into the wake region. The Coriolis forces have also augmented the secondary flow along the shroud and this is also feeding low p* fluid into the wake region.

The gradients of p* and relative velocity between the wake's core and the potential flow region are the strongest in any of the three flows described. These strong gradients are not effaced because turbulent mixing is suppressed by stabilising forces due to curvature and rotation, which are also strongest at this flow condition. The stabilising forces essentially prevent mixing because when a low p* fluid particle strays into a higher p* region, the stabilising forces very rapidly induce a secondary flow to return the particle to its initial location, before it has time to mix out with the higher p* fluid.

4.15 Station 5

The p* contours (Figure 4.33) show a large increase in the wake area between Stations 4 and 5. The minimum observed p* has also increased slightly between the two stations, which implies that some mixing has occurred. This has been permitted because the blades have essentially unloaded, as depicted by the reduced static pressure diagram (Figure 4.35) and so the stabilisation of the steep gradients of p* has weakened allowing mixing to occur. Also, as the fluid in the wake is moving so slowly, it has a relatively longer time to achieve its mixing.

The wake region has moved even further along the shroud and the velocity diagram (Figure 4.34) shows that this is because the suction side passage vortex is still feeding fluid into the shroud/

suction-side corner region. This fluid is also the most likely source for the high p* fluid required for the mixing in the wake region. There is now a tendency for the fluid with the lowest p* to move towards the stable location on the suction surface. This movement can be seen in the velocity diagram (Figure 4.34), but it also shows the flow up the suction surface preventing the bulk of the wake fluid from reaching its stable location. The velocity contours also show how the velocities have become more uniform over the potential flow region between Stations 4 and 5; the fluid on the pressure side of the passage having accelerated and converged, while the fluid on the suction side has decelerated and diffused. This diffusion in the suction-side/hub corner region also provides a source for fluid travelling in the secondary flow up the suction side wall.

4.16 Mass-averaged pressures

The mass-averaged rotary stagnation pressure (Figure 4.36) shows only a significant reduction between Station 3 and the outlet, particularly between Stations 4 and 5, where most of the mixing in the wake region occurred.

The reduced static pressure shows a rise between Stations 1 and 2, where some diffusion occurred as the tangential velocity of the flow decreased through the inducer. However, beyond Station 2, the reduced static pressure remains virtually constant. The rise in static pressure, therefore represents only a centrifugal pressure rise.

4.17 Flow property spectra

The rotary stagnation pressure spectra (Figure 4.37), when compared with the similar spectra for the 'design' flow condition (Figure 3.20), illustrate the difference in losses in the two flows. The two spectra at Station 5 are very similar, but in the 'design' flow most of this loss had occurred at Station 2, whereas at the

higher flow rate, the major loss is the mixing, which occurs in the final radial section of the impeller passage. Both losses seem to be associated with the diffusion of low p* fluid, either in a boundary layer or within the wake region, which leads to a mixing loss when this fluid mixes out with higher p* fluid so that it can continue its journey down the passage.

The relative velocity spectra (Figure 4.38) shows how most of the flow (with W<20m/s) diffuses between Stations 1 and 2, which is achieved because the circumferential velocity components are reduced as the flow passes through the inducer. The fluid, with a relative velocity greater than 20m/s at Station 1, is the fluid close to the pressure surface in the upper half of the passage, which accelerated around the blade leading edge as it entered the passage. This fluid diffuses and decelerates between Stations 1 and 2, but as the blades change their loading, a similar quantity of fluid near the suction blade surface accelerates, to form a new high velocity (W>20m/s) region there. This fluid in the suction-side/shroud corner region, diffuses only slightly between Stations 2 and 3, as the pressure only rises slightly (P_r<0.05), but this fluid does diffuse significantly in the final section of the axial-to-radial bend, between Stations 3 and 4. The fluid on the hub has a corresponding acceleration between Stations 3 and 4, because of the reduction in the gradient of pressure in the hub-to-shroud direction. Finally, as the blades unload, the velocities become much more uniform in the potential flow region, while those in the wake remain fairly low.

CHAPTER 5

DISCUSSION OF THE LOSSES IN THE CENTRIFUGAL COMPRESSOR

5.1 Introduction

The previous two chapters have described the details of the flow through the Ghost impeller at three flow rates. In this chapter, the main features of the three flows are discussed with particular reference to how the losses in p* and hence the losses in efficiency might be reduced by altering the impeller geometry.

5.2 Impeller Efficiency

The isentropic efficiency of the impeller can be expressed, for an incompressible flow, as

$$\frac{\text{Static Pressure Rise}}{\text{Static Pressure Rise + Rotary Stagnation Pressure Loss}} \quad -5.1$$

as shown in Appendix 4. This efficiency is evaluated between the inlet duct and Station 5 and the results are

Flow Rate	'Design'	'Below design'	'Above design'
Isentropic Efficiency	88.3%	78.5%	86.2%

within an estimated accuracy of $\pm$10%.

These efficiencies show that, to some extent, the losses are minimised at the 'design' flow rate. They also illuminate the problems of running the impeller at a 'below design' flow rate, because of the increased severity of the shroud boundary layer separation. Based on the single 'above design' operating condition, it appears that the impeller can be run above design with a relatively high efficiency.

5.3 Rotary Stagnation Pressure Losses

In the impeller flows, there were three main sources of rotary stagnation pressure loss.

5.3.1 Losses due to the Incidence of the Flow at the Impeller Inlet

The large negative incidence (as low as -20.2 degrees) on the

pressure surface of the blade at the 'above design' flow rate caused the most serious incidence loss observed in the present study. The loss however corresponded to a loss in efficiency (evaluated with the aid of Equation 5.1) of only about 3%. The incidence at the 'below design' flow rate was as high as 18.3 degrees on the suction side near the hub and the p* contours at Station 2 (Figure 4.5) indicate a region of loss from the core of the wake along the suction surface towards the hub, which might be attributed to this large incidence. From these results, it may be concluded that the impeller flow rate is constrained by the incidence angles, which have to have a magnitude less than about 15 degrees, if incidence losses at the leading edges of the blades are to be avoided.

5.3.2 Losses due to Separation of the Shroud Boundary Layer

When the p* contour diagrams towards the end of the inducer, at Station 2, are compared for the three flow rates (Figures 3.7, 4.5 and 4.24), it is clear that the lower the flow rate, the more severe the effects of the shroud boundary layer separation become. In chapters 3 and 4, the adverse pressure gradient in the suction-side/shroud corner region, which was held responsible for this separation, was discussed. Figure 5.1 shows the variation in pressure along a streamline close to the suction-side/shroud corner, for the three flow rates. Now, let us define the probable location of separation as the measurement station where flow, with a relative velocity less than 20% of the maximum relative velocity observed in the inlet plane (i.e. less than $0.2x\ \frac{2}{\rho}(p^*_{max}-p^*_{min})^{\frac{1}{2}} \triangleq 5m/s$), first occurred over significant areas of the passage (greater than 1% of the cross-sectional area). We then find that separation occurred near Station 2 in the 'below design' flow, near Station 3 in the 'design' flow and near Station 4 in the 'above design' flow. Furthermore, we see from Figure 5.1, that separation occurred in each flow just after a large rise in reduced static pressure of $\Delta P_r \triangleq 0.2$.

The mixing associated with the separation of the shroud boundary layer corresponds to a loss in efficiency (calculated from Equation 5.1) of up to 18% at the 'below design' flow rate and therefore it would be very advantageous to either prevent this separation or at least delay it, so that the mixing losses are reduced as they were at the 'above design' flow rate. Firstly, let us look at the adverse pressure gradient, which causes the separation. Clearly, if we are to achieve any diffusion of the relative flow, there must be a rise in reduced static pressure through the impeller, but why is this adverse pressure gradient so severe along the shroud, particularly in the inducer at the low flow rates? The key to this question is the change in the gradient of p_r in the hub-to-shroud direction and in the blade-to-blade plane.

Let us compare the meridional gradient of reduced static pressure generated at the inlet, with the meridional pressure gradient required to turn the flow around the axial-to-radial bend. At the inlet, from the velocity triangle

$$W^2 = U^2 + \omega^2 r^2 \qquad -5.2$$

and along a streamline by Bernoulli

$$p^* = p_r + \tfrac{1}{2}\rho W^2 \qquad -5.3$$

Differentiating Equation 5.3 with respect to r

$$\frac{\partial p^*}{\partial r} = \frac{\partial p_r}{\partial r} + \rho W \frac{\partial W}{\partial r} \qquad -5.4$$

But, as an incompressible, inviscid flow is uniform in p*, at the inlet $\frac{\partial p^*}{\partial r}=0$ and $\frac{\partial W}{\partial r}$ is given by differentiating Equation 5.2

$$\frac{\partial p_r}{\partial r} = -\rho U \frac{\partial U}{\partial r} - \rho \omega^2 r \qquad -5.5$$

At the inlet, the second term on the right hand side of this equation is dominant and is independent of the flow rate.

In the axial-to-radial bend

$$\frac{\partial p_r}{\partial n} = -\frac{\rho W^2}{R_n} - 2\rho\omega W_\theta \doteq -\frac{\rho(W_z^2+W_r^2)}{R_{nb}} \qquad -5.6$$

as W_θ is small

Where R_{nb} is the radius of curvature of the axial-to-radial bend. The magnitude of this pressure gradient increases with the flow rate.

As can be seen from the reduced static pressure contours for the 'above design' flow rate at Station 1 (Figure 4.23) and at Station 3 (Figure 4.29), the magnitude of the meridional pressure gradient at the inlet and in the axial-to-radial bend are about equal. However, at lower average relative velocities and hence lower flow rates, the pressure gradient in the axial-to-radial bend (see Equation 5.6), is reduced and so the pressure on the shroud rises between the inlet and the axial-to-radial bend, increasing the likelihood of an early separation of the shroud boundary layer.

In the blade-to-blade direction there will also be a pressure gradient, which will alter in magnitude through the inducer and influence the shroud boundary layer separation. Initially as the flow enters the impeller, there will be no blade-to-blade pressure gradient. The blades will then load however and this causes the reduction in p_r observed in the suction-side/shroud corner region in Figure 5.1. This loading continues for a distance into the inducer determined by the incidence at the inlet. The 'below design' flow loads the blades immediately whereas, in contrast the other two flows do not load the blades completely until Station 2 is reached. The delayed blade loading therefore delays the onset of the adverse pressure gradient in the suction-side/shroud corner region in the 'design' and 'above design' flows, but not at the 'below design' flow rate.

How then, does the impeller designer reduce the loss of stagnation pressure due to the boundary layer separation, which is associated with this adverse pressure gradient?

The designer has to try to provide an impeller geometry, which will diffuse the high relative velocities found near the shroud at

the inlet. This will necessitate an adverse pressure gradient in the suction-side/shroud corner region, but this pressure gradient must be sufficiently weak that it does not cause the shroud boundary layer to separate or at least not in the early part of the passage. The pressure gradient necessary to cause separation of the boundary layer is dependent on the rate of mixing occurring within the boundary layer. If mixing is suppressed by either curvature or rotation, separation is more likely to occur, as low momentum fluid is brought to rest more easily by an adverse pressure gradient, as the fluid is unable to increase its momentum by mixing out. This implies that if the designer is to reduce the likelihood of shroud boundary layer separation, he must have only a weak adverse pressure gradient in the axial-to-radial bend where mixing is suppressed, particularly as secondary flows will deliver further low p* fluid to the shroud, which will also have to mix out if separation is to be prevented. Stronger adverse pressure gradients along the shroud wall can be tolerated in the inducer and in the final radial section of the impeller, where mixing is not so strongly suppressed.

When this 'improved impeller' pressure gradient in the suction-side/shroud corner region is compared with the curve obtained for the Ghost impeller 'design' flow (Figure 5.1), the modifications to the adverse pressure gradient, which are apparently desirable are (a) The removal of the favourable pressure gradient in the inducer between Stations 1 and 2, (b) The reduction in the magnitude of the adverse pressure gradient in the axial-to-radial bend (Station 2 to 3/4) and (c) The increase in the magnitude of the pressure gradient in the final radial section of the passage (Stations 3/4 to 5).

(a) could be achieved by loading the blades at the inlet, as occurred in the 'below design' flow, but the inducer's curvature will also have to be reduced, so that the circumferential velocity component isn't diffused as quickly as in the 'below design' flow.

This has been achieved by some designers since 1950, by designing impellers with long inducers. Alternatively, the inducer bend can be extended into the axial-to-radial bend, so that the circumferential velocity component is diffused more slowly, without increasing the overall length of the impeller. This is done in Eckardt's impeller [54], where the flow has a circumferential component of relative velocity through most of the impeller passage.

(b) would require the modification of the shroud wall profile. To improve the profile, the curvature of the shroud wall would commence at the inlet (as occurs in Eckardt's impeller) and would have a magnitude such that the streamline curvature Equation 5.6 is satisfied along the shroud. The circumferential component of velocity W_θ decreases and the axial component of velocity W_z increases through the impeller and so the curvature of the axial-to-radial bend ($1/R_{nb}$) will increase, from zero, through the inducer, giving the desired $\partial p_r/\partial r$ and hence $\partial p_r/\partial s$ along the shroud. The magnitude of $\partial p_r/\partial r$ will also decrease through the passage though, as $\partial p_r/\partial s$ is larger near the shroud than for the passage as a whole, as at the outlet there will be little or no pressure gradient in the hub-to-shroud direction. This means that the curvature of the shroud will decrease again in the axial-to-radial bend. The curvature will not however become zero, until the outlet is reached in order that (c) is achieved. It is clear that considerable work is required on boundary layer separation to determine the critical values of $\partial p_r/\partial s$ for separation as a function of the stabilisation due to curvature and rotation.

5.3.3 Losses due to mixing

Large mixing losses are most likely to occur where there is a steep gradient of relative velocity between two substantial regions of fluid and where turbulent mixing between the two regions is unsuppressed. In the centrifugal compressor impeller passage, steep

gradients of p* occur in the boundary layers, but as these are thin, only small quantities of low p* fluid mix out here. However, steep gradients of p* also exist between the substantial low p* area of separated flow (or wake) and the potential flow region. Suppression of mixing is provided by both Coriolis and streamline curvature forces and is therefore strongest at the stable location for low p* fluid. This suppression is fairly weak in the inducer, where the stable location is on the suction surface close to the shroud corner. In the axial-to-radial bend, curvature strengthens this suppression near the stable location on the shroud wall. There is no mixing suppression on the shroud wall in the final radial section of the passage, although suppression is provided by the Coriolis forces on the suction surface.

It is apparent therefore, that if separation of the shroud boundary layer occurs in the inducer, turbulent mixing will occur on the shroud wall, but this mixing will then be greatly suppressed in the axial-to-radial bend. Mixing will again occur in the final radial section of the passage, if the wake is located on the shroud, but mixing out of a wake on the suction surface will be suppressed until the blades unload. This was verified by the results obtained in the Ghost impeller (Figures 3.19, 4.17 and 4.36), where substantial mixing losses were observed when the shroud boundary layer separated in the inducer (at the 'below design' and 'design' flow rates), but very little loss was observed in the axial-to-radial bend in any of the three flows. The 'above design' flow was the only flow where the wake was entirely on the shroud at the outlet and indeed, the greatest p* loss due to mixing in the radial section was observed at this flow rate (Figure 4.36). Some p* loss was also observed in the 'design' flow case however, as the wake was partially located on the shroud (Figure 3.19).

Mixing losses in the inducer can be prevented almost entirely

by preventing the separation of the shroud boundary layer, but if separation does occur, mixing within the separated region can be reduced by commencing the meridional curvature of the shroud wall at the inlet, so that curvature forces suppress the mixing. This was in fact the same remedy as was suggested for prevention of the shroud boundary layer separation.

Mixing losses in the final radial section of the impeller can be reduced by always ensuring that the wake is located on the suction surface. This occurred at the 'below design' flow rate in the Ghost, but as concluded in chapter 4, the wake's position is essentially determined by the Rossby Number associated with the axial-to-radial bend and therefore the impeller designed with a low Rossby Number will result in a wake flow on the suction surface. However, the positioning of the wake on the suction surface is not necessarily desireable, as the wake's position will very likely alter the nature of the flow in the diffuser and hence the losses in the diffuser. We therefore should ask another question: What wake location at the impeller discharge will minimise the losses in the diffuser?

5.4 Losses in the Diffuser

The main source of loss in the diffuser is mixing. Mixing in the blade-to-blade plane was studied by Dean and Senoo [40] and they concluded that the wake mixed out very rapidly indeed in the diffuser. In fact, Johnston and Dean [41] used a simplified flow model, which assumed that mixing out occurred instantaneously and this was shown by Senoo and Ishida [42] to calculate the losses in the diffuser within 1% of stage efficiency. Mixing occurs so very rapidly in the blade-to-blade plane because, when the blade trailing edge is reached, there is an interface between the wake fluid from one passage and the potential flow fluid from the neighbouring passage. The high shear in velocity present between these two regions, causes

a very rapid and violent transfer of momentum, see Dean [57]. However Dean concluded that mixing in the meridional plane would be much more restrained. In fact, it seems reasonable to suppose that mixing will occur, beyond the outlet, at approximately the same rate as it did within the impeller, as the discharge will not greatly affect the interface, in the meridional plane, between the wake and the potential flow.

5.5 Selection of an Impeller/Diffuser Combination

When the designer wishes to produce an impeller/diffuser combination he can choose from two alternatives: (a) To design an impeller with a low Rossby Number, which will have a wake on the suction surface at the impeller outlet and hence will have suffered only a small mixing loss in the radial section of the impeller, but there will probably then be a much larger loss in the diffuser or (b) To divide the mixing loss between the impeller and diffuser, by placing the wake on the shroud by using an impeller of high Rossby Number. Very little information is available however on the relative merits of these two schemes, but it is interesting to speculate that as the mixing in the blade-to-blade plane is so violent in the diffuser, it is likely to involve a considerable p^* loss and therefore scheme (b) is probably to be preferred.

If the designer adopts approach (b), he has to ensure that the wake remains on the shroud, but he does not have to do this by designing the impeller with a large Rossby Number. An alternative, which has become popular in recent years, is to curve the impeller blades backwards in the passage beyond the axial-to-radial bend. This means that the Coriolis forces induced in the blade-to-blade plane, which initiate the secondary flows which carry low p^* fluid onto the suction surface, will be opposed by forces due to the curvature of the backward-swept blades and if this curvature is made sufficiently strong, any tendency for low p^* fluid to migrate to the

suction surface will be removed. This technique has the additional advantage that the absolute velocity of the discharge flow is reduced and so the diffusion which has to be achieved in the diffuser is decreased.

5.6 Conclusions drawn from the Experimental Work

1. The wake flows observed in the present study are accumulations of fluid, with low rotary stagnation pressure p*, which form in the suction-side/shroud corner region of the impeller passage. The two phenomena which contribute to the formation and development of these wake flows are

(a) The adverse gradient of reduced static pressure in the streamwise direction, along the shroud, and

(b) The convection of low p* fluid by secondary flows, which are generated in the boundary layers, due to the curvature and rotation of the impeller passage.

2. In the suction-side/shroud corner region, an adverse pressure gradient occurs downstream of a low pressure region in the inducer. At the 'below design' flow rate the pressure rises continuously from close to the blade leading edge to the impeller exit. As the flow rate is increased however, the pressure difference between the hub and shroud walls becomes larger and the pressure rise in the suction-side/shroud corner region occurs later in the passage; thus the flow separation associated with this adverse pressure gradient moves from the inducer into the axial-to-radial bend.

3. The results from the 'above design' flow rate show the build-up of low p* fluid upstream of the point where the first large scale departures from potential flow are observed in the contours of meridional velocity. This low p* fluid has two sources

(a) From the separation of the flow from the pressure surface of the blade leading edge, close to the shroud, and

(b) From the thickening of the suction side boundary layer.

The low p* fluid is observed to migrate to the suction-side/shroud corner region, where the wake is formed. The author therefore concludes that, at the 'above design' flow rate, the formation of the wake is a direct consequence of secondary flow.

4. The axial-to-radial bend dominates the secondary flow pattern through most of the impeller. Two opposing passage vortices are induced, one on the suction side and one on the pressure side of the passage. On the suction side, low p* fluid is carried by the vortex along the wall to the wake region. The passage vortex on the pressure side, creates a secondary flow along the shroud towards the suction surface. This flow is enhanced by the action of Coriolis forces due to the passage rotation. The low p* fluid, in these two flows, collides in the wake region and moves away from the shroud wall.

5. The strength of the two passage vortices, induced in the axial-to-radial bend, increases with the flow rate and hence with the Rossby Number ($W/\omega R_n$). The inertia of the suction side passage vortex prevents the wake from moving from the shroud, to its stable location on the suction side wall at the outlet, at the 'design' and 'above design' flow rates. At the 'below design' flow rate, the inertia of this vortex is overcome by the secondary flow along the shroud wall, which is induced by the Coriolis forces, and the wake migrates onto the suction side wall of the passage.

6. The development of the wake flow in the Ghost impeller, operating with a tip speed of 23.8m/s, and at the 'design' flow rate, is very similar to that in Eckardt's impeller [51], with a tip speed of 293.0m/s. This is because the relative influences of curvature and rotation are of approximately equal importance in the flows in these two impellers.

7. Significant mixing losses occur in the suction-side/shroud corner region when the boundary layer fluid experiences an adverse pressure gradient and mixing is not strongly suppressed by either curvature or rotation. In the Ghost impeller, the largest mixing loss occurred in the suction-side/shroud corner region in the inducer at the 'below design' flow rate and a smaller loss also occurred in

this region in the 'design' flow case. Mixing was strongly suppressed by curvature in the axial-to-radial bend at all flow rates, but in the final radial section of the impeller passage, mixing is not suppressed on the shroud and therefore mixing losses occurred here at the 'above design' flow rate, as in this flow the wake was located on the shroud.

8. A large improvement in impeller efficiency would be achieved, if the separation of the shroud boundary layer could be prevented, or at least delayed. This separation is governed by the adverse pressure gradient along the shroud and the modification to the turbulent mixing within the shroud boundary layer by curvature and rotation. Both these factors are strongly influenced by the shroud profile in the meridional plane and it is therefore believed that modifications to this profile would benefit the impeller's efficiency significantly.

9. The diffuser efficiency is highly dependent on the flow delivered to it from the impeller. It seems probable that a wake on the shroud mixes out more efficiently than one on the suction surface and that a low mean discharge velocity is to be preferred. It is suggested that, as backward-swept blades at the outlet of the impeller lead to lower absolute discharge velocities and a wake on the shroud, these impellers are likely to improve diffuser performance.

CHAPTER 6

SECONDARY FLOW THEORY IN ROTATING BENDS

6.1 Introduction

It was suggested in the last chapter that the designer should attempt to achieve more mixing out of the wake within the impeller, by keeping the wake on the shroud wall in the radial section of the impeller channel. The factors governing the wake's position were discussed, but in this chapter, it is intended to introduce a quantitative, even if rather simplistic, model of the secondary flows. This model may assist the designer in predicting where the wake is likely to develop within his impeller and how its core may move in the latter part of the passage, as the flow approaches the impeller discharge.

Firstly, the equation for the generation of streamwise vorticity, which was mentioned in Chapter 1, will be derived.

6.2 Secondary flow theory

In the work of Hawthorne, Smith, Wu, and Lakshminarayana and Horlock [27,28,29,30], the equation for absolute vorticity generation along a relative streamline is derived using the relative velocity triangle equation

$$\underline{V} = \underline{W} + \underline{\omega} \times \underline{r} \qquad -6.1$$

and the definition of absolute vorticity

$$\underline{\Omega} = \nabla \times \underline{V} = \nabla \times \underline{W} + 2\underline{\omega} \qquad -6.2$$

Resolving the absolute vorticity into a component along the relative streamline and a component normal to it, we obtain

$$\underline{\Omega} = \left(\frac{\underline{W} \cdot \underline{\Omega}}{\underline{W} \cdot \underline{W}} \right) \underline{W} + \frac{(\underline{W} \times \underline{\Omega}) \times \underline{W}}{\underline{W} \cdot \underline{W}} \qquad -6.3$$

Now, by taking the divergence of Equation 6.2 and after considerable simplification

$$\left(\frac{\underline{W}\cdot\underline{\Omega}}{\rho W^2}\right)\underline{\nabla}\cdot(\rho\underline{W})+\rho\underline{W}\cdot\underline{\nabla}\left(\frac{\underline{W}\cdot\underline{\Omega}}{W^2}\right)=\frac{2\underline{W}x(\underline{W}\cdot\underline{\nabla})\underline{W}\cdot\underline{W}x\underline{\Omega}}{W^4}+\frac{2\underline{\omega}\cdot\underline{W}x\underline{\Omega}}{W^2}-\frac{\underline{W}\cdot\nabla x(\underline{W}x\underline{\Omega})}{W^2} \qquad -6.4$$

Now using the continuity equation

$$\underline{\nabla}\cdot(\rho\underline{W}) = 0 \qquad -6.5$$

and the component of absolute vorticity along the relative streamline

$$\underline{\Omega}_s = \frac{\underline{W}\cdot\underline{\Omega}}{W} \qquad -6.6$$

and the vector expression for the binormal to the relative streamline $\hat{\underline{b}}$

$$\frac{W^3}{R_n}\hat{\underline{b}} = \underline{W}x(\underline{W}\cdot\underline{\nabla})\underline{W} \qquad -6.7$$

and the equation of motion in the rotating co-ordinate system for an inviscid incompressible fluid

$$\frac{1}{\rho}\underline{\nabla}p^* = \underline{W}x\underline{\Omega} \qquad -6.8$$

where $p^* = p+\frac{1}{2}\rho W^2-\frac{1}{2}\rho\omega^2r^2$ $\qquad -6.9$

Equation 6.4 can be reduced to

$$\rho W\frac{\partial}{\partial s}\left(\frac{\Omega_s}{\rho W}\right) = \frac{2}{R_n W}\hat{\underline{b}}\cdot\frac{1}{\rho}\underline{\nabla}p^* + \frac{2\underline{\omega}}{W}\cdot\frac{1}{\rho}\underline{\nabla}p^* \qquad -6.10$$

or

$$\frac{\partial}{\partial s}\left(\frac{\Omega_s}{W}\right) = \frac{2}{\rho W^2}\left(\underbrace{\frac{1}{R_n}\frac{\partial p^*}{\partial b}}_{\text{Curvature Term}} + \underbrace{\frac{\omega}{W}\frac{\partial p^*}{\partial z'}}_{\text{Rotation Term}}\right) \qquad -6.11$$

Where the z' direction is along the axis of rotation.

This is the equation introduced earlier (Equation 1.9), which shows that absolute streamwise vorticity and hence secondary flow will be generated whenever a moving fluid with a gradient of p^* turns around a bend (Radius R_n) or is rotated about an axis z' (with angular velocity ω). A gradient of p^* might result from a non-uniform inlet velocity profile or a reduction of p^* in the boundary

layers due to viscous dissipation.

6.3 Secondary flow theory for a general streamtube

Now, consider a streamtube of fluid (see Figure 6.1) which has a radius of curvature R_n and is rotating about a general axis $\underline{z}'$ with angular velocity $\underline{\omega}$. The fluid relative speed is $\underline{W}$ and the streamtube has a normal gradient of rotary stagnation pressure $\frac{\Delta p^*}{D}$ at an angle $\emptyset$ with the streamtube binormal $\underline{b}$. It is assumed in the analysis that $\frac{\Delta p^*}{D}$ remains constant along the streamtube and that the fluid rotates as a solid body about the streamtube axis.

With reference to Figure 6.1,

$$\underline{\nabla} p^* = \begin{pmatrix} \frac{\partial p^*}{\partial s} \text{ Sin } \theta + \frac{\partial p^*}{\partial n} \text{ Cos } \theta \\ -\frac{\partial p^*}{\partial b} \\ \frac{\partial p^*}{\partial n} \text{ Sin } \theta - \frac{\partial p^*}{\partial s} \text{ Cos } \theta \end{pmatrix} \qquad -6.12$$

By Bernoulli's equation in a rotating co-ordinate system

$$\frac{\partial p^*}{\partial s} = 0 \qquad -6.13$$

Assuming Δp^* to be small

$$\frac{\partial p^*}{\partial n} = -\frac{\Delta p^*}{D} \text{ Sin } \emptyset \qquad -6.14$$

and

$$\frac{\partial p^*}{\partial b} = \frac{\Delta p^*}{D} \text{ Cos } \emptyset \qquad -6.15$$

and also as $\underline{\omega} = \omega \underline{z}' = \begin{pmatrix} \omega_x \\ \omega_y \\ \omega_z \end{pmatrix} \omega$ $\qquad -6.16$

Equation 6.11 becomes

$$\frac{\partial}{\partial s}\left(\frac{\nu_s}{W}\right) = \frac{2\Delta p^*}{\rho W^2 D}\left(\frac{1}{R_n}\text{Cos}\emptyset - \frac{\omega\omega_x}{W}\text{Sin}\emptyset\ \text{Cos}\theta - \frac{\omega\omega_y}{W}\text{Cos}\emptyset - \frac{\omega\omega_z}{W}\text{Sin}\emptyset\ \text{Sin}\theta\right) \qquad -6.17$$

But $\quad \nu_s = 2\frac{\partial \emptyset}{\partial t} + 2\underline{\omega}.\hat{\underline{s}}$

and $\quad W = \frac{ds}{dt}$ and $s = R_n \theta$

so, $$\frac{d^2\phi}{d\theta^2} = \frac{\Delta p^* R_n}{\rho W^2 D}\left\{\cos\phi - \frac{\omega R_n}{W}(\omega_x \sin\phi \cos\theta + \omega_y \cos\phi + \omega_z \sin\phi \sin\theta)\right\}$$

$$- \frac{\omega R_n}{W}(\omega_x \cos\theta + \omega_z \sin\theta) \qquad -6.18$$

Now, introducing two dimensionless quantities,

the rotary stagnation pressure gradient strength $St = \frac{\Delta p^* R_n}{W^2 D}$ -6.19

and the Rossby Number $Ro = \frac{W}{\omega R_n}$

we obtain

$$\frac{d^2\phi}{d\theta^2} = St\left\{\cos\phi - \frac{1}{Ro}(\omega_x \sin\phi \cos\theta + \omega_y \cos\phi + \omega_z \sin\phi \sin\theta)\right\}$$

$$- \frac{1}{Ro}(\omega_x \cos\theta + \omega_z \sin\theta) \qquad -6.20$$

This equation can be simplified to give an analytically soluble linear differential equation for several simple flows.

6.4 Solution for a stationary bend (see Figure 6.2)

Set $\omega = 0$ in Equation 6.18

$$\frac{d^2\phi}{d\theta^2} = \frac{\Delta p^* R_n}{\rho W^2 D} \cos\phi \qquad -6.21$$

For ϕ close to $\frac{\pi}{2}$ (i.e. Low p* fluid on the inside of the bend) this can be approximated by

$$\frac{d^2\phi}{d\theta^2} + \frac{\Delta p^*}{\rho W^2}\frac{R_n}{D}\left(\phi - \frac{\pi}{2}\right) = 0 \qquad -6.22$$

This is the simple harmonic motion equation, the period of oscillation is

$$\phi^* = 2\sqrt{\frac{\rho W^2 D}{\Delta p^* R_n}} = 2\sqrt{\frac{Ro}{St}} \qquad -6.23$$

Alternatively from Equation 6.9

$$p^* = p + \tfrac{1}{2}\rho W^2 \qquad -6.24$$

or if Δp^* is small

$$\Delta p^* = \rho W \Delta W \qquad -6.25$$

Equation 6.21 now becomes that obtained by Hawthorne [27]

$$\frac{d^2\phi}{d\theta^2} = \frac{\Delta W}{W}\frac{R_n}{D}\cos\phi \qquad -6.26$$

and $$\phi^* = 2\pi\sqrt{\frac{D}{R_n}\frac{W}{\Delta W}} \qquad -6.27$$

A simple pendulum is a good analogy with the flow in a stationary pipe bend (see Figure 6.3). When the low p* fluid is on the inside of the bend, the pendulum hangs vertically downwards, and the flow is stable. If the flow is disturbed slightly the flow, like the pendulum, will oscillate about its stable location. When the low p* fluid is on the outside of the bend, the pendulum bob is vertically above the point of suspension and the flow is therefore unstable. If it is disturbed, it will oscillate with large amplitude about the stable location of low p* fluid on the inside of the bend. Other orientations of the lowest p* fluid at the inlet to the bend will result in oscillations of amplitudes equal to the distance of the lowest p* fluid from its stable location.

Precise solutions to Equation 6.21 can be obtained by using elliptical integral tables, (see Appendix 5). The author however, wished to solve Equation 6.21 by a finite difference technique, which could then be used for more complex geometries, where tables giving solutions to the correspondingly more complex equations were not available.

6.5 The Finite Difference Technique

The streamtube is divided into short sections, not necessarily of the same length. The boundary conditions at the first point are set i.e. ϕ_1 and $(d\phi/d\theta)_1$ are given values.

Now, let us consider the calculations which are necessary at the n^{th} point, where the values of ϕ_n and $(d\phi/d\theta)_n$ are known, in order to obtain the values of ϕ_{n+1} and $(d\phi/d\theta)_{n+1}$. Firstly, as an initial approximation, we set $\phi_{n+1}=\phi_n$ and $(d\phi/d\theta)_{n+1}=(d\phi/d\theta)_n$. Now, we have an equation of the form

$$\left(\frac{d^2\phi}{d\theta^2}\right)_n = f(\phi_n, \theta_n) \qquad -6.28$$

which in its general form is Equation 6.20. Equation 6.28 enables us

and $$\emptyset^* = 2\pi\sqrt{\frac{D}{R_n}\frac{W}{\Delta W}} \qquad -6.27$$

A simple pendulum is a good analogy with the flow in a stationary pipe bend (see Figure 6.3). When the low p* fluid is on the inside of the bend, the pendulum hangs vertically downwards, and the flow is stable. If the flow is disturbed slightly the flow, like the pendulum, will oscillate about its stable location. When the low p* fluid is on the outside of the bend, the pendulum bob is vertically above the point of suspension and the flow is therefore unstable. If it is disturbed, it will oscillate with large amplitude about the stable location of low p* fluid on the inside of the bend. Other orientations of the lowest p* fluid at the inlet to the bend will result in oscillations of amplitudes equal to the distance of the lowest p* fluid from its stable location.

Precise solutions to Equation 6.21 can be obtained by using elliptical integral tables, (see Appendix 5). The author however, wished to solve Equation 6.21 by a finite difference technique, which could then be used for more complex geometries, where tables giving solutions to the correspondingly more complex equations were not available.

6.5 The Finite Difference Technique

The streamtube is divided into short sections, not necessarily of the same length. The boundary conditions at the first point are set i.e. $\emptyset_1$ and $(d\emptyset/d\theta)_1$ are given values.

Now, let us consider the calculations which are necessary at the n^{th} point, where the values of $\emptyset_n$ and $(d\emptyset/d\theta)_n$ are known, in order to obtain the values of $\emptyset_{n+1}$ and $(d\emptyset/d\theta)_{n+1}$. Firstly, as an initial approximation, we set $\emptyset_{n+1}=\emptyset_n$ and $(d\emptyset/d\theta)_{n+1}=(d\emptyset/d\theta)_n$. Now, we have an equation of the form

$$\left(\frac{d^2\emptyset}{d\theta^2}\right)_n = f(\emptyset_n, \theta_n) \qquad -6.28$$

which in its general form is Equation 6.20. Equation 6.28 enables us

to calculate values for $(d^2\phi/d\theta^2)_n$ and $(d^2\phi/d\theta^2)_{n+1}$, which can then be used to obtain a value for the first differential

$$\left(\frac{d\phi}{d\theta}\right)_{n+1} = \left(\frac{d\phi}{d\theta}\right)_n + \left\{ \left(\frac{d^2\phi}{d\theta^2}\right)_n + \left(\frac{d^2\phi}{d\theta^2}\right)_{n+1} \right\} \frac{(\phi_{n+1} - \phi_n)}{2} \qquad -6.29$$

and from this, the value of

$$\phi_{n+1} = \phi_n + \left\{ \left(\frac{d\phi}{d\theta}\right)_n + \left(\frac{d\phi}{d\theta}\right)_{n+1} \right\} \frac{(\phi_{n+1} - \phi_n)}{2} \qquad -6.30$$

Now, this value of ϕ_{n+1} will be a better approximation to the correct value than the value we used in Equation 6.28. So, we now use are new value of ϕ_{n+1} in Equation 6.28 to get a better value of $(d^2\phi/d\theta^2)_{n+1}$ and we repeat the calculations using Equations 6.29 and 6.30. The new value of ϕ_{n+1} obtained from Equation 6.30 is then compared with the previous value and the calculations repeated again, unless the alteration of ϕ_{n+1} with further computation would be negligible. The values of ϕ_{n+1} and $(d\phi/d\theta)_{n+1}$ have thus been obtained and the calculations can proceed to the next point along the streamtube.

Equation 6.21 was solved numerically by this finite difference technique using points at 1 degree intervals around a 90 degree bend. The value of $St=(\Delta p^* R_n/\rho W^2 D)$ was 16. Solutions are presented graphically in Figure 6.4 for 36 different inlet locations of the lowest p* fluid. These values of ϕ, calculated by finite difference technique, were compared with values obtained from elliptical integral tables and were found to be the same within 1%.

6.6 Solution for a Rotating Straight Pipe (see Figure 6.5)

Set $\omega_x = \omega_y = 0$; $\omega_z = 1$; $\phi = \frac{\pi}{2}$ and let $R_n \to \infty$ in Equation 6.18

$$D^2 \frac{d^2\phi}{ds^2} = -\frac{\omega D}{W} \frac{\Delta p^*}{\rho W^2} \sin \phi \qquad -6.31$$

For small ϕ (i.e. Lowest p* on the suction side) this equation can be approximated by

$$D^2 \frac{d^2\phi}{ds^2} + \frac{\omega D}{W} \frac{\Delta p^*}{\rho W^2} \phi = 0 \qquad -6.32$$

This is a s.h.m. equation, with period

$$\frac{s^*}{D} = 2\pi \sqrt{\frac{W}{\omega D} \frac{\rho W^2}{\Delta p^*}} \qquad -6.33$$

Using Equation 6.25, Equation 6.31 reduces to the equation derived by Hawthorne [27]

$$\frac{s^*}{D} = 2\pi \sqrt{\frac{W}{\omega D} \frac{W}{\Delta \bar{W}}} \qquad -6.34$$

This solution is similar to that for the stationary bend, the stable location for the lowest p* fluid is on the suction side (ϕ=0). When the lowest p* fluid is on the pressure side (ϕ=90°), the flow is unstable and it will oscillate about the stable location on the suction side (ϕ=0).

Exact solutions of Equation 6.31 are presented graphically in Figure 6.6 for 36 different inlet locations of the lowest p* fluid.

6.7 Solution for a Rotating Bend (see Figure 6.7)

Set $\omega_x = \omega_z = 0$ and $\omega_y = 1$ in Equation 6.18

$$\frac{d^2\phi}{d\theta^2} = \frac{\Delta p^* R_n}{\rho W} \frac{}{D} \left(1 - \frac{\omega R_n}{W}\right) \cos \phi \qquad -6.35$$

In a rotating bend, there are contributions to secondary circulation due to curvature and rotation. The dimensionless quantity Ro (the Rossby Number) compares the magnitude of these two contributions. If Ro is small, rotation effects dominate the flow; if Ro is large, curvature effects dominate. If the Rossby Number were unity, no secondary flow would occur. In this condition the outside of the bend is also the suction side. In a 2-dimensional impeller, this implies that less secondary flow will occur in impellers with backward-swept blades.

Equation 6.35 can again be approximated to a s.h.m. equation with period

$$\phi^* = 2\pi\sqrt{\frac{Ro}{St(Ro-1)}} \qquad \text{for } Ro > 1$$

$$\phi^* = 2\pi\sqrt{\frac{Ro}{St(1-Ro)}} \qquad \text{for } Ro < 1 \qquad -6.36$$

The stable location for lowest p* fluid is the pressure surface for Ro>1 and the suction surface for Ro<1.

Exact solutions of Equation 6.35 are of the same form as those for the stationary bend and the rotating straight pipe.

Experimental measurements were recently taken by Anand and Lakshminarayana [32] in an axial flow inducer, which is essentially a long bend of the type shown in Figure 6.7. The Rossby Number evaluated for this inducer at a radius of 0.565 of the tip radius was Ro=0.67 and therefore, it is to be expected that the secondary flows in this inducer will be dominated by rotation. The effect of rotation is to induce secondary flows which carry low p* fluid to the outside of the bend and these secondary velocities were indeed observed as radial velocities by Anand and Lakshminarayana.

The general result in the three flows so far considered, is that curvature induces streamline curvature forces which move low p* fluid towards the inside of the bend and rotation produces Coriolis forces which move low p* fluid towards the suction surface.

Equation 6.20, for more complex geometries, cannot be approximated to the s.h.m. equation or solved by the use of elliptical integral tables and therefore has to be solved by finite difference techniques on a computer.

6.8 Solution for a Rotating Axial-to-Radial Bend (see Figure 6.8)

Set $\omega_x = \omega_y = 0$ and $\omega_z = 1$ in Equation 6.20

$$\frac{d^2\phi}{d\theta^2} = \underbrace{St\ Cos\ \phi}_{\substack{\text{Curvature}\\ \text{Term.}}} - \underbrace{\frac{St}{Ro}\ Sin\ \phi\ Sin\ \theta}_{\substack{\text{Rotation}\\ \text{Term.}}} - \underbrace{\frac{1}{Ro}\ Sin\ \theta}_{\substack{\text{Co-ordinate}\\ \text{Term.}}} \qquad -6.37$$

In an axial-to-radial bend, the contributions from curvature and rotation are perpendicular to each other. The curvature

contribution is of the same strength throughout, but the rotation term increases as the flow turns towards the radial direction. At the inlet, relative to the pipe bend, the fluid is rotating with angular velocity ω and so a relative swirl exists. This swirl will be convected to the outlet where it will represent an absolute swirl as well as a relative one. As Ω_s is the absolute vorticity about a relative streamline, the co-ordinate term is required in Equation 6.37 to represent the increase in absolute vorticity due to the convection of the relative swirl from the inlet to the outlet.

Equation 6.37 was solved numerically using points at 1 degree intervals of θ around the 90 degree bend. The value of St used was 10 and the value of Ro was 1. The solutions for 36 different inlet locations of the lowest p* fluid are presented graphically in Figure 6.9.

6.8.1 Discussion of the axial-to-radial bend solution

At the inlet, there is already a relative vorticity, which initially rotates the flow in a pressure surface/outside/suction surface/inside direction. The low p* fluid initially seeks the inside of the bend and so, low p* initially on the pressure surface is being driven anticlockwise and that initially on the suction surface clockwise. The low p* fluid initially near the outside of the bend, but on the pressure side of it ($\phi_i = 240^\circ$ to 270°) is carried across the outside of the bend ($\phi = 270^\circ$) by the inlet swirl before sufficient vorticity is generated in the anticlockwise direction to move it towards the pressure surface.

Each flow solution oscillates about the stable location of the low p* fluid (where $d^2\phi/d\theta^2 = 0$). The stable location will move from the inside of the bend towards the suction surface as the flow turns towards the radial direction and hence the Coriolis forces become stronger. The period of oscillation is dependent on the amplitude of oscillation. The small amplitude solutions, where the low p* fluid

was near the stable location initially ($\phi_i \simeq 90^o$), have a short period completing almost one oscillation in the 90^o bend. The larger amplitude solutions ($\phi_i \simeq 270^o$) have a much longer period. The solution for $\phi_i = 230^o$ barely completes a quarter of an oscillation.

The theory used in this analysis is inviscid and as Hawthorne [27], showed when comparing experimental data with a theoretical solution for a pipe bend, the viscous friction will alter not only the theoretical amplitude of the oscillation, but also its period. Wall friction will account for a reduction in the predicted amplitude of an oscillation, this means the 'overshoot' of the low p* fluid beyond its stable location is less than predicted and this fluid therefore turns back towards its stable location sooner, i.e. the period has been reduced. However, a second effect of viscosity is to reduce the value of Δp^* across the passage as the flow 'mixes out' and hence the 'strength' (St) used in the equations is reduced, which will increase the period. Therefore, in a viscid flow, the location of the low p* fluid at the outlet for each of the inlet locations will be closer to the stable location at the outlet ($\phi_o = 33^o$ in this case) than in these inviscid solutions.

6.9 Centrifugal Impeller Representation - Eckardt's Impeller

In order to represent a compressor impeller passage, a rotating duct, which has the same centre of area path as the impeller passage was considered (see Figure 6.11). This path can be approximately calculated for elliptical blade sections as shown in Appendix 6. The cross-sectional area of the duct is constant. This path was first calculated for Eckardt's impeller (Figure 6.10), the geometry was described by Moore [54].

The development of secondary vorticity was calculated by representing the 'centre of area' path line by about 100 steps, each step corresponding to a short length of a pipe bend. The radius of curvature and directions of the streamline, normal and binormal were

recalculated at each step. The flow was taken as incompressible and the mean velocity was therefore constant through the duct. The mean velocity does not vary greatly in Eckardt's measurements [52,53,54].

6.9.1 Discussion of Eckardt's Impeller Passage Solutions

The results from the program are presented graphically (Figure 6.12). The figure shows the locations of the lowest p* fluid through the duct for 36 different inlet locations. At the inlet, the fluid close to the hub will have a lower circumferential relative velocity than the fluid close to the shroud and hence, in the relative frame, the flow appears to have a pre-swirl which rotates the flow in a pressure side/hub/suction side/shroud direction. In the inducer bend, the low p* fluid will in each case seek the stable location close to the shroud. This can be seen as a slight convergence of the curves near the shroud (s/s_m=0.2). It is clear that as the stable location is on the shroud, rotation dominates the secondary flow pattern in the inducer.

Beyond s/s_m=0.2, the axial-to-radial bend continues to move low p* fluid towards the shroud (the inside of this bend). The convergence of the curves close to the shroud becomes quite marked (s/s_m=0.5). The oscillatory nature of the solutions is shown as the curves 'overshoot' the stable location for the lowest p* fluid close to the shroud (s/s_m=0.7). By this point in the duct, the flow direction is almost radial and therefore the Coriolis forces once more influence the flow. The vorticity generated due to rotation, moves the low p* fluid towards the suction surface. The 'average' location for the lowest p* fluid at the outlet appears to be $\phi_o=117^o$ or about 30% of the way between the centre of the shroud and the centre of the suction side. The stable location for low p* fluid at the outlet however, is $\phi_o=165^o$, so the inertia of the secondary flows has carried the lowest p* fluid beyond its stable location.

The stable location line is the locus of points where the rate

of streamwise vorticity generation is zero ($d^2\emptyset/d\theta^2=0$). In Appendix 7, the equation for this line is derived for a general streamtube and it is shown that the stable location at the impeller outlet can be altered by varying the Rossby Number or the Strength St.

There are many approximations made in this analysis. The duct is taken as circular in cross-section and the flow assumed to be incompressible and inviscid. The gradient of $\Delta p^*/D$ across the duct is set fairly arbitrarily and although this will not greatly affect the stable location for the low p* fluid it will alter the oscillation's amplitude and period. However, some qualitative results for secondary flow development come to light.

The influence of the inducer bend is small, because its associated Rossby Number is small and as the inducer bend is short, secondary vorticity has little time to develop. The axial-to-radial bend however, has a large influence on the flow. The Rossby Number is close to unity indicating that the bend's curvature is likely to contribute as much to the vorticity generation as the rotation. This bend is also longer allowing substantial secondary flow development. The secondary flow developed in this bend causes a migration of the low p* fluid from the boundary layers towards a stable location on the shroud. This stable location moves towards the suction surface as the rotation effects increase as the flow turns towards the radial direction.

In the boundary layers (see Figure 6.13), the low p* fluid will be convected towards the suction-side/shroud corner. Eckardt [53] calls these regions of low p* fluid, which are moving across the passage, 'Boundary Layer Wall Jets'. In a shrouded centrifugal impeller passage there are two 'Jets'; The main 'Jet' along the shroud and a weaker 'Jet' along the suction surface. Low p* fluid initially on the pressure and suction surfaces will migrate rapidly in the first half of the passage. The Coriolis forces will cause

increased movement of the low p* fluid on the hub and shroud walls in the latter half of the passage, as the flow turns towards the radial direction. The shroud 'Jet' will be made up of low p* fluid, which was initially convected across the pressure surface and then across the shroud and so benefits from both the curvature and Coriolis accelerations. The suction surface 'Jet' however, does not benefit significantly from the Coriolis forces and is therefore weaker.

These boundary layer 'Wall Jets' will interact on the shroud. Early in the passage, the 'Jets' will carry little low p* fluid and as the 'Jet' fluid approaches the stable location on the shroud, the only driving force will be the weak Coriolis force and the 'Jet' will probably be slowed to rest by viscous friction. However, later in the passage, as more low p* fluid is transported by the 'Jets', the inertia of the secondary flow will not be dissipated by viscous friction and the 'Jets' will collide near the stable location.

Eckardt [53] suggests that "the boundary layer rolls up in the wake area due to the collision of the boundary layer 'Wall Jets' 1 and 2+3, thus initiating and/or reinforcing the separation onset". His 'Wall Jets' are (1) shroud surface boundary layer, (2) suction surface boundary layer and (3) tip leakage.

The interaction of these 'Jets' and the onset of separation is a complex 3-dimensional flow problem. When the 'Wall Jets' collide, they must turn quite sharply as they merge. This will make the higher p* fluid near the surface of the boundary layer move towards the centre of the combined 'Jet', the lower p* fluid is pushed to the boundaries of the combined 'Jet'. As more boundary layer fluid joins this combined 'Jet', the fresh high p* fluid will migrate to the centre of the combined 'Jet', pushing fluid up into the passage. This action may result in the two secondary vortices seen in Eckardt's wake [52,53,54].

Eckardt also comments [54], 'the circumferential position of its (the wake's) core in the present case at y/t=0.65 shifts between y/t=0.5 to 0.8 depending on mass flow and speed'. The position of the stable location for the lowest p* fluid, which must influence the position of the core of the wake at the outlet, is influenced by the Rossby Number. From Equation 6.11, an increase in rotational speed (a decrease in Rossby Number) increases the Coriolis generated secondary flows and hence moves the stable location for low p* fluid towards the suction surface. An increase in mass flow rate (an increase in Rossby Number) moves the stable location closer to the shroud because of the increased strength of the secondary flow generated by curvature. In Eckardt's impeller this will alter the location of the wake's core, but in addition, an increase in rotational speed is likely to increase the strength of the tip leakage 'Jet', which will move the wake across the shroud towards the pressure surface.

6.10 Solution for the Ghost Impeller Passage

A Ghost impeller passage was represented by a pipe bend in a similar manner to Eckardt's impeller passage. Figure 6.14 shows the solutions for the Ghost, for 36 different inlet locations of the lowest p* fluid, at the 'design' flow rate. The relative swirl at the inlet, due to the lower circumferential velocity near the hub, is detectable in Figure 6.14, as it was for Eckardt's impeller (Figure 6.12). One significant difference between the results for the two impellers is the stable location for low p* fluid at the impeller inlets. This difference is due to two differences in the inducer geometries. Firstly, Eckardt's impeller has a much stronger meridional curvature at the inlet than the Ghost impeller and secondly blade-to-blade curvature is stronger at the inlet of the Ghost impeller. Therefore, in Eckardt's impeller, as the blade-to-blade curvature is weak, the stable location for low p* fluid

appears very close to the shroud, whereas in the Ghost, where the blade-to-blade curvature is stronger, but the meridional curvature is relatively weaker, the stable location is close to the suction-side/shroud corner.

The solutions for the Ghost impeller (Figure 6.14) show the convergence of the various solutions between Stations 2 and 3 in the suction-side/shroud corner. The 'overshoot' of the solutions for $\emptyset_i = 130^o$ to 300^o beyond the stable location line, is representative of the action of the strong vortex which was observed on the suction side of the passage in Figure 3.11. Similarly, the solutions for $\emptyset_i = -20^o$ to 120^o at Station 3 (see Figure 6.14), represent the other passage vortex on the pressure side of the passage in Figure 3.11. At Station 4, most of the solutions give a value of $\emptyset$ which is less than the stable location value $\emptyset_{ST}$. This shows theoretically that the inertia of the passage vortex on the suction side will move the core of the wake towards the shroud. At the outlet, most of the solutions are showing the start of a trend towards the suction surface, and the average position for the solutions at the outlet ($\emptyset_o = 125^o$) is about one third of the way between the centre of the shroud and the centre of the suction surface. As discussed previously, viscosity will tend to damp the oscillations of the flow about the stable location and therefore a viscid calculation would predict solutions which would be less 'fanned out' and closer to the stable location at the outlet. An important feature of the experimental results, which is not represented in the theoretical model is the separation of the shroud boundary layer. This separation resulted in a region of low p* fluid in the suction-side/shroud corner region at Station 2 (see Figure 3.7). The theoretical solutions for $\emptyset_i = 110^o$ to 130^o are therefore representative of the secondary flow developed due to this boundary layer separation. If these solutions are weighted in the estimate of the 'average' solution at the outlet,

this 'average' solution would be close to the suction-side/shroud corner, which compares reasonably with the observed wake position (see Figure 3.16).

6.10.1 'Below' and 'Above Design' Flows

Having considered the 'design' flow case, it is of interest to calculate the solutions for the 'below design' flow rate, which are presented in Figure 6.15 and for the 'above design' flow rate, which are presented in Figure 6.16. It is immediately apparent that although the stable location line clearly shows that the effects of curvature increase and those of rotation decrease as the flow rate is increased, there are no major differences between the solutions for the three flow rates. However, in the experiments the wake moved from the suction surface to the shroud as the flow rate was increased (see Figures 3.16, 4.14 and 4.33). A major influence on the results for the 'below design' flow rate must be the separation of the shroud boundary layer. In the 'below design' flow, the separation was more severe than in the 'design' flow and a substantial region of low p* fluid occurred on the shroud at Stations 1 and 2 (see Figures 4.2 and 4.5). The secondary flow developed in this region can perhaps be best represented by the solutions for $\phi_i = 90^o$ to 110^o and these solutions should dominate the 'average' solution at the outlet and so a region of low p* fluid close to the centre of the suction surface is predicted and this is where the wake was observed experimentally in Figure 4.14.

The 'above design' flow case does not have any substantial low p* regions in the early passage (see Figures 4.21 and 4.24) and therefore it may be assumed that an unbiased average of all the 36 solutions in Figure 6.16 at the outlet should be reasonably representative of the flow. This 'average' solution at the outlet predicts the location of the wake to be at $\phi_o = 122^o$ or about a third of the way between the centre of the shroud and the centre of the suction

surface. This is a fair prediction when compared with the actual position of the wake (see Figure 4.33).

6.11 Conclusions drawn from the Theoretical Work

1. In any rotating and/or curved duct, with a gradient of rotary stagnation pressure p* normal to the primary flow, an oscillatory flow about the axis of the duct will develop. The period of oscillation increases with the amplitude.

2. In centrifugal impellers, the inertia of the secondary flow developed in the axial-to-radial bend will carry boundary layer fluid beyond its stable location and therefore a region of low p* fluid will often be found on the shroud at the outlet, although the stable location for low p* fluid is on the suction surface.

3. The changes in Rossby Number, associated with the changes in flow rate made in the experiments in the Ghost impeller, only alter the theoretical model solutions slightly. Only when, in the estimation of the 'average' location of the low p* fluid at the impeller outlet, account is made of the low p* regions produced by the shroud boundary layer separation in the early part of the passage, can a good correlation, between the theoretical prediction and the experimental observation of the location of the wake in the 'below design' and 'design' flow rates, be achieved.

REFERENCES

1. DEAN,R.C.,Jr., 'On the unresolved Fluid Dynamics of the Centrifugal Compressor', Advanced Centrifugal Compressors, ASME special publication, 1971, p1-55.

2. SMITH,R. and BENSTEIN,E.H., 'Potential Gas Turbine Power for General Aviation in 1988', presented at the 1979 ASME Gas Turbine Conference, San Diego California.

3. SMITH,J.A., 'Notes on some Experimental researches of Internal flow in Centrifugal Pumps and allied Machines', Engineering, Vol. LXXIV, Dec 5th 1902, p763.

4. GIBSON,A.H., 'Hydraulics and its applications', Constable 1st Edition, 1908.

5. CARRARD,A., 'Sur le Calcul des Roues Centrifuges', La Technique Moderne, T.XV No. 3 p65-71 and No.4 p100-104, Feb 1923.

6. CARRARD,A., 'On Calculations for Centrifugal Wheels', translation by MOORE,J., Univ. of Cambridge, Dept. of Engineering, Report No. CUED/A/Turbo/TR 73,1975.

7. MOORE,J., 'A Wake and an Eddy in a Rotating, Radial-Flow Passage (Part 1: Experimental Observations, Part 2: Flow Model), ASME J. of Eng. for Power, Ser.A, Vol.95 No.3, 1973, p205-219.

8. FLUGEL,G., 'Ein neues Verfahren der graphischen Integration', Dissertation, Munich 1914.

9. KEARTON,W.J., 'Influence of the number of impeller blades on the Pressure generated in a Centrifugal Compressor and on its General Performance', Proc. Inst. Mech. Engs., Vol.124, 1933, p481-568.

10. CHURCH,A.H., 'Centrifugal Pumps and Blowers', 1944, reprinted by Robert E. Krieger, Huntington New York, 1972.

11. HAMRICK,J.T., MIZISIN,J., MICHEL,D.J., 'Study of three-dimensional Internal Flow distribution based on measurements in a 48 inch radial-inlet Centrifugal Impeller', NACA TN 3101, 1954.

12. HAMRICK,J.T., 'Some Aerodynamic Investigations in Centrifugal Impellers', Trans. ASME, April 1956, p591-602.

13. MOORE,J., MOORE,J.G., JOHNSON,M.W., 'On Three-Dimensional Flow in Centrifugal Impellers', Aeronautical Research Council, CP No.1384, 1977.

14. FUJIE,K., 'Study of 3-dimensional internal flows in Impellers of Centrifugal Blowers with Straight-Radial Blades and Logarithmic-spiral Blades in Radial Part only', Bull. of JSME, Vol.1, No.3, 1958, p275-282.

15. FOWLER,H.S., 'The Distribution and Stability of Flow in a Rotating Channel', ASME J. of Eng. for Power, Vol.90, No.3, July 1968.

16. LENNEMANN,E. and HOWARD,J.M.G., 'Unsteady Flow Phenomenon in Rotating Centrifugal Impeller Passages', ASME J. of Eng. for Power, Vol.92, No.1, Jan 1970.

17. HOWARD,J.M.G. and LENNEMANN,E., 'Measured and Predicted Secondary Flows in a Centrifugal Impeller', ASME J. of Eng. for Power, Vol.93, No.1, Jan 1971.

18. McDONALD,G.B., LENNEMANN,E., HOWARD,J.M.G., 'Measured and Predicted Flow near the Exit of a Radial-Flow Impeller', ASME J. of Eng. for Power, Vol.93, No.4, Oct 1971.

19. OLIVARI,D. and SALASPINI,A., 'Measurement of Velocity Distribution at the impeller exit of a radial compressor', Von Karman Institute TN106, March 1975.

20. ELLIS,G.O., 'A study of Induced Vorticity in Centrifugal Compressors', ASME J. of Eng. for Power, Vol.86, No.1, Jan 1964, p63-76.

21. FOWLER,H.S., 'Some Measurements of the Flow pattern in a Centrifugal Compressor Impeller', ASME Paper 65-GA/GTP-7, 1965.

22. FOWLER,H.S. 'An investigation of the Flow processes in a Centrifugal Compressor Impeller', NRC of Canada, Mech. Eng. Report ME-220, July 1966.

23. SENOO,Y., YAMAGUCHI,M., NISHI M., 'A Photographic study of the 3-dimensional Flow in a Radial Compressor , ASME J. of Eng. for Power, July 1968, p237-244.

24. WOOD,M.D. and MARLOW,A.V., 'The use of numerical methods for the investigation of flow in water pump impellers', Proc. Inst. Mech. Engs., Vol.181, Pt.1, 1966-7, p725-748.

25. HAMRICK,J.T., GINSBURG,A., OSBORN,W.M., 'Method of analysis for compressible flow through mixed-flow centrifugal impellers of arbitrary design', NACA TN 1082, 1952.

26. KATSANIS T., 'A computer programme for Calculating Velocities and Streamlines on a Blade-to-Blade Stream Surface of Turbomachines', NASA TN-D4525, 1968.

27. HAWTHORNE,W.R., 'Secondary Circulation in Fluid Flow', MIT, Gas Turbine Report, May 1950.

28. SMITH,A.G. 'On the Generation of a Streamwise Component of Vorticity in a Rotating Passage', Aero. Quart., Vol.8, 1957, p369-383.

29. WU,C., 'A General Theory of Three-Dimensional Flow in Subsonic and Supersonic Turbomachines of Axial, Radial and Mixed Flow', NASA TN 2604.

30. LAKSHMINARAYANA,B. and HORLOCK,J.H., 'Generalised Expressions for Secondary Vorticity using Intrinsic Co-ordinates', J. of Fluid Mech., Vol.59,1973, p97-115.

31. HAWTHORNE,W.R., 'Secondary Vorticity in Stratified Compressible Fluids in Rotating Systems', Univ. of Cambridge, Dept. of Eng., Report No. CUED/A-Turbo/TR 63, 1974.

32. ANAND,A.K. and LAKSHMINARAYANA,B., 'An experimental study of three-dimensional turbulent boundary layer and turbulence characteristics inside a Turbomachinery rotor passage', ASME J. of Eng for Power, Oct 1978, p676-690.

33. JOHNSTON,J.P., 'The suppression of Shear Layer Turbulence in Rotating Systems', ASME J. of Fluid Eng., Vol.95, Ser.1, 1973, p229-239.

34. JOHNSTON,J.P., 'The Effects of Rotation on Boundary Layers in Turbomachinery Rotors', Fluid Mechanics, Acoustics and Design of Turbomachinery Rotors', NASA SP-304, 1974, p207-250.

35. JOHNSTON,J.P. and EIDE,S.A., 'Turbulent Boundary Layers on Centrifugal Compressor blades: Prediction of the effects of surface curvature and rotation', ASME J. of Fluids Eng., Sept 1976, p374-381.

36. ROTHE,P.H. and JOHNSTON,J.P., 'Effects of system rotation on the performance of 2-dimensional diffusers', ASME J. of Fluids Eng., Sept 1976, p422-430.

37. BRADSHAW,P., 'The analogy between Streamline Curvature and Buoyancy in Turbulent Shear Flow', J. of Fluid Mech., Vol.36, 1969, p177-191.

38. BRADSHAW,P., 'Effects of Streamline Curvature on Turbulent Flow', AGARDograph 169, 1973.

39. LAKSHMINARAYANA,B. and HORLOCK,J.H., 'Review: Secondary Flow and losses in Cascades and Axial Flow Turbines', Int. J. Mech. Sci., Vol.5, 1963, p287-307.

40. DEAN,R.C.,Jr. and SENOO,Y., 'Rotating Wakes in Vaneless Diffusers', ASME J. of Basic Eng., Vol.82, 1960, p563-574.

41. JOHNSTON,J.P. and DEAN,R.C.,Jr., 'Losses in Vaneless Diffusers of Centrifugal Compressors and Pumps', ASME J. of Eng. for Power, Vol.88, 1966, p49-60.

42. SENOO,Y. and ISHIDA,M., 'Behaviour of Severely Assymmetric Flow in a Vaneless Diffuser', ASME J. of Eng. for Power, Vol.97, 1975, p375-387.

43. REBERNIK,B., 'Investigations on induced vorticity in Vaneless Diffusers of Radial flow Pumps', Proc. of the 4^{th} conference on Fluid Machinery, Budapest 1972, p1129-1139.

44. JOHNSTON,J.P., 'Experimental Data on 3-dimensional flow in a Centrifugal Compressor Diffuser', MIT Gas Turbine Laboratory, Dec 1954.

45. JANSEN,W., 'Incompressible Fluid Flow in a Radial Vaneless Diffuser', MIT Gas Turbine Lab., Report No.52, May 1959.

46. JANSEN,W., 'Steady Fluid Flow in a Radial Vaneless Diffuser', ASME J. of Basic Eng., Ser.D, Vol.86, 1964, p607-619.

47. DEAN,R.C.,Jr., 'The Fluid Dynamic Design of Advanced Centrifugal Compressors', Creare TN-153, Sept 1972, p38.

48. PATANKAR,S.V. and SPALDING,D.P., 'A Calculation Procedure for Heat, Mass and Momentum Transfer in Three-Dimensional Parabolic Flows', Int. J. of Heat and Mass Transfer, 15, 1972, p1787-1806.

49. MAJUMDAR,A.K., PRATAP,V.S., SPALDING,D.B., 'Numerical computation of Flow in Rotating Ducts', ASME Paper No. 76-FE-25, presented at a meeting March 21-25, 1976.

50. ECKARDT,D., 'Applications of Dynamic Measurement Techniques for Unsteady Flow Investigations in Centrifugal Compressors', Von Karman Institute Lecture Series 66, Advanced Radial Compressors, 1974, p101.

51. ECKARDT,D., 'Detailed Flow Investigations within a High-Speed Centrifugal Compressor Impeller', ASME J. of Fluids Eng., Vol.98, 1976, p390-402.

52. ECKARDT,D., 'Instantaneous Measurements in the Jet-Wake Discharge Flow of a Centrifugal Compressor Impeller', ASME J. of Eng. for Power, Vol.97, No.3, July 1975, p337-346.

53. ECKARDT,D., 'Investigations of the Disturbed Flow Pattern within and at the Discharge from a High-Loaded Centrifugal Compressor Impeller', DLB-FB 75-39, 1975.

54. MOORE,J., 'Eckardt's Impeller - A Ghost from Ages Past', CUED/A-Turbo/TR 83/1976.

55. ELDER,J.W., 'Steady flow through non-uniform gauzes of arbitrary shape', J. of Fluid Mech., Vol.5, Pt.3, April 1959, p355-368.

56. TAYLOR,G.I. and BACHELOR,G.K., 'The Effects of Wire Gauze on Small Disturbances in a Uniform Stream', Quart. J. of Mech. and App. Maths., Vol.2, 1949, p1-29.

57. DEAN,R.C.,Jr., 'Sudden mixing losses produced by Centrifugal Impeller Wakes in Compressible Flow Air - k=1.387', Creare Incorporated Technical Memorandum M-46, Oct 1967.

58. KARMAN,T.V. and BIOT,A., 'Mathematical Methods in Engineering', McGraw-Hill, New York, 1940, p788.

APPENDIX 1

GHOST IMPELLER GEOMETRY

In this section linear dimensions are in mm.

The main dimensions of the impeller are

Outside diameter = 909.3,

Inlet shroud diameter = 571.5,

Hub diameter = 177.8.

The impeller has 19 blades which have radial sections. The camber-line geometry is defined by Moore [54], in a cylindrical co-ordinate system (r, γ, z''), where z'' is taken as the axial distance upstream of the impeller hub at the outlet. The variation of the blade angle γ, with z'' is represented by an ellipse

$$\left(\frac{\gamma}{a}\right)^2 + \left(\frac{z''-d}{b}\right)^2 = 1, \text{ for } z'' \geq d, \qquad \text{-A1.1}$$

and by

$$\gamma = a, \text{ for } 0 \leq z'' \leq d, \qquad \text{-A1.2}$$

where a=31.983 degrees, b=182.73 and d=72.39.

The shroud profile is defined by a circular arc

$$(r-r_0)^2 + (z''-z_0'')^2 = R^2, \text{ for } 72.39 \leq z'' \leq 212.09, \qquad \text{-A1.3}$$

where r_0=425.45, z_0''=212.09, and R=139.7

and by $r = 285.75$, for $212.09 \leq z'' \leq 237.49$, -A1.4

and by $z'' = 72.39$, for $425.45 \leq r \leq 454.66$. -A1.5

The hub profile is defined by two circular arcs, of the form of Equation A1.3, where

r_0=342.90, z_0''=266.19 and R=254.00, for $25.4 \leq z'' \leq 241.3$,

r_0=416.56, z_0''=482.60 and R=482.60, for $0.0 \leq z'' \leq 25.4$,

and by $z''=0.0$, for $416.56 \leq r \leq 454.66$. -A1.6

The blade thickness is given by the following table, where the symbols and stations are as defined in Figure A1.

Station Number.	Section in Fig.	r_1	r_2	r_3	t_1	t_2	t_3	γ
1	B	103.3	285.7		12.62	1.02		0°
2	B	105.2	285.7		13.56	2.74		3° 0'47"
3	B	107.7	285.7		14.33	4.09		6°45'54"
4	B	111.0	286.3		15.06	5.08		9°11'24"
5	B	115.1	288.1		15.93	5.87		11°11'31"
6	B	119.9	291.0		17.12	6.45		12°51'18"
7	B	125.6	295.3		17.98	7.01		14°14' 7"
8	B	132.2	301.0		18.80	7.37		15°22'20"
9	B	139.8	308.4		19.43	7.62		16°17'36"
10	B	148.5	317.7		19.91	7.77		17° 1'35"
11	B	158.5	329.6		20.12	7.77		17°34'49"
12	B	170.1	345.1		20.07	7.54		17°58' 6"
13	B	183.4	367.3		19.69	6.88		18°11'54"
14	A	199.1	425.5	454.7	19.08	3.99	1.02	18°16'29"
15	A	218.1	433.1	454.7	18.31	4.47	1.50	18°16'29"
16	A	242.0	433.1	454.7	17.25	5.38	1.96	18°16'29"
17	A	275.8	433.1	454.7	15.57	6.22	2.44	18°16'29"
18	A	325.6	433.1	454.7	13.08	7.01	2.92	18°16'29"
19	B	416.6	454.7		8.46		3.25	18°16'29"

Table A1 Blade thickness, linear dimensions in mm.

APPENDIX 2

MEASUREMENT STATIONS

Co-ordinates of the intersections of the measurement planes with the hub and shroud walls are presented in Table A2. The intersections are shown in Figure A2, but the accuracy of the co-ordinates is only $\pm$2mm, since they represent intersections between planes and surfaces of revolution. The total meridional distance x_0, along the shroud, from inlet to outlet of the impeller is 274. mm.

Station	x/x_0	Shroud		Hub	
		r	z"	r	z"
1	0.02	285.8	232.	91.2	232.
2	0.17	287.3	191.	148.	103.
3	0.41	311.	132.	240.	28.
4	0.69	372.	83.	344.	5.5
5	0.97	447.	72.4	447.	0.0

Table A2 Measurement plane co-ordinates, dimensions in mm.

APPENDIX 3

IMPELLER FLOW PROPERTIES

The passage flow rates at each station are calculated by the computer program as described in Chapter 2. These values are then averaged and the standard deviation of the flow rate between Stations is also calculated.

The values of p^*_{max} and p^*_{min} are estimated from the data taken at Station 1 (also described in Chapter 2).

The axial velocity just upstream of the impeller passage is calculated from the average flow rate through the impeller passage in which the flow measurements were made. This axial velocity value is then used with the value of p^*_{max} in Bernoulli's equation to calculate the average value of static pressure just upstream of this passage. The static pressure at Station 5 is calculated by adding the centrifugal pressure rise to the value of $\overline{p}_r$ obtained from the flow measurements by the computer program.

The boundary layers at the inlet to the impeller are very thin on all the walls, except the shroud. The shroud boundary layer develops along the wall of the inlet duct and is probably thickened because of the rotating seal and the gap between the stationary inlet duct and the rotating shroud. For this reason, the displacement and momentum thicknesses, which were calculated from the axial velocity measurements made at Station 1, are presented here. These boundary layer parameters did not vary significantly in the blade-to-blade direction.

Flow property	Impeller flow		
	Design	Below Design	Above Design
Passage volumetric flow rate in m^3/s			
Station 1	0.1268	0.1050	0.1403
Station 2	0.1214	0.1044	0.1268
Station 3	0.1167	0.1021	0.1464
Station 4	0.1157	0.0968	0.1384
Station 5	0.1005	0.0858	0.1505
Average	0.1162	0.0988	0.1405
Standard deviation	0.0088	0.0071	0.0081
Mass flow rates in kg/s			
Passage	0.1424 $\pm$0.009	0.1211 $\pm$0.007	0.1721 $\pm$0.008
Equivalent impeller	2.705 $\pm$0.17	2.300 $\pm$0.13	3.270 $\pm$0.15
Pressures in N/m^2			
p^*_{max}	-270 $\pm$10	-275 $\pm$10	-250 $\pm$10
p^*_{min}	-585 $\pm$30	-565 $\pm$30	-650 $\pm$30
$\bar{p}$ just upstream of the passage inlet	-325.6 $\pm$30	-315.2 $\pm$30	-331.3 $\pm$30
$\bar{p}$ at Station 5	-40.2 $\pm$30	-58.0 $\pm$30	-100.9 $\pm$30
Shroud boundary layer parameters in mm			
Displacement thickness	1.37 $\pm$0.2	4.22 $\pm$0.2	1.86 $\pm$0.2
Momentum thickness	2.41 $\pm$0.4	6.66 $\pm$0.4	2.97 $\pm$0.4

Table A3 Impeller flow properties

APPENDIX 4

ISENTROPIC IMPELLER EFFICIENCY

Consider a reversible, adiabatic and hence isentropic compressor, which compresses a fluid from State 1 to State 2. Now for a perfect gas

$$\Delta h_{12s} = C_p \Delta T_{12}$$
$$= \frac{C_p}{R} \Delta\left(\frac{p}{\rho}\right)_{12} \qquad \text{-A4.1}$$

from the perfect gas relation $p=R\rho T$. But if air undergoes an isentropic process

$$\frac{p}{\rho^{\gamma}} = \text{CONSTANT} \qquad \text{-A4.2}$$

$$\Delta h_{12s} = \frac{\gamma}{(\gamma-1)} \left(\frac{p_1}{\rho_1}\right) \left\{ \left(\frac{p_2}{p_1}\right)^{\frac{\gamma-1}{\gamma}} - 1 \right\} \qquad \text{-A4.3}$$

For small $\Delta p = p_2 - p_1$, the Binomial expansion can be used and

$$\Delta h_{12s} = \frac{\Delta p}{\rho} \qquad \text{-A4.4}$$

Now, the real irreversible compressor can be represented by an isentropic compressor followed by a throttle valve, which drops the pressure by the stagnation pressure loss Δp^*_{12}. Now, as the overall pressure rise is Δp_{12}, the isentropic compressor will have a pressure rise $\Delta p_{12} + \Delta p^*_{12}$ and therefore, as the throttle is isenthalpic

$$\Delta h_{12} = \frac{\Delta p_{12} + \Delta p^*_{12}}{\rho} \qquad \text{-A4.5}$$

and hence the isentropic efficiency of the impeller is given by

$$\eta = \frac{\Delta h_{12s}}{\Delta h_{12}} = \frac{\Delta p_{12}}{\Delta p_{12} + \Delta p^*_{12}} \qquad \text{-A4.6}$$

APPENDIX 5

ANALYTICAL SOLUTION OF THE SIMPLE HARMONIC MOTION EQUATION

From Karman and Biot [58], the solution of

$$m \frac{d^2x}{dt^2} = g(x) \qquad \text{-A5.1}$$

is obtained by using

$$\frac{d^2x}{dt^2} = \frac{1}{2} \frac{d}{dx} \left[\left(\frac{dx}{dt} \right)^2 \right] \qquad \text{-A5.2}$$

and is given by

$$t = \int_{x_0}^{x} \frac{dx}{\sqrt{\left(\frac{dx}{dt} \right)_i^2 + \frac{2}{m} \left[G(x_i) - G(x) \right]}} \qquad \text{-A5.3}$$

where $G(x) = -\int_0^x g(x)dx$ -A5.4

Now, for example the solution for a straight rotating pipe (see Section 6.6)

$$\frac{x}{s^*} = \frac{1}{2\pi} \int_{\phi_0}^{\phi} \frac{d\phi}{\sqrt{2(\cos \phi - \cos \phi_i)}} \qquad \text{-A5.5}$$

As $\cos \phi = 1 - 2 \sin^2(\phi/2)$ -A5.6

$$\frac{x}{s^*} = \frac{1}{4\pi \sin(\phi_0/2)} \int_{\phi_0}^{\phi} \frac{d\phi}{\sqrt{1 - \frac{\sin^2(\phi/2)}{\sin^2(\phi_i/2)}}} \qquad \text{-A5.7}$$

However, we can not use tables for $\int_0^{\phi} \frac{d\Psi}{\sqrt{1 - k^2 \sin^2 \Psi}}$, here as

$k^2 = \operatorname{Cosec}^2(\phi_0/2) \geq 1$, for all ϕ_i and the tables only give solutions of the integral for $k^2 < 1$. We therefore now substitute

$$\sin \Psi = \frac{\sin (\phi/2)}{\sin (\phi_i/2)} \qquad \text{-A5.8}$$

$$\therefore \cos \Psi \, d\Psi = \frac{1}{2} \frac{\cos (\phi/2)}{\sin (\phi_i/2)} d\phi \qquad \text{-A5.9}$$

$$\frac{x}{s^*} = \frac{1}{4\pi \sin (\phi_0/2)} \int_{\phi_0}^{\phi} \frac{2 \sin (\phi_0/2) \cos \Psi \, d\Psi}{\cos (\phi/2) \sqrt{1 - \sin^2 \Psi}} \qquad \text{-A5.10}$$

But, $$\text{Cos } (\phi/2) = \sqrt{1 - \text{Sin}^2(\phi/2)}$$

$$= \sqrt{1 - \text{Sin}^2(\phi_i/2)\ \text{Sin}^2\psi} \qquad \text{-A5.11}$$

$$\therefore \frac{x}{s^*} = \frac{1}{2\pi} \int_{\psi = \pi/2}^{\psi = \frac{\text{Sin } (\phi/2)}{\text{Sin } (\phi_i/2)}} \frac{d\psi}{\sqrt{1 - \text{Sin}^2(\phi_i/2)\text{Sin}^2\psi}} \qquad \text{-A5.12}$$

Now, $k = \text{Sin } (\phi_i/2) \leq 1$ for all ϕ_i, so the tables can be used to find the complete solutions.

APPENDIX 6

THE CENTRE OF AREA LINE FOR AN ELLIPTICAL BLADE SECTION IMPELLER

With reference to Figure A3, let

$$R_N = \frac{R_{N1} + R_{N2}}{2} \qquad \text{-A6.1}$$

and at the inlet

$$r_m^2 = \frac{r_1^2 + r_2^2}{2}$$

$$= \frac{(R_1 - R_{N1})^2}{2} + \frac{(R_2 - R_{N2})^2}{2}$$

but, $R = r_M + R_N$

$$\therefore R = \left\{\frac{(R_1 - R_{N1})^2}{2} + \frac{(R_2 - R_{N2})^2}{2}\right\}^{\frac{1}{2}} + \frac{(R_{N1} + R_{N2})}{2} \qquad \text{-A6.2}$$

At the outlet,

$$Z_M = \frac{(z_1 + z_2)}{2}$$

but, $Z_M = z + R_N$

and $$Z = \frac{(Z_1 + Z_2)}{2} \qquad \text{-A6.3}$$

The equation of the centre of area of the passage is

$$R_N^2 = (z_M - Z)^2 + (r_M - R)^2$$

or $$\left\{\frac{R_{N1} + R_{N2}}{2}\right\}^2 = \left\{z_M - \frac{(Z_1 + Z_2)}{2}\right\}^2 + \left\{r_M - \frac{(R_{N1} + R_{N2})}{2} - \left[\frac{(R_1 - R_{N1})^2}{2} + \frac{(R_2 - R_{N2})^2}{2}\right]^{\frac{1}{2}}\right\}^2 \qquad \text{-A6.4}$$

The blade surface equations A1.1 and A1.2 were used to calculate the circumferential position of the centre of area of the passage.

APPENDIX 7

STABLE LOCATION LINE

The stable location line is the locus of lowest p* locations, through a duct, where the generation of streamwise vorticity is zero and a fluid particle with this lowest value of p* will, when given a small disturbance from this stable location, oscillate about the location.

Algebraically

$$\frac{\partial^2 \phi}{\partial \theta^2} = 0 \qquad \text{-A7.1}$$

or from Equation 6.20

$$St\ \{\text{Cos}\ \phi_{ST} - \frac{1}{Ro}(\omega_x \text{Sin}\ \phi_{ST} \text{Cos}\ \theta + \omega_y \text{Cos}\ \phi_{ST} + \omega_z \text{Sin}\ \phi_{ST}$$
$$\text{Sin}\ \theta)\} - \frac{1}{Ro}(\omega_x \text{Cos}\ \theta + \omega_z \text{Sin}\ \theta) = 0 \qquad \text{-A7.2}$$

At the impeller exit,

$$\underline{s} = \begin{pmatrix} 1 \\ 0 \\ 0 \end{pmatrix};\ \underline{z}' = \begin{pmatrix} 0 \\ 0 \\ 1 \end{pmatrix};\ \theta = \frac{\pi}{2}$$

and so $$St\ (Ro\ \text{Cos}\ \phi_{ST} - \text{Sin}\ \phi_{ST}) - 1 = 0 \qquad \text{-A7.3}$$

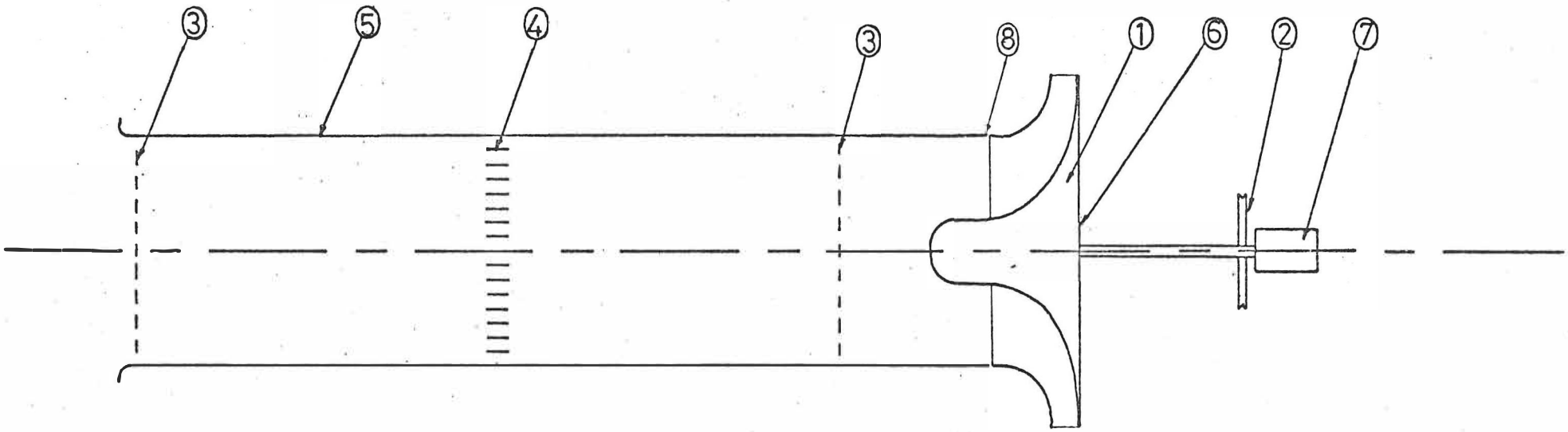

1. IMPELLER 2. PULLEY DRIVEN BY MOTOR 3. SCREENS 4. HONEYCOMB 5. INLET DUCT
6. PRESSURE TRANSDUCERS AND AMPLIFIERS 7. SLIP RINGS 8. SEAL

0 1 2

metres

Figure 2.1 Schematic of test rig.

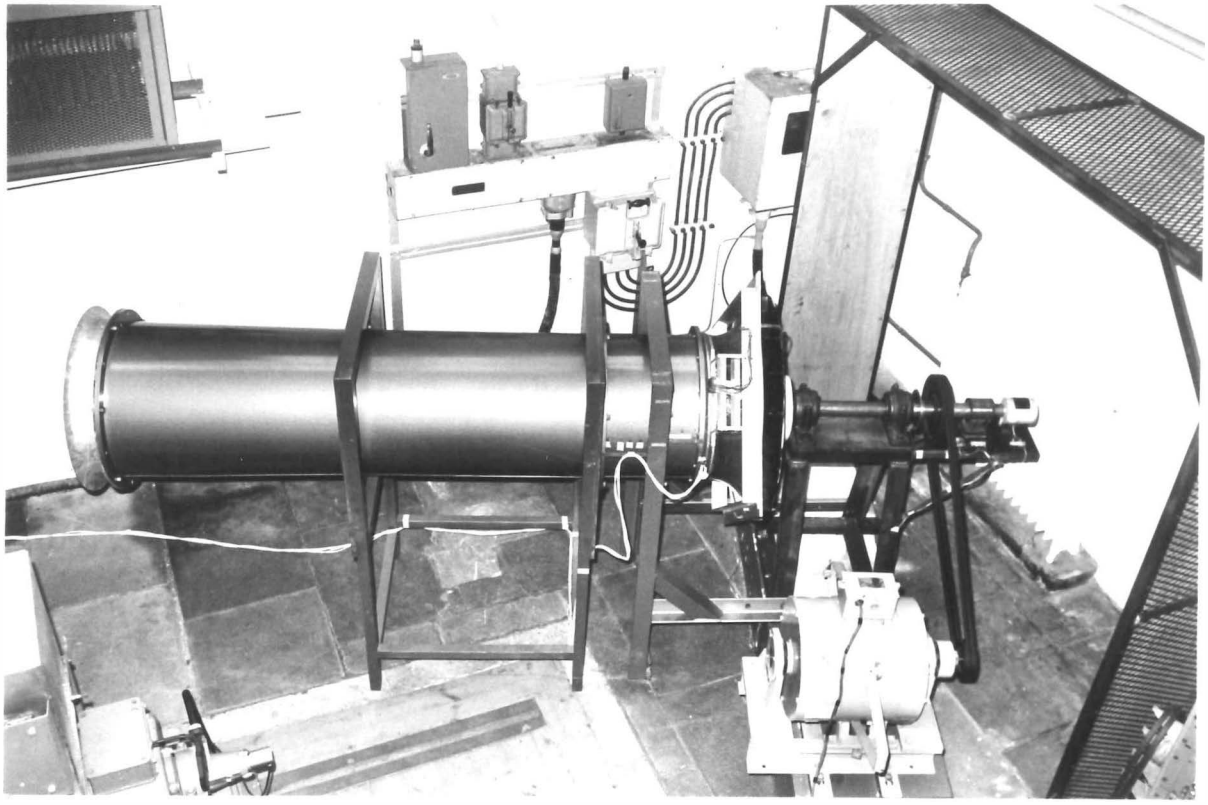

Figure 2.2 Centrifugal Compressor Impeller Rig.

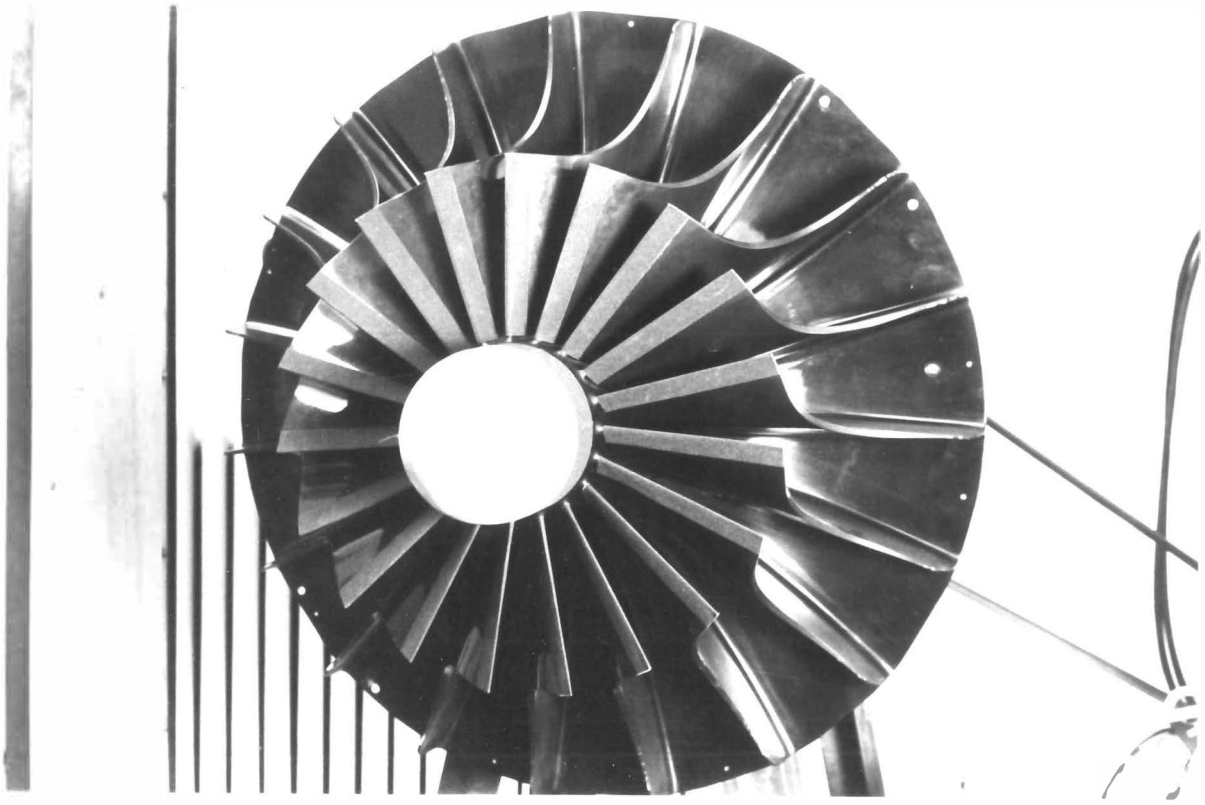

Figure 2.3 Ghost Impeller.

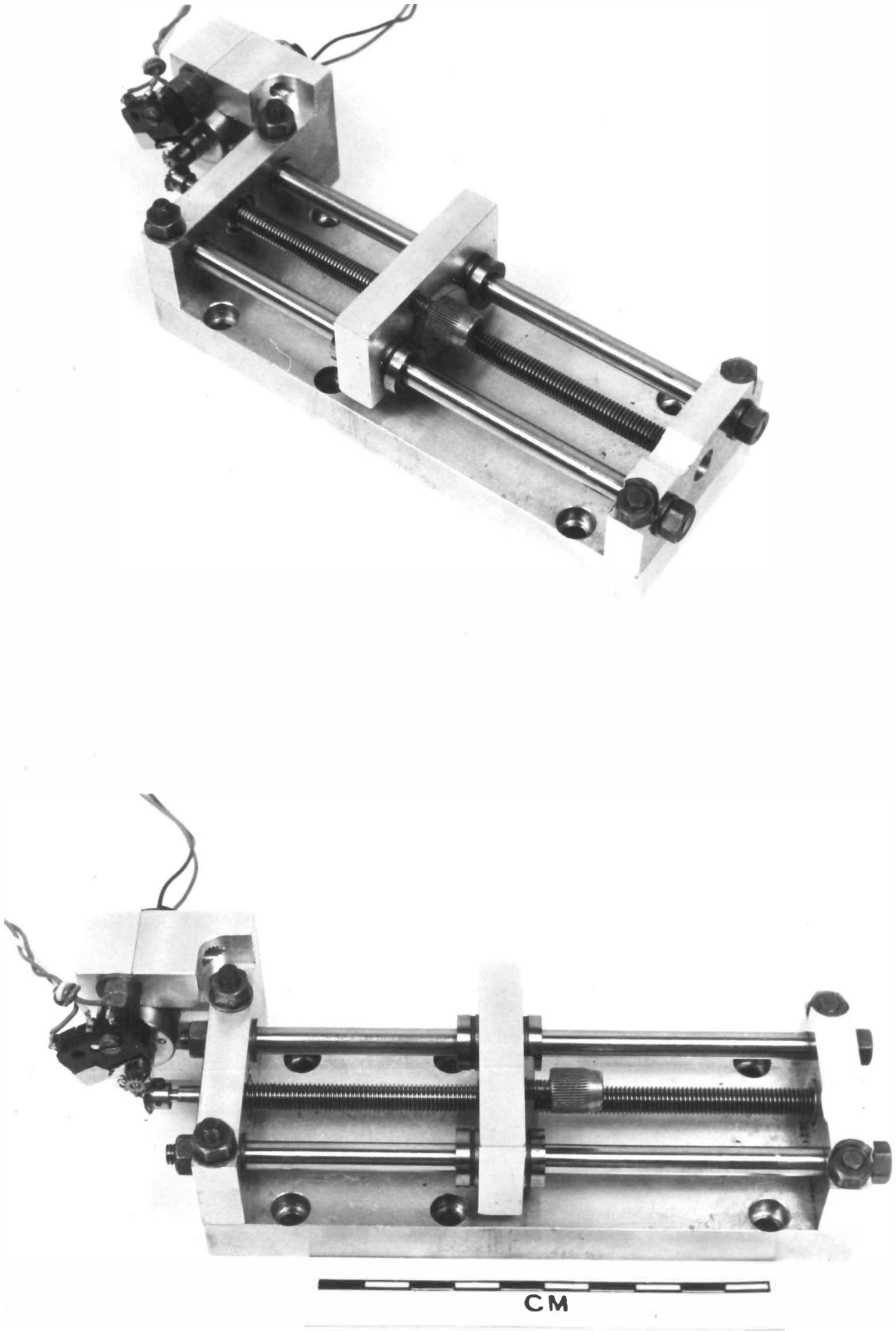

Figure 2.4 Right Angle Drive Traversing Gear.

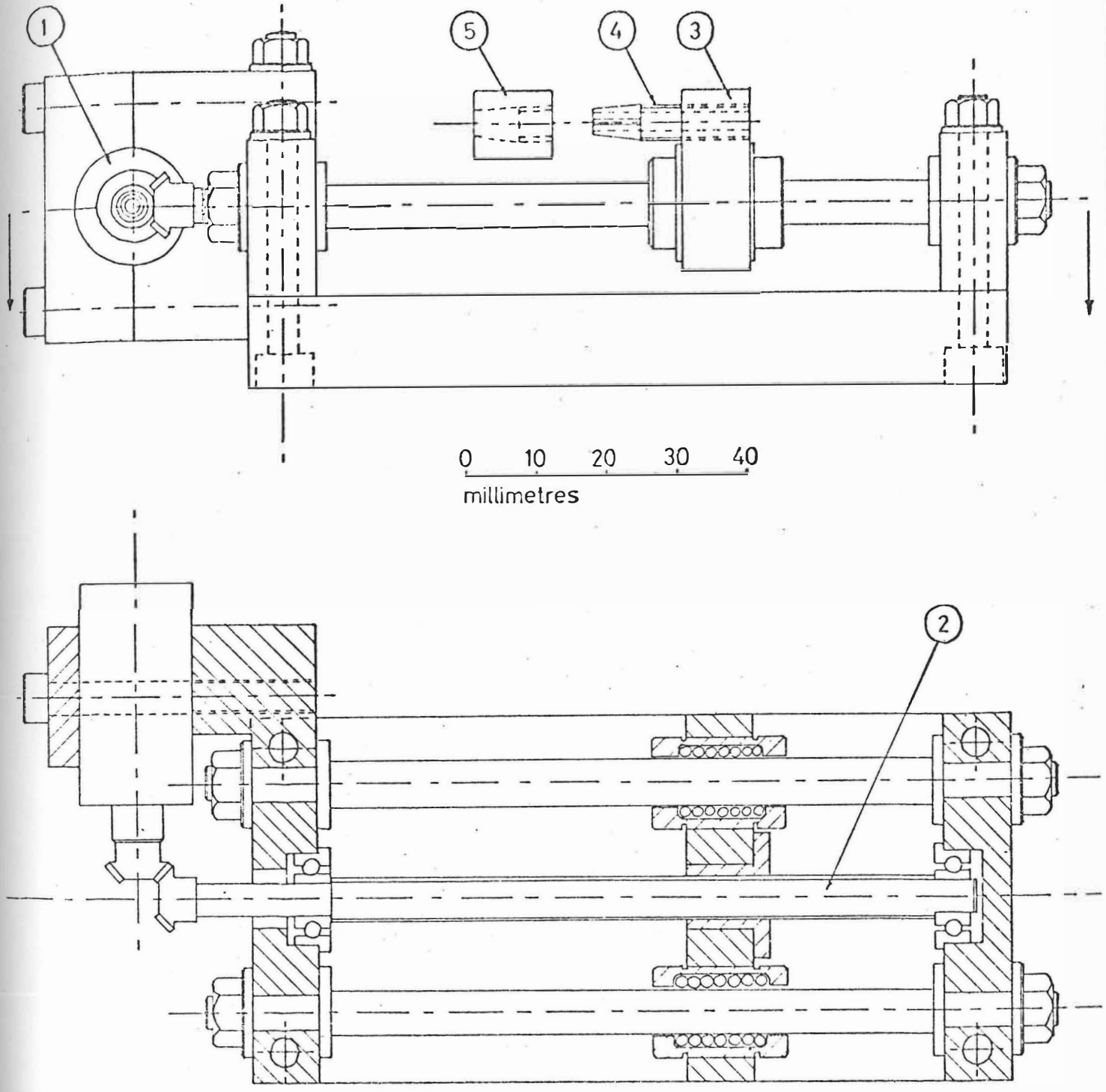

Figure 2.5 Right angle drive traversing gear.

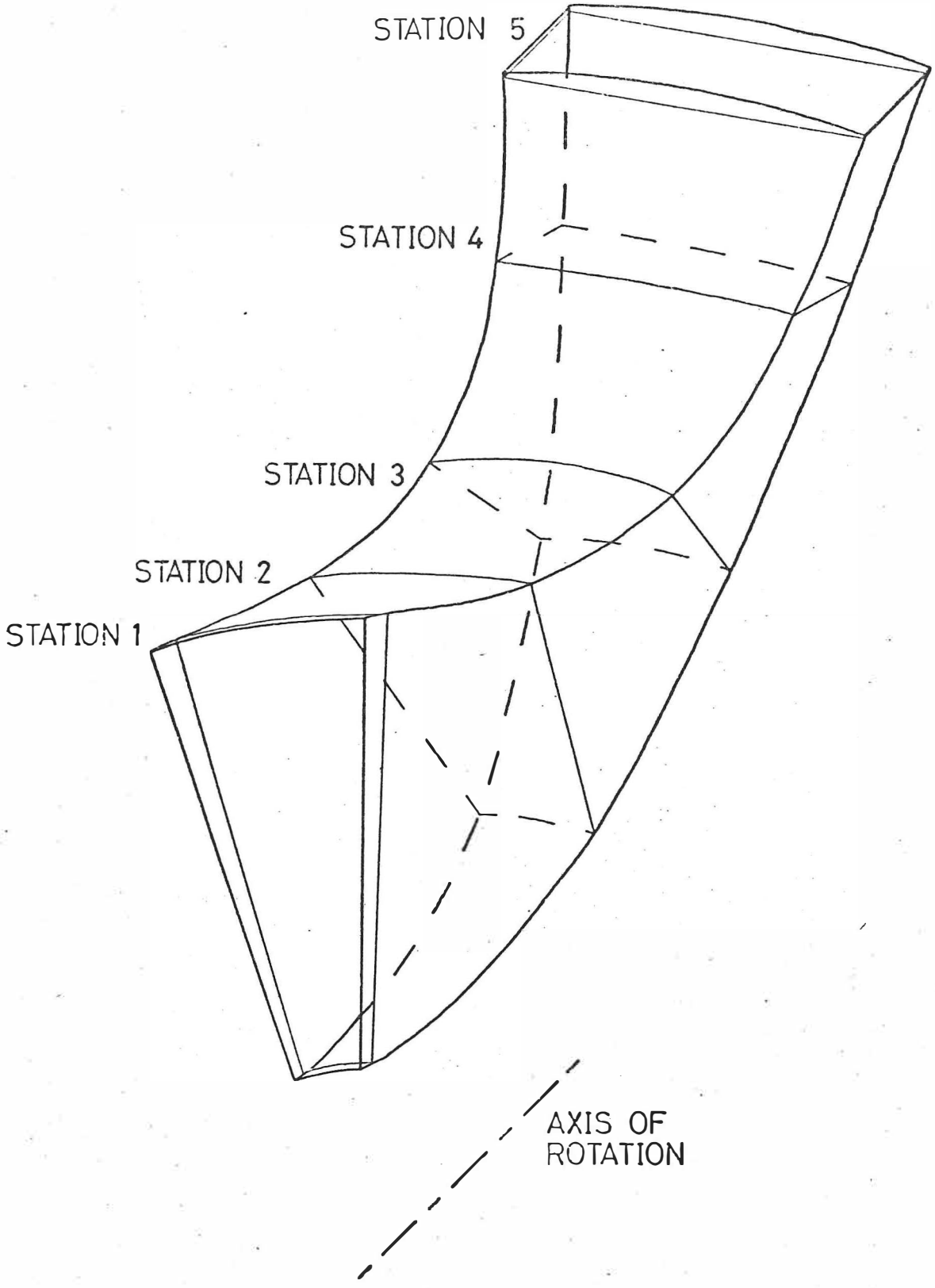

Figure 2.6 Ghost impeller passage.

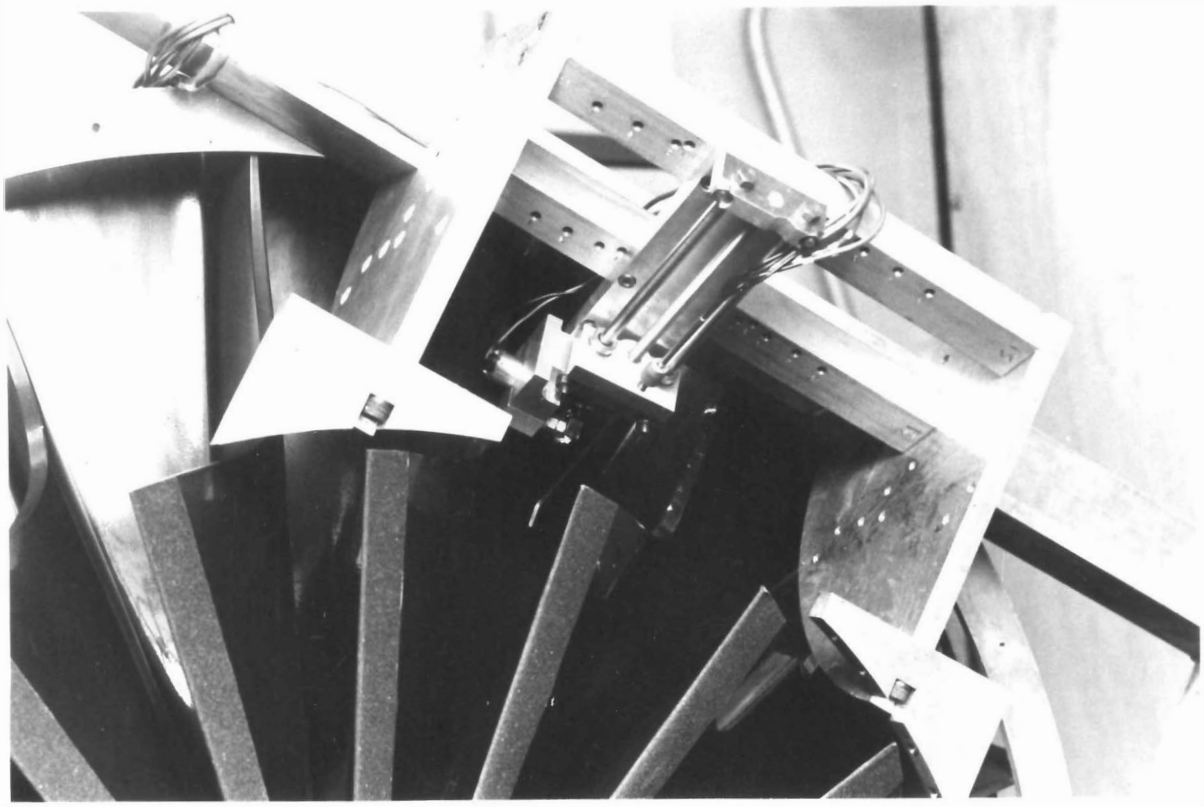

Figure 2.7 Traversing Gear Mounting.

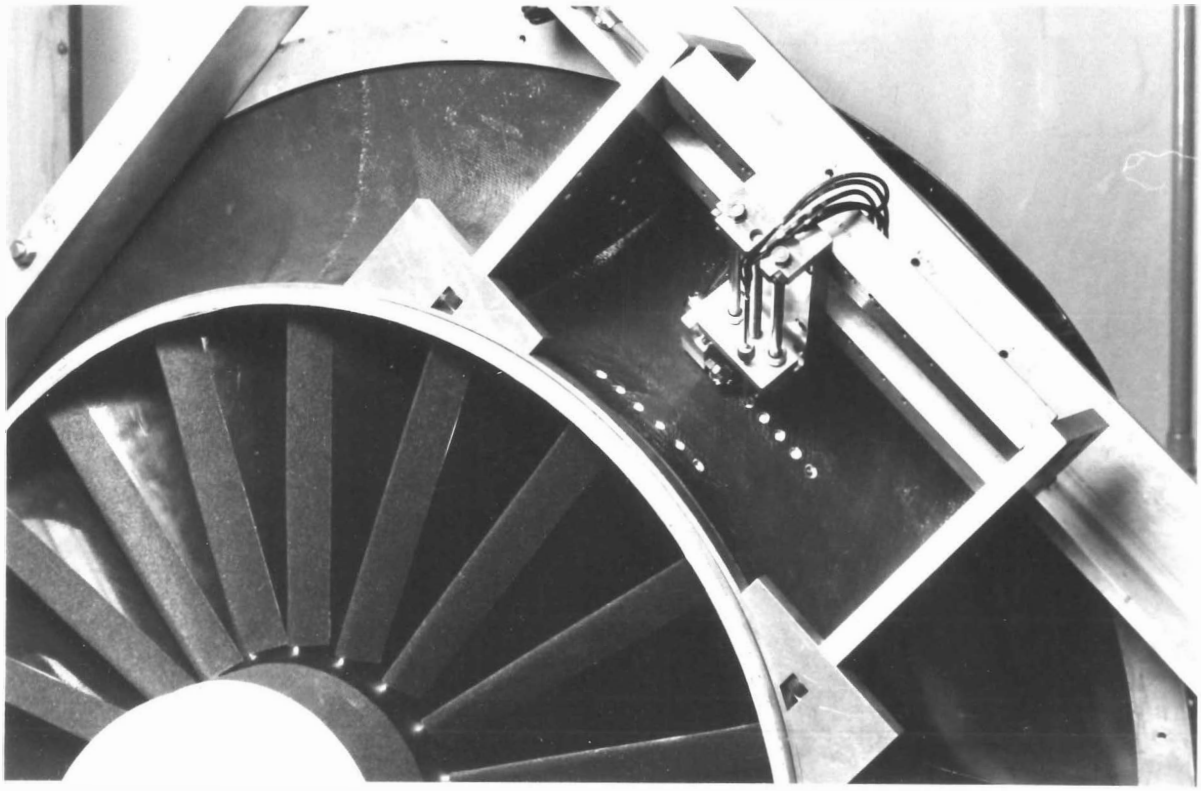

Figure 2.8 Measuring Probe passing through the Impeller Shroud.

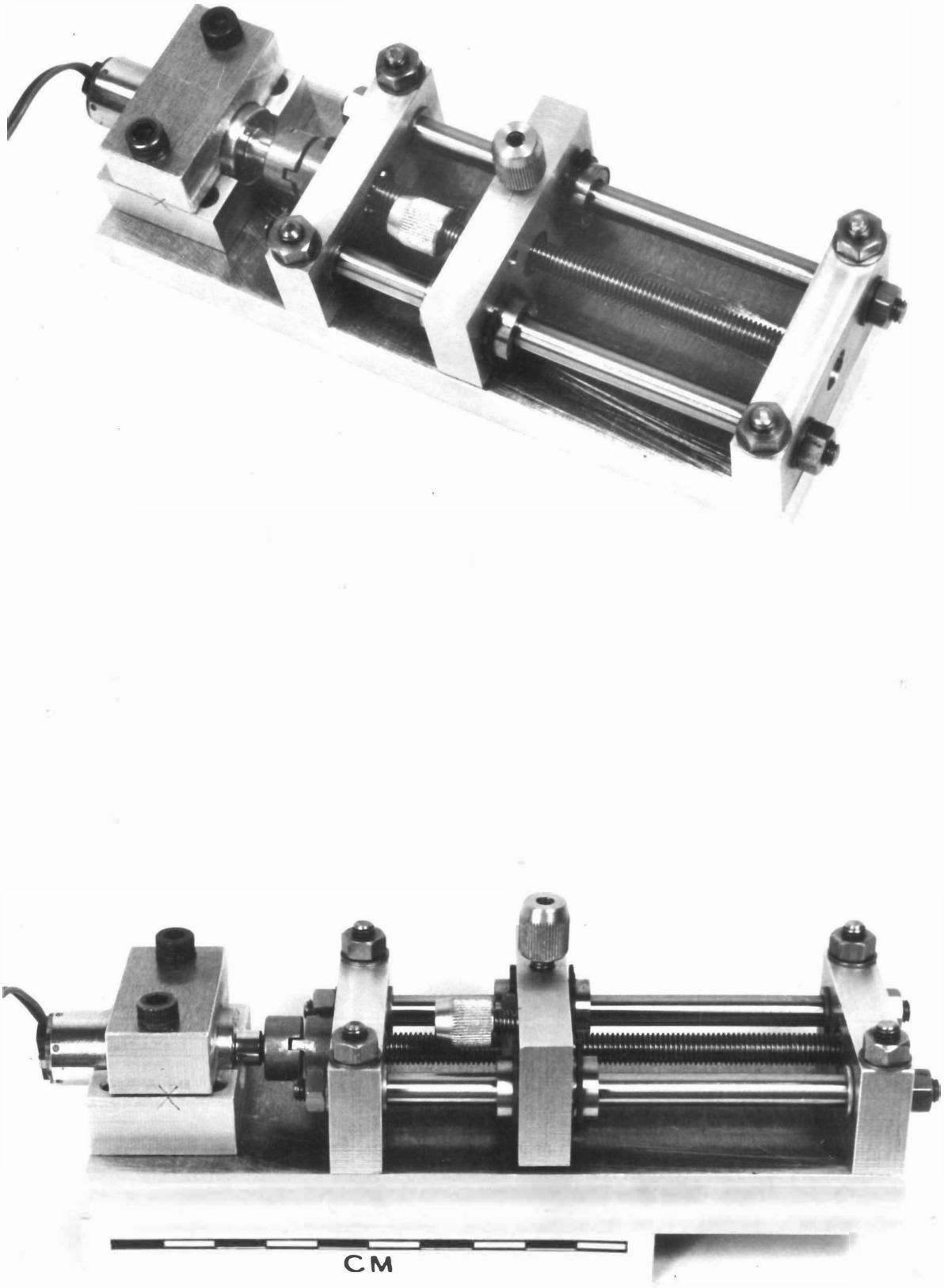

Figure 2.9 Straight Drive Traversing Gear.

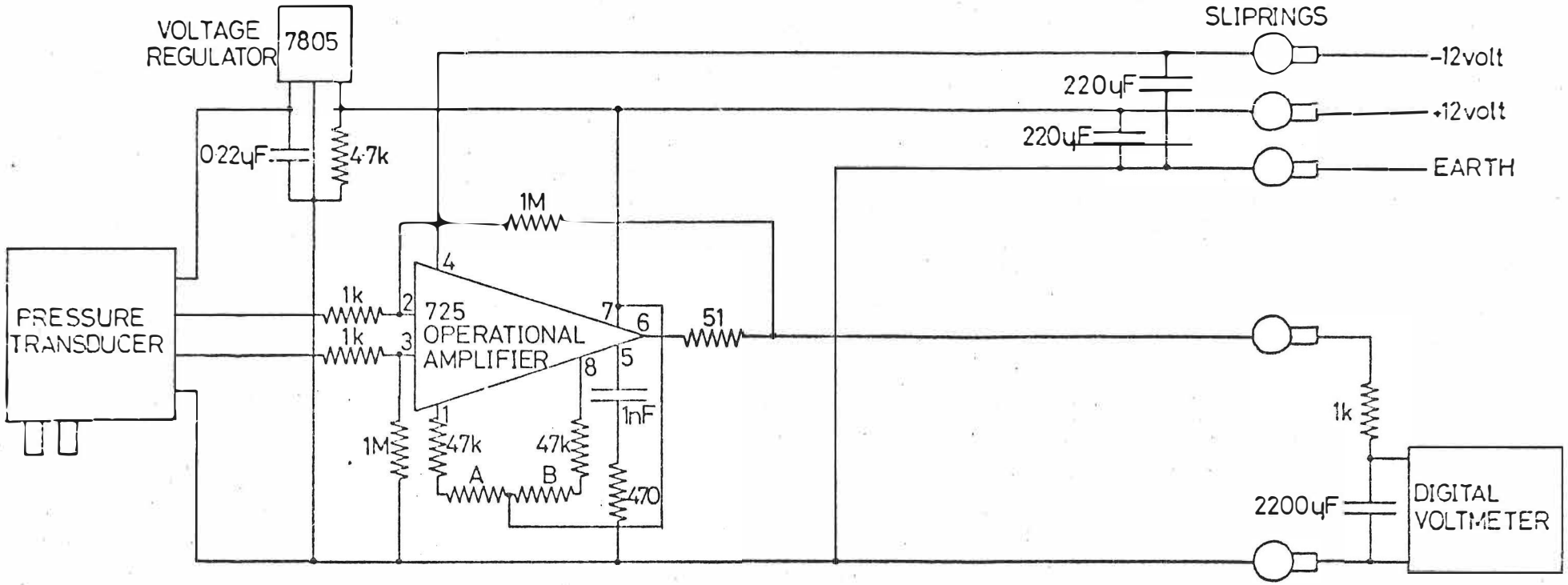

Figure 2.10 Pressure transducer amplifier.

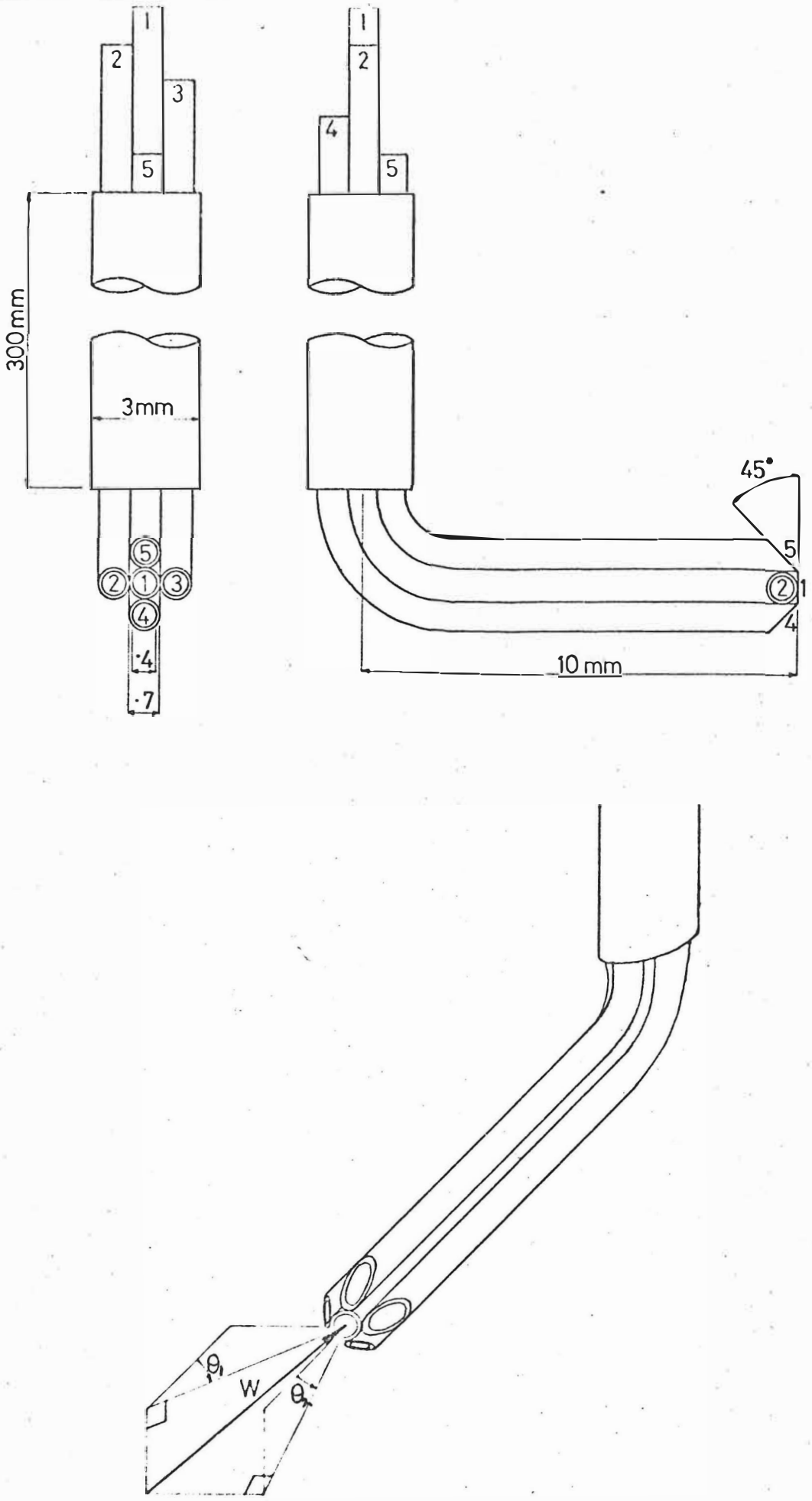

Figure 2.11 5-Hole Velocity Probe.

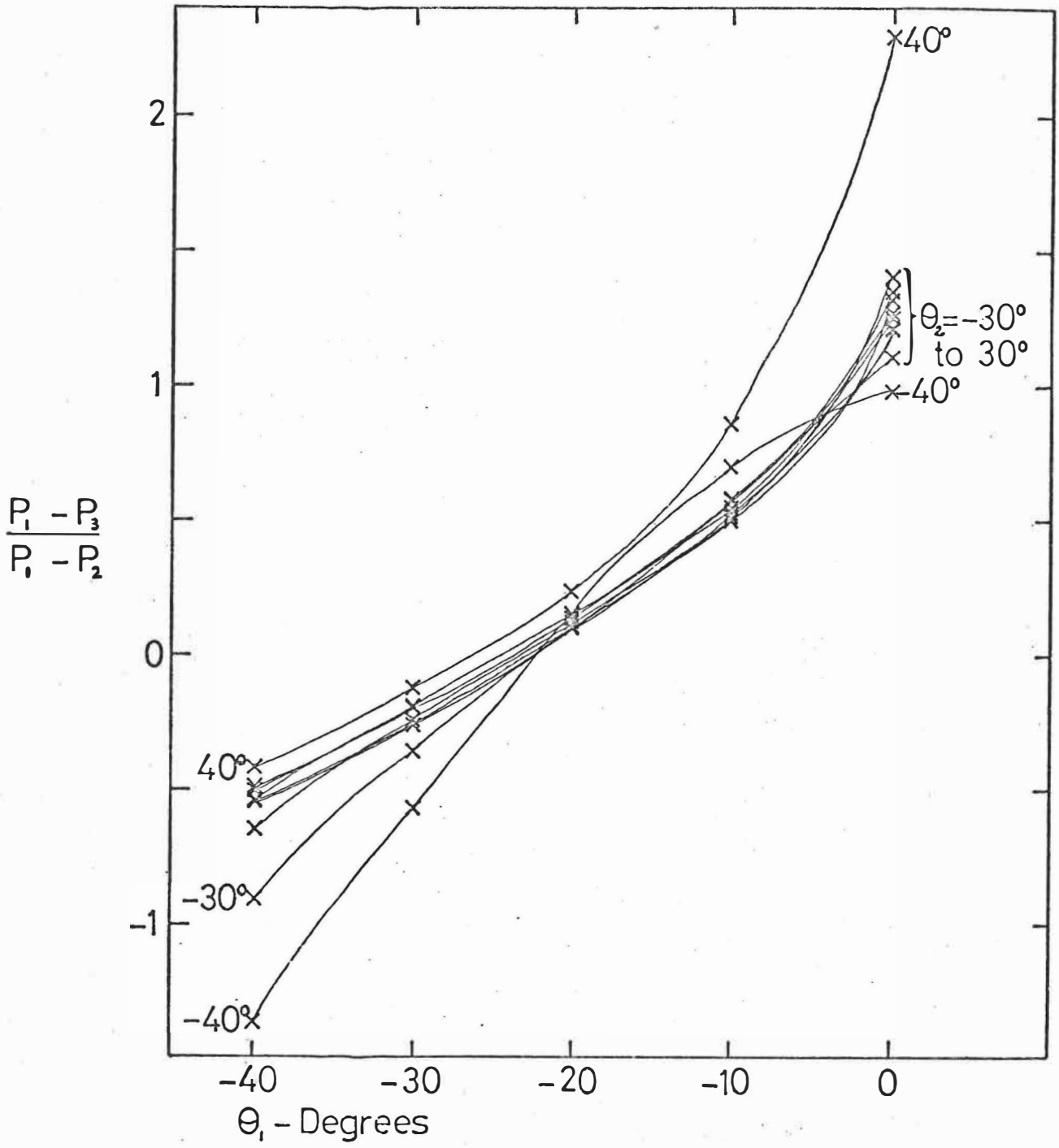

Figure 2.12 5-hole probe calibration curves. Set A.

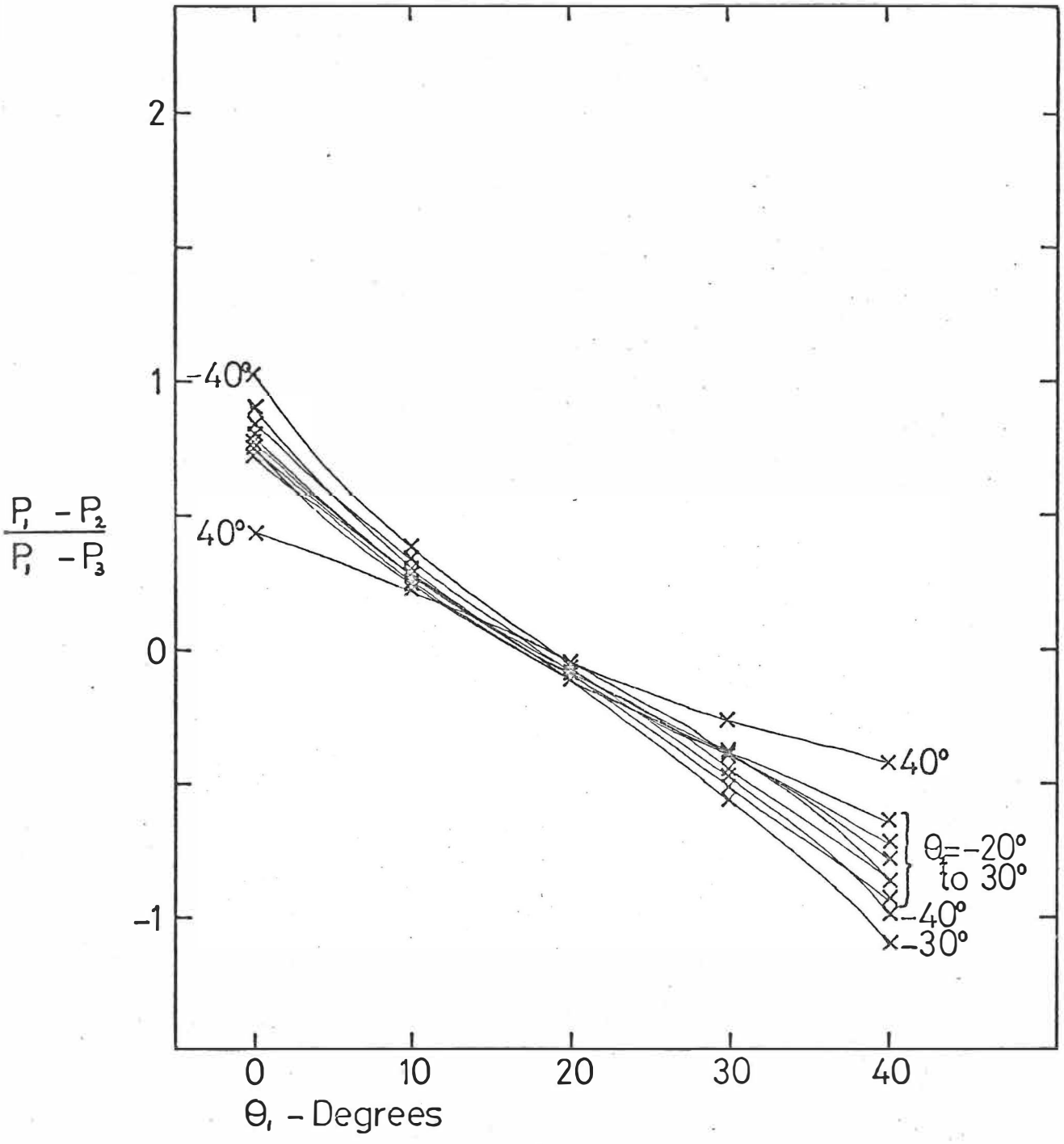

Figure 2.13 5-hole probe calibration curves. Set A.

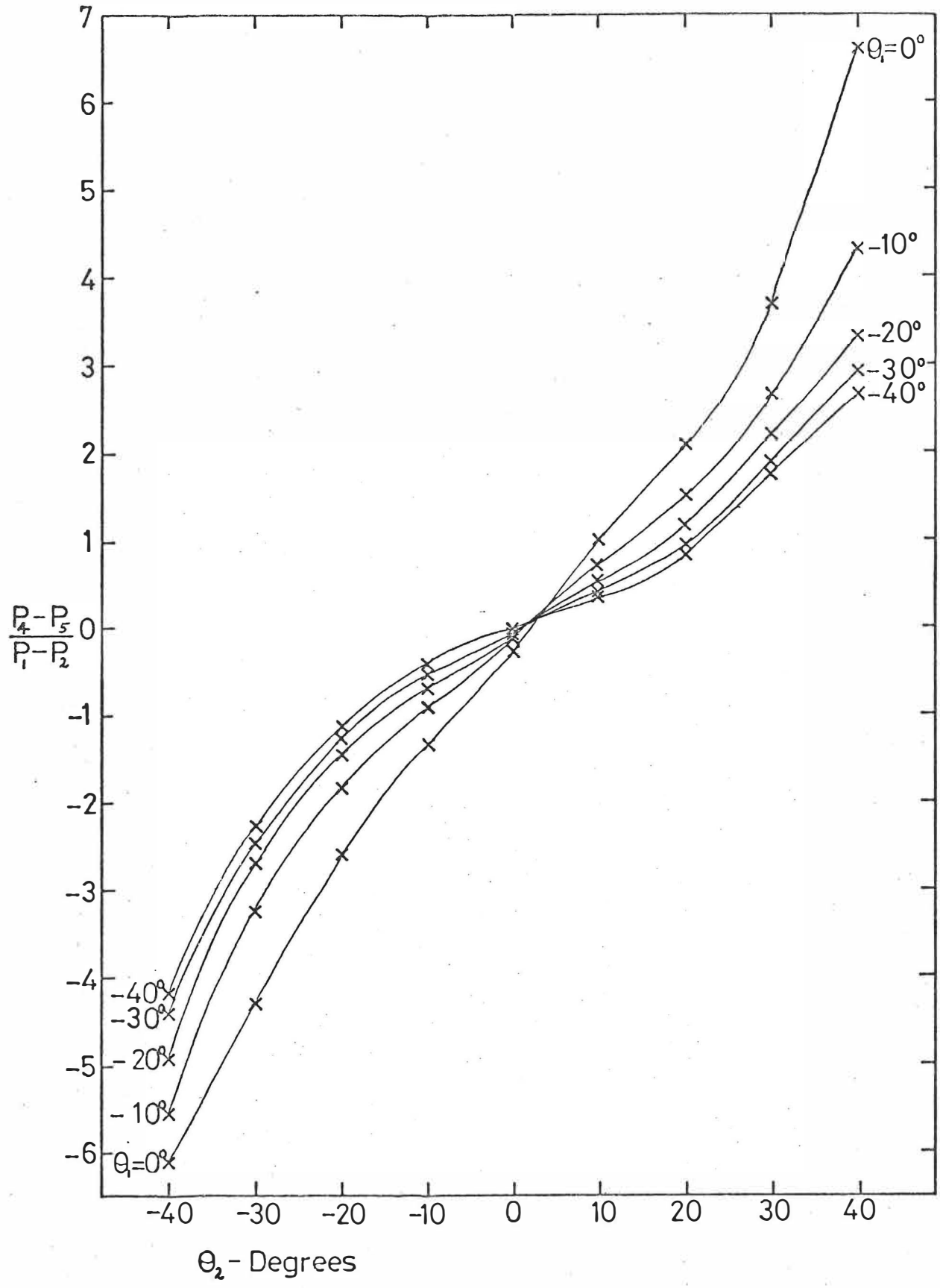

Figure 2.14 5-hole probe calibration curves. Set B.

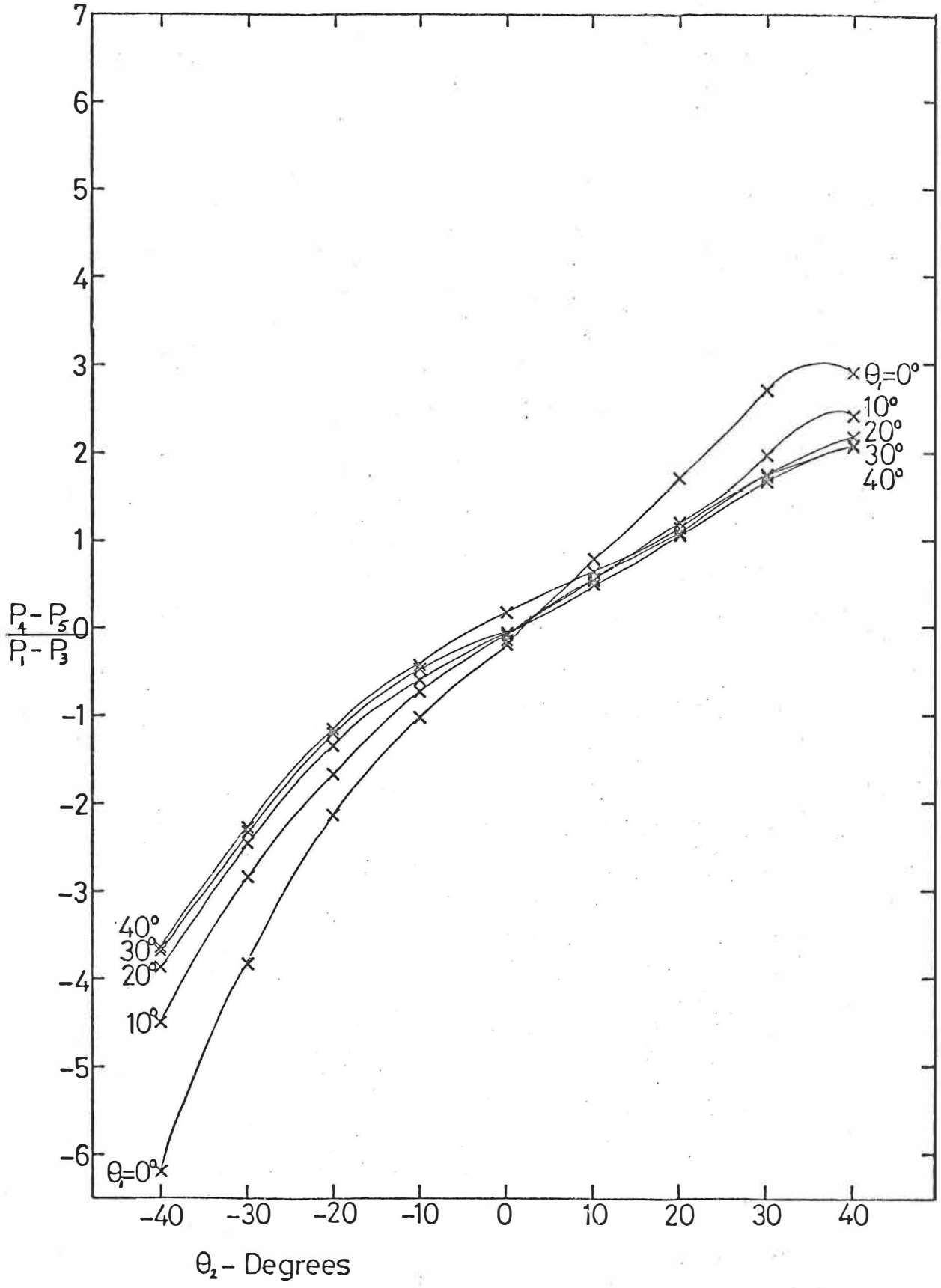

Figure 2.15 5-hole probe calibration curves. Set B.

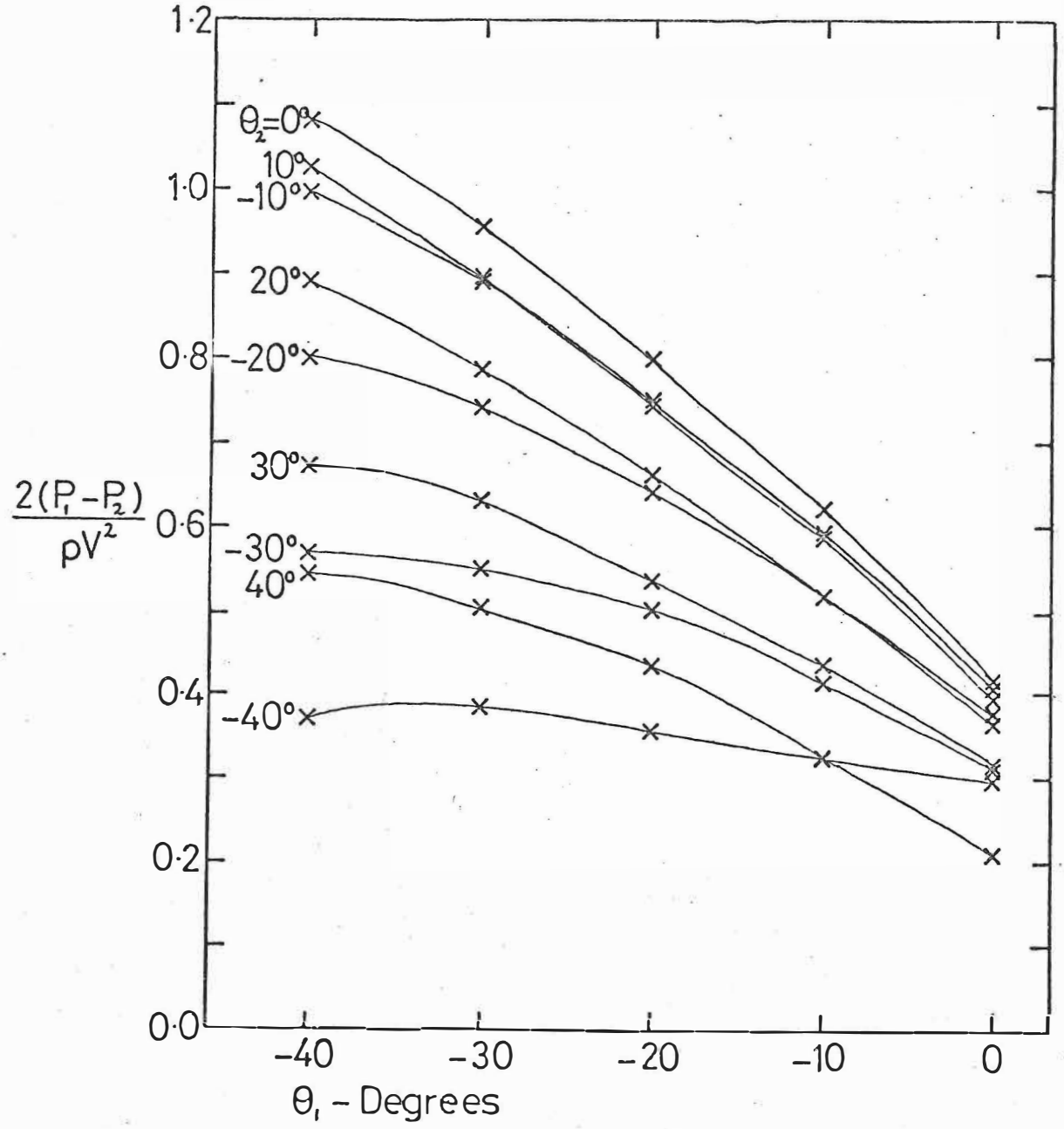

Figure 2.16 5-hole probe calibration curves. Set C.

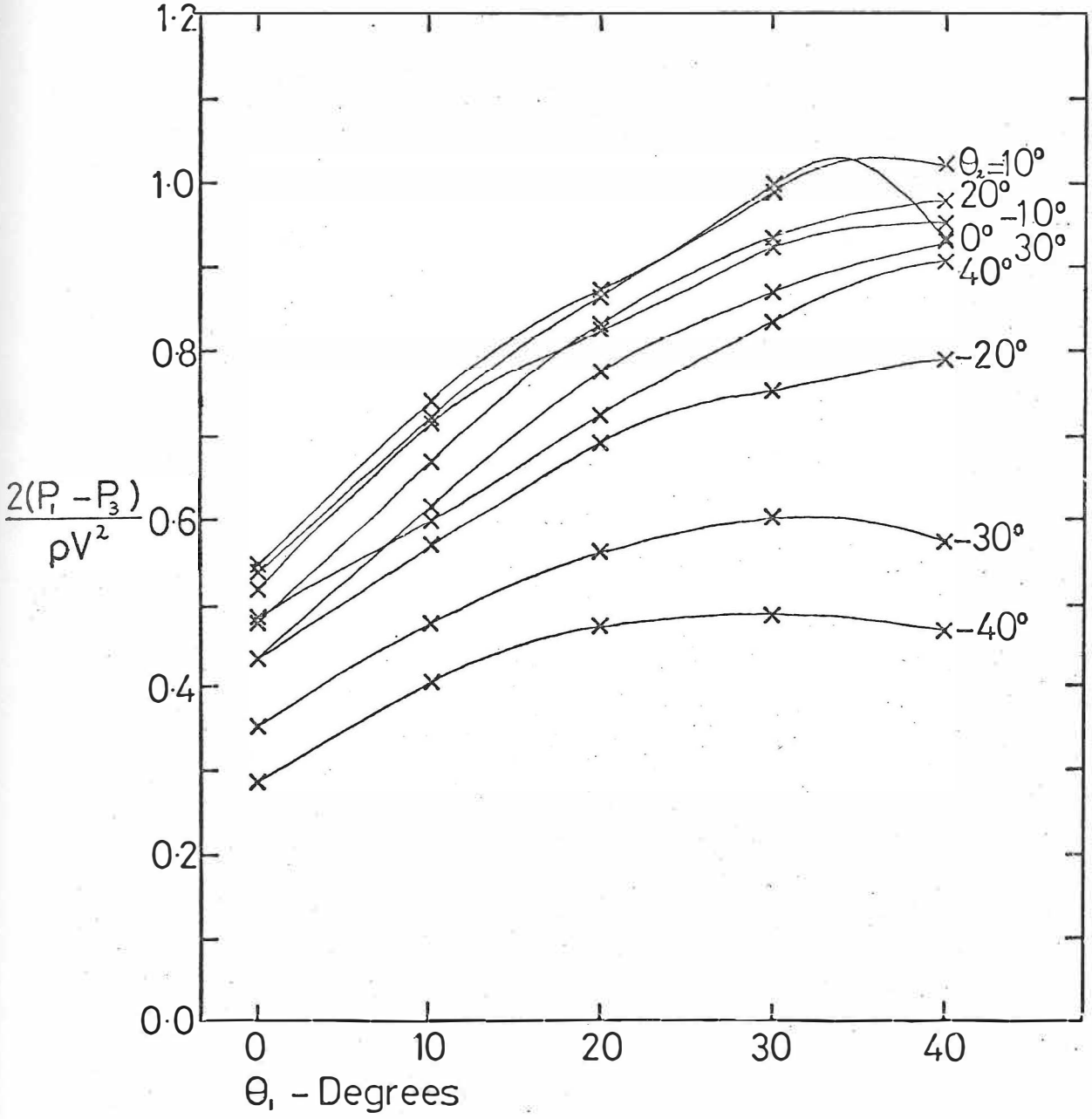

Figure 2.17 5-hole probe calibration curves. Set C.

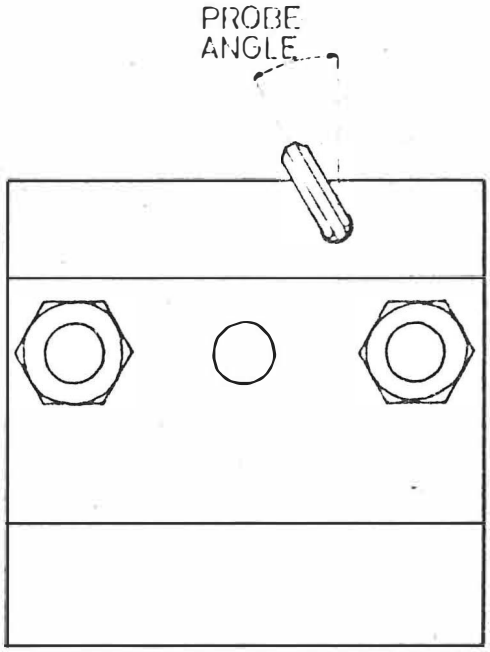

Figure 2.18 Definition of Probe Angle.

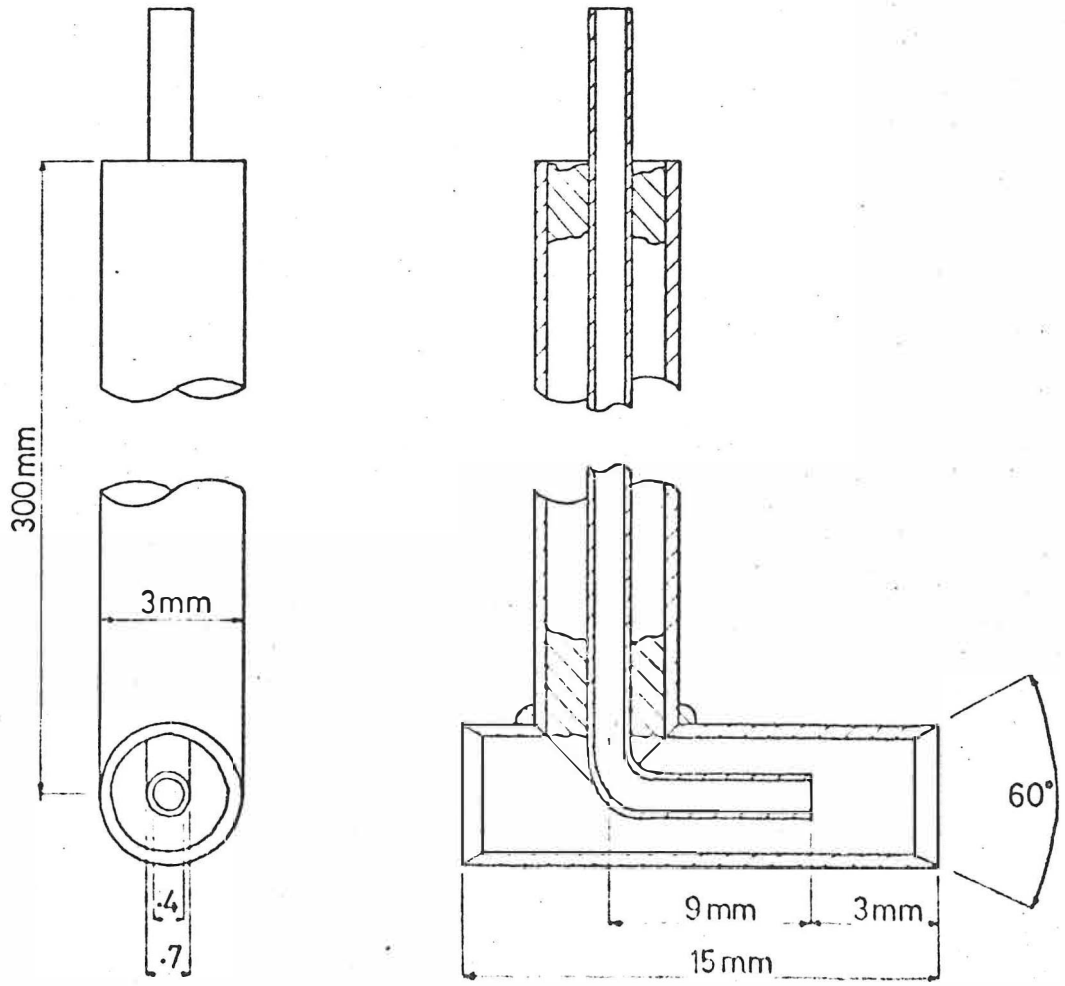

Figure 2.19 Kiel Probe.

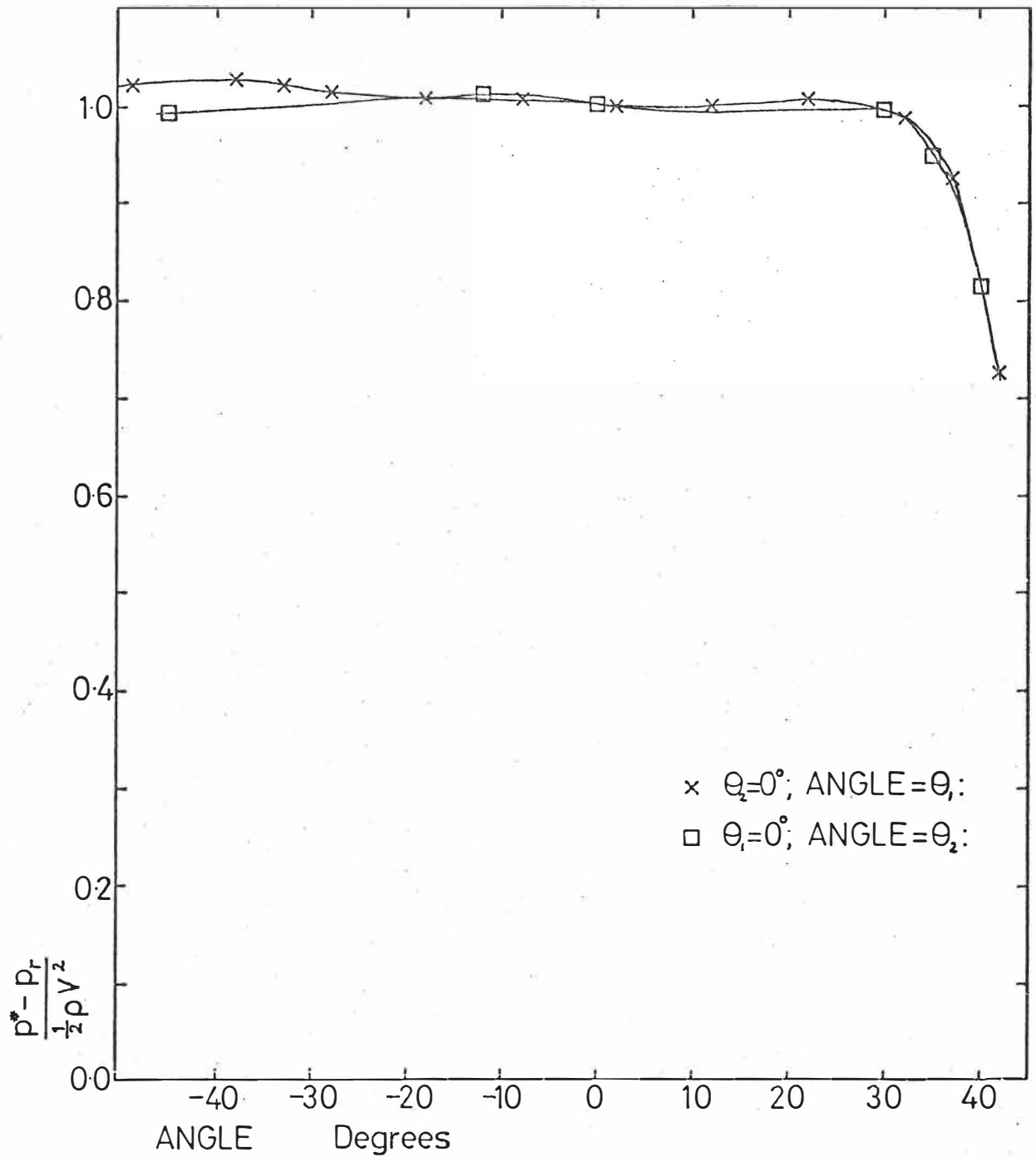

Figure 2.20 Kiel probe calibration curves.

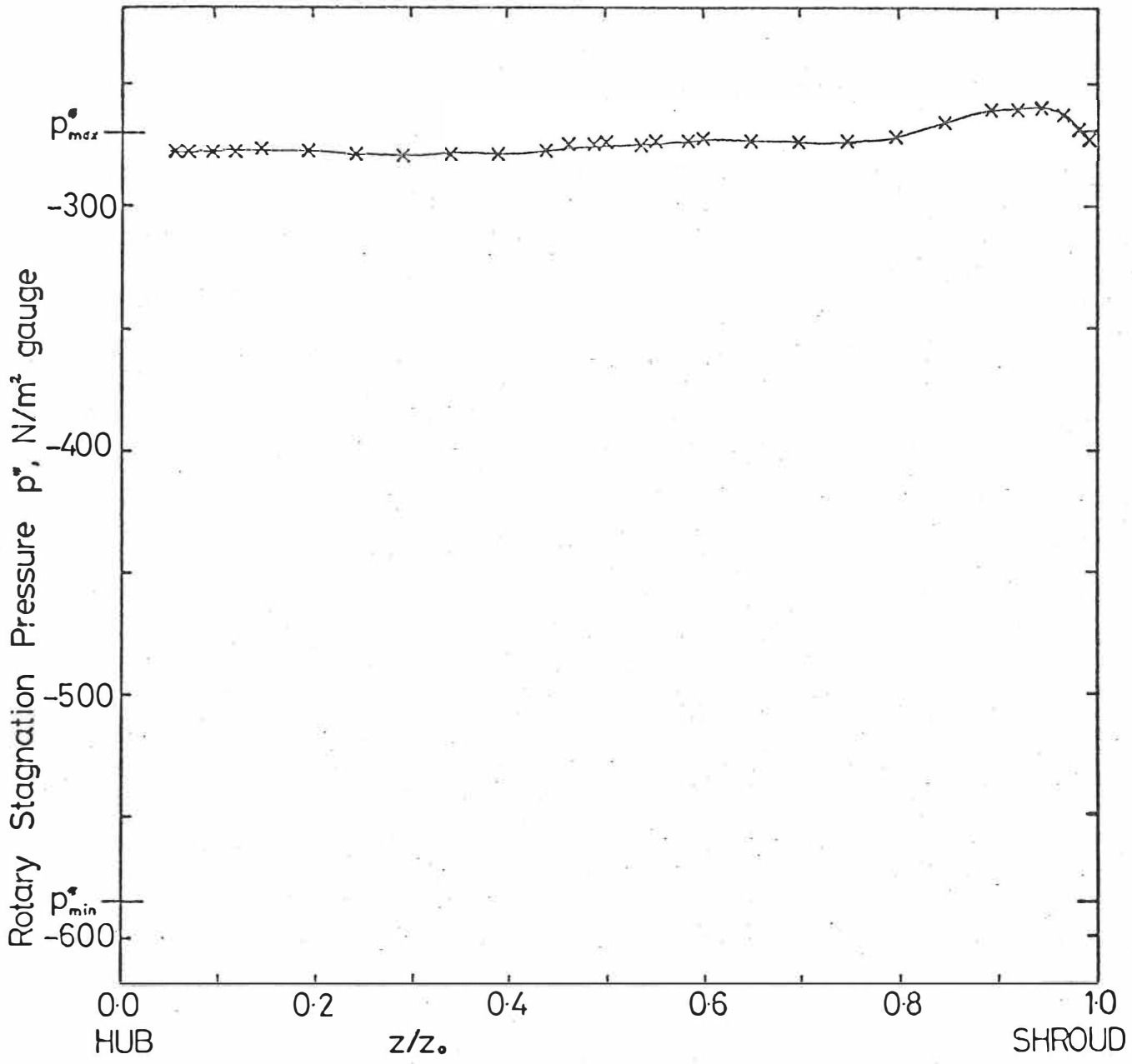

Figure 3.1 'Design' flow. Inlet duct. Rotary stagnation pressure p*.
(Averaged in the circumferential direction)

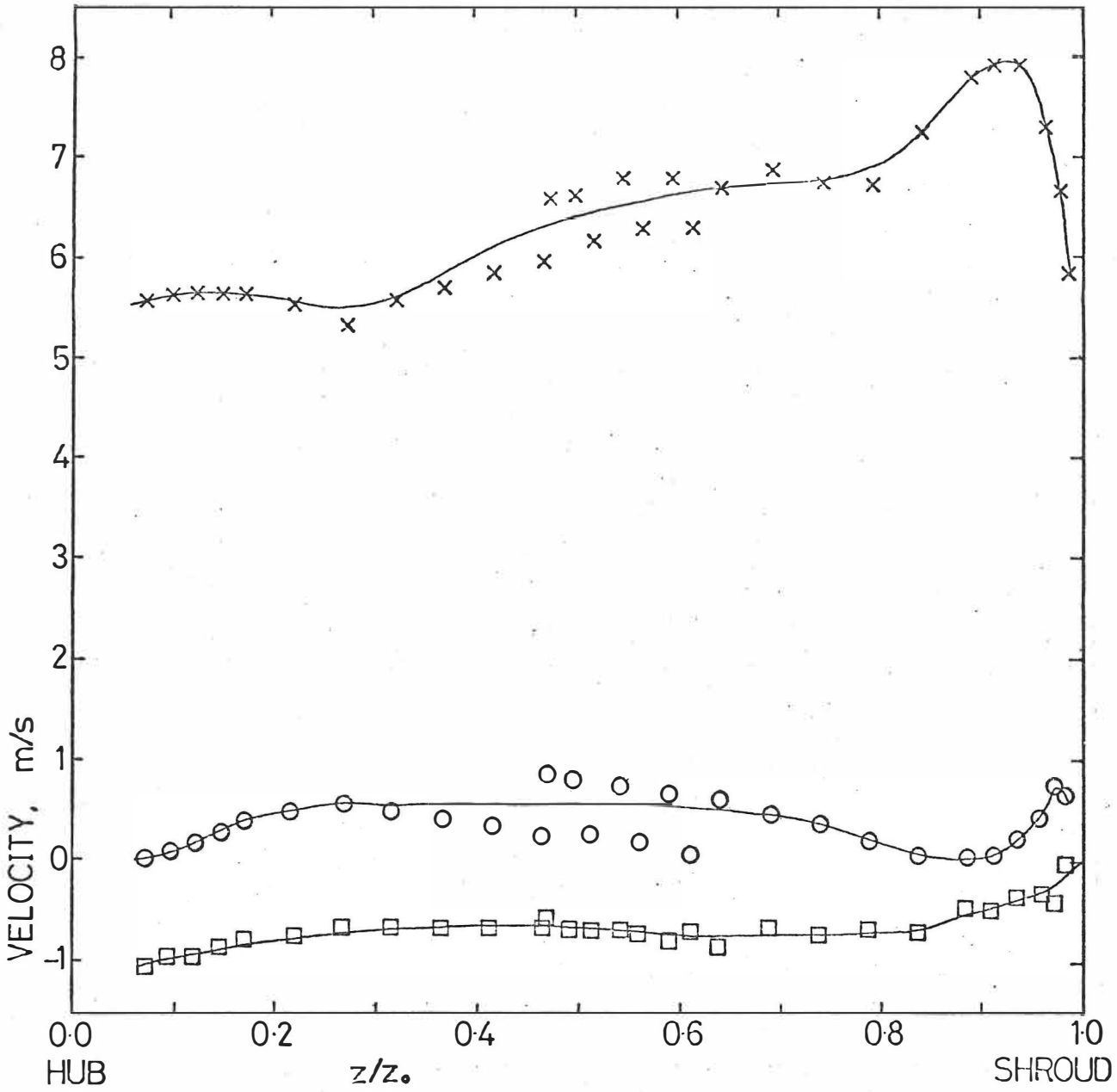

× Axial component, U

□ Circumferential component, V

○ Radial component, W

Figure 3.2 'Design' flow. Inlet duct. Absolute Velocities.
(Averaged in the circumferential direction)

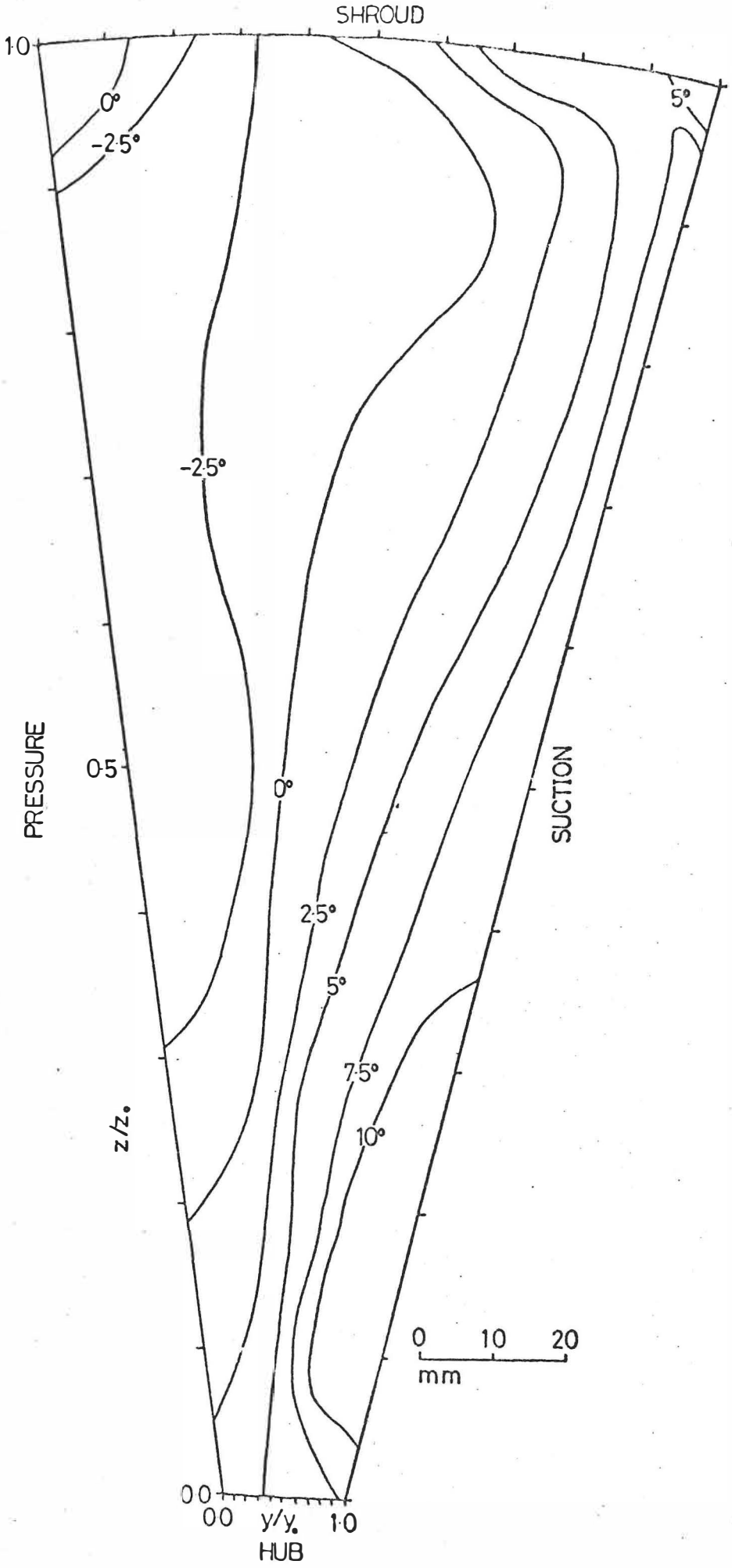

Figure 3.3 'Design' flow. Station 1. Incidence angles at impeller inlet.

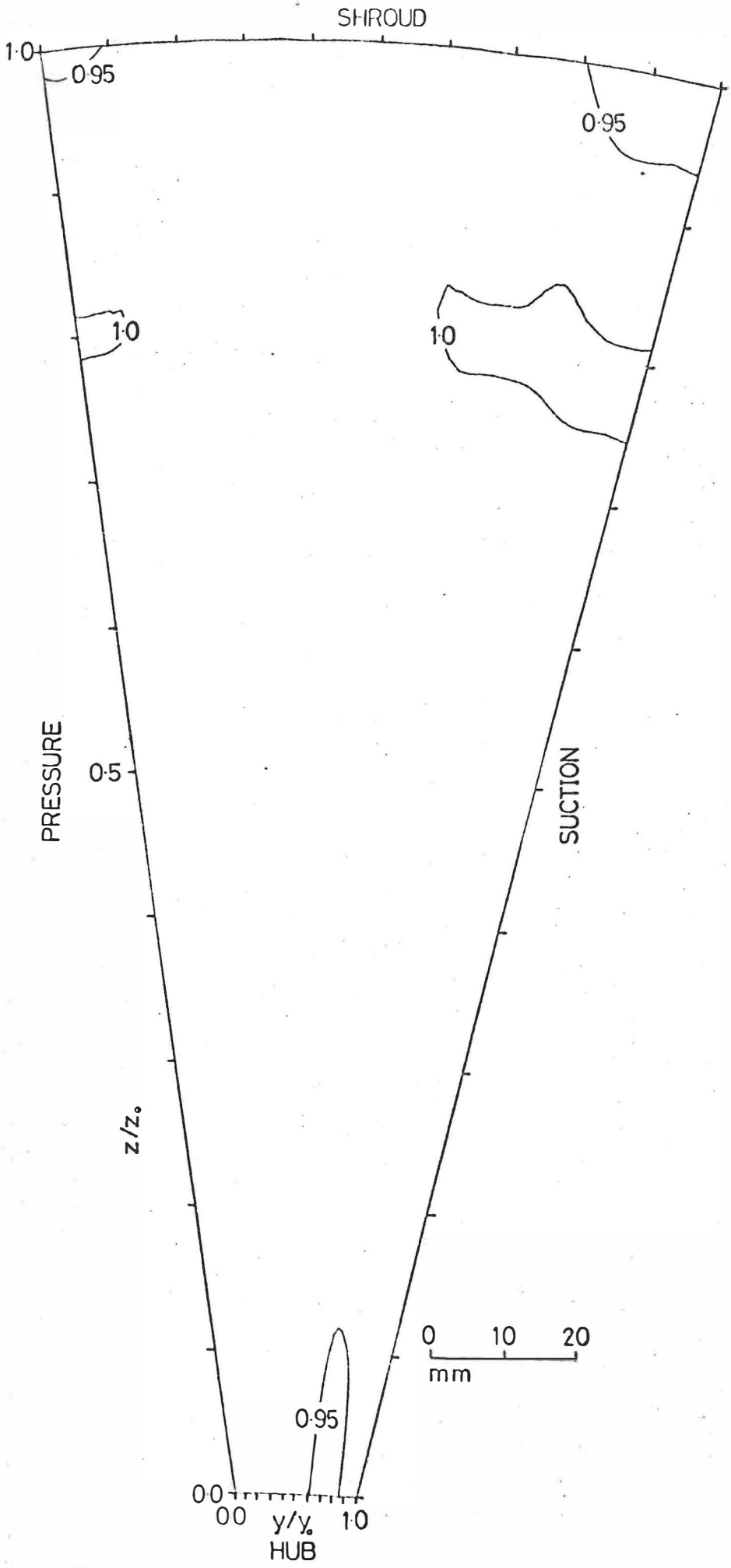

Figure 3.4 'Design' flow. Station 1. Dimensionless rotary stagnation pressure P*.

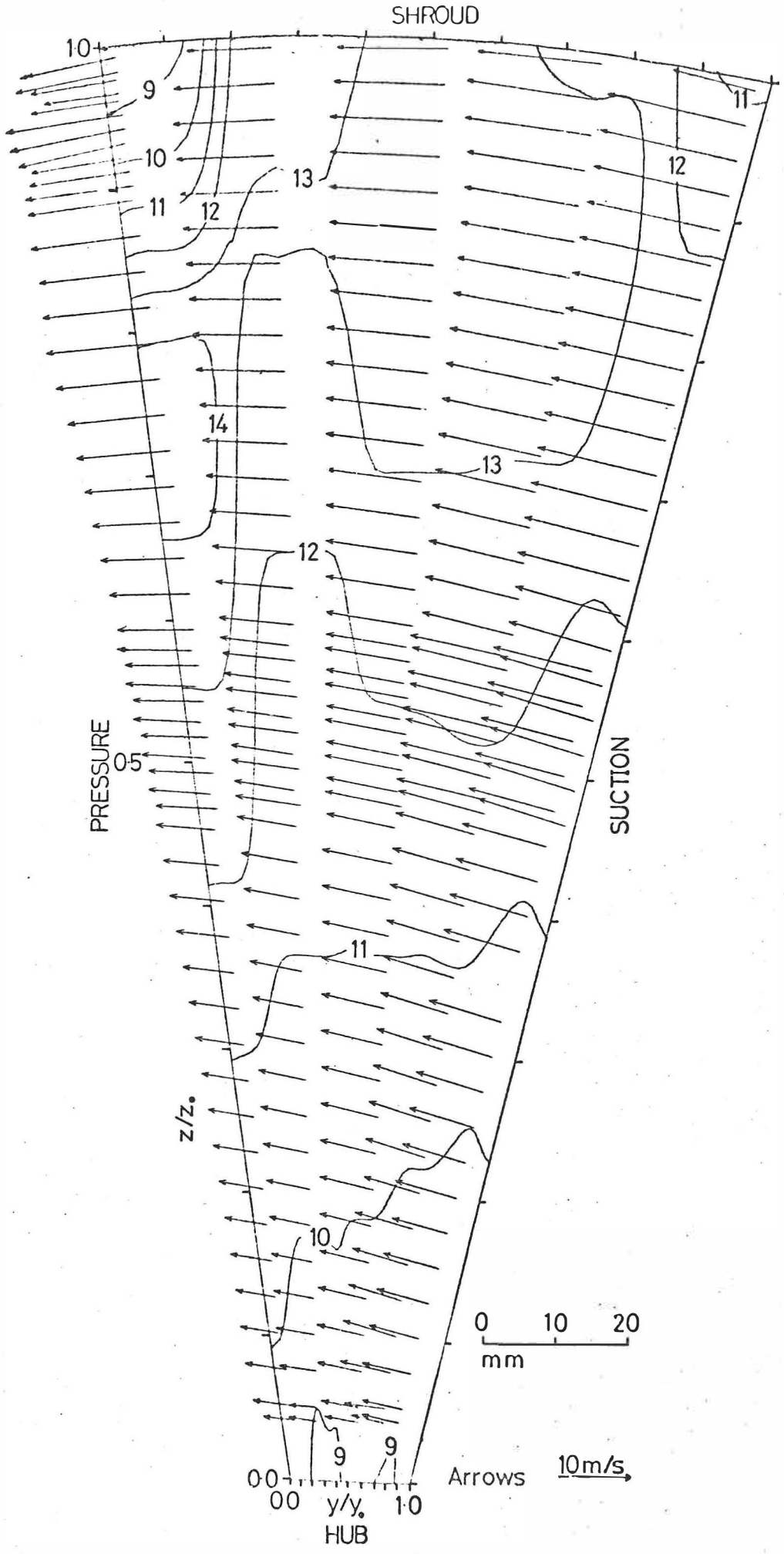

Figure 3.5 'Design' flow. Station 1. Relative velocities - contours in m/s.

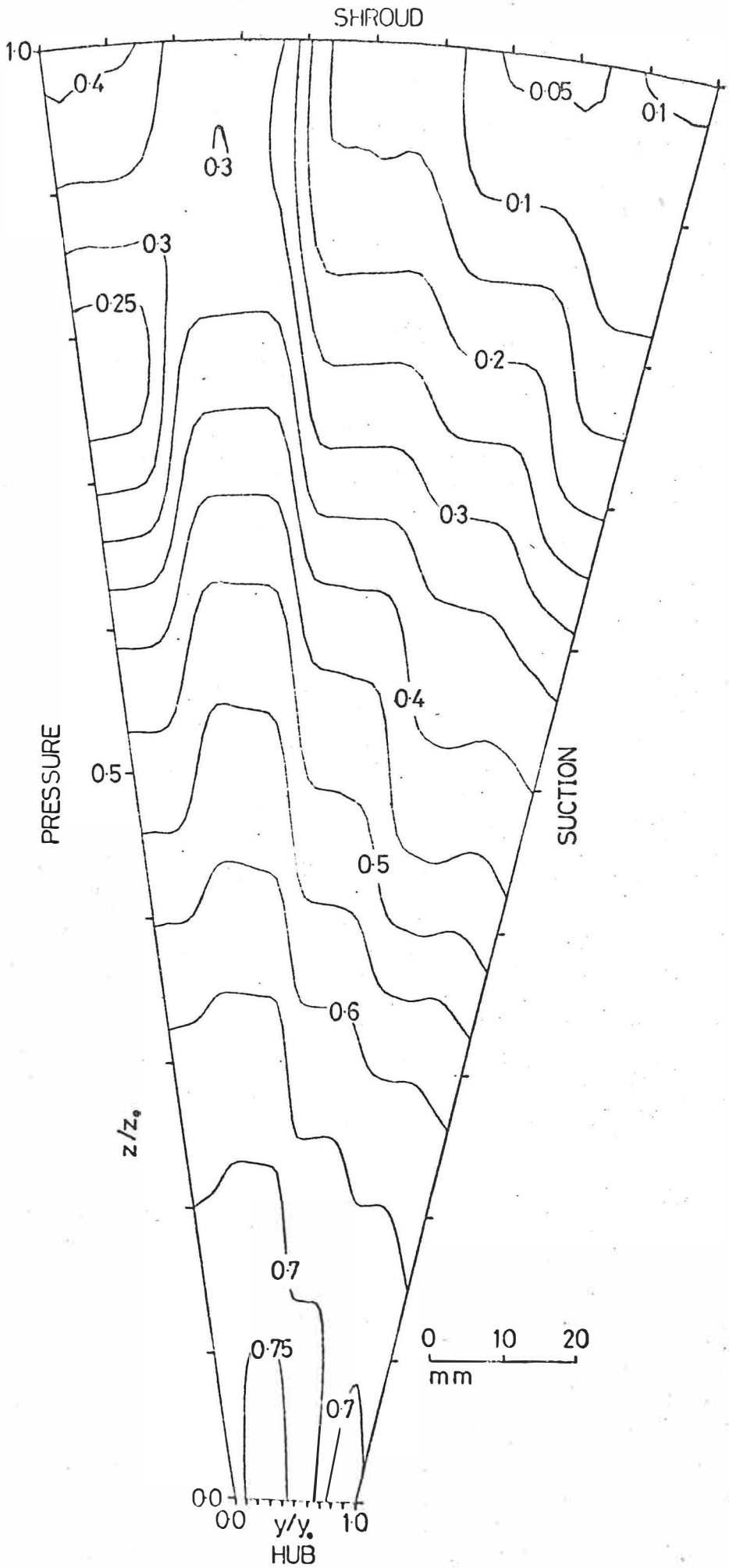

Figure 3.6 'Design' flow. Station 1. Dimensionless reduced static pressure P_r.

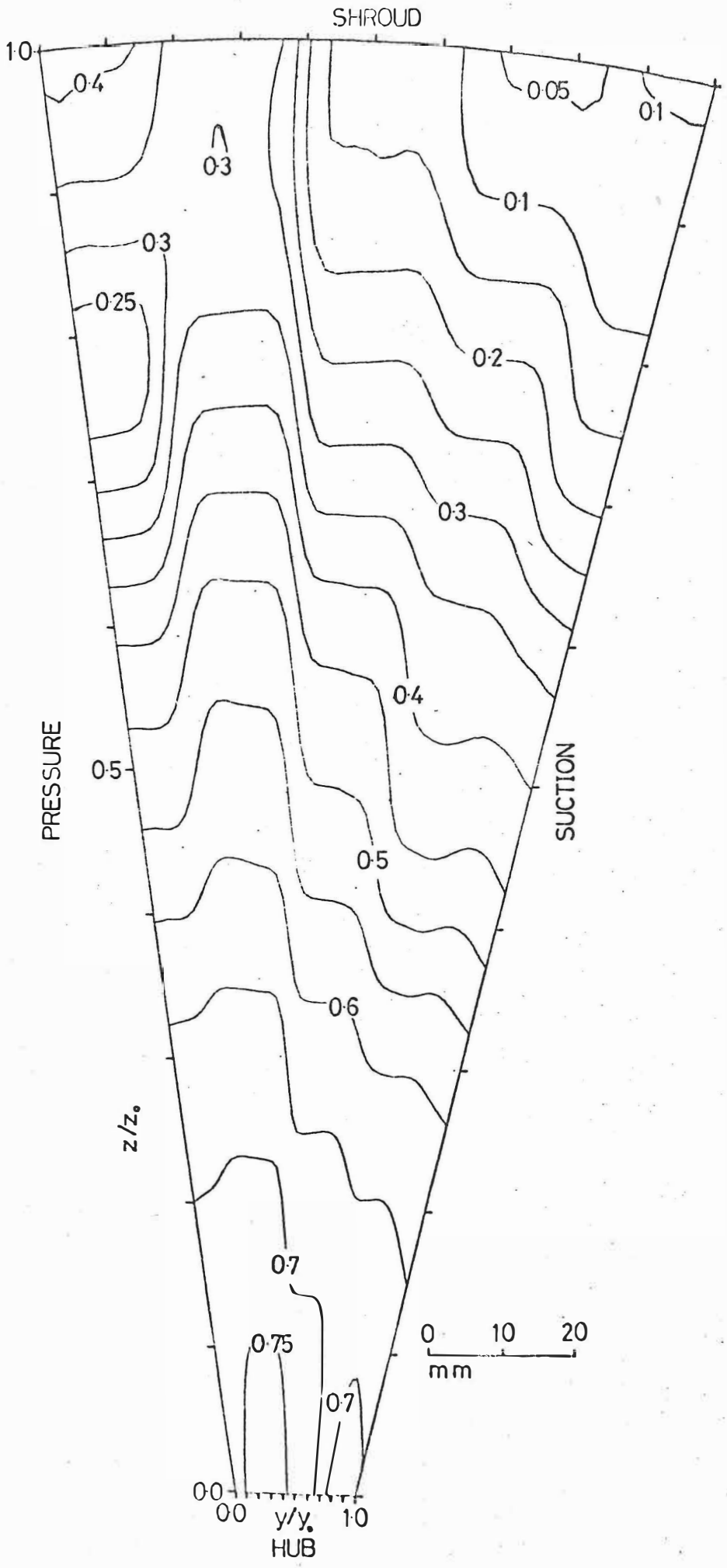

Figure 3.6 'Design' flow. Station 1. Dimensionless reduced static pressure P_r.

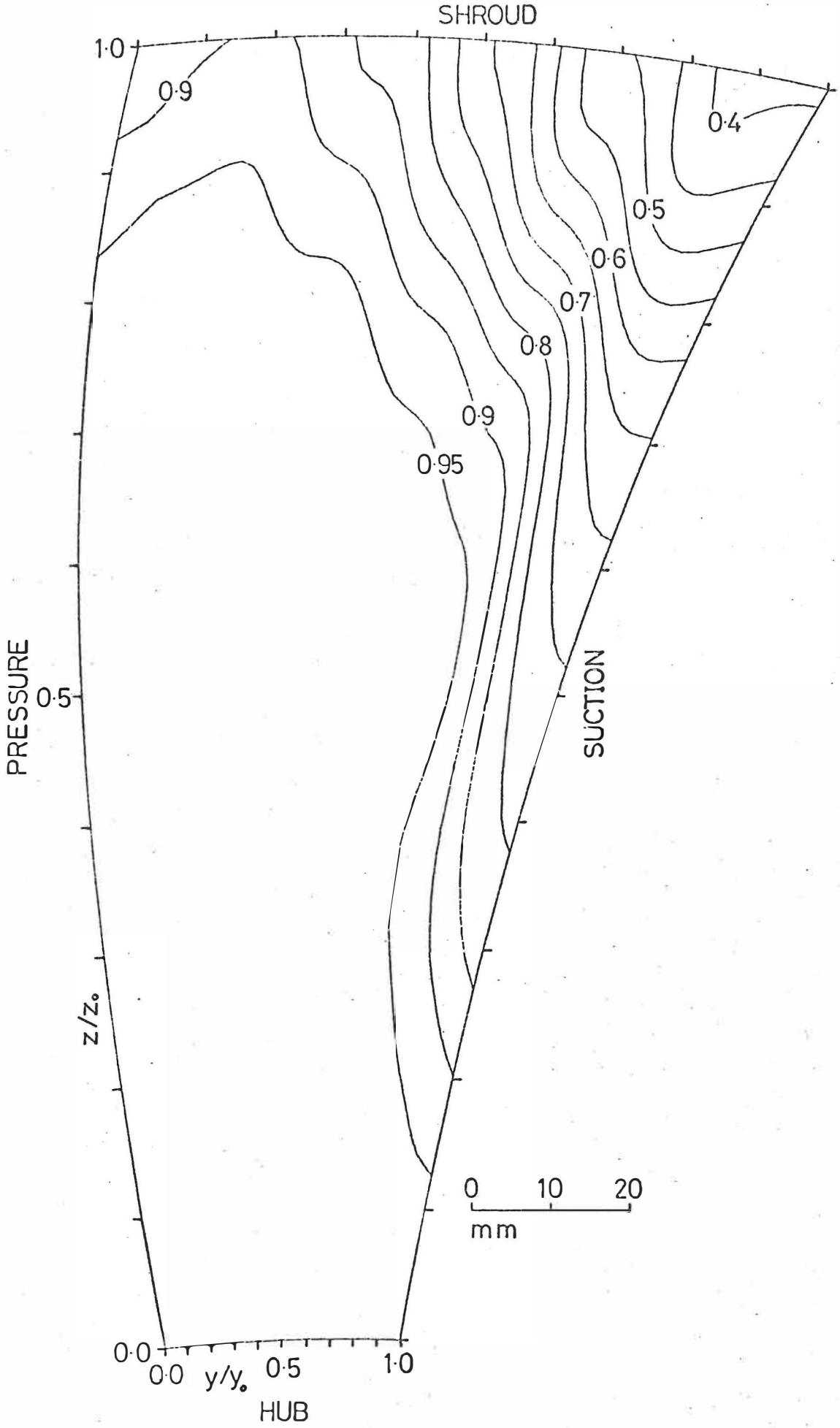

Figure 3.7 'Design' flow. Station 2. Dimensionless rotary stagnation pressure P*.

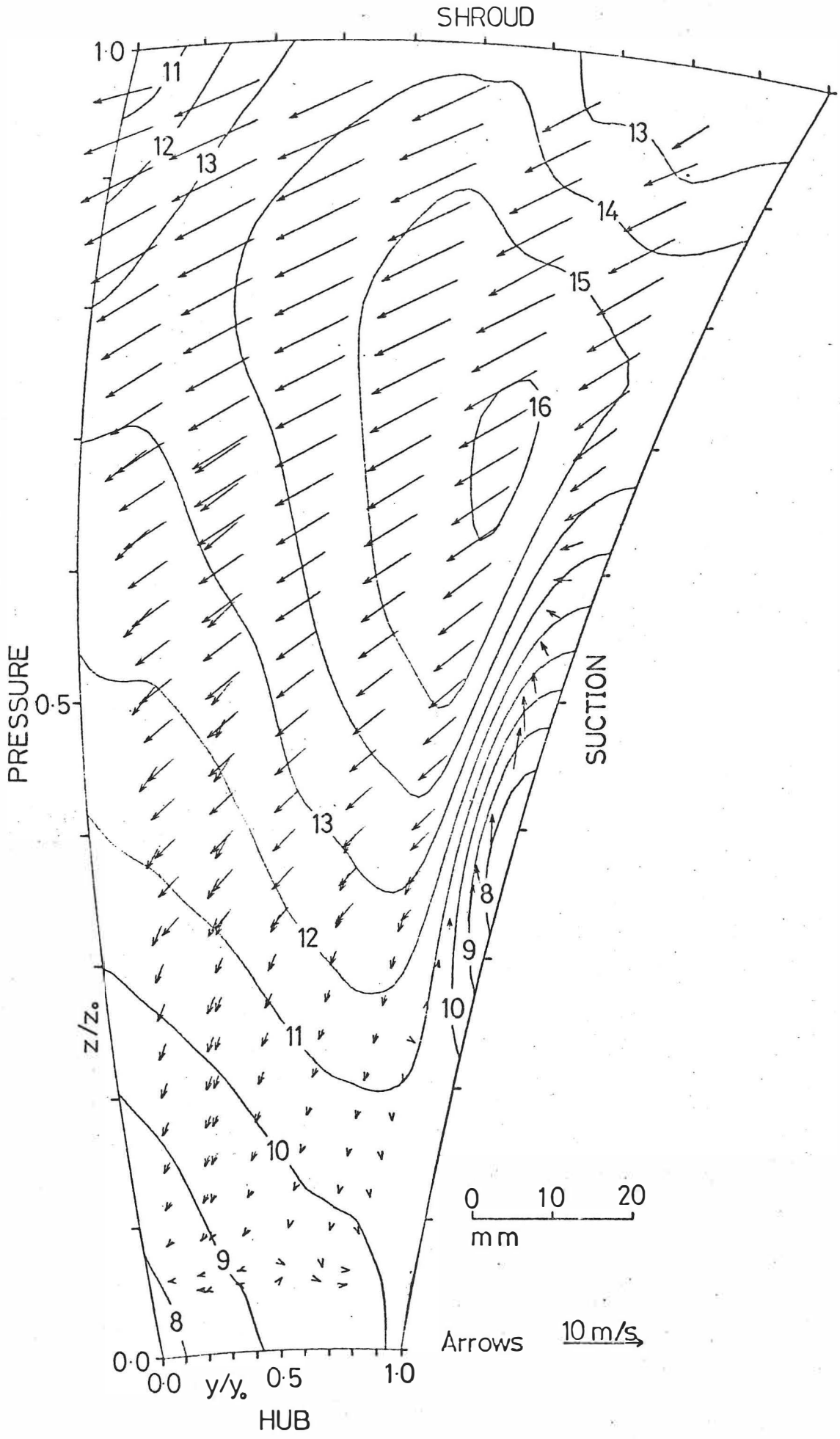

Figure 3.8 'Design' flow. Station 2. Relative velocities - contours in m/s.

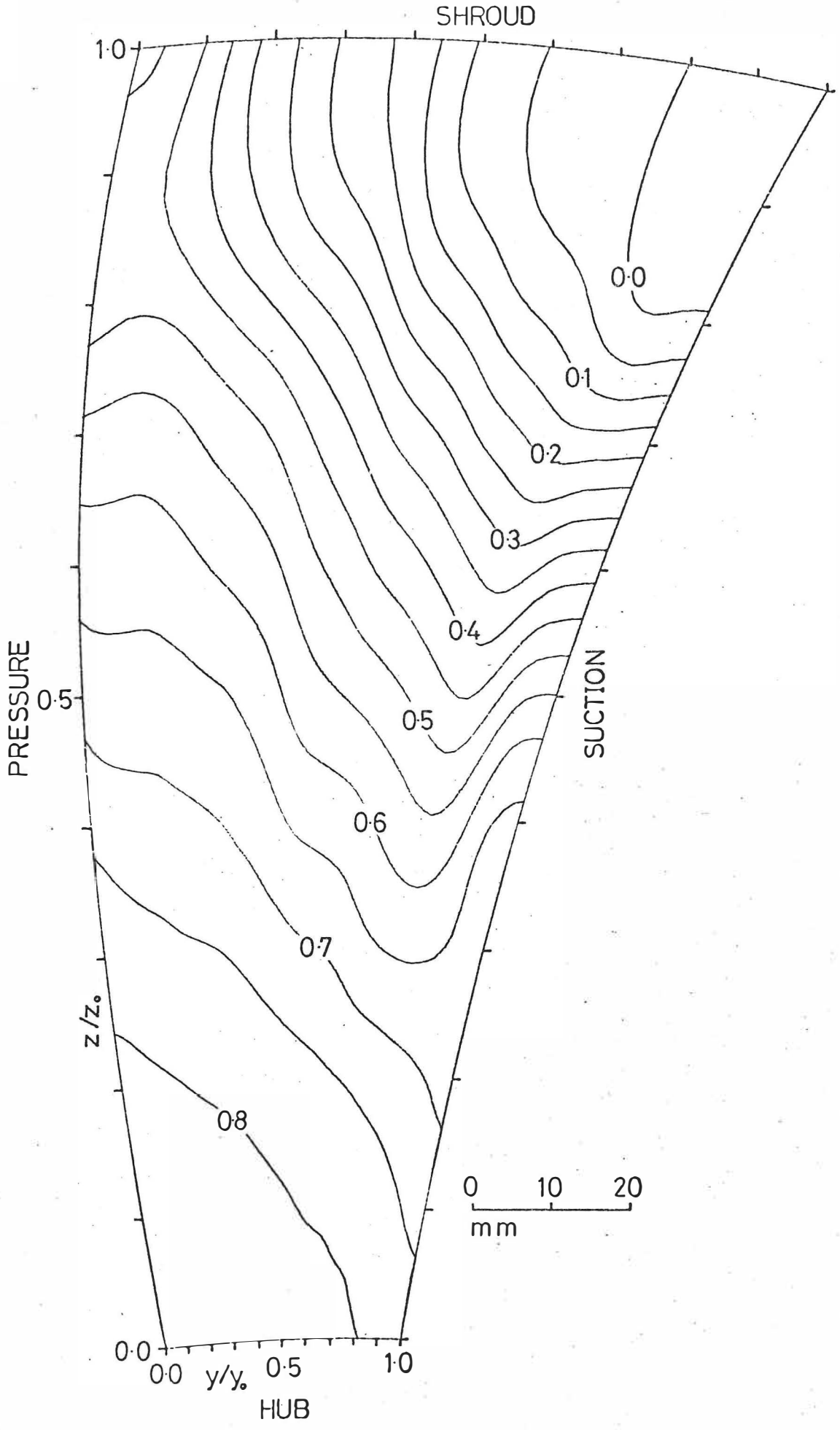

Figure 3.9 'Design' flow. Station 2, Dimensionless reduced static pressure P_r.

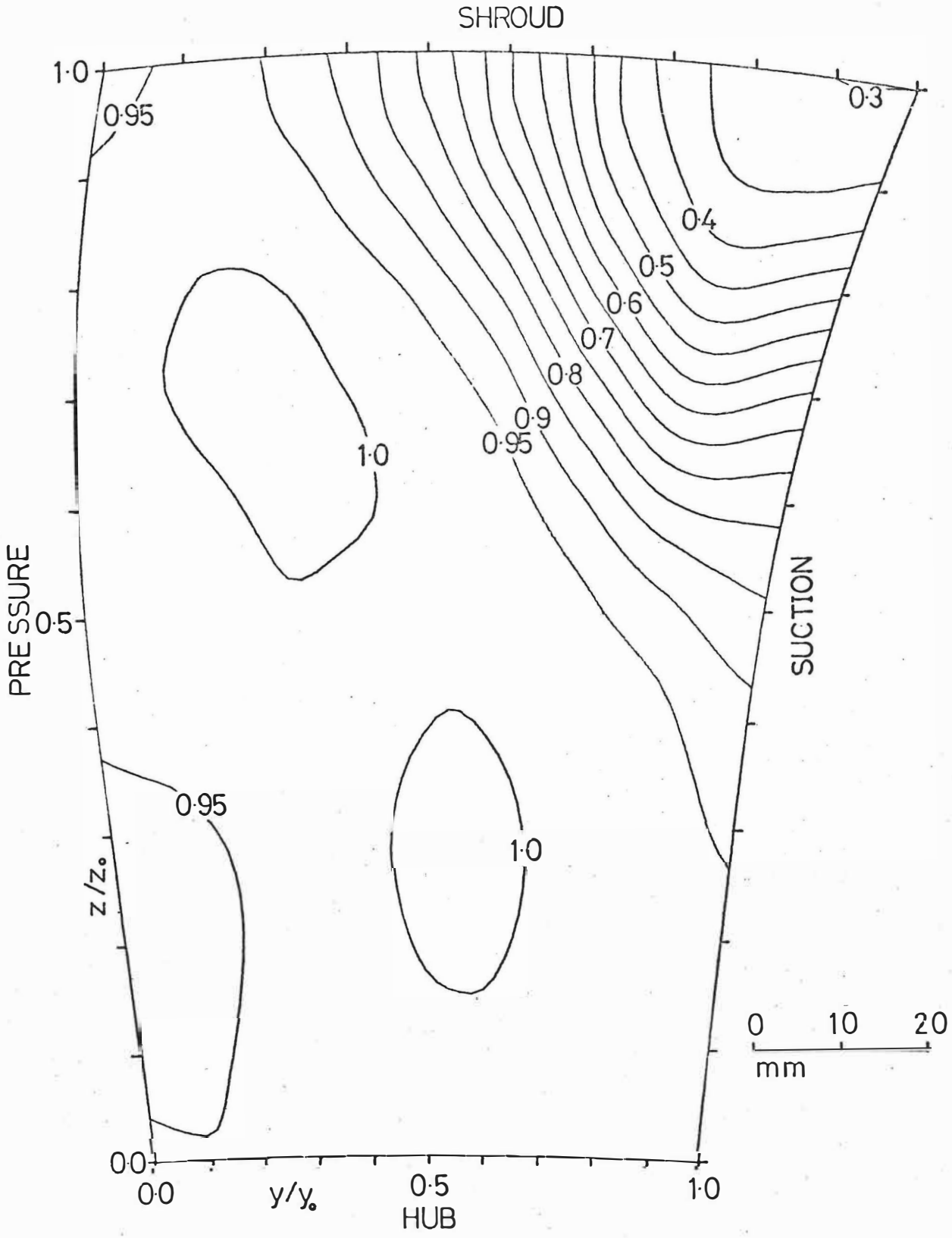

Figure 3.10 'Design' flow. Station 3. Dimensionless rotary stagnation pressure P*.

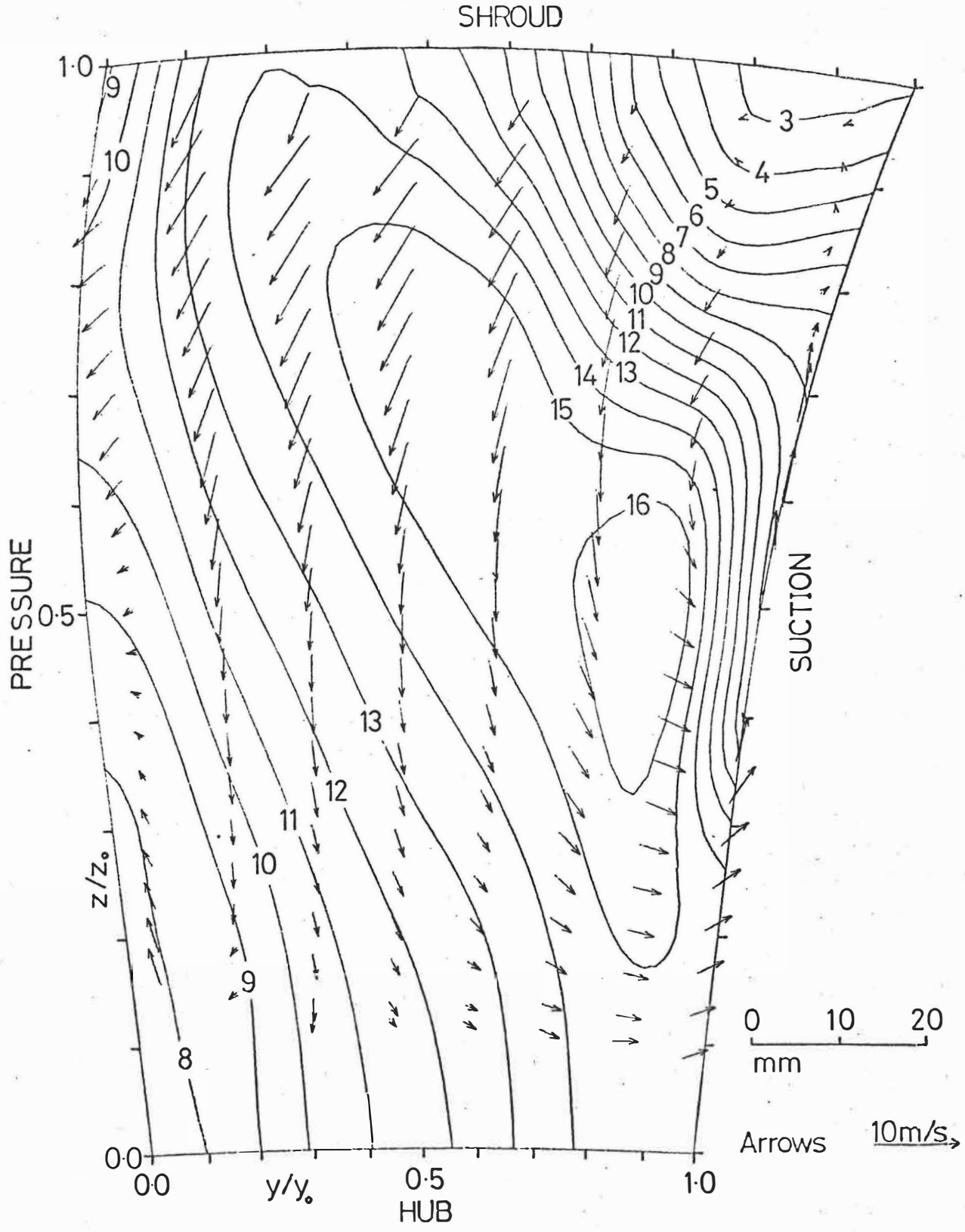

Figure 3.11 'Design' flow, Station 3. Relative velocities - contours in m/s.

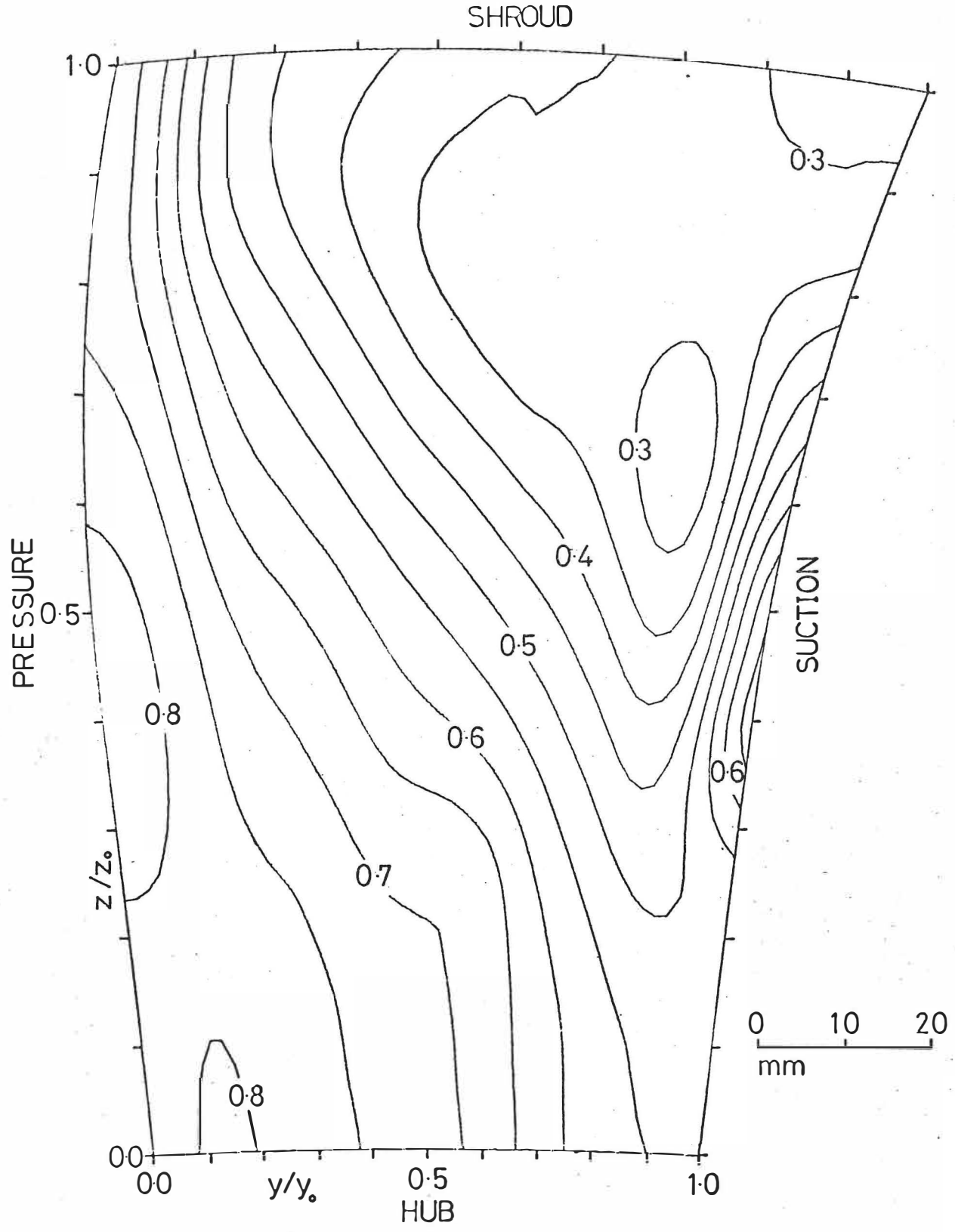

Figure 3.12 'Design' flow. Station 3. Dimensionless reduced static pressure P_r.

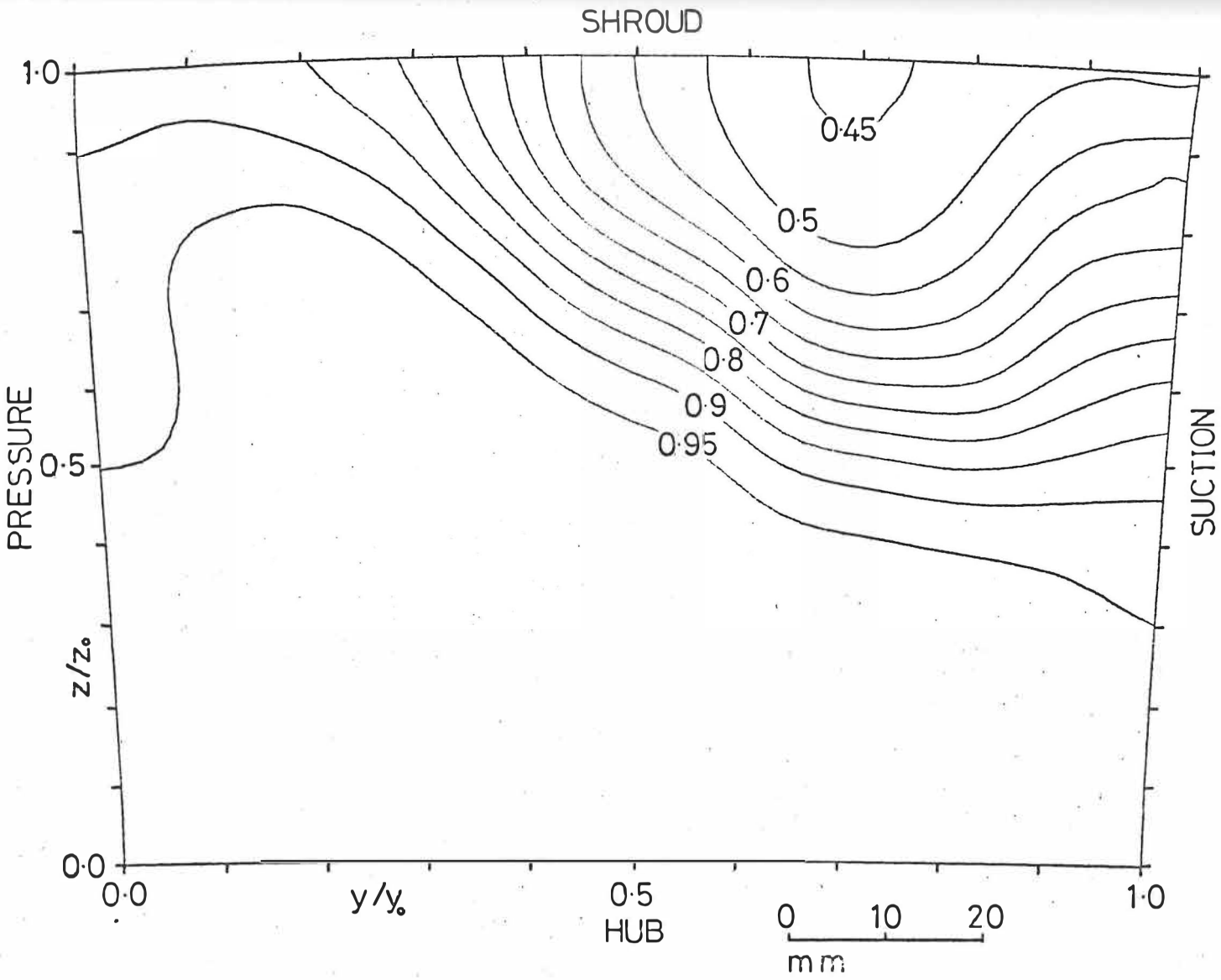

Figure 3.13 'Design' flow. Station 4. Dimensionless rotary stagnation pressure P*.

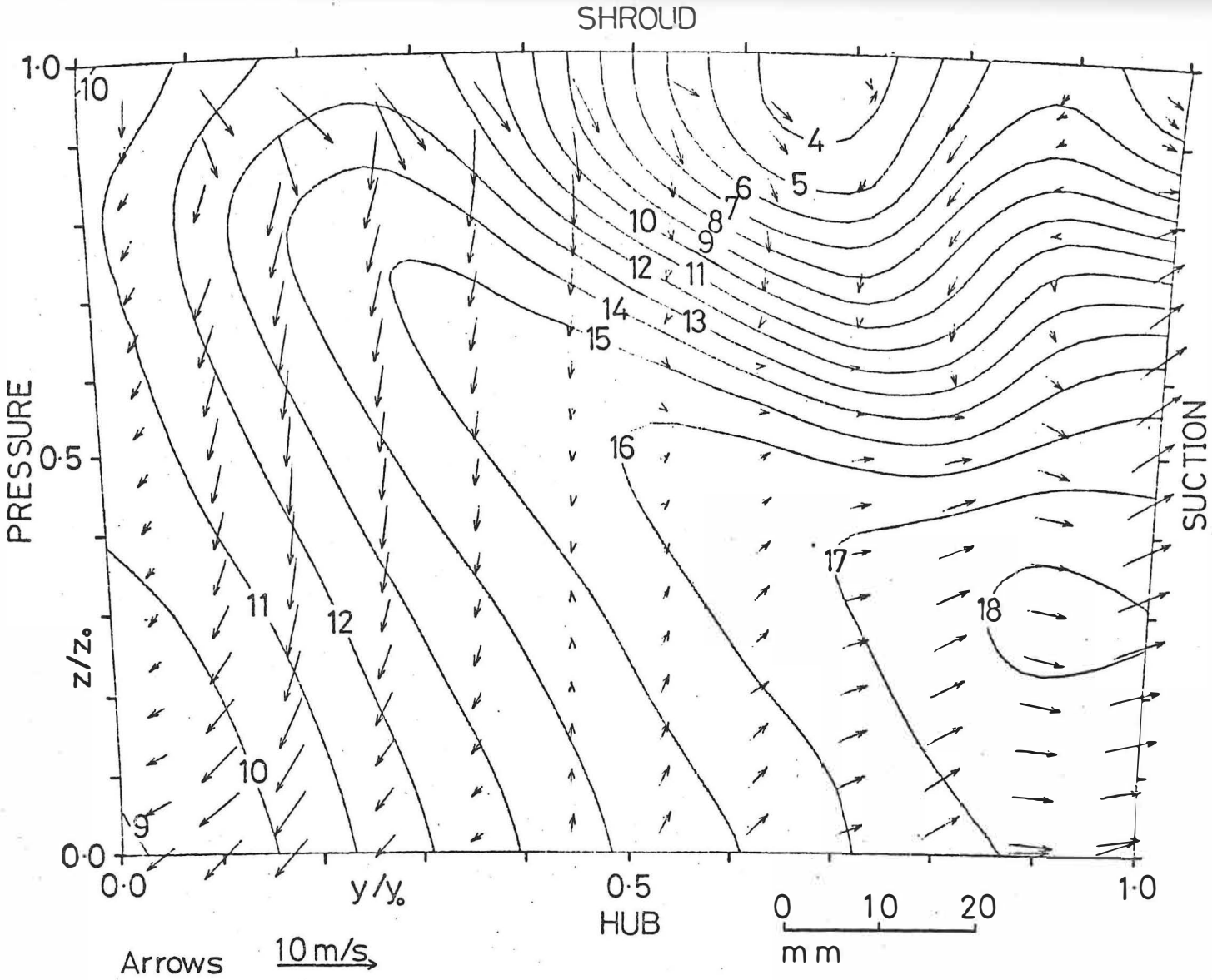

Figure 3.14 'Design' flow. Station 4. Relative velocities - contours in m/s.

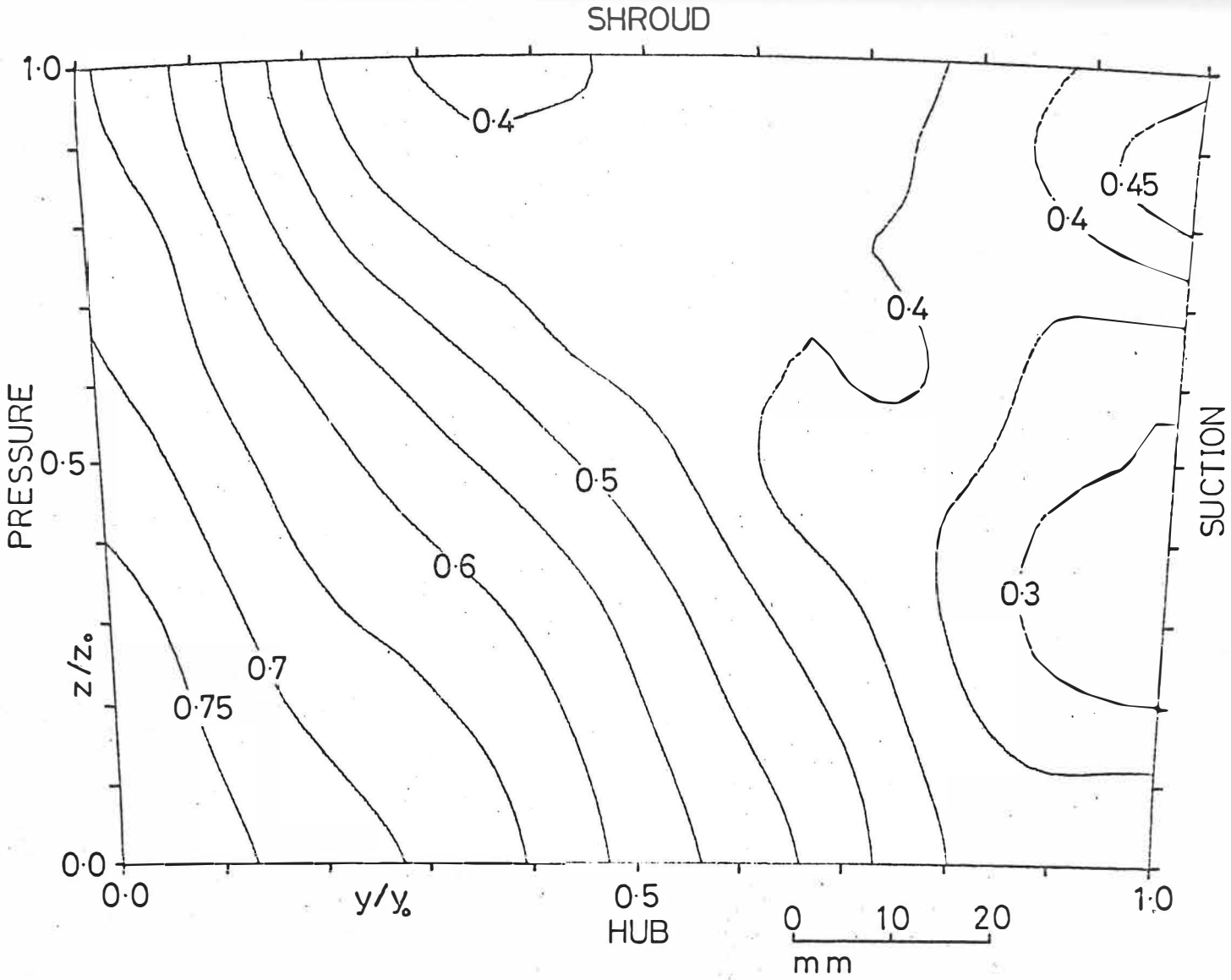

Figure 3.15 'Design' flow. Station 4. Dimensionless reduced static pressure P_r.

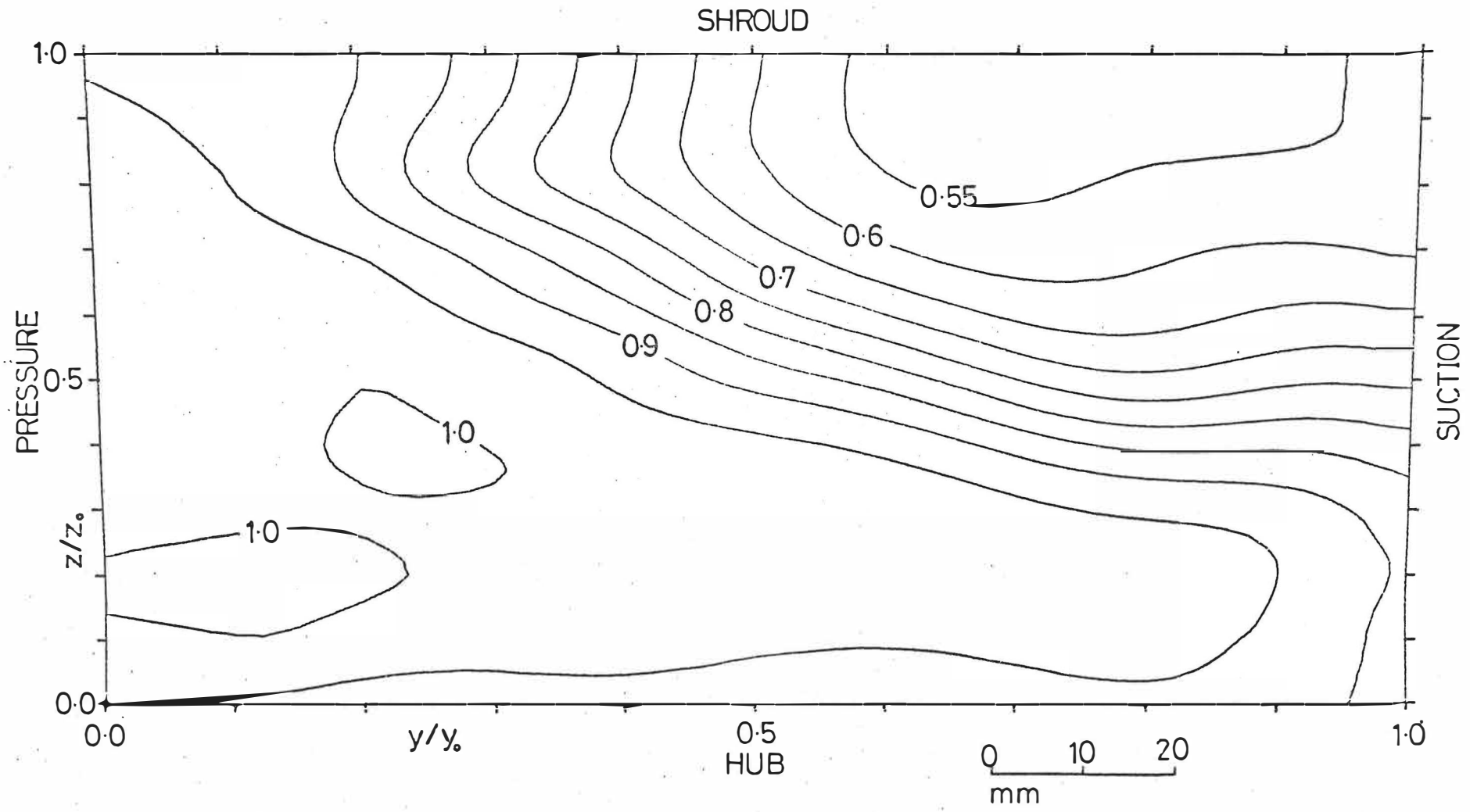

Figure 3.16 'Design' flow, Station 5. Dimensionless rotary stagnation pressure P*.

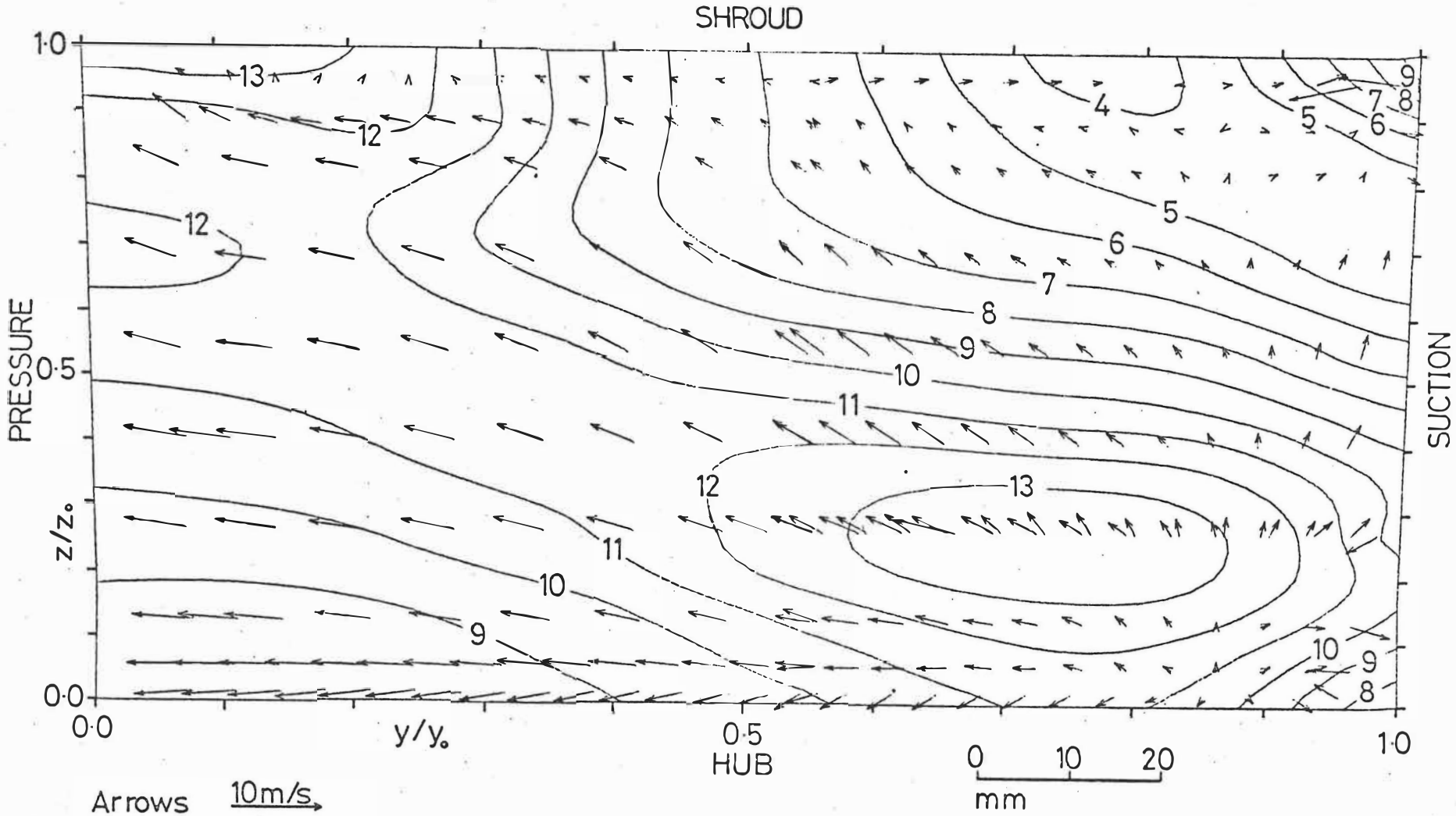

Figure 3.17 'Design' flow. Station 5. Relative velocities - contours in m/s.

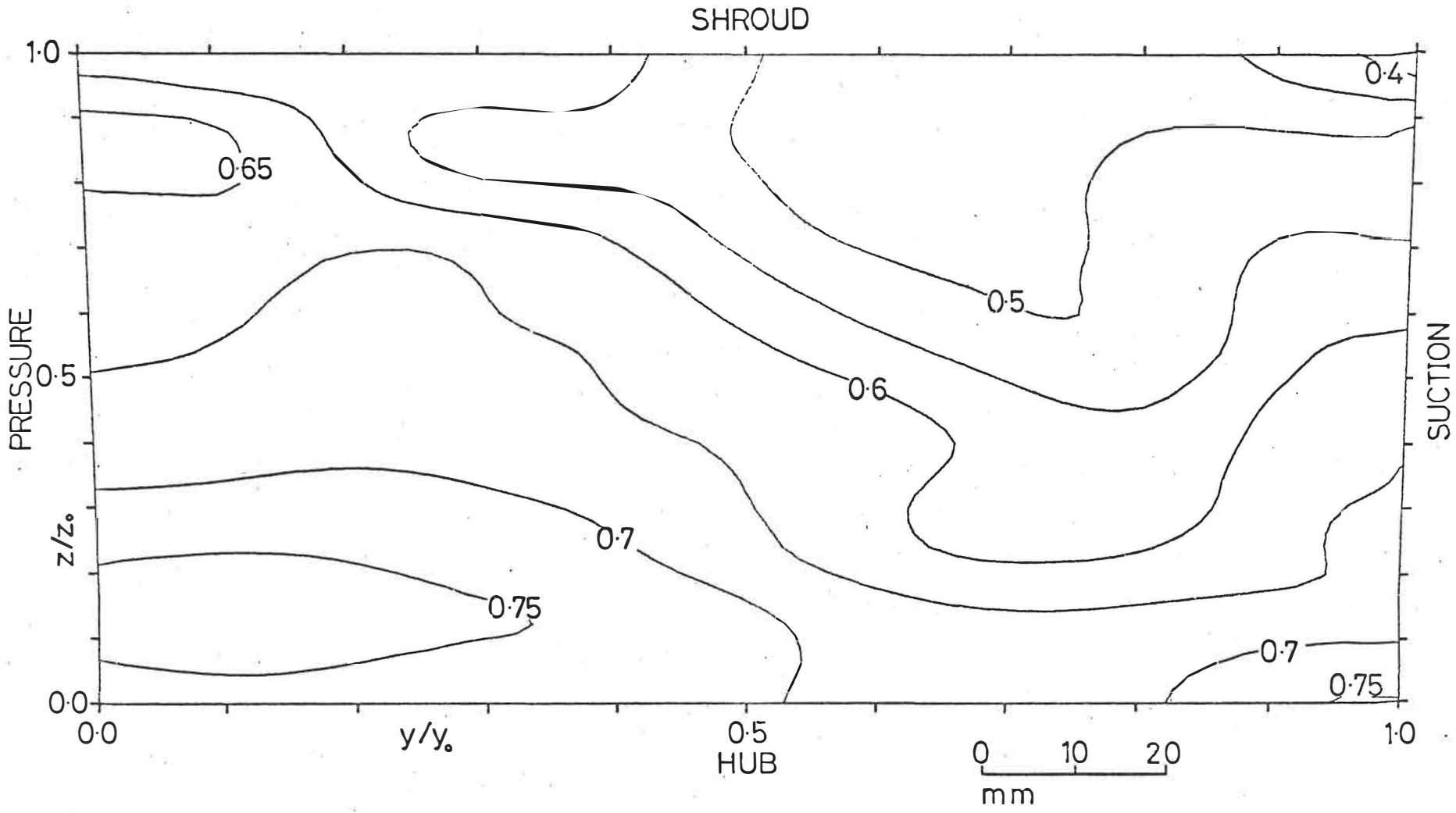

Figure 3.18 'Design' flow. Station 5. Dimensionless reduced static pressure P_r.

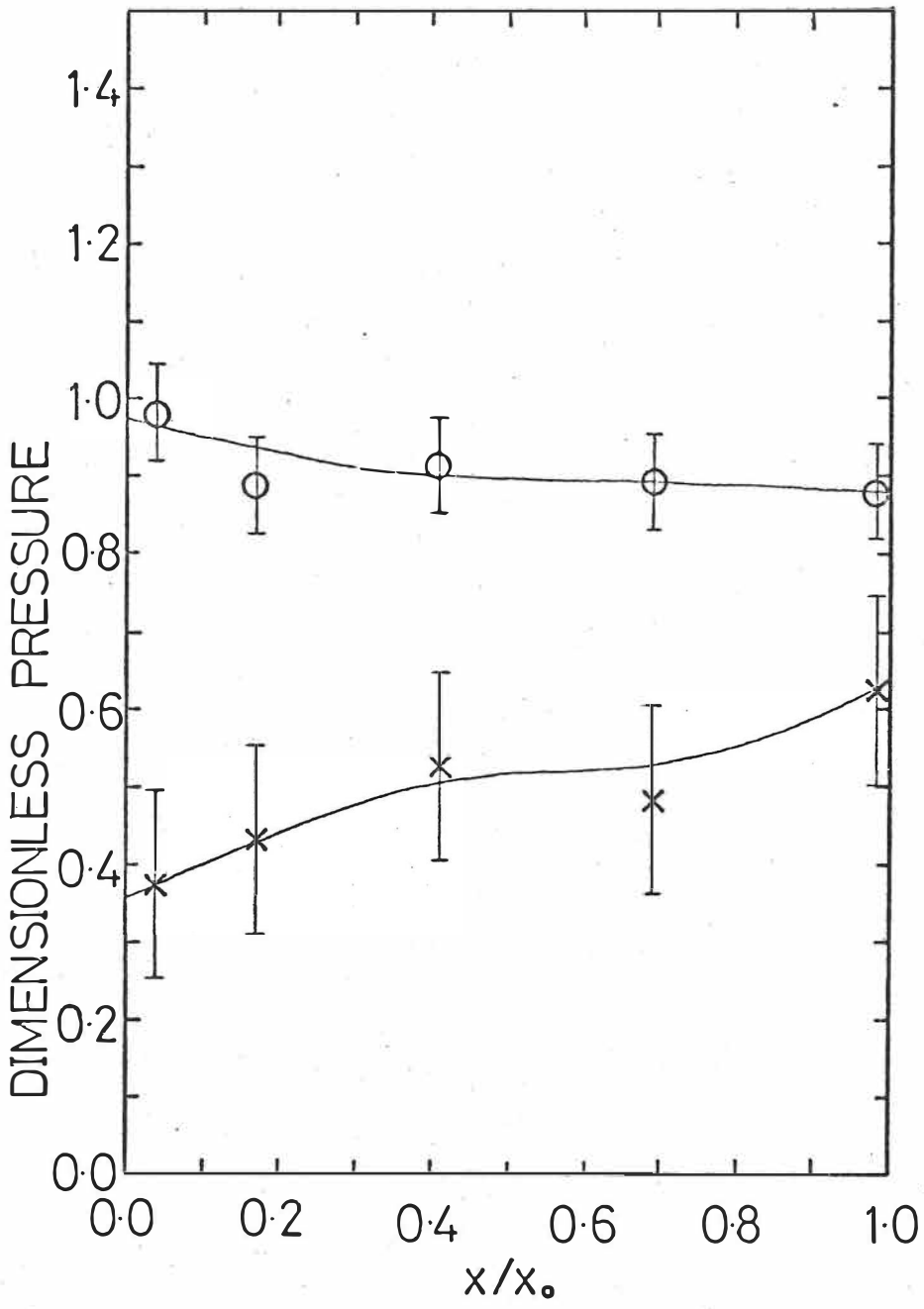

× P_r – Dimensionless Reduced Static Pressure

○ P^* – Dimensionless Rotary Stagnation Pressure

Figure 3.19 'Design' flow. Mass-averaged dimensionless pressures.

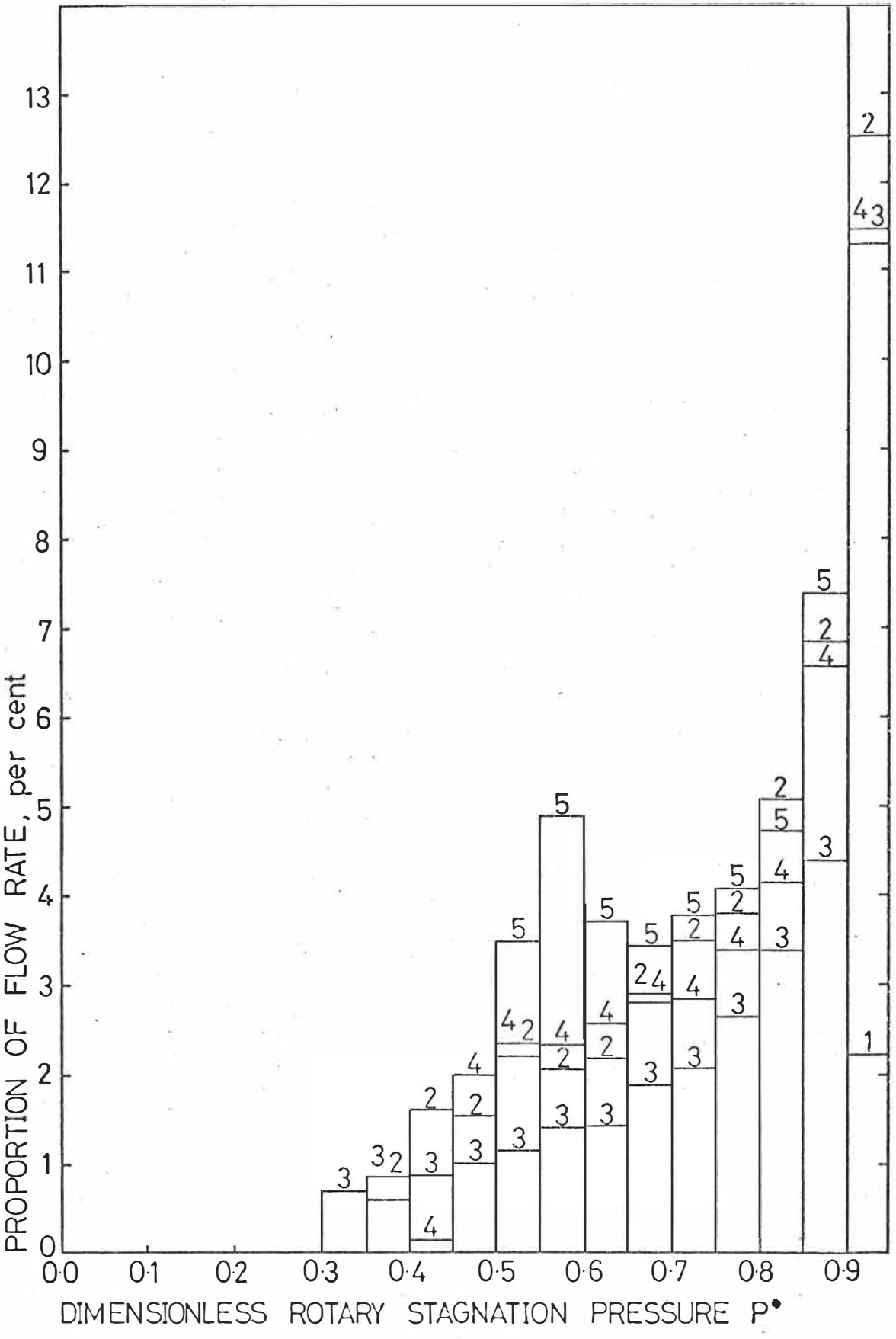

Figure 3.20 'Design' flow. Distribution of dimensionless rotary stagnation pressure P*.

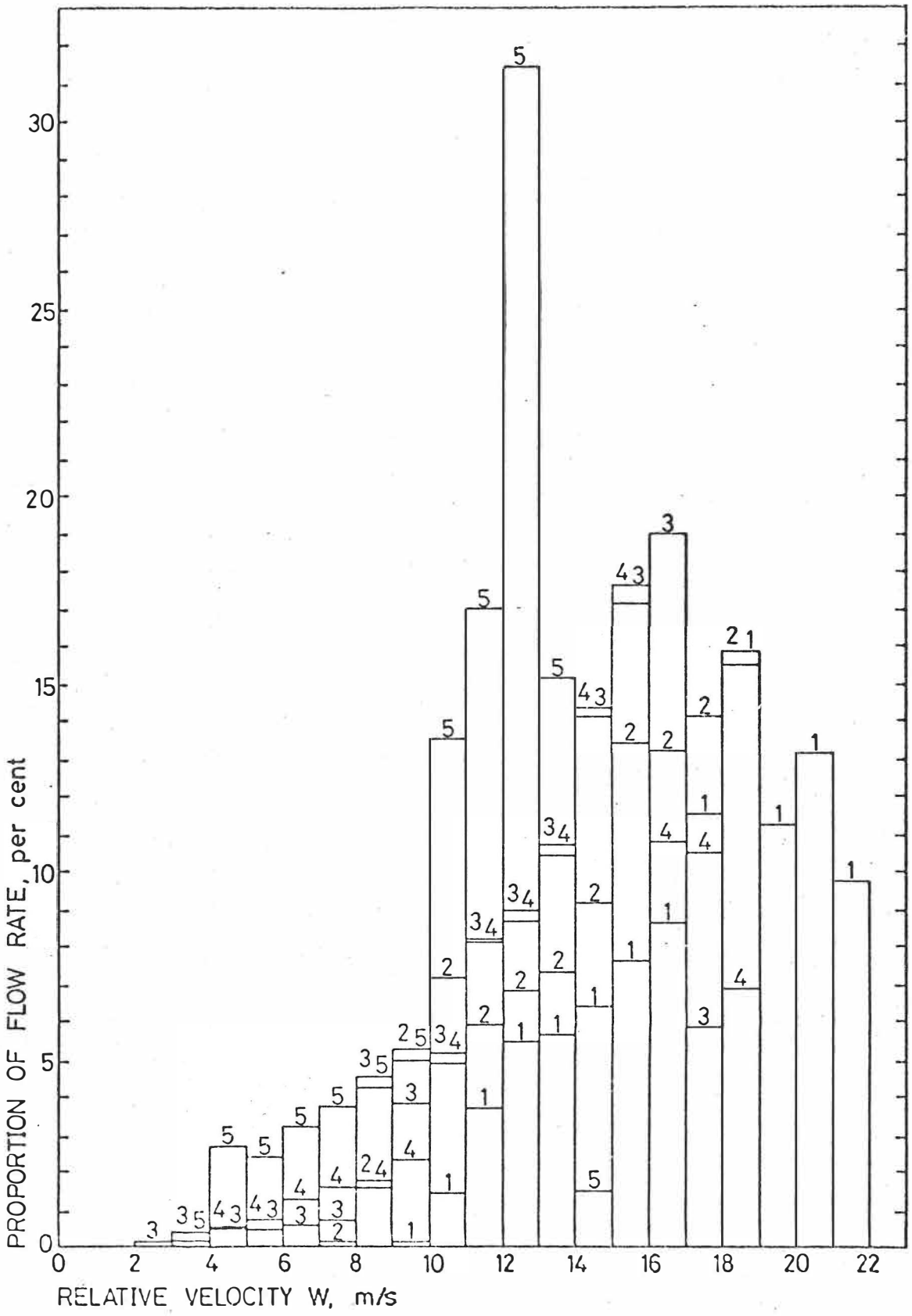

Figure 3.21 'Design' flow. Distribution of relative velocity.

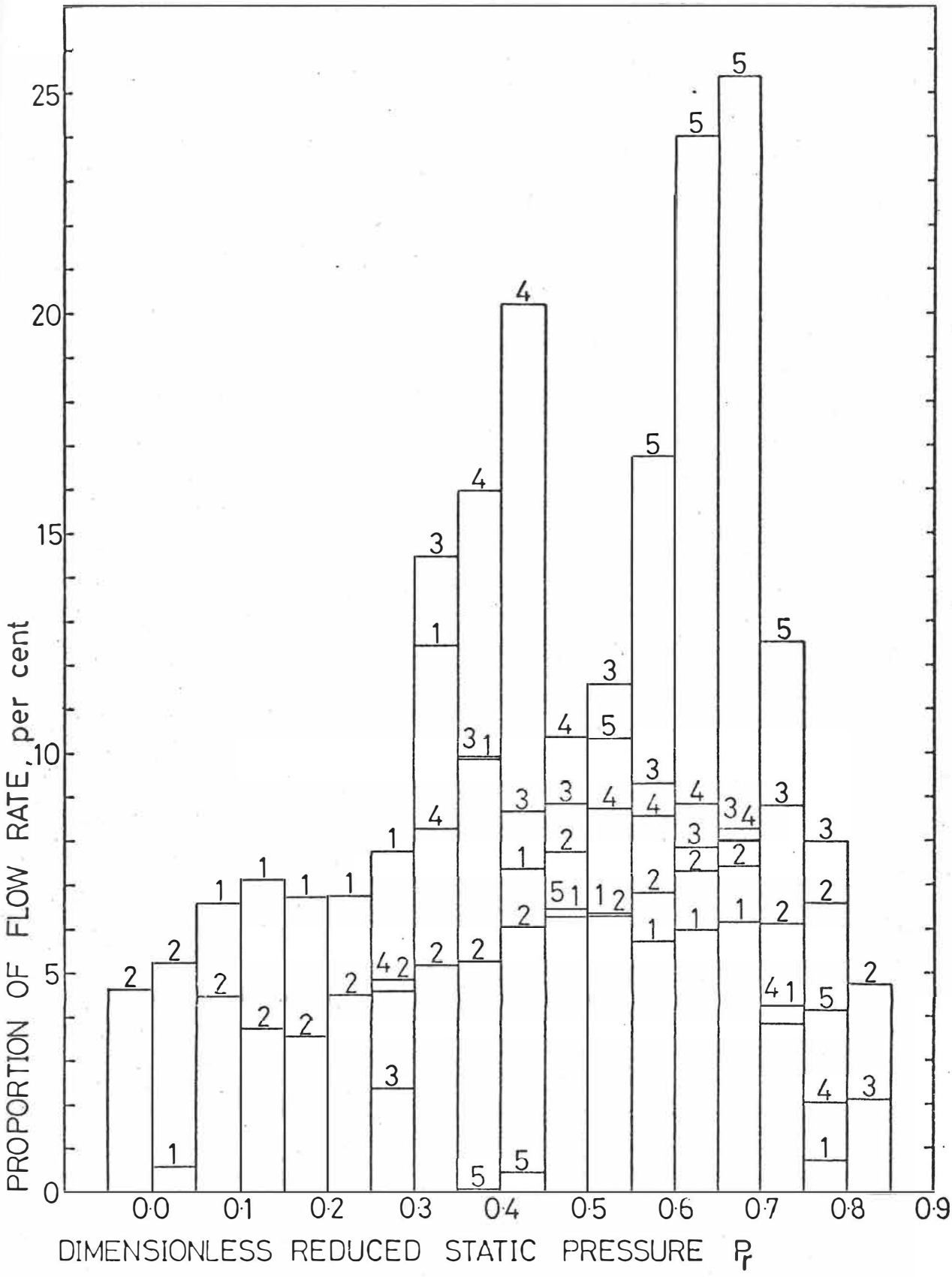

Figure 3.22 'Design' flow. Distribution of dimensionless reduced static pressure.

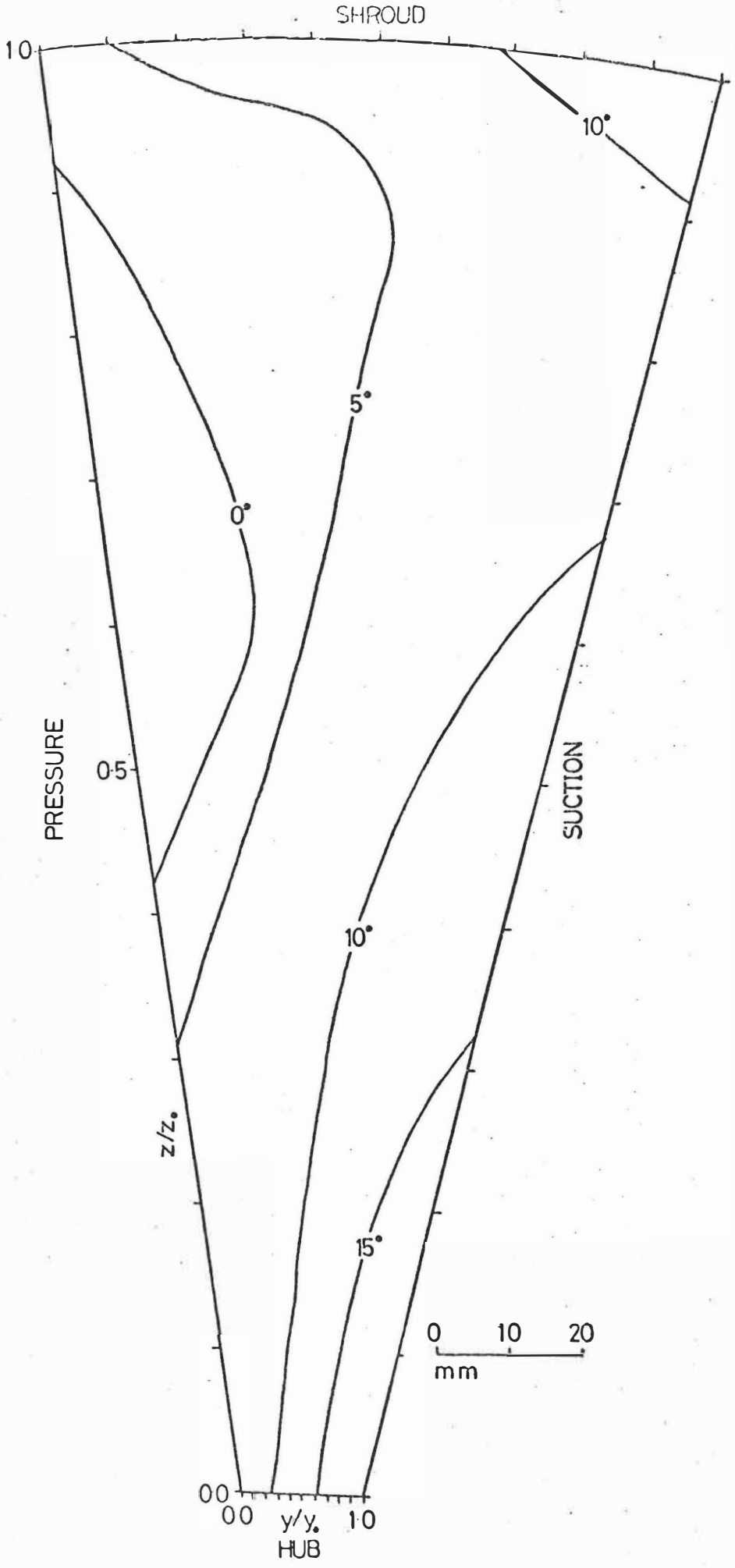

Figure 4.1 'Below design' flow. Station 1. Incidence angles at impeller inlet.

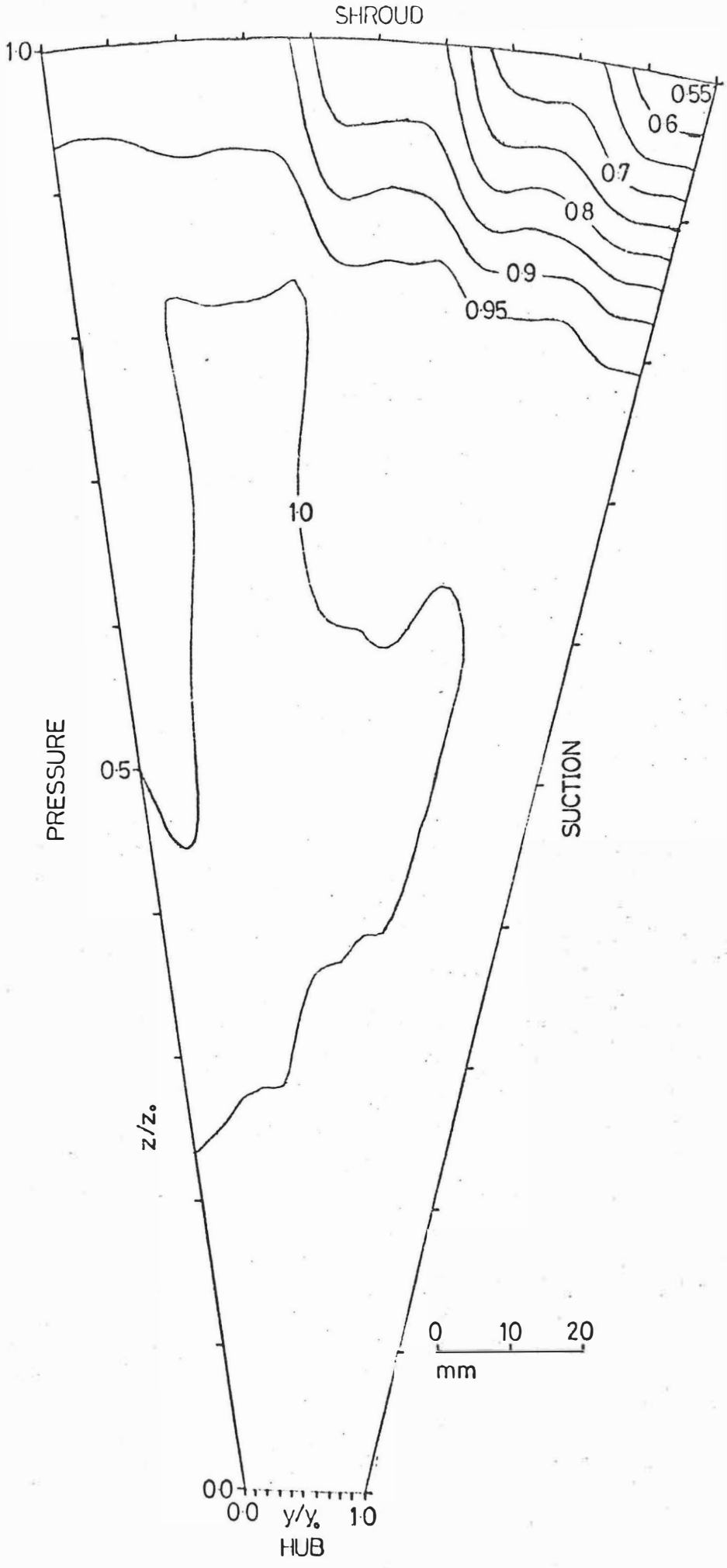

Figure 4.2 'Below design'flow. Station 1. Dimensionless rotary stagnation pressure P*.

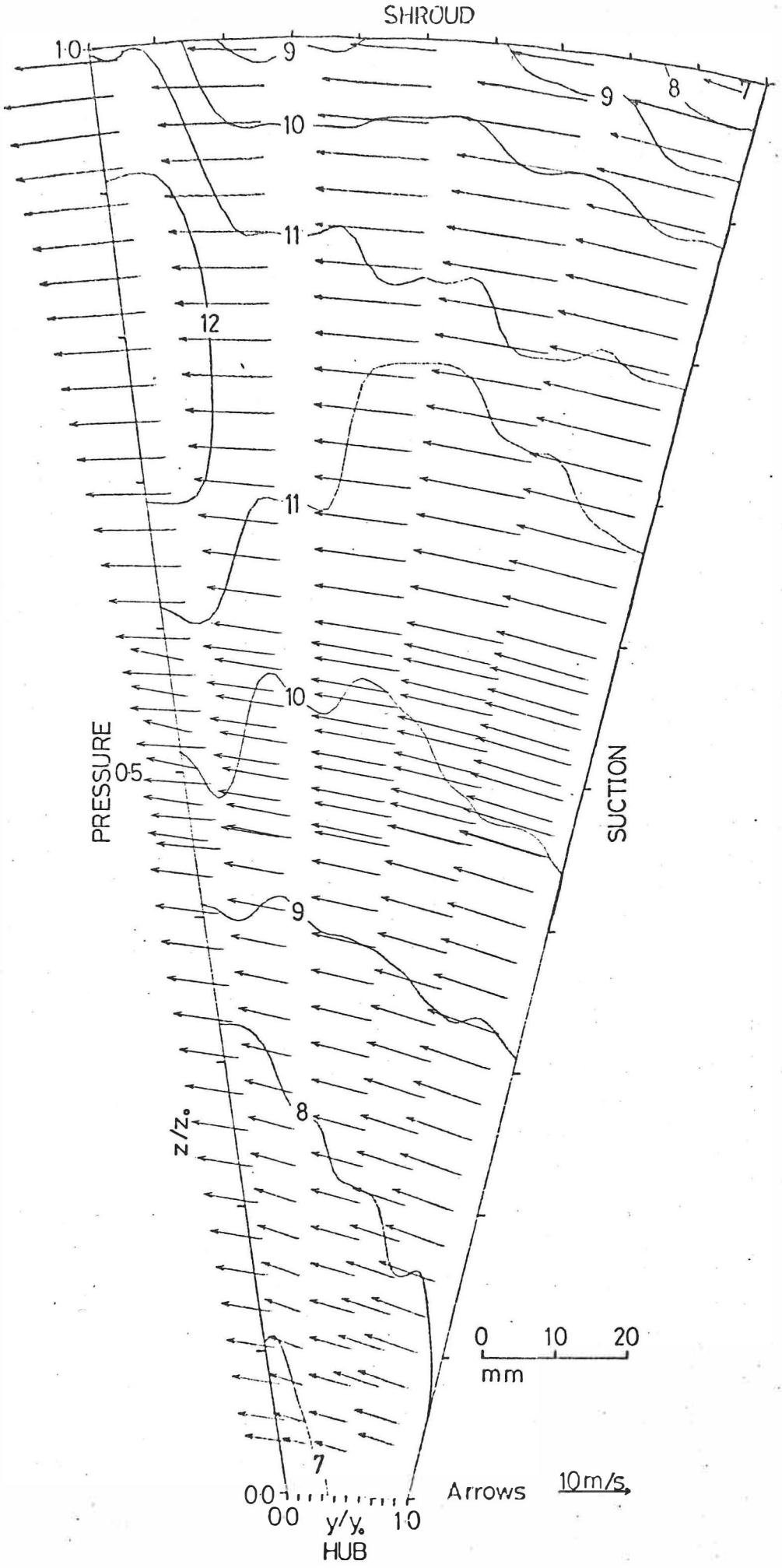

Figure 4.3 'Below design' flow. Station 1. Relative velocities contours in m/s.

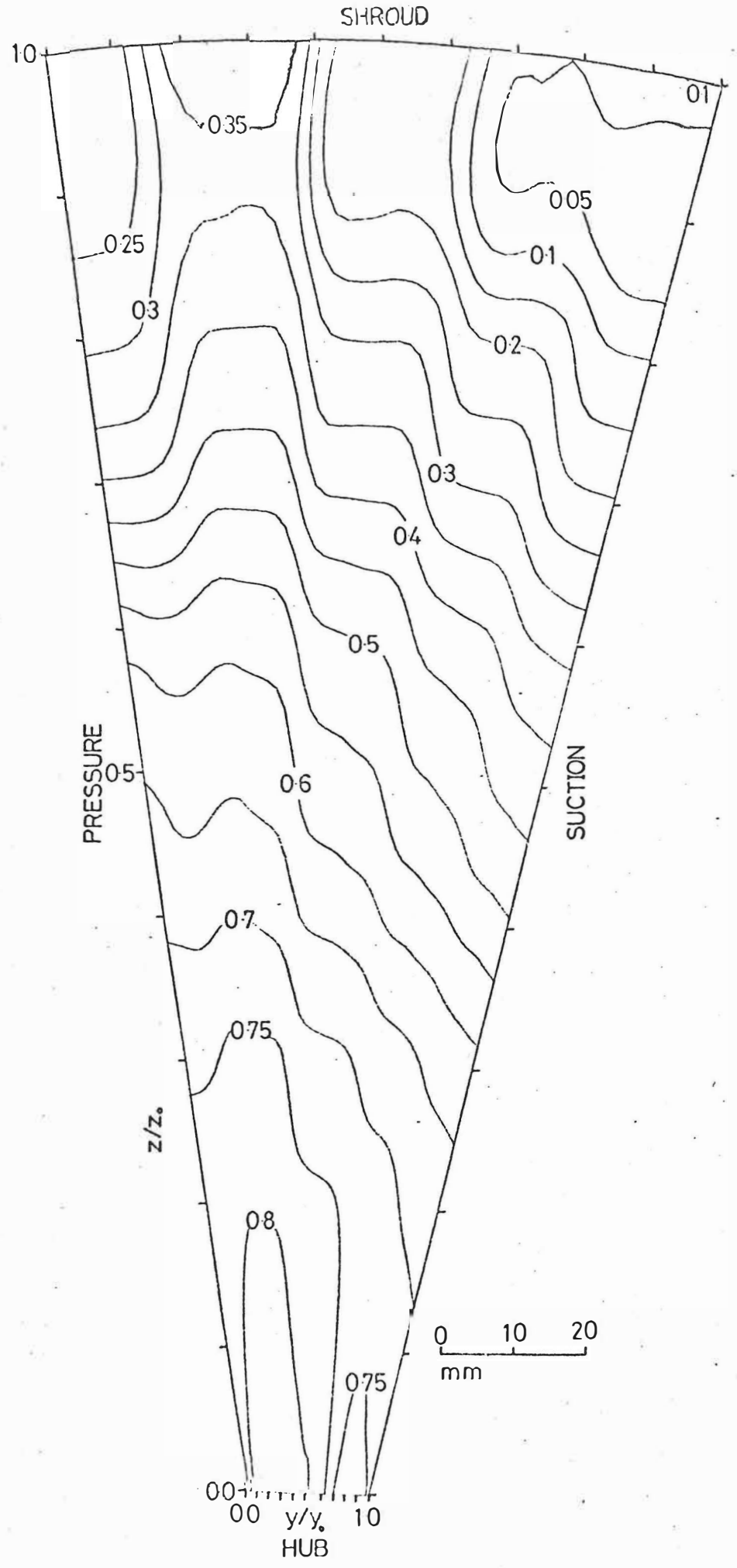

Figure 4.4 'Below design' flow. Station 1. Dimensionless reduced static pressure P_r.

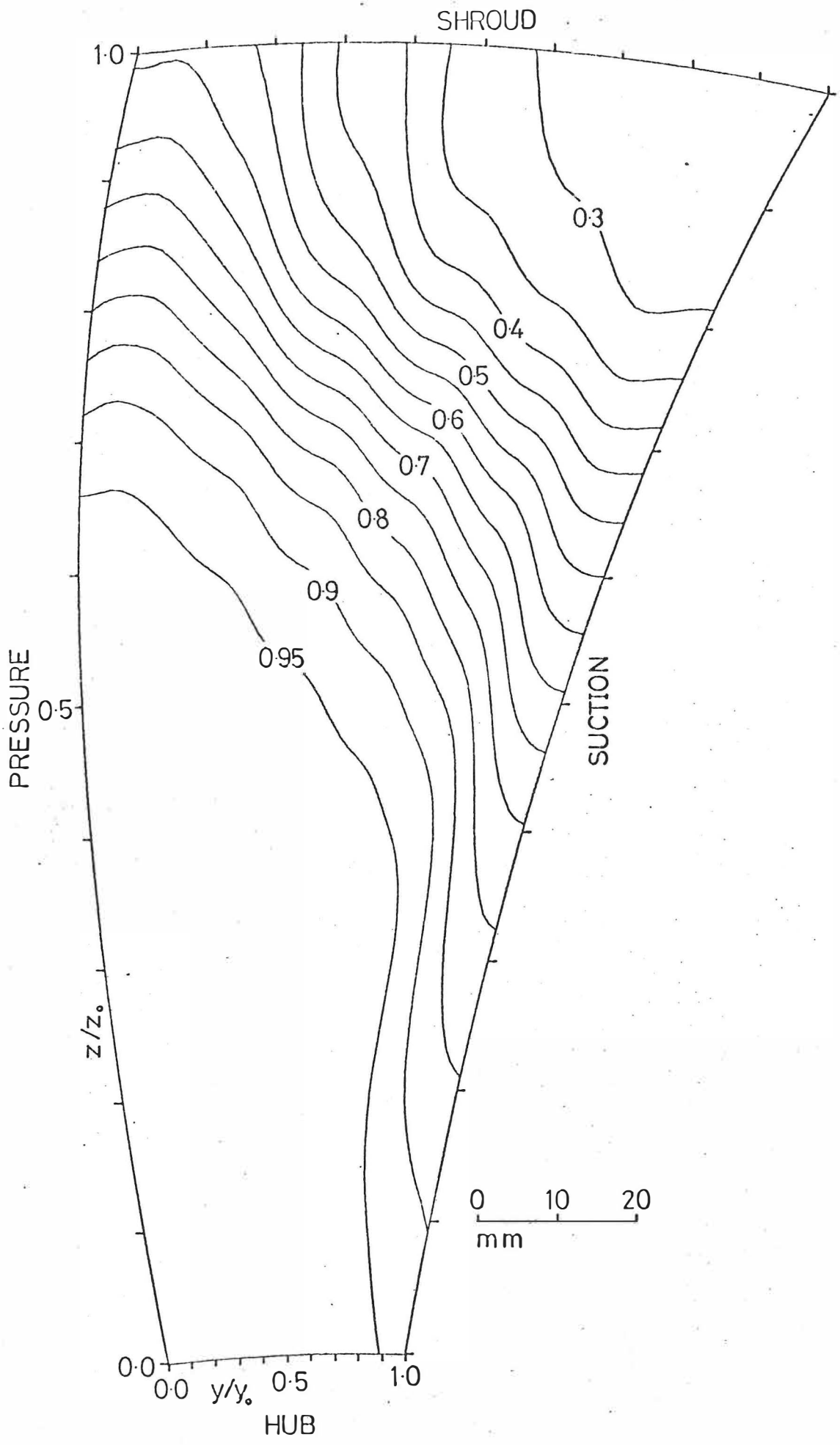

Figure 4.5 'Below design' flow. Station 2. Dimensionless rotary stagnation pressure P*.

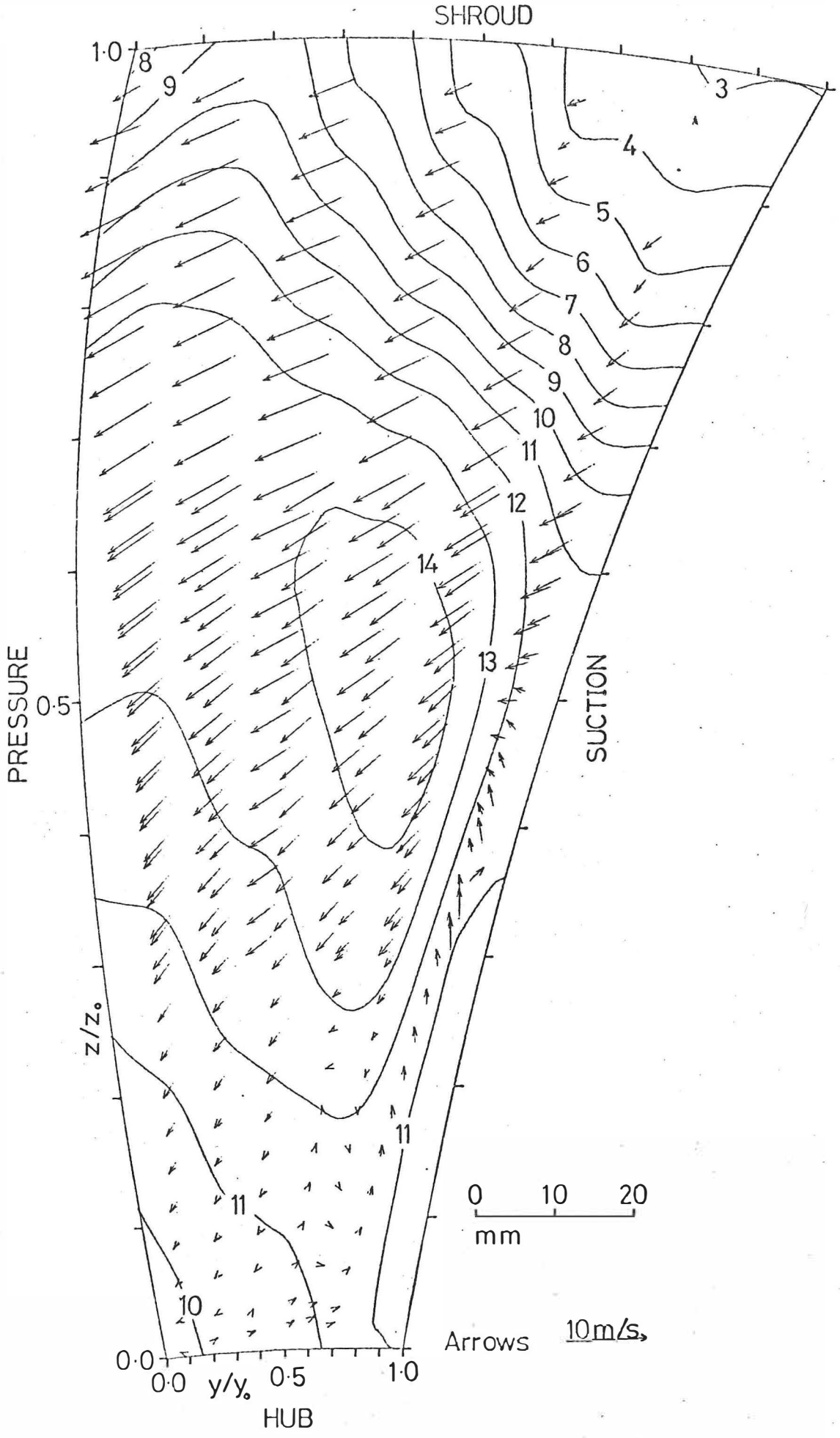

Figure 4.6 'Below design' flow. Station 2. Relative velocities contours in m/s.

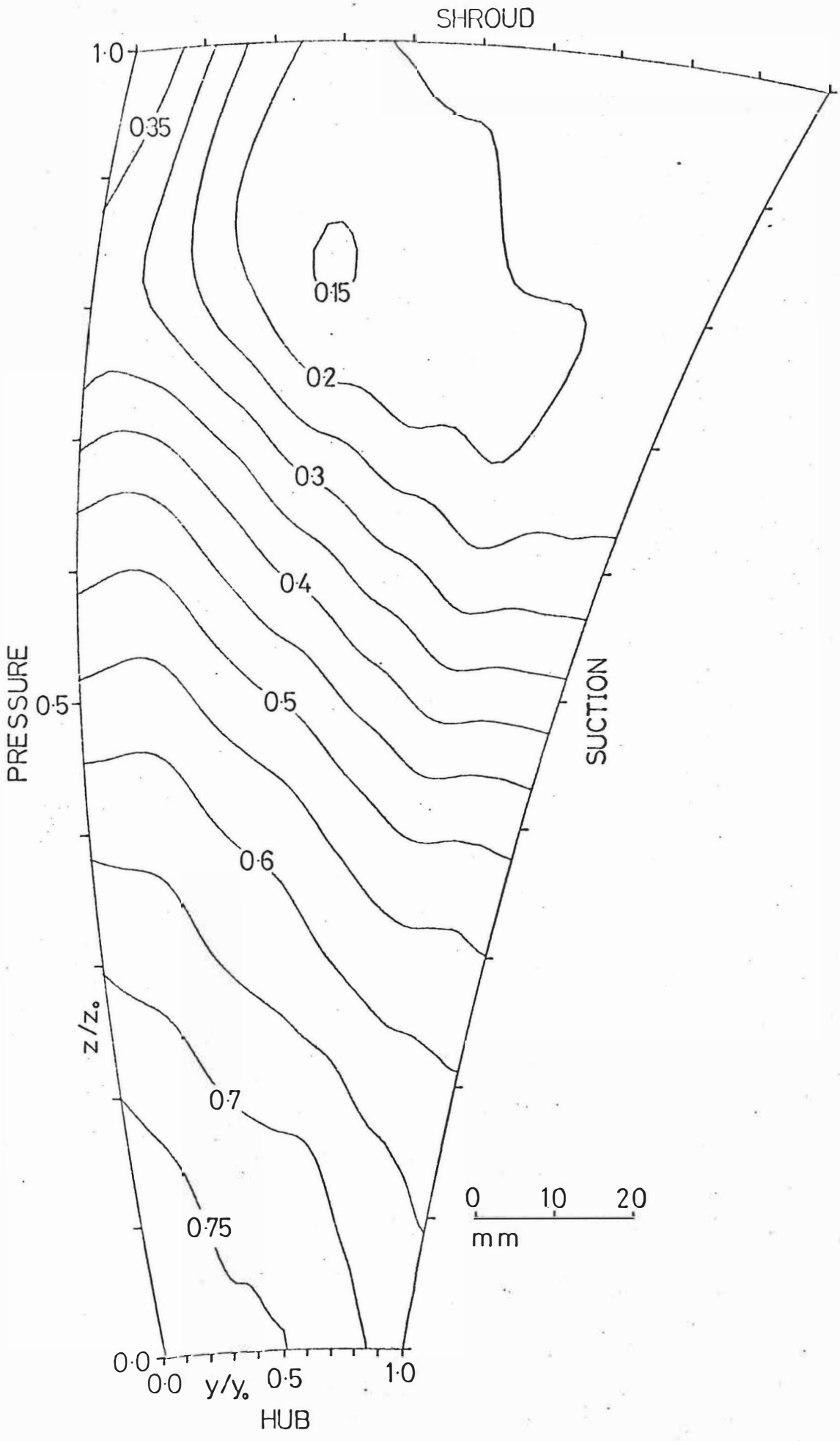

Figure 4.7 'Below design' flow. Station 2. Dimensionless reduced static pressure P_r.

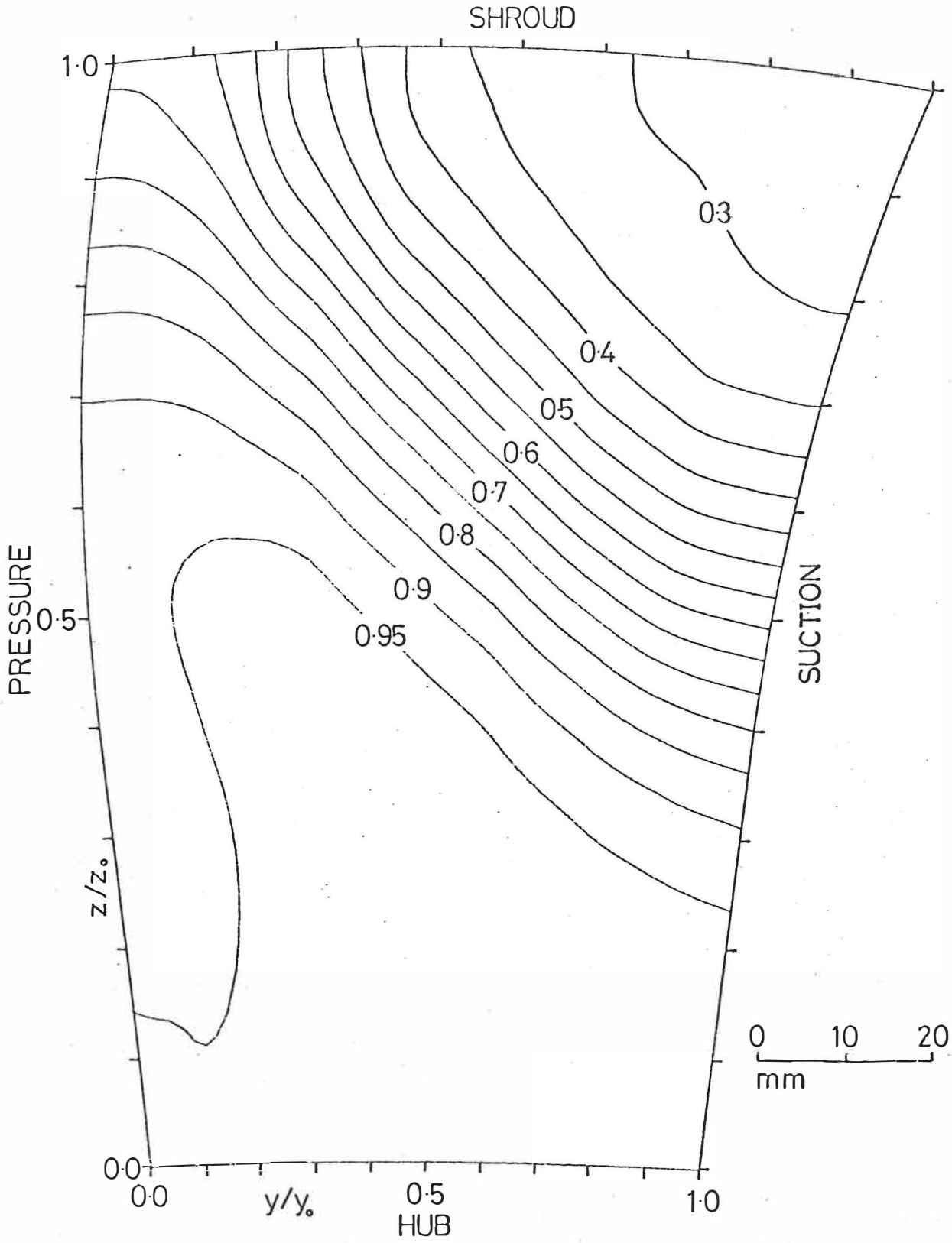

Figure 4.8 'Below design' flow. Station 3. Dimensionless rotary stagnation pressure P*.

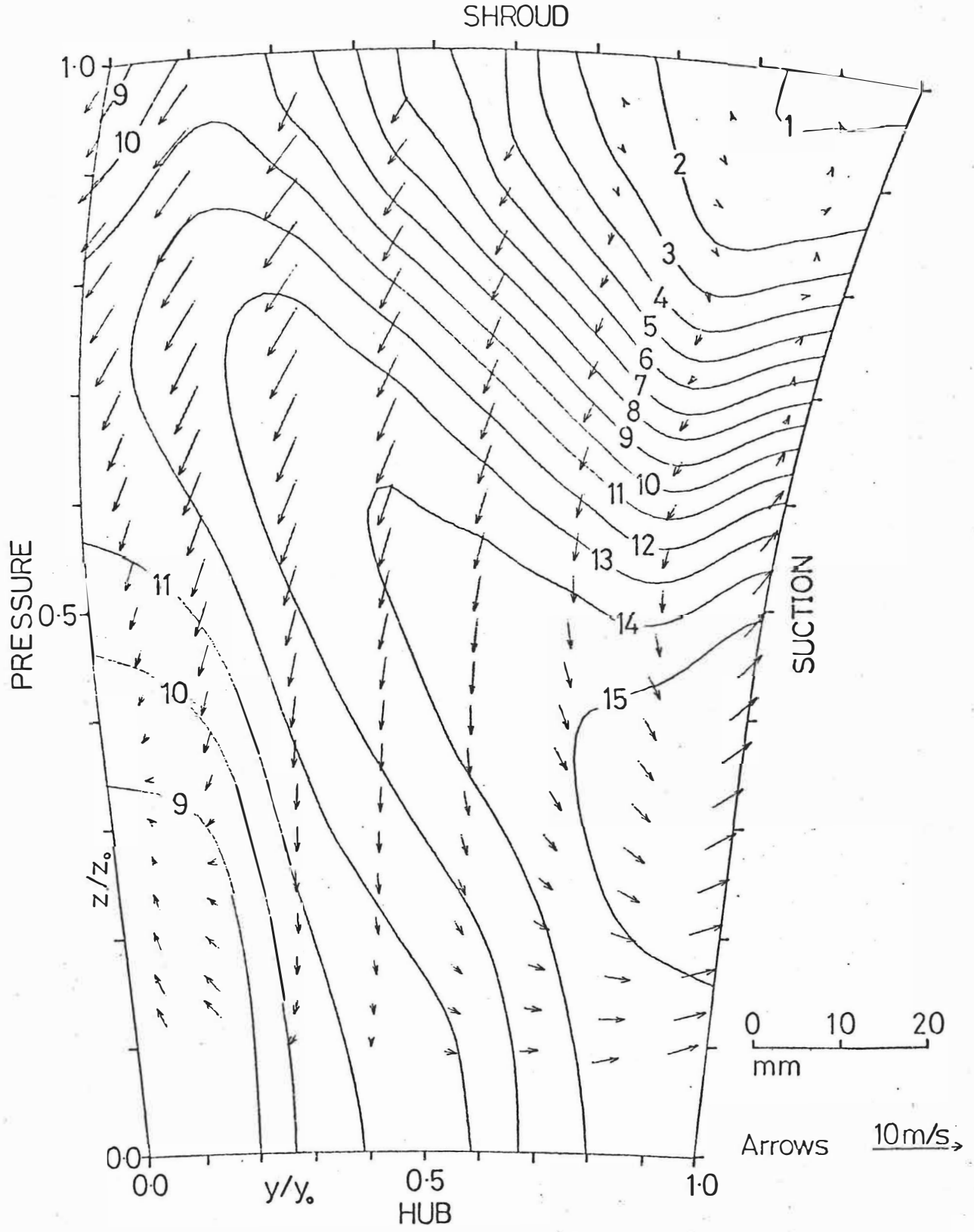

Figure 4.9 'Below design' flow. Station 3. Relative velocities contours in m/s.

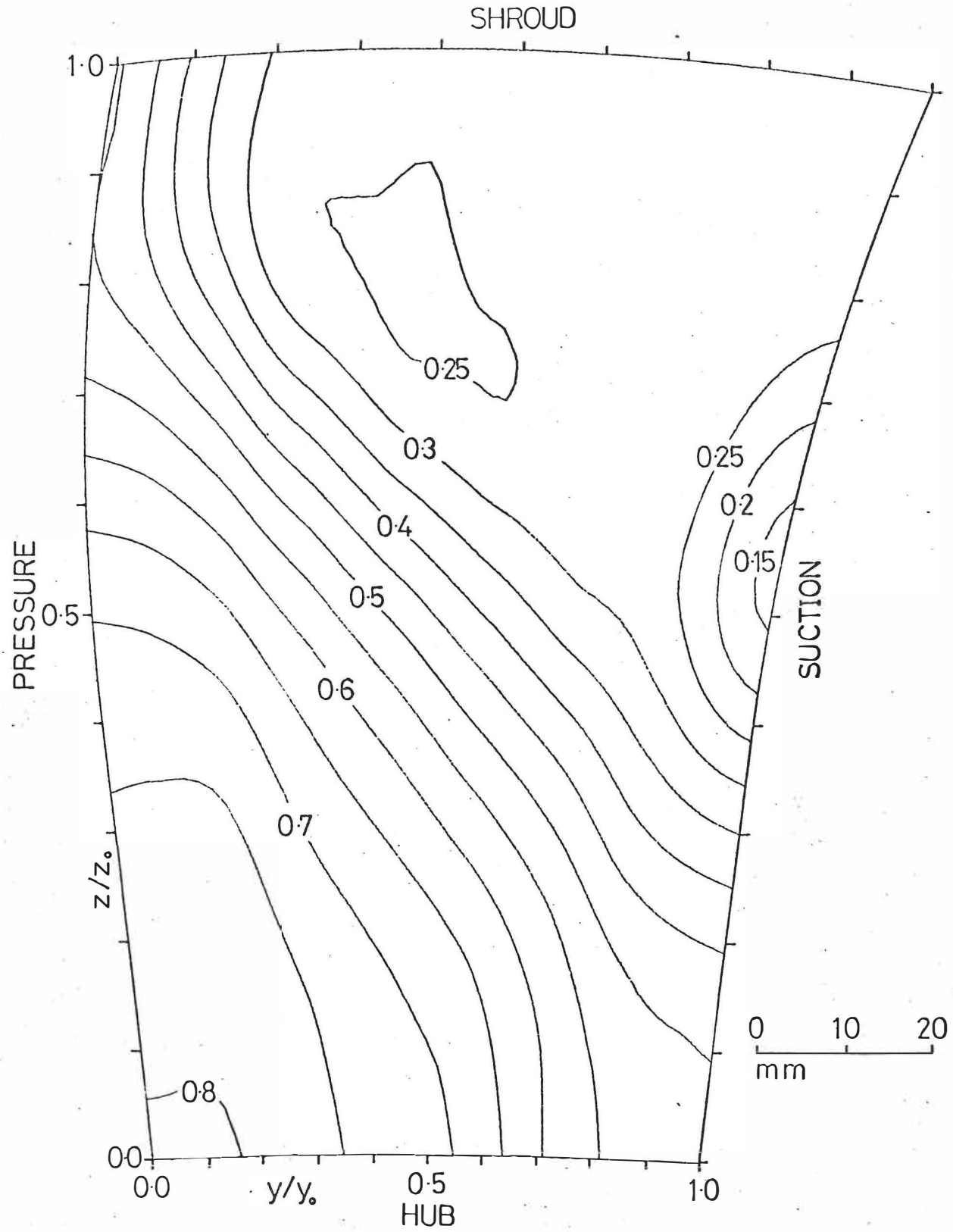

Figure 4.10 'Below design' flow. Station 3. Dimensionless reduced static pressure P_r.

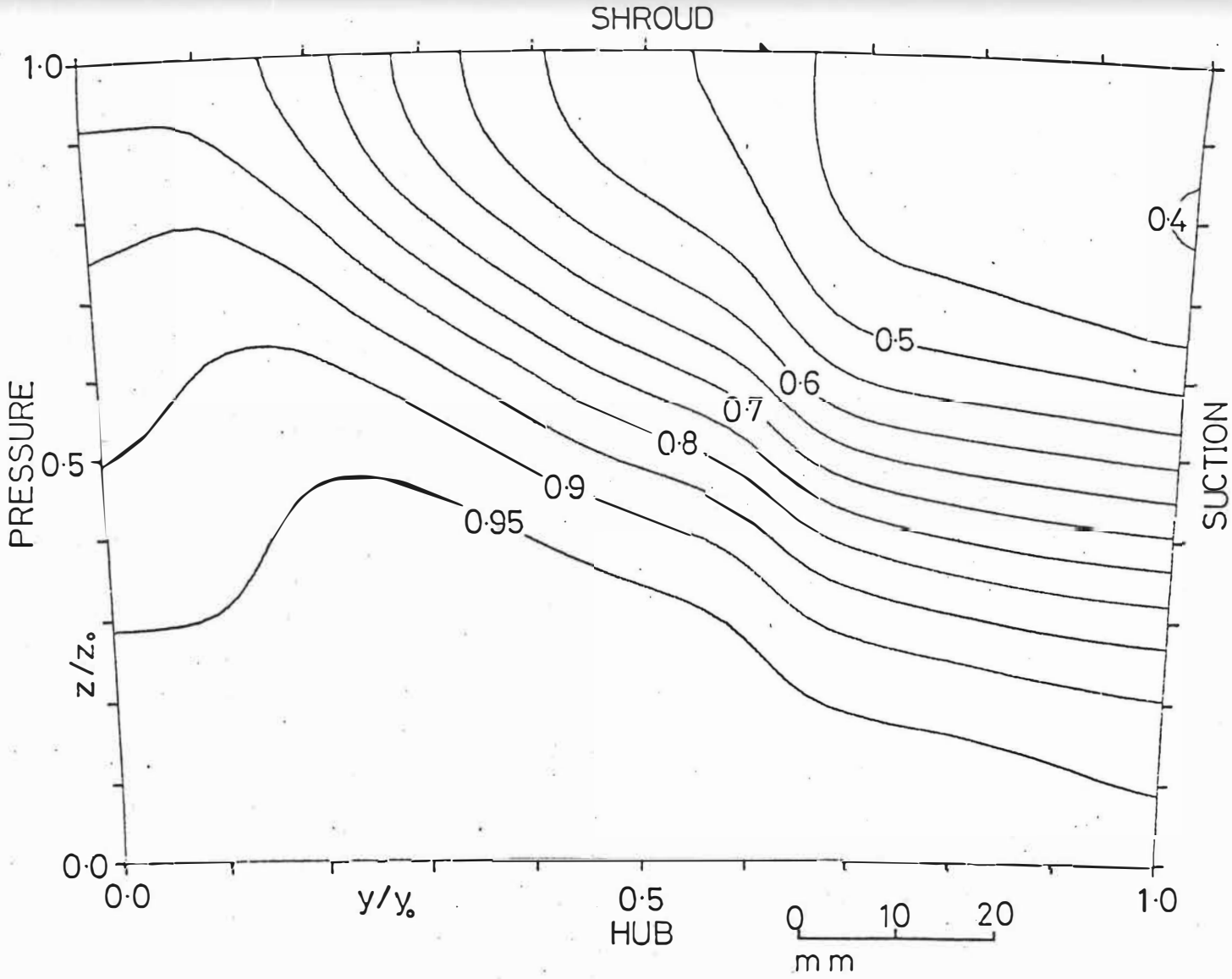

Figure 4.11 'Below design' flow. Station 4. Dimensionless rotary stagnation pressure P*.

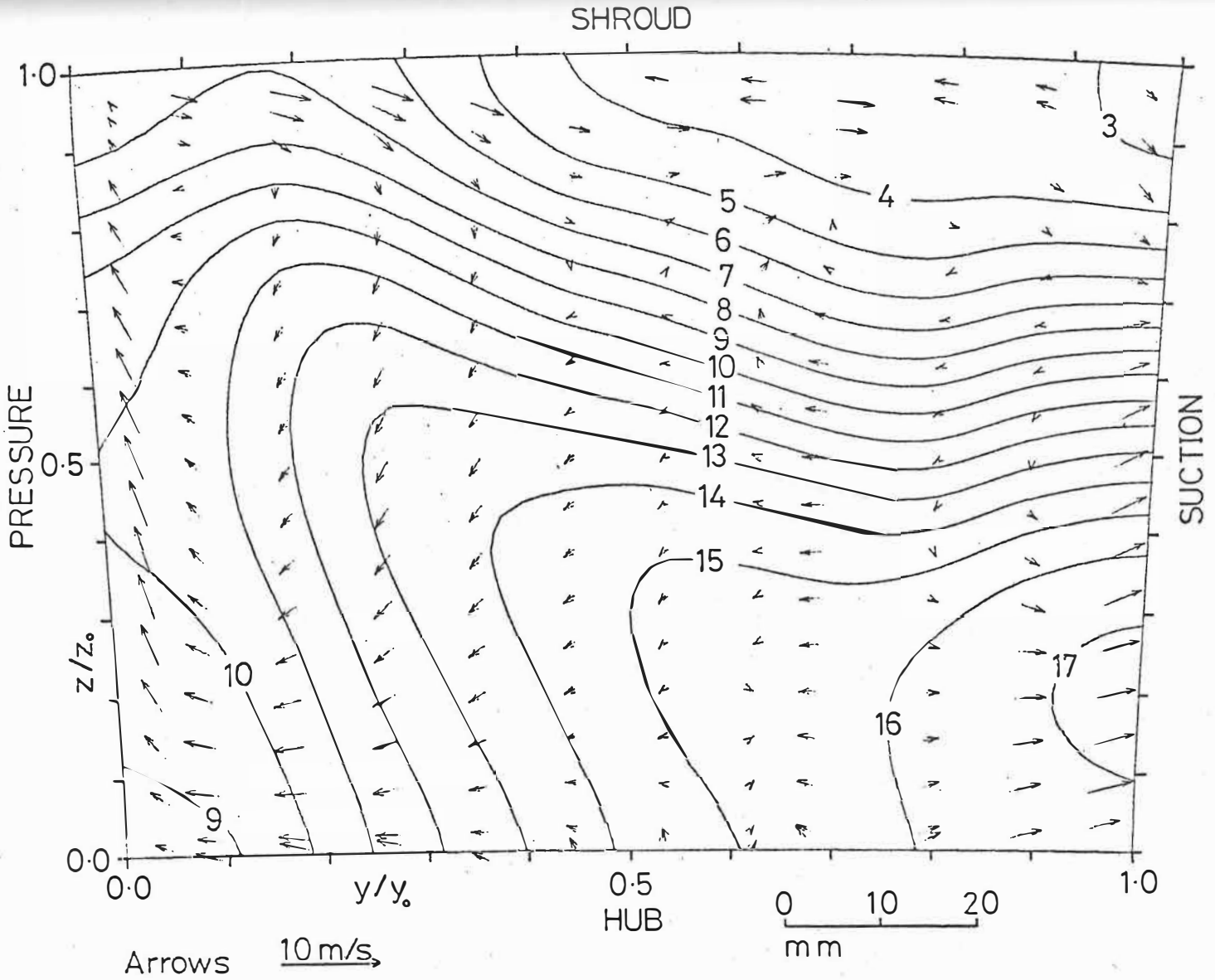

Figure 4.12 'Below design' flow. Station 4. Relative velocities - contours in m/s.

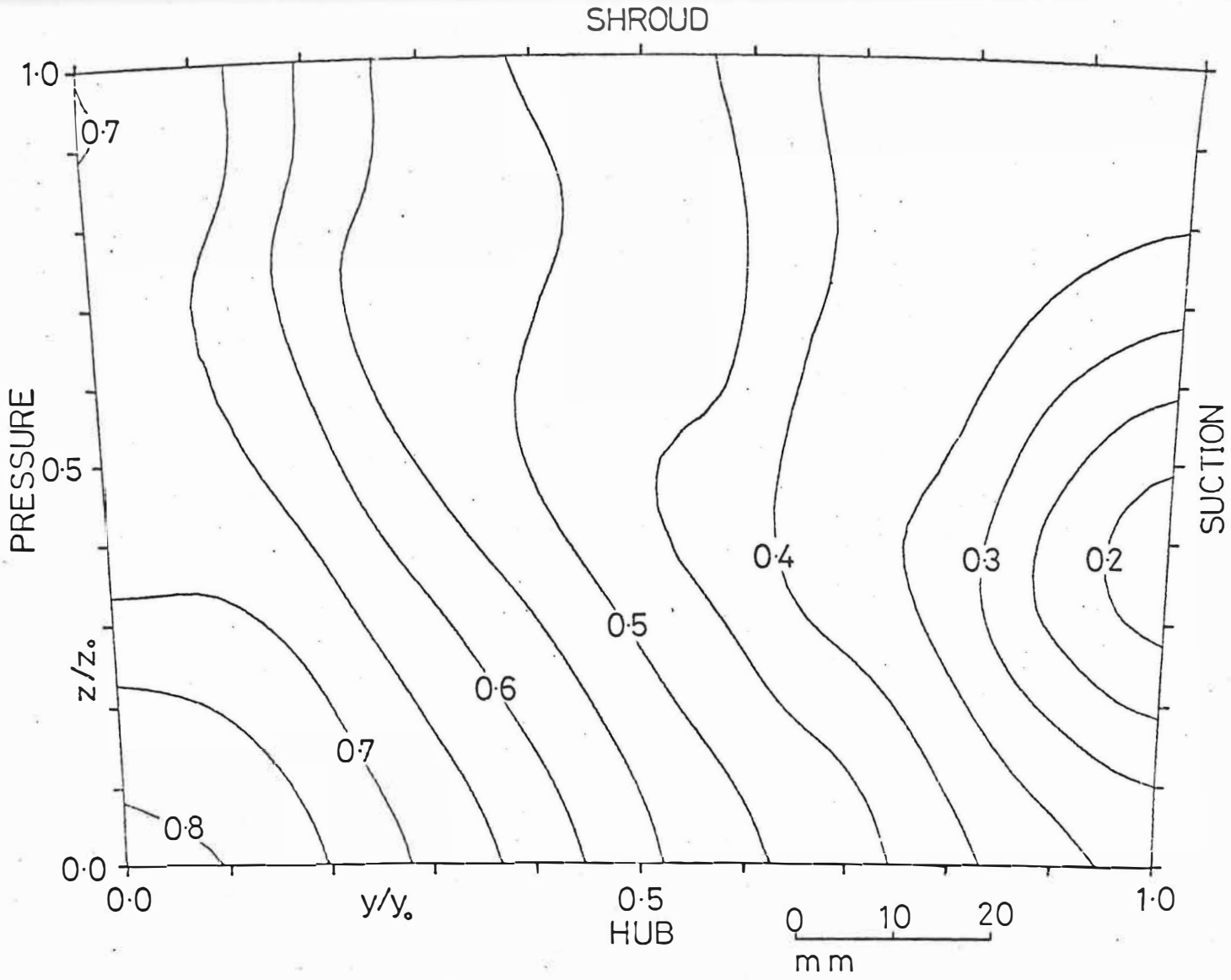

Figure 4.13 'Below design' flow. Station 4. Dimensionless reduced static pressure P_r.

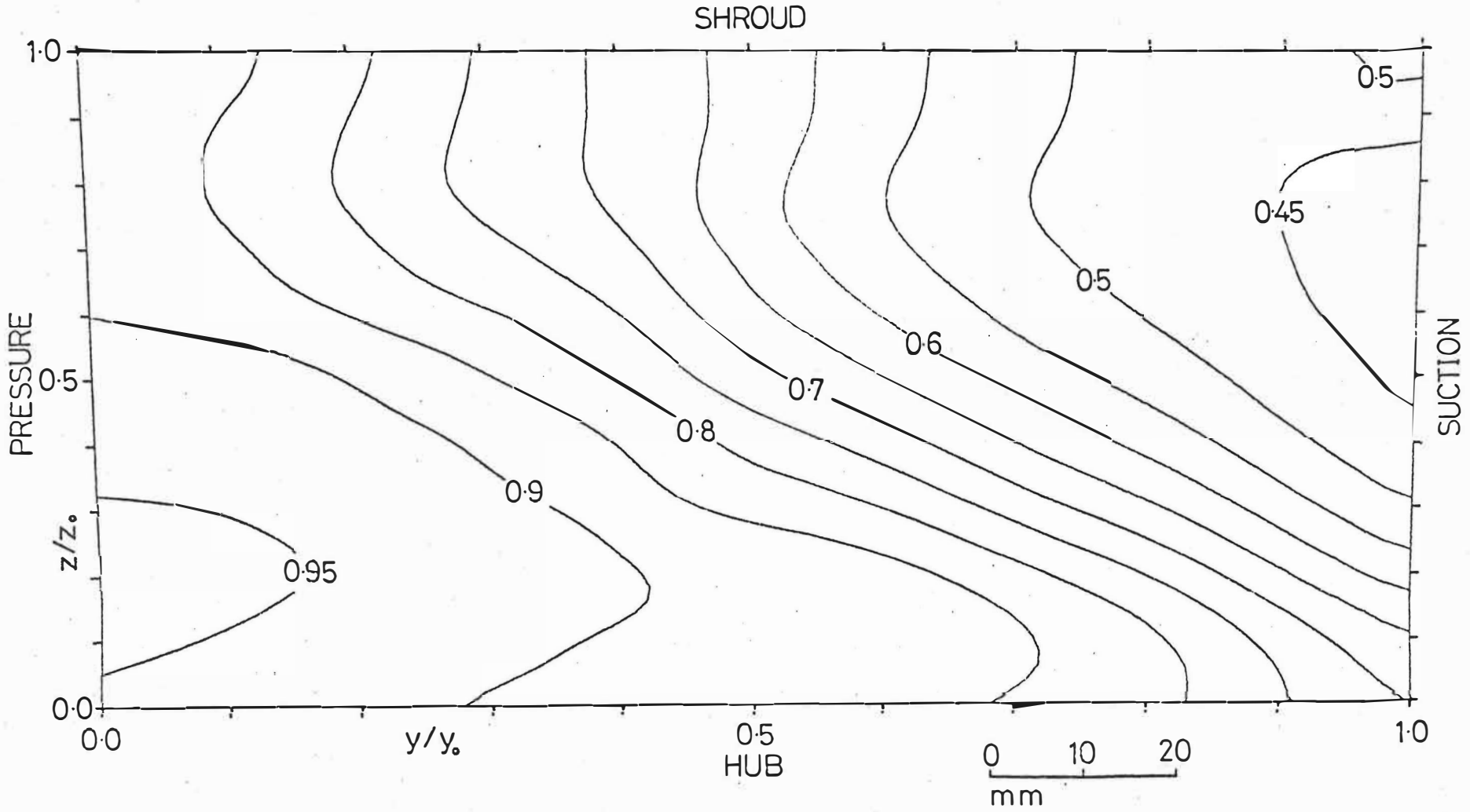

Figure 4.14 'Below design' flow. Station 5. Dimensionless rotary stagnation pressure P*.

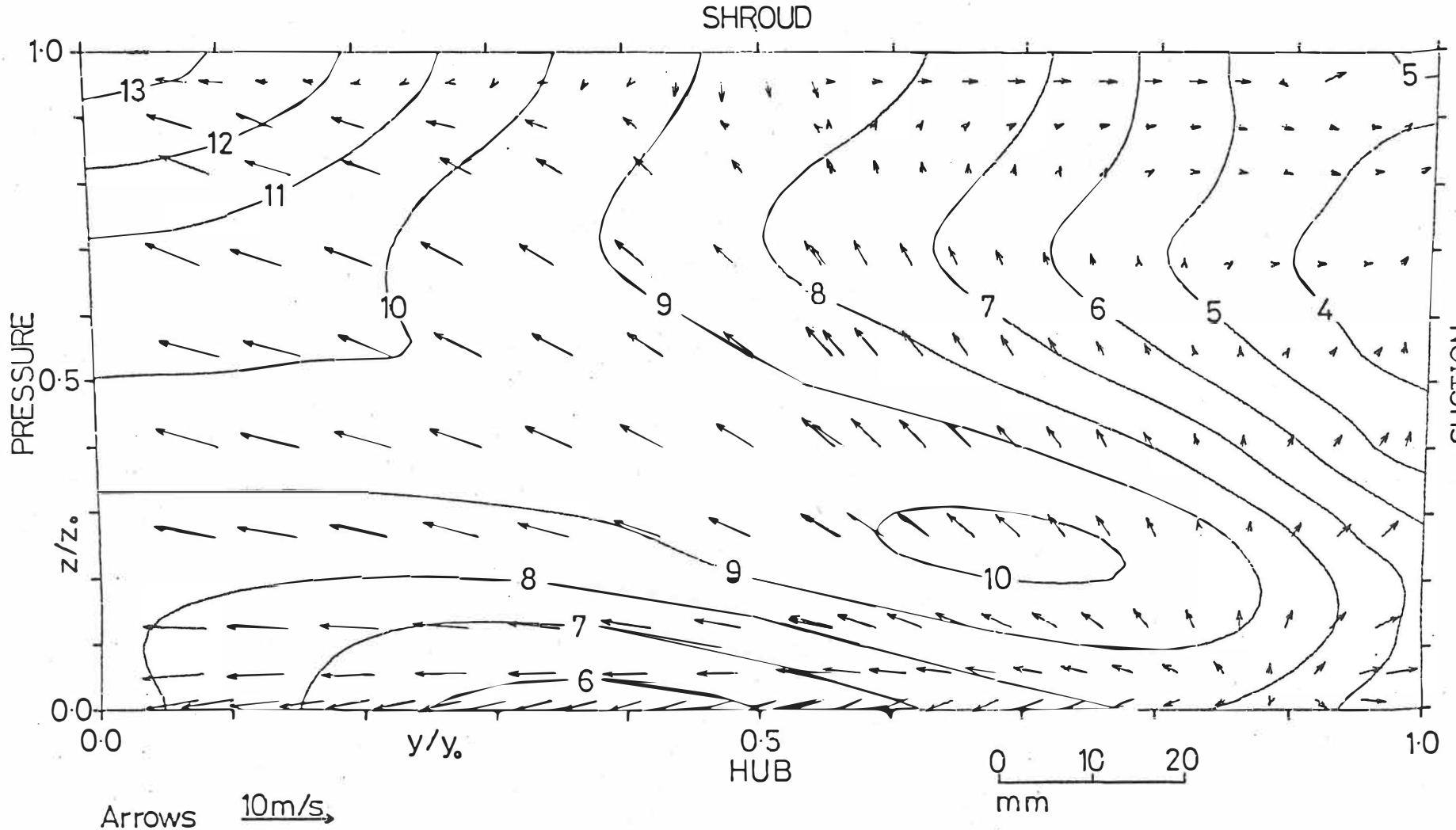

Figure 4.15 'Below design' flow. Station 5. Relative velocities - contours in m/s.

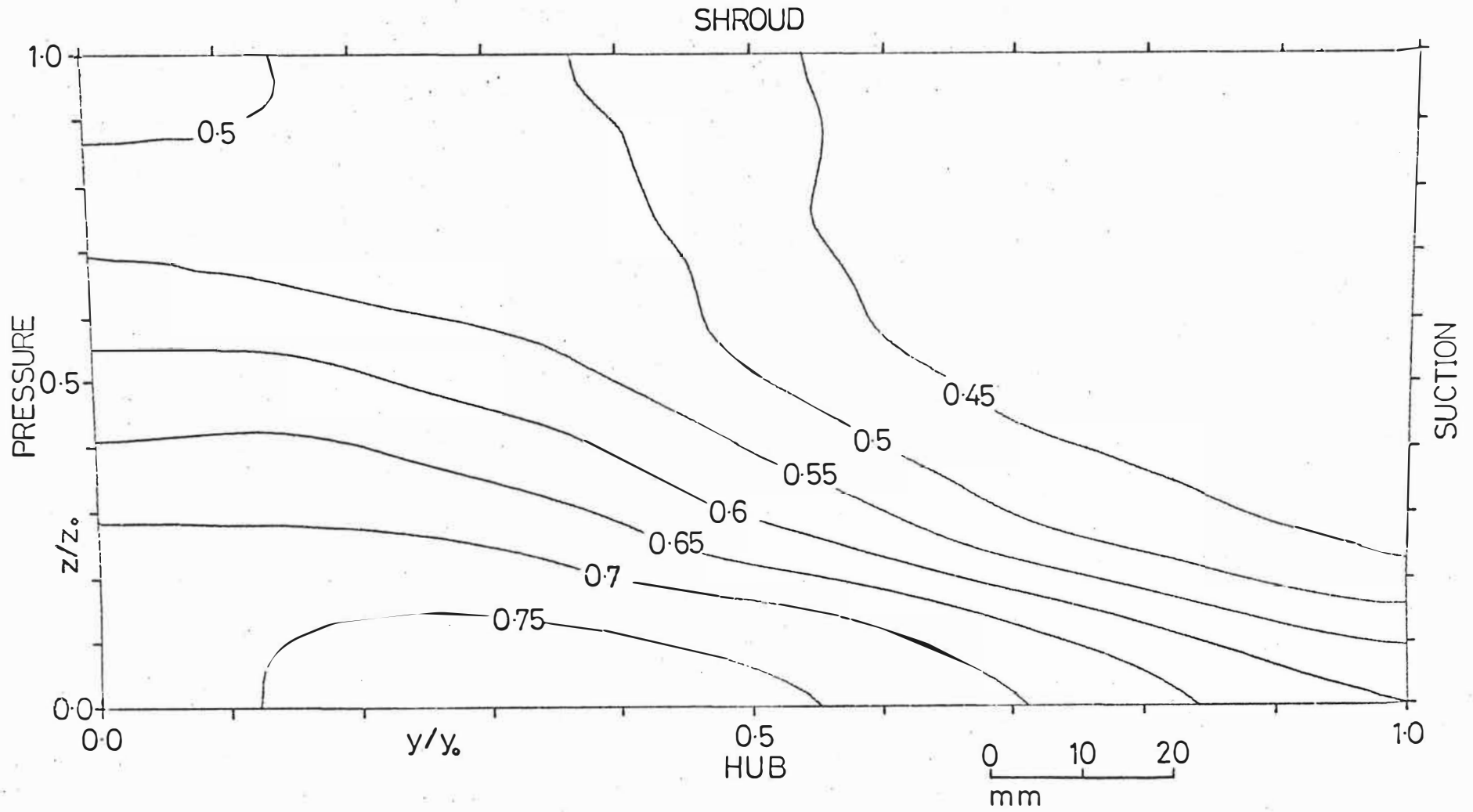

Figure 4.16 'Below design' flow. Station 5. Dimensionless reduced static pressure P_r.

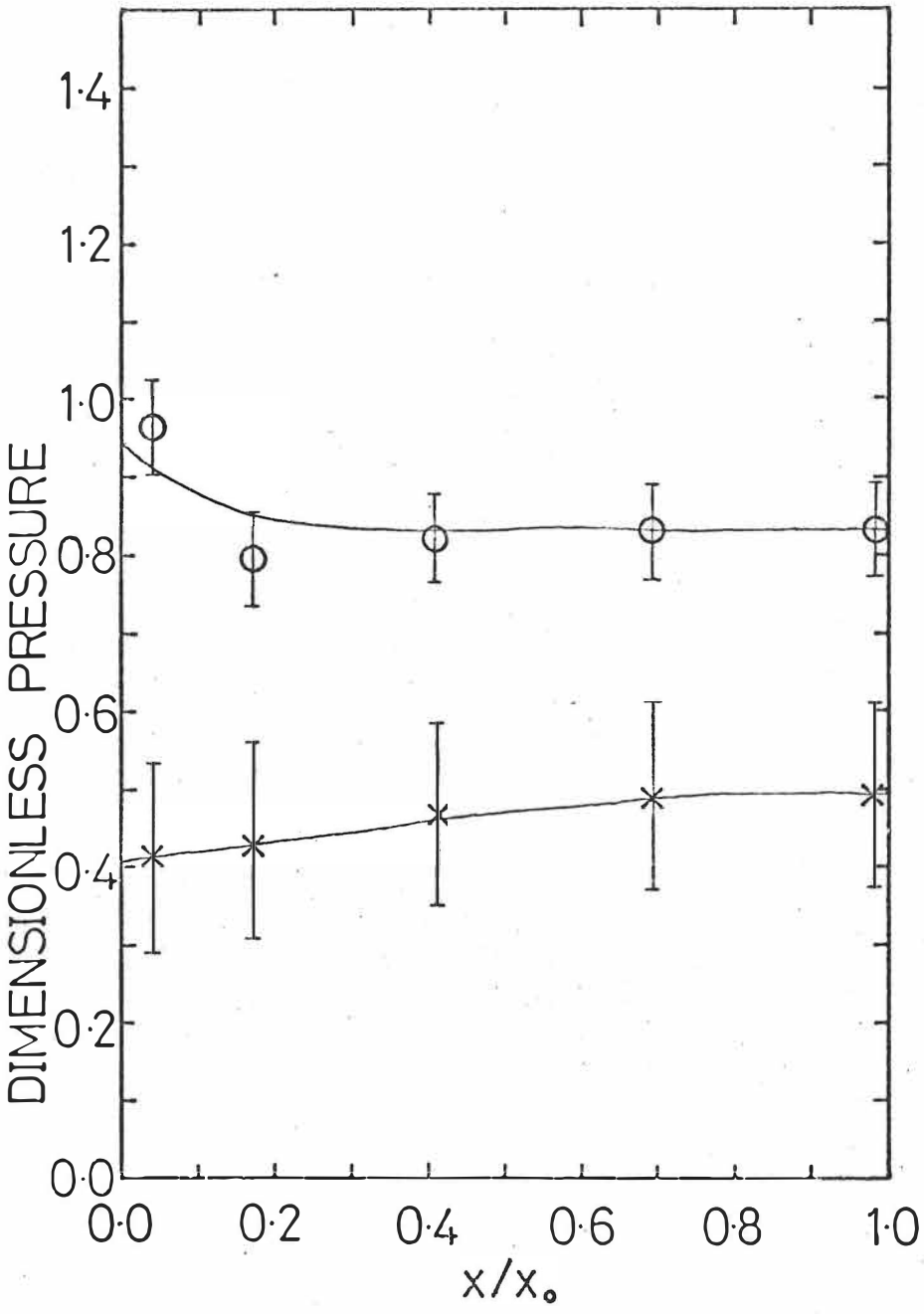

× P_r – Dimensionless Reduced Static Pressure

o P^* – Dimensionless Rotary Stagnation Pressure

Figure 4.17 'Below design' flow. Mass-averaged dimensionless pressures.

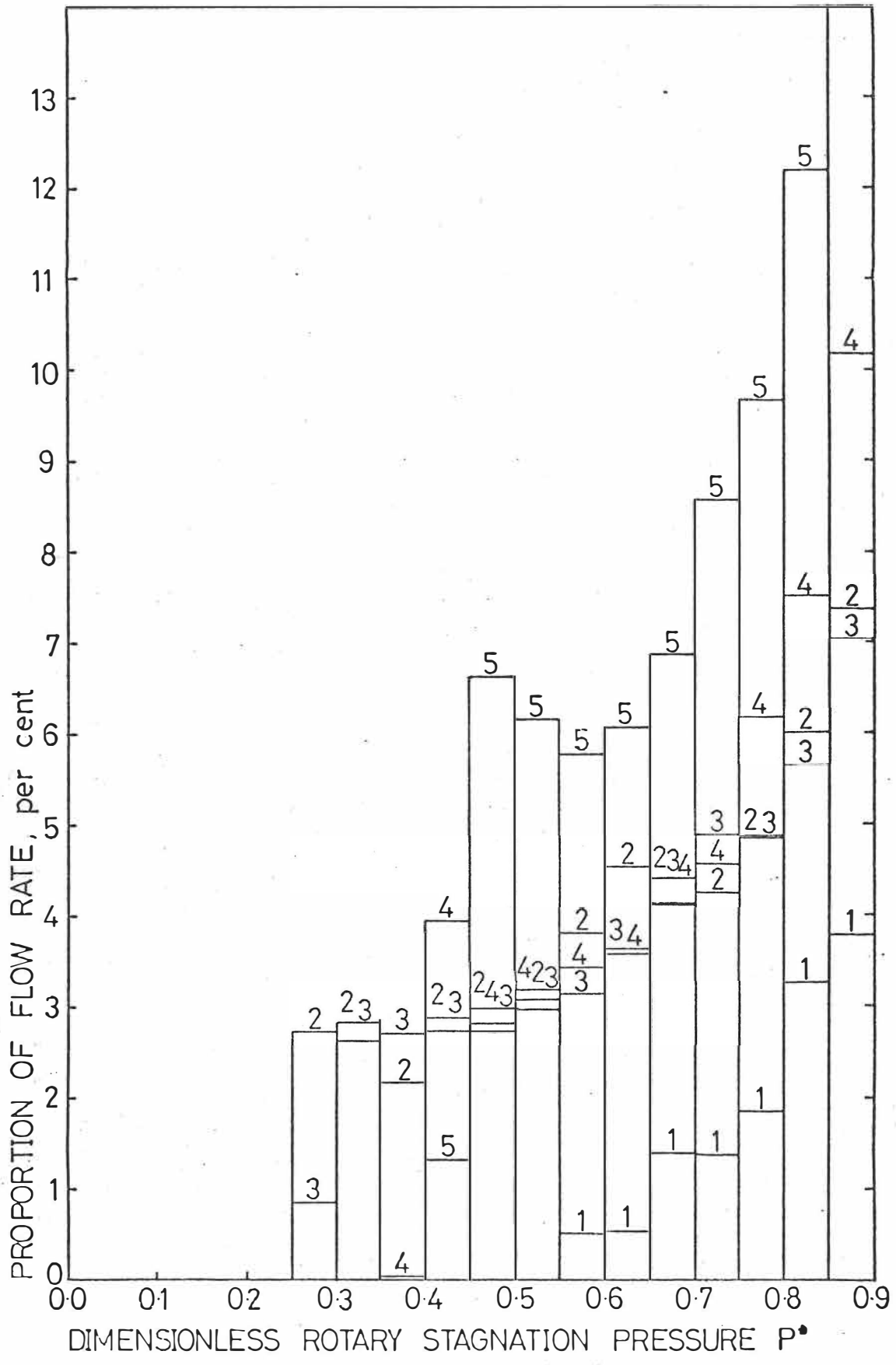

Figure 4.18 'Below design' flow. Distribution of dimensionless rotary stagnation pressure P*.

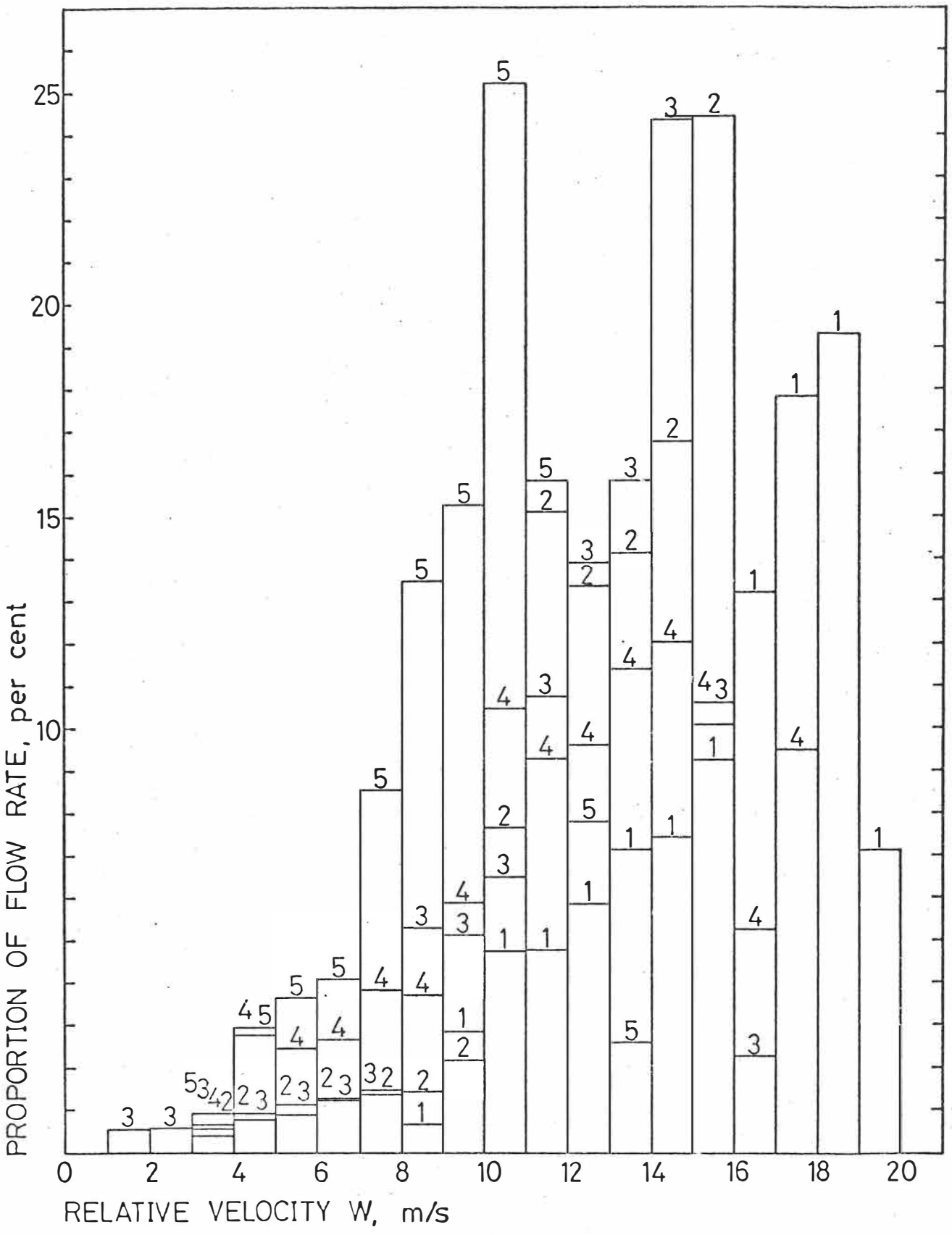

Figure 4.19 'Below design' flow. Distribution of relative velocity.

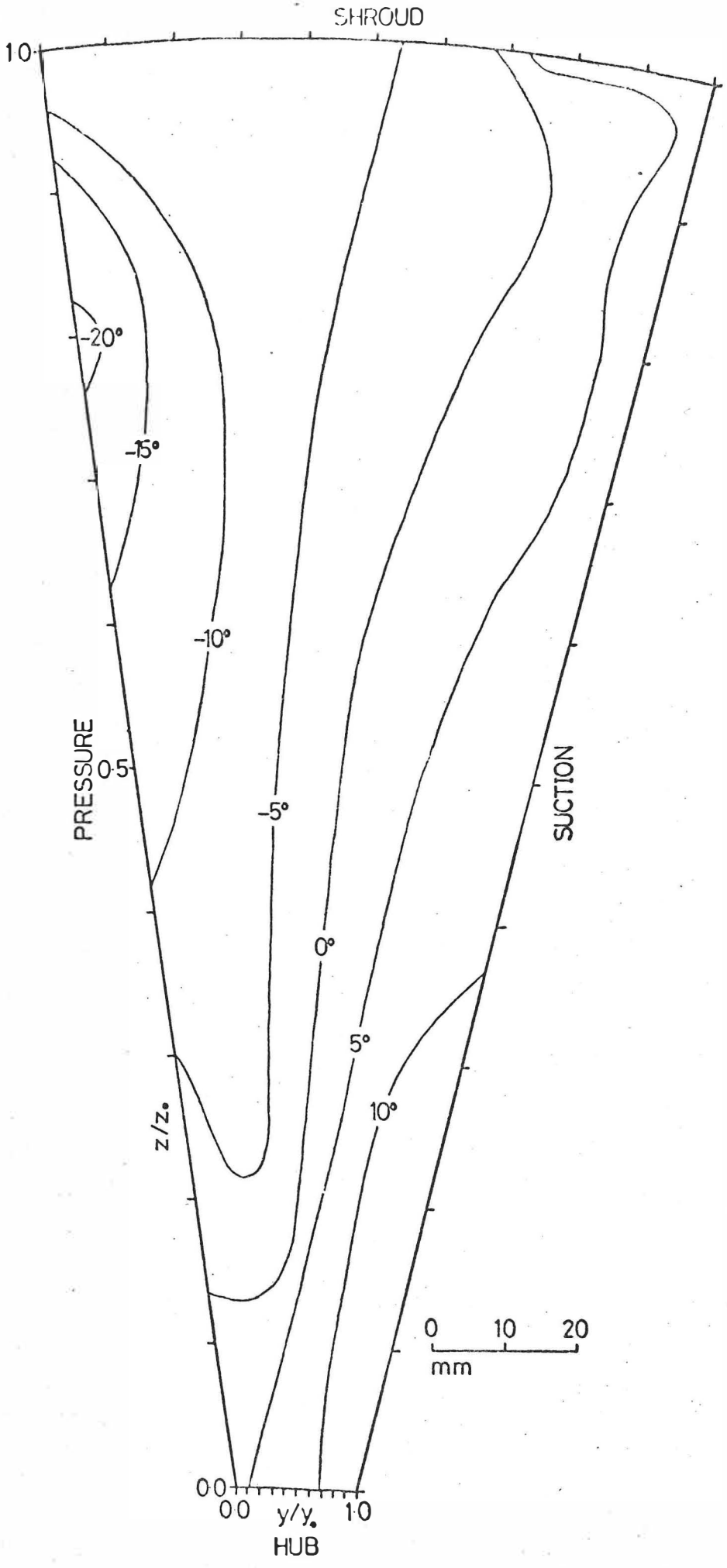

Figure 4.20 'Above design' flow. Station 1. Incidence angles at impeller inlet.

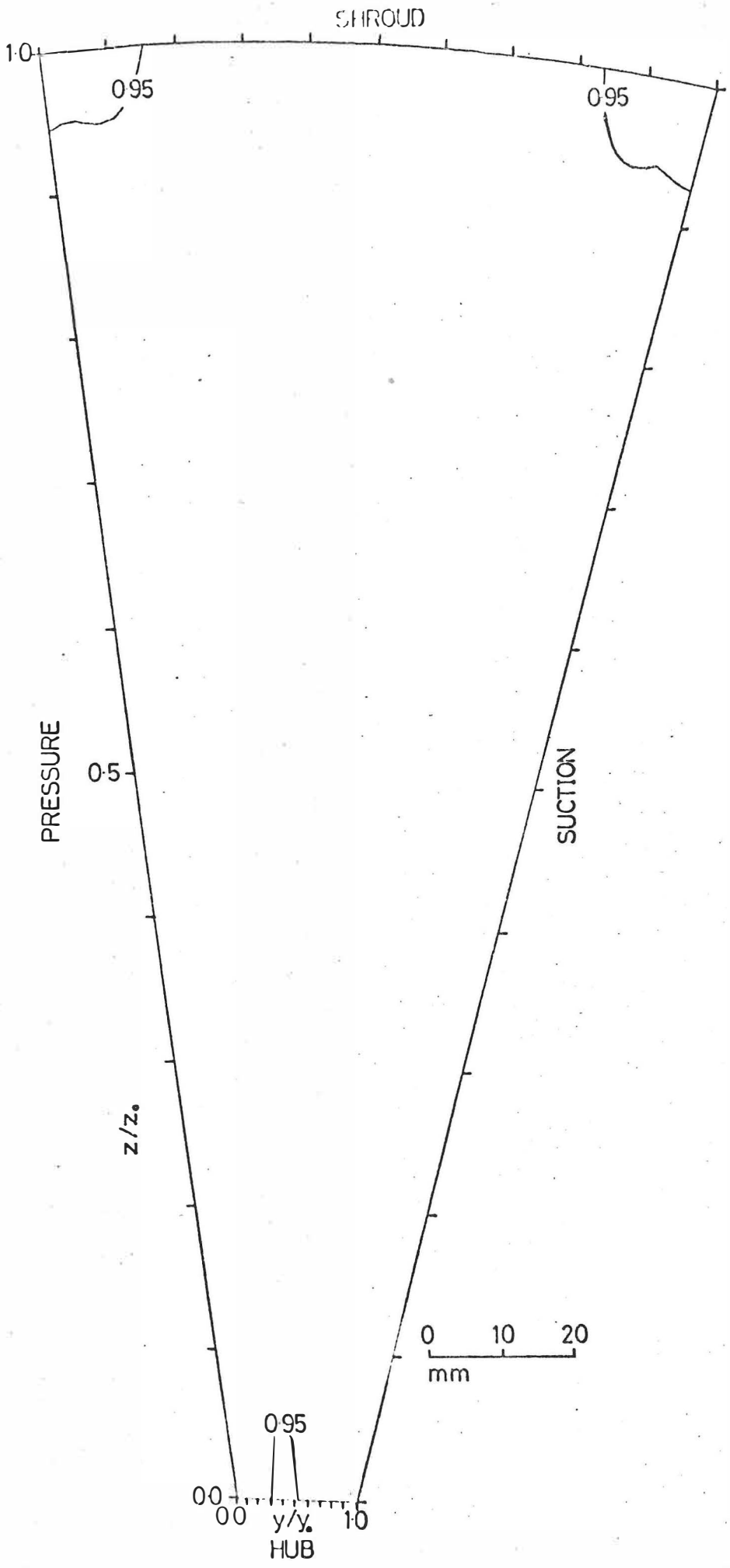

Figure 4.21 'Above design' flow. Station 1. Dimensionless rotary stagnation pressure P*.

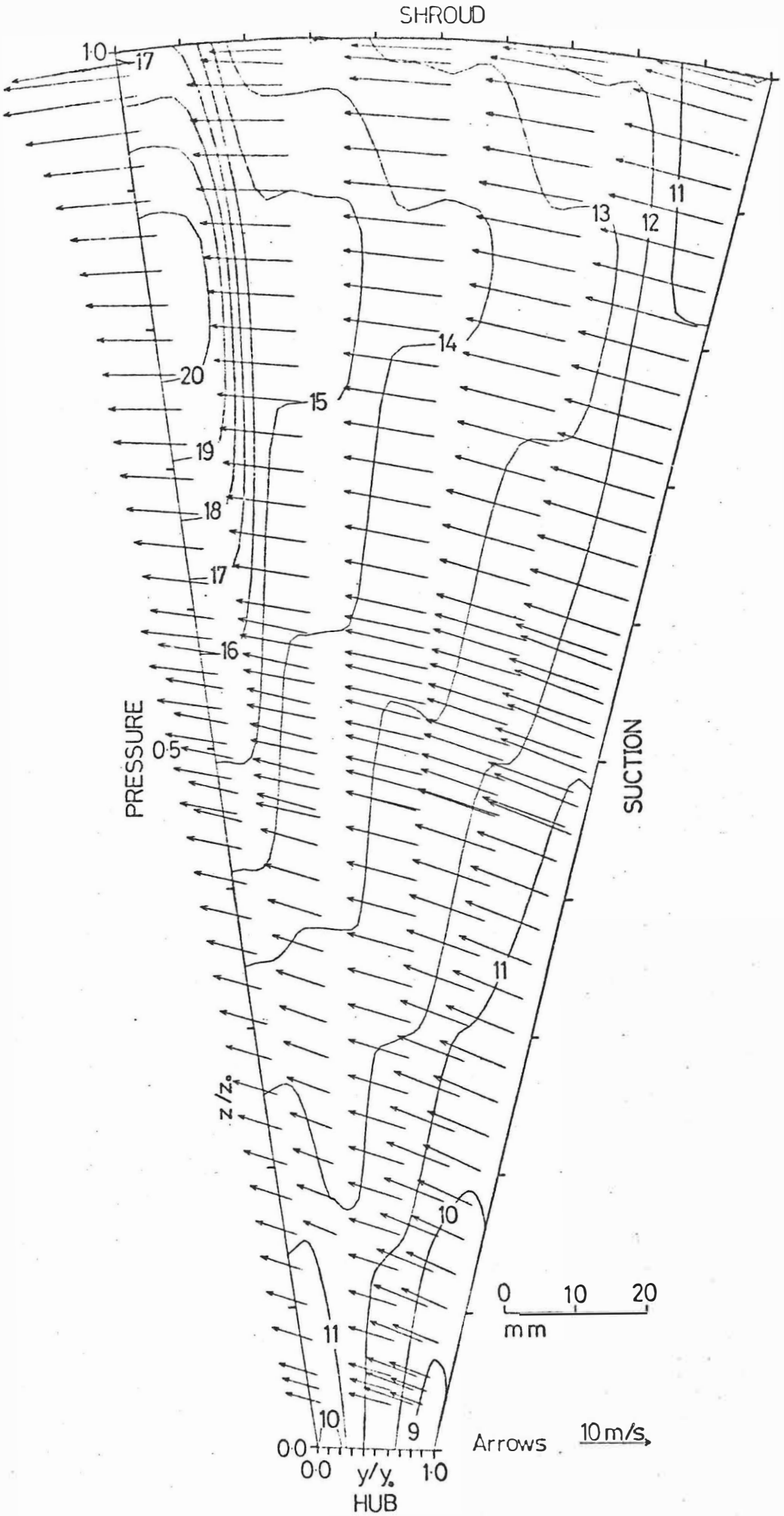

Figure 4.22 'Above design' flow. Station 1. Relative velocities contours in m/s.

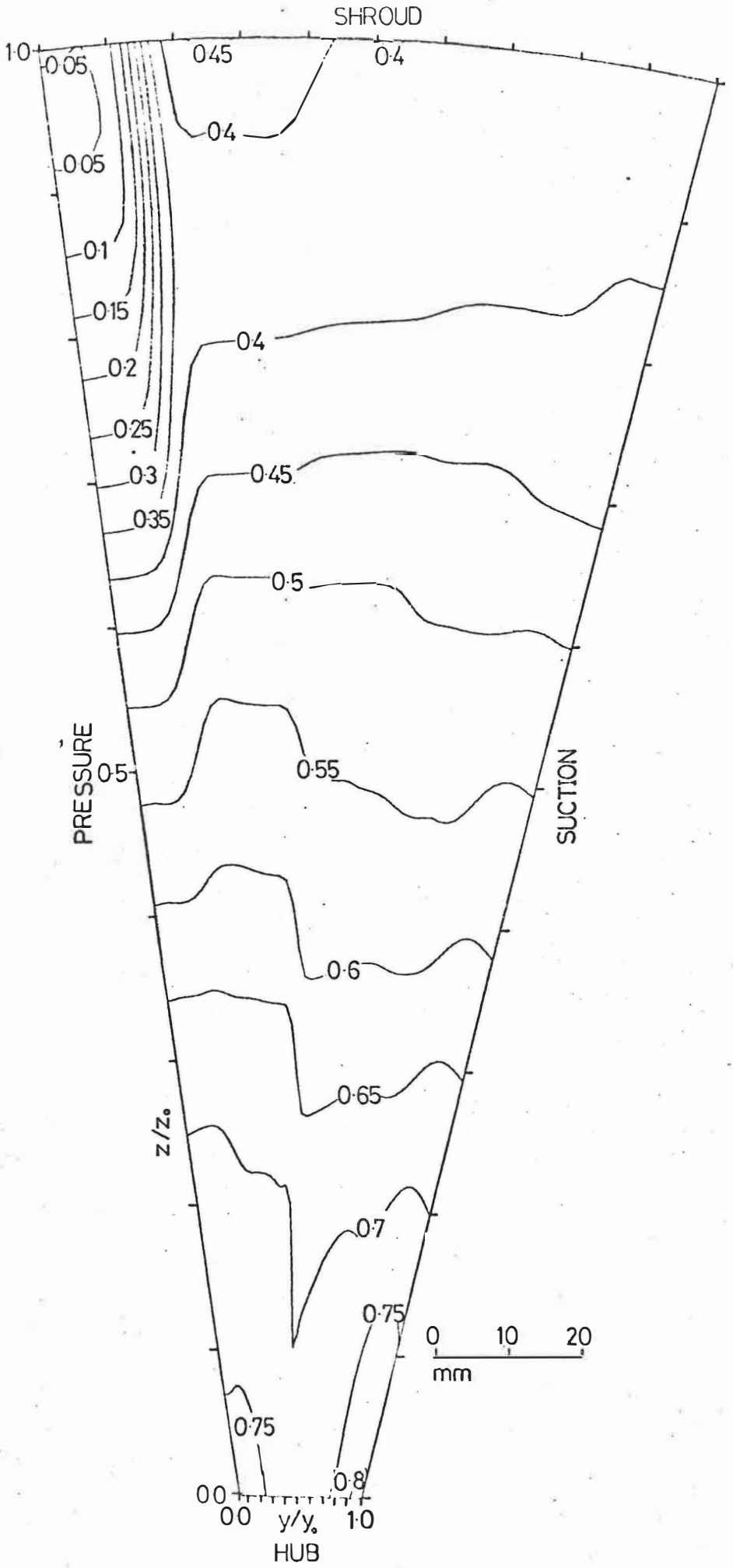

Figure 4.23 'Above design' flow. Station 1. Dimensionless reduced static pressure P_r.

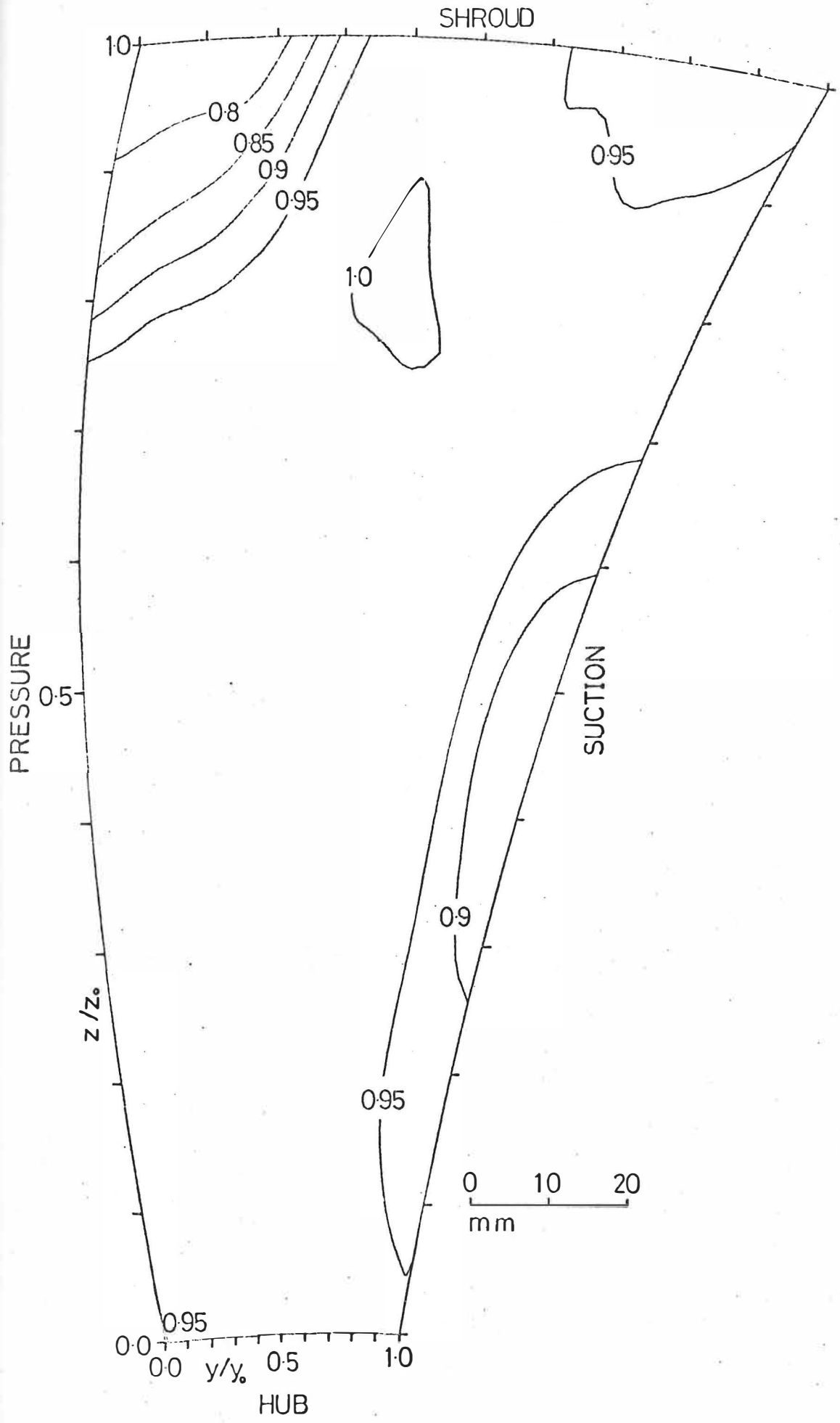

Figure 4.24 'Above design' flow. Station 2. Dimensionless rotary stagnation pressure P*.

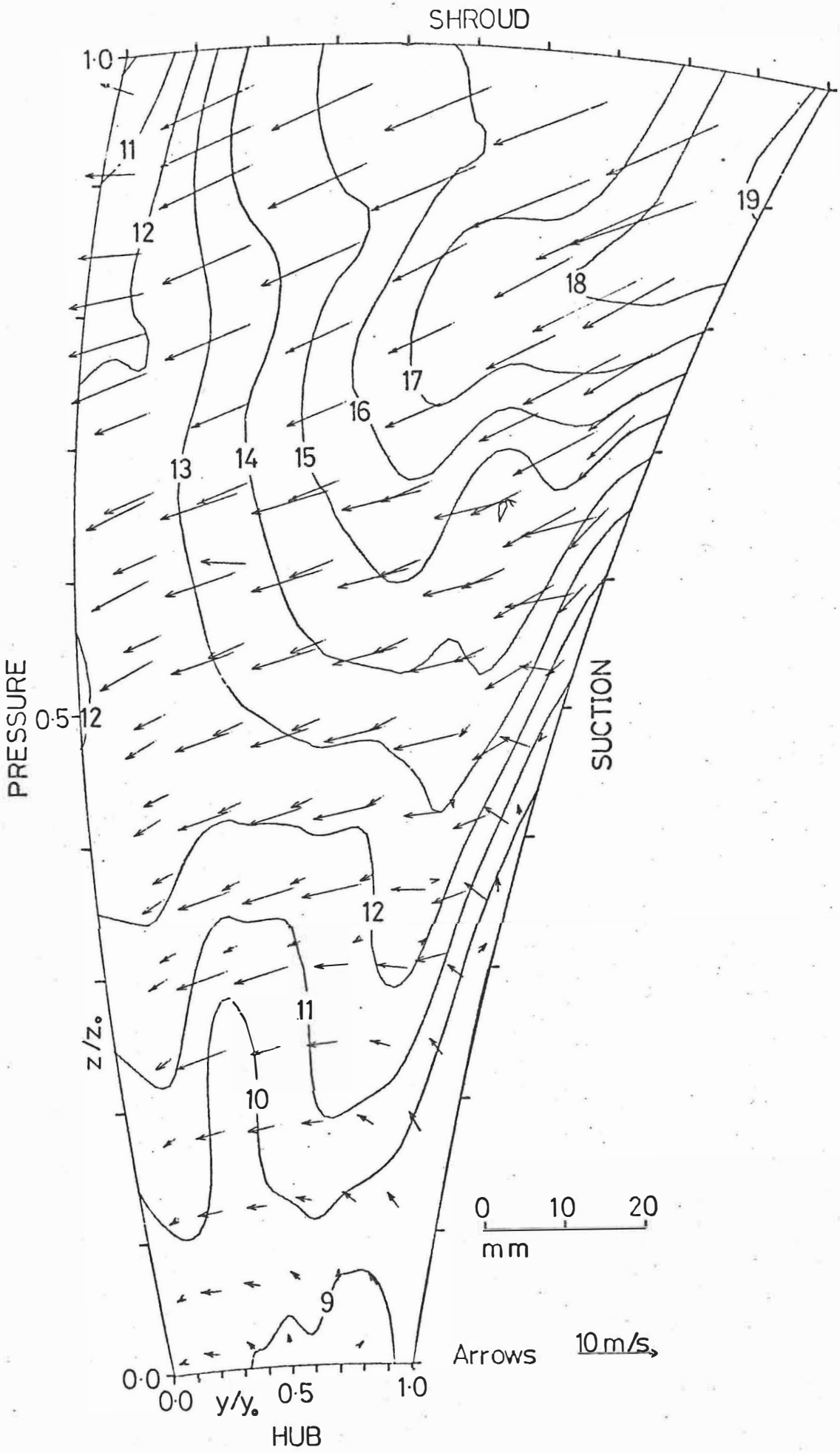

Figure 4.25 'Above design' flow. Station 2. Relative velocities contours in m/s.

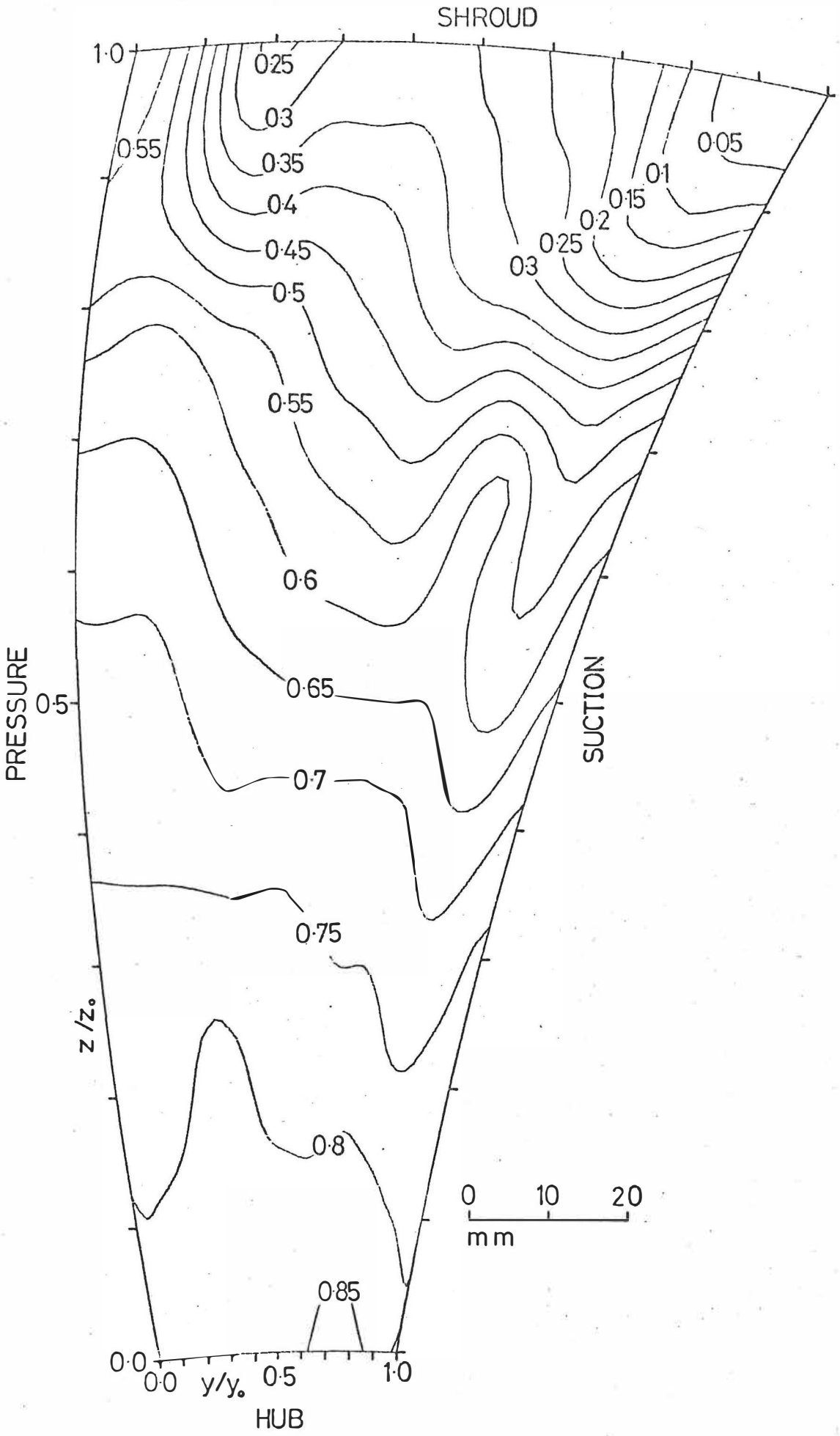

Figure 4.26 'Above design' flow. Station 2. Dimensionless reduced static pressure P_r.

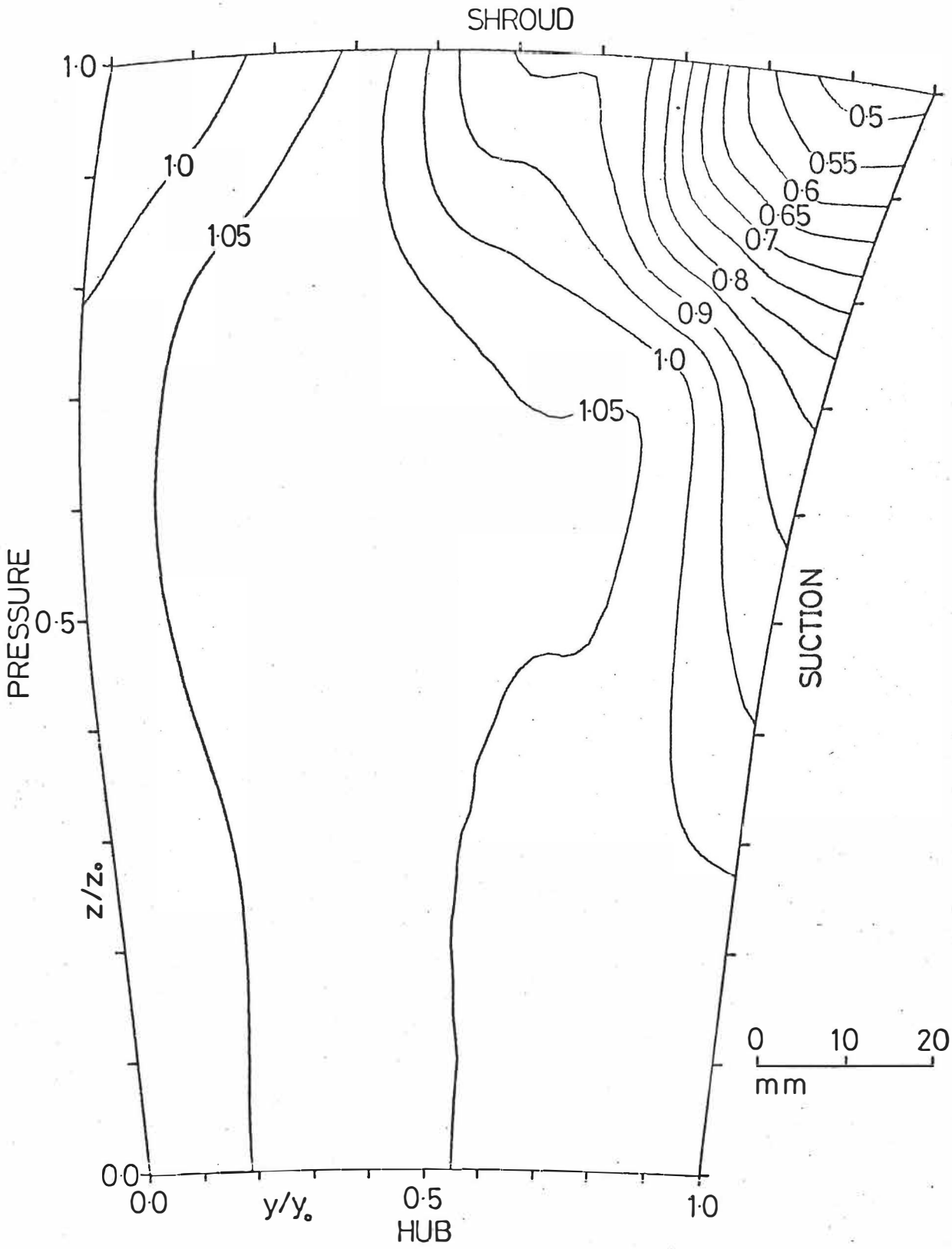

Figure 4.27 'Above design' flow. Station 3. Dimensionless rotary stagnation pressure P*.

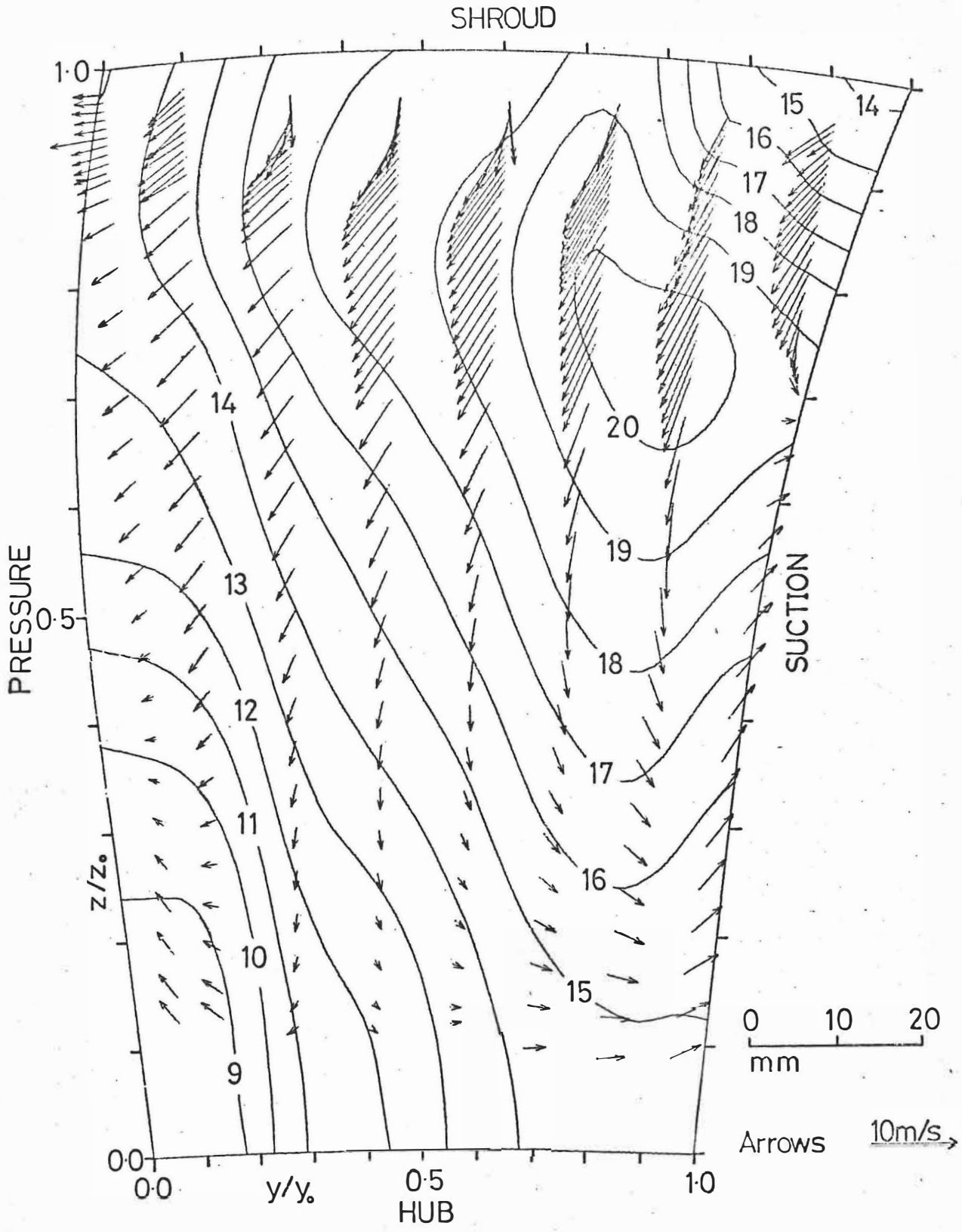

Figure 4.28 'Above design' flow. Station 3. Relative velocities contours in m/s.

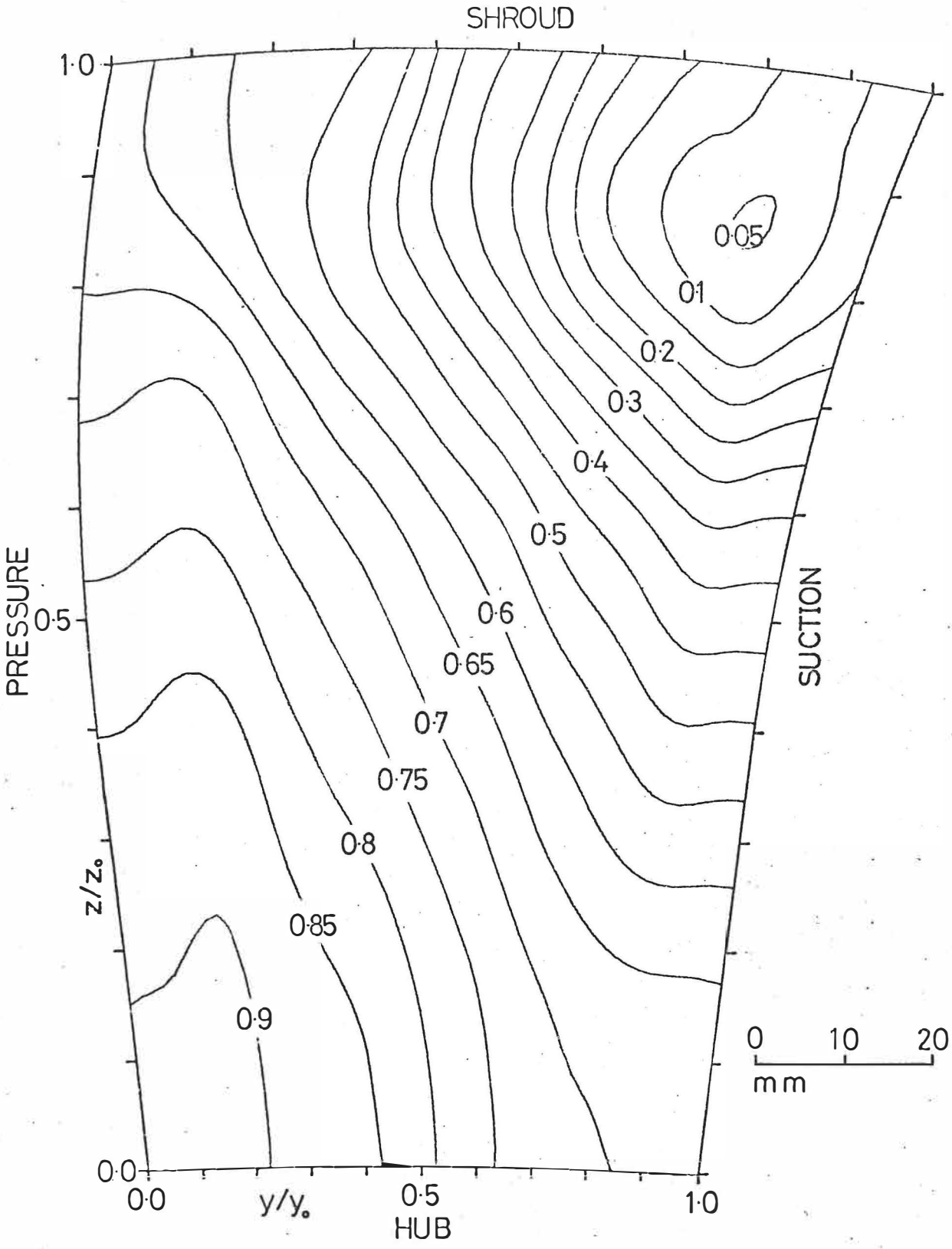

Figure 4.29 'Above design' flow. Station 3. Dimensionless reduced static pressure P_r.

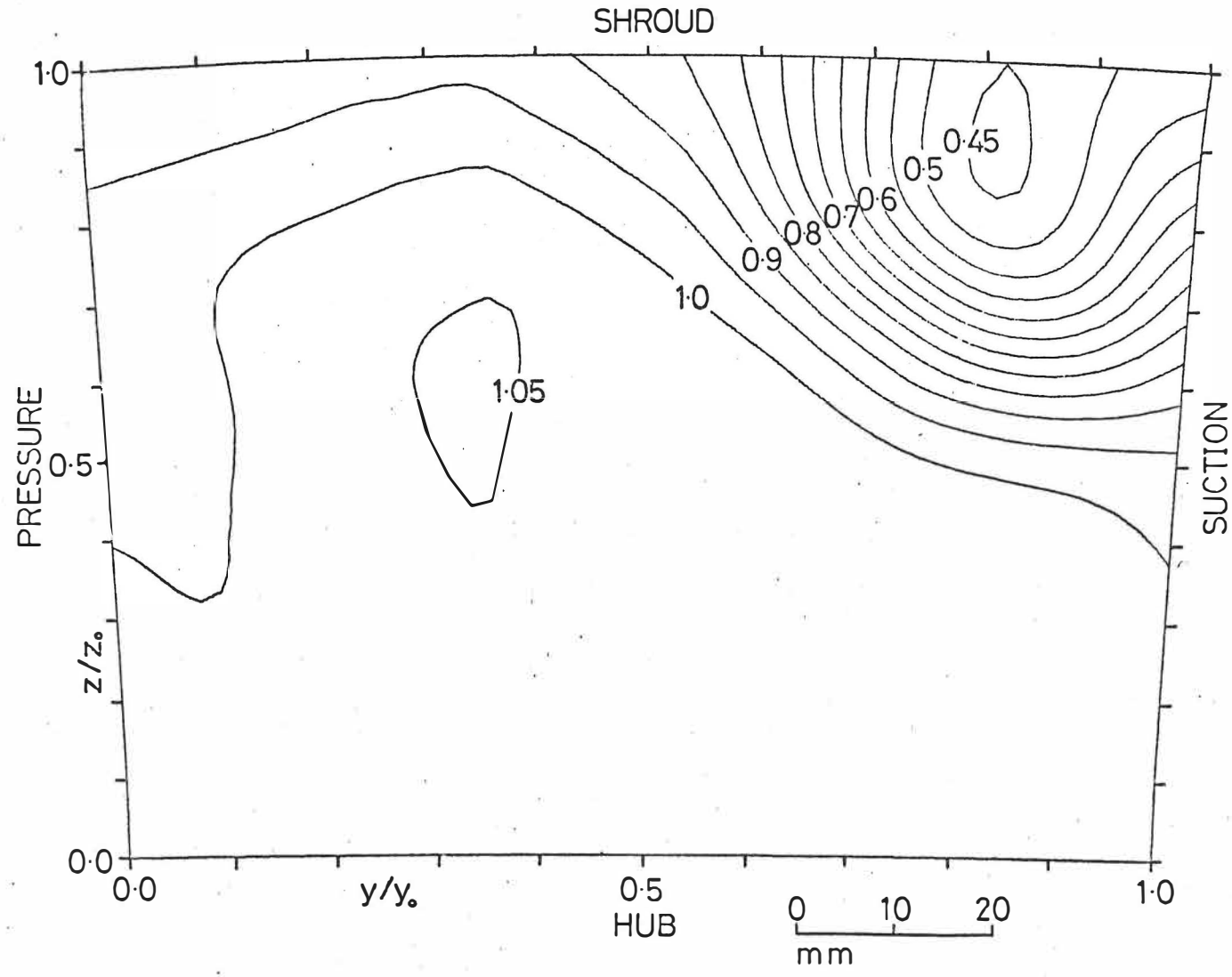

Figure 4.30 'Above design' flow. Station 4. Dimensionless rotary stagnation pressure P*.

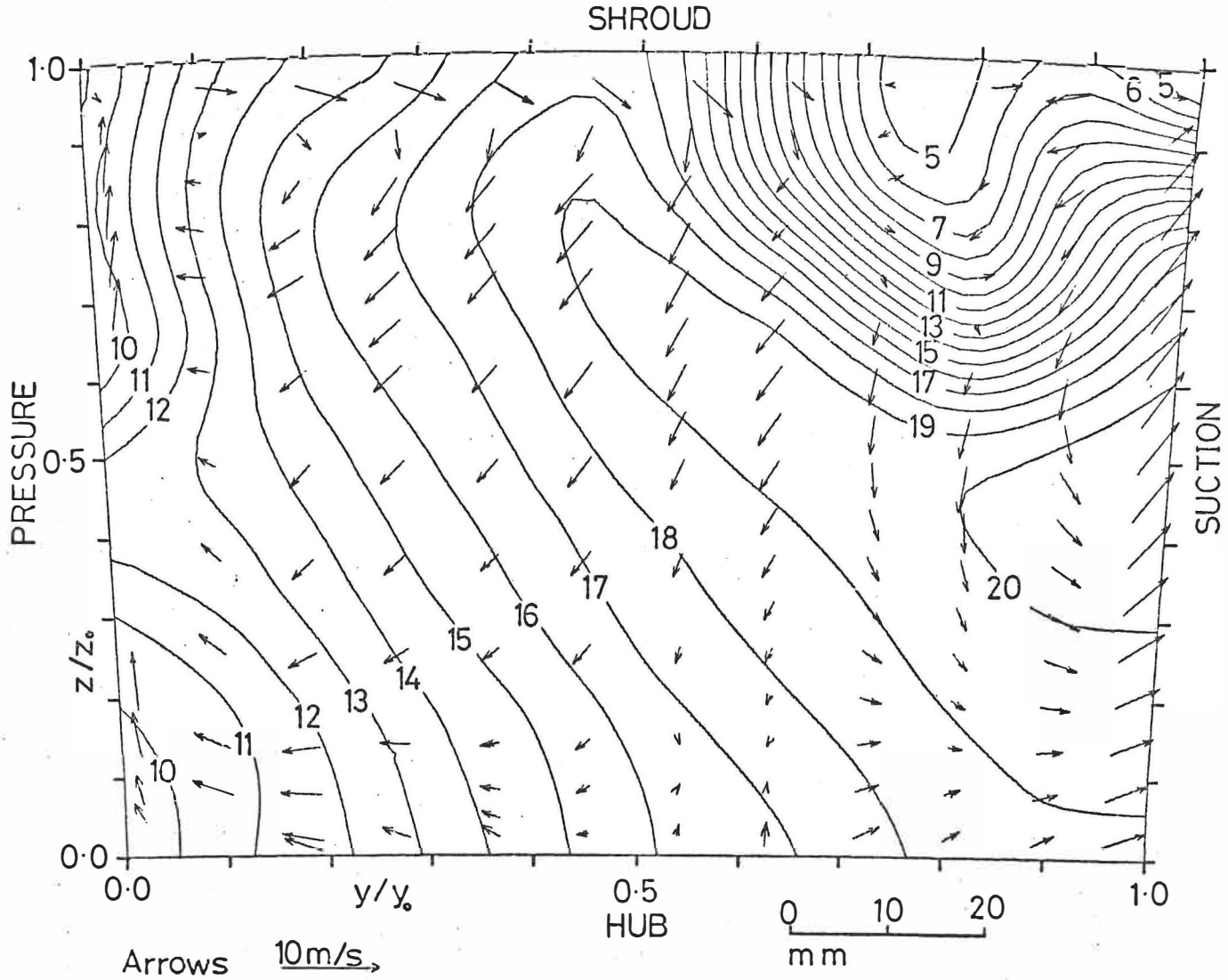

Figure 4.31 'Above design' flow. Station 4. Relative velocities - contours in m/s.

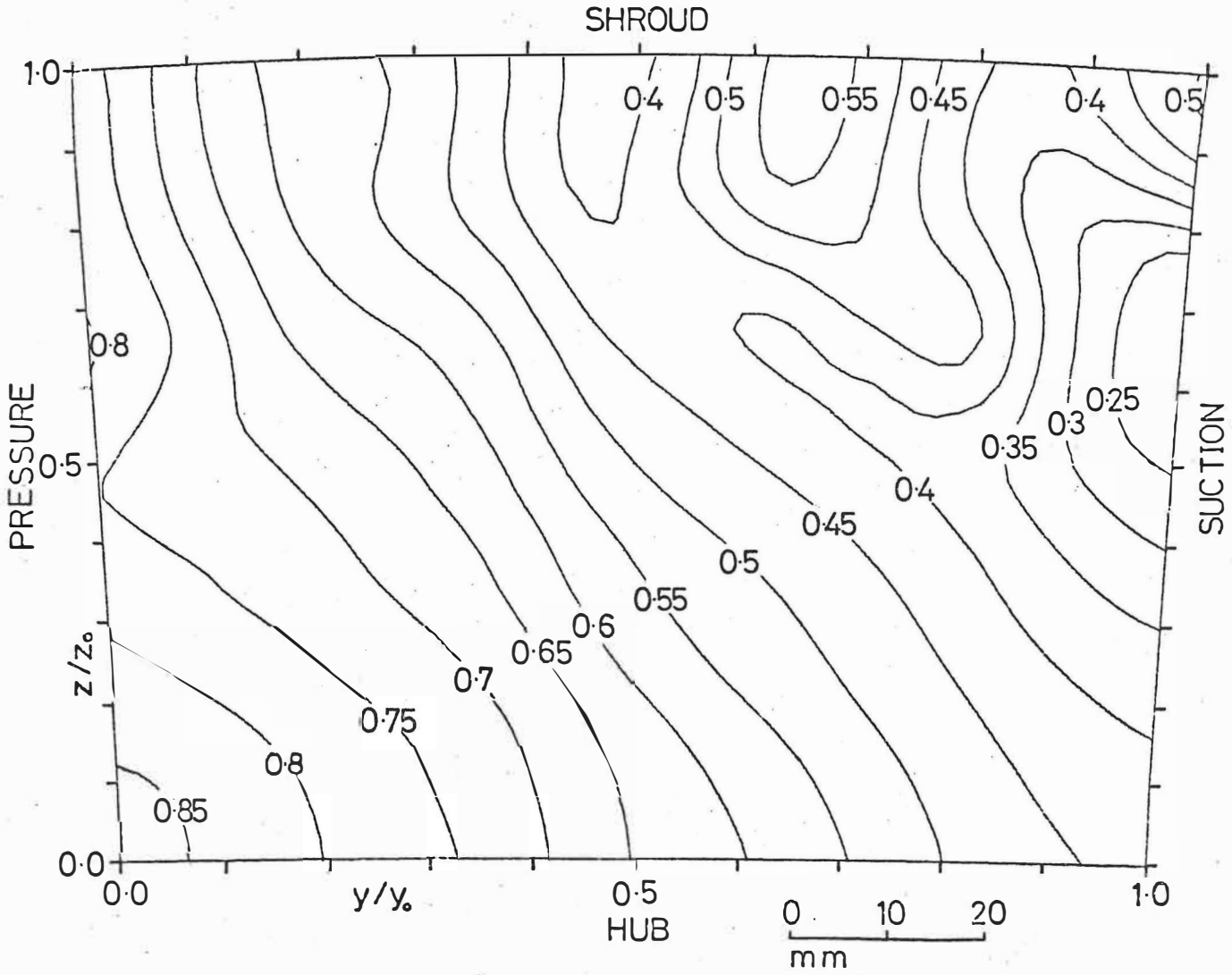

Figure 4.32 'Above design' flow. Station 4. Dimensionless reduced static pressure P_r.

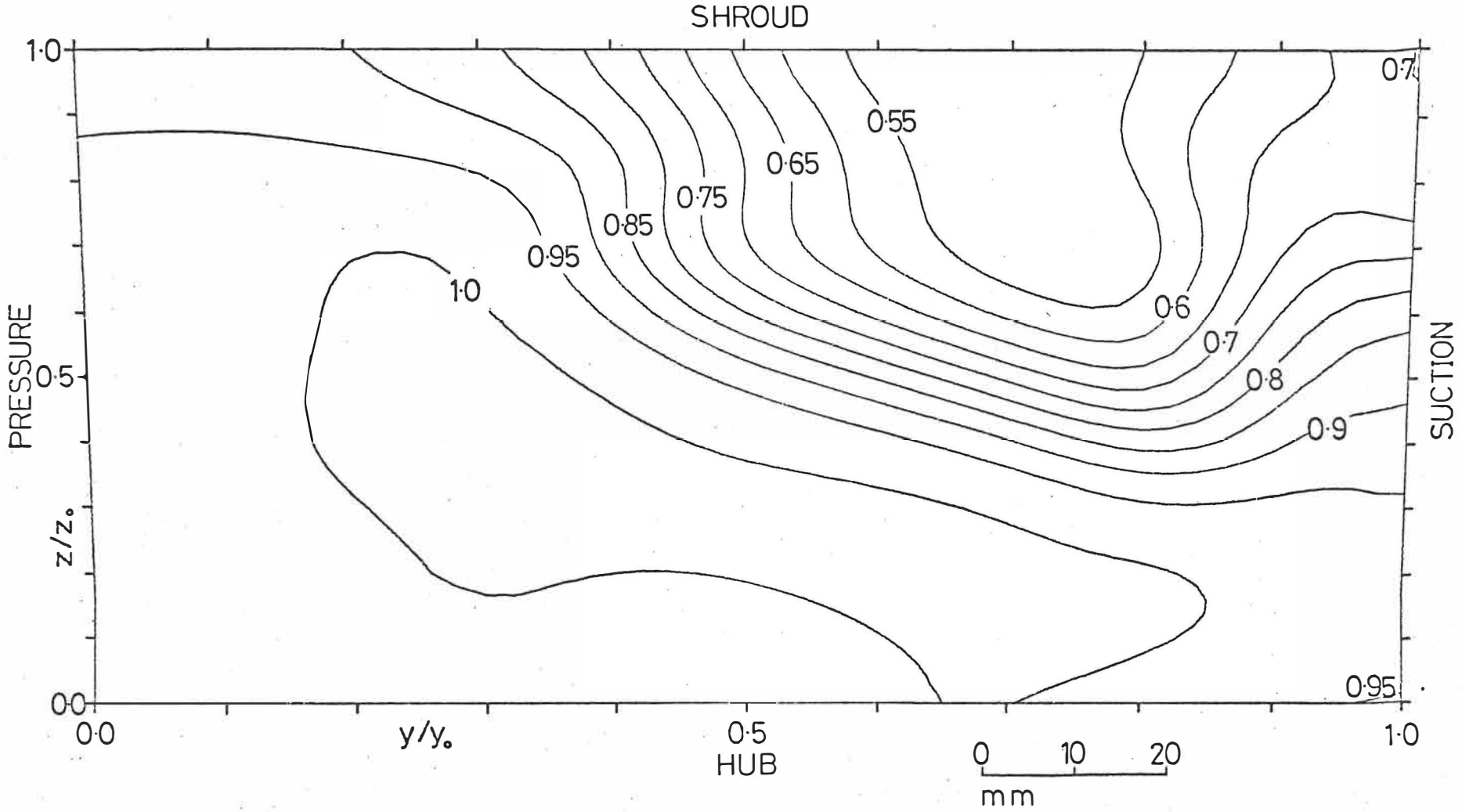

Figure 4.33 'Above design' flow. Station 5. Dimensionless rotary stagnation pressure P*.

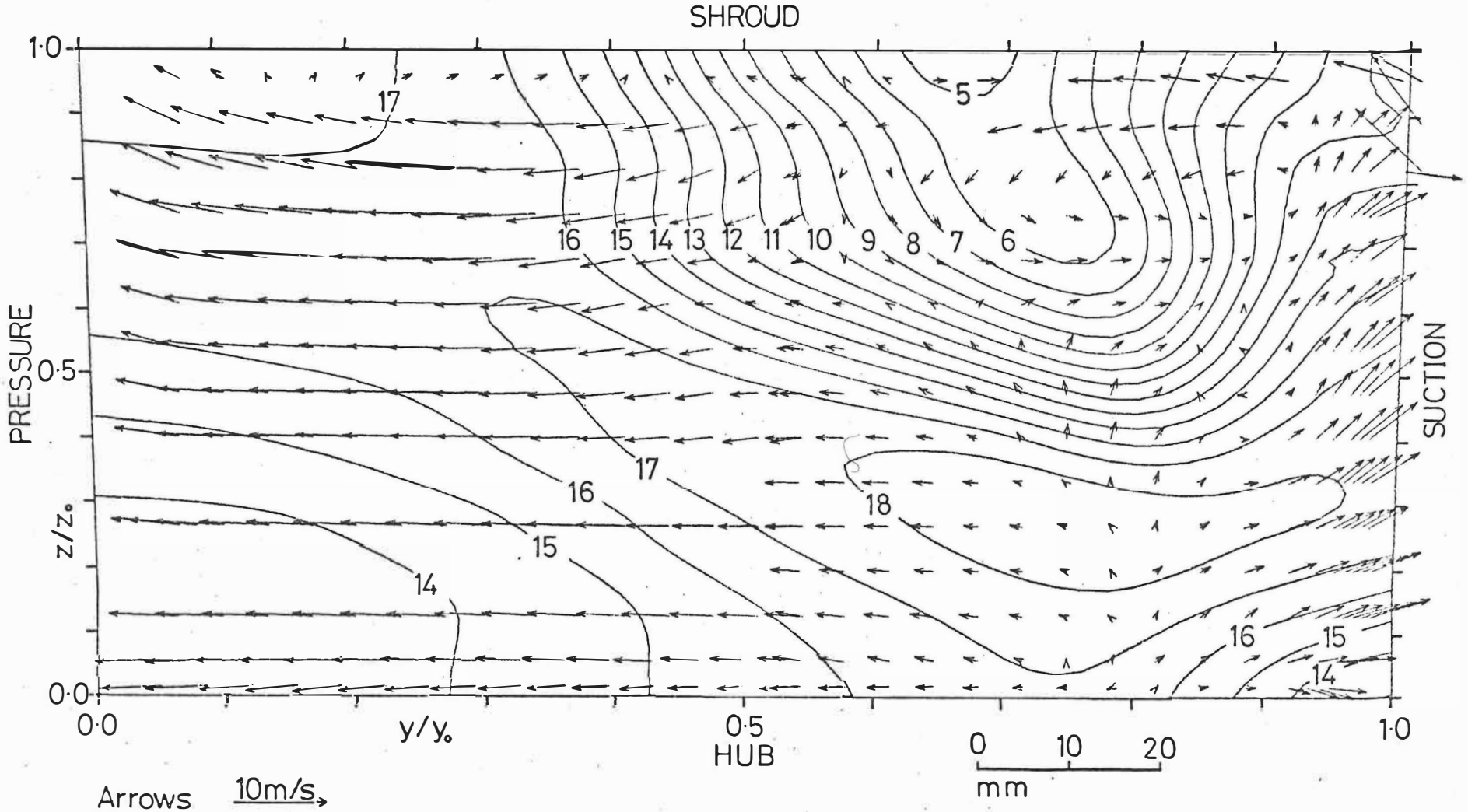

Figure 4.34 'Above design' flow. Station 5. Relative velocities - contours in m/s.

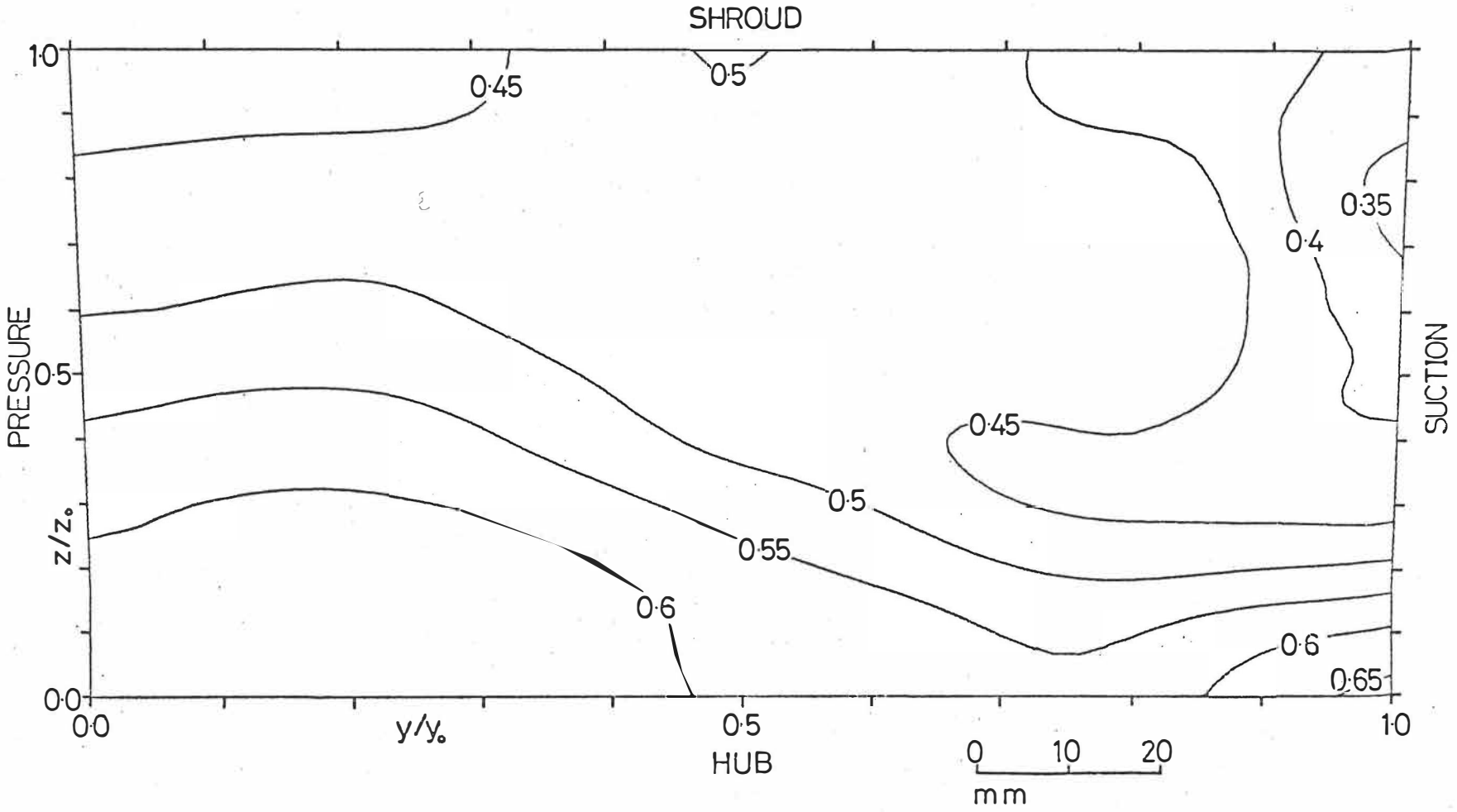

Figure 4.35 'Above design' flow. Station 5. Dimensionless reduced static pressure P_r.

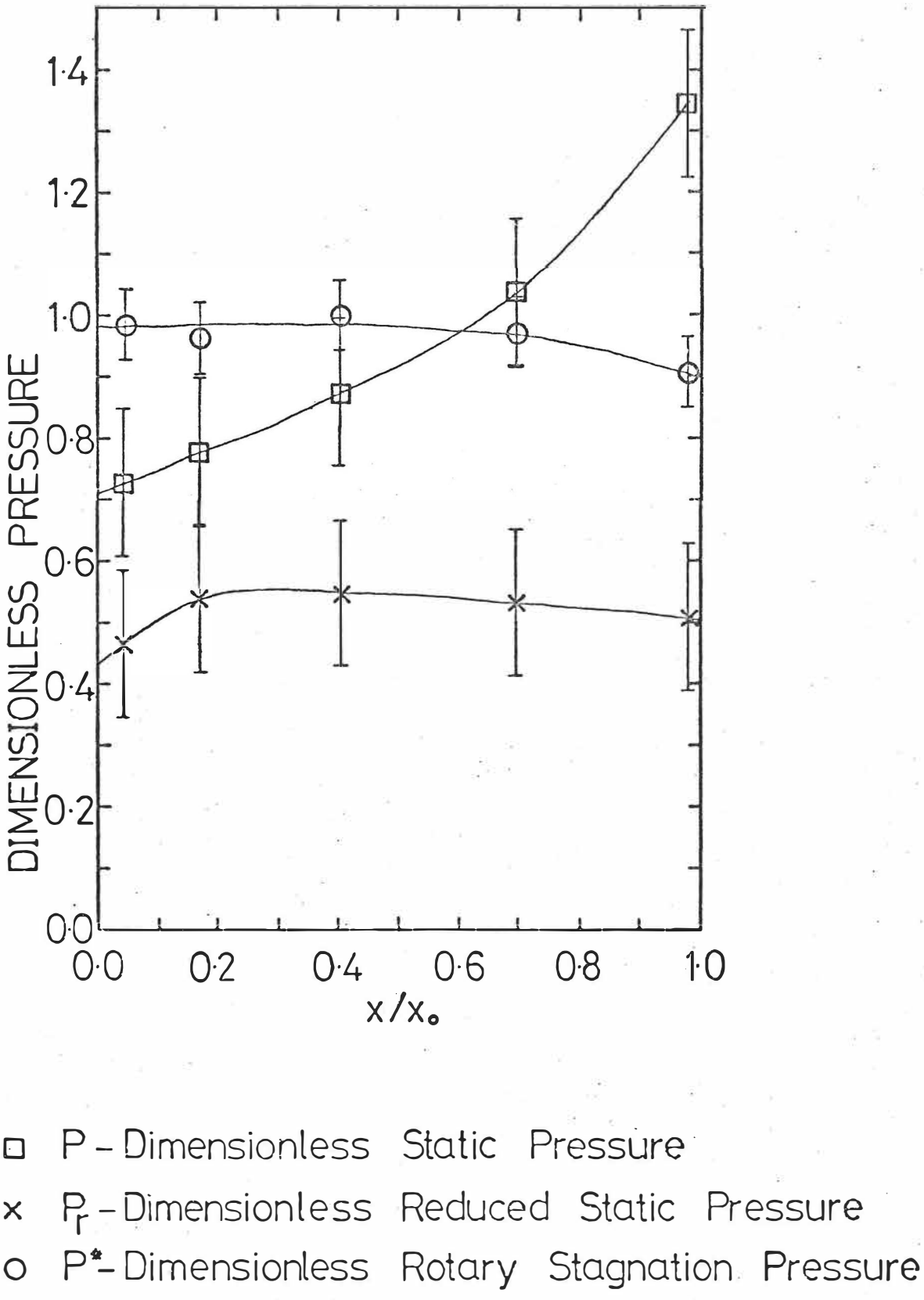

Figure 4.36 'Above design' flow. Mass-averaged dimensionless pressures.

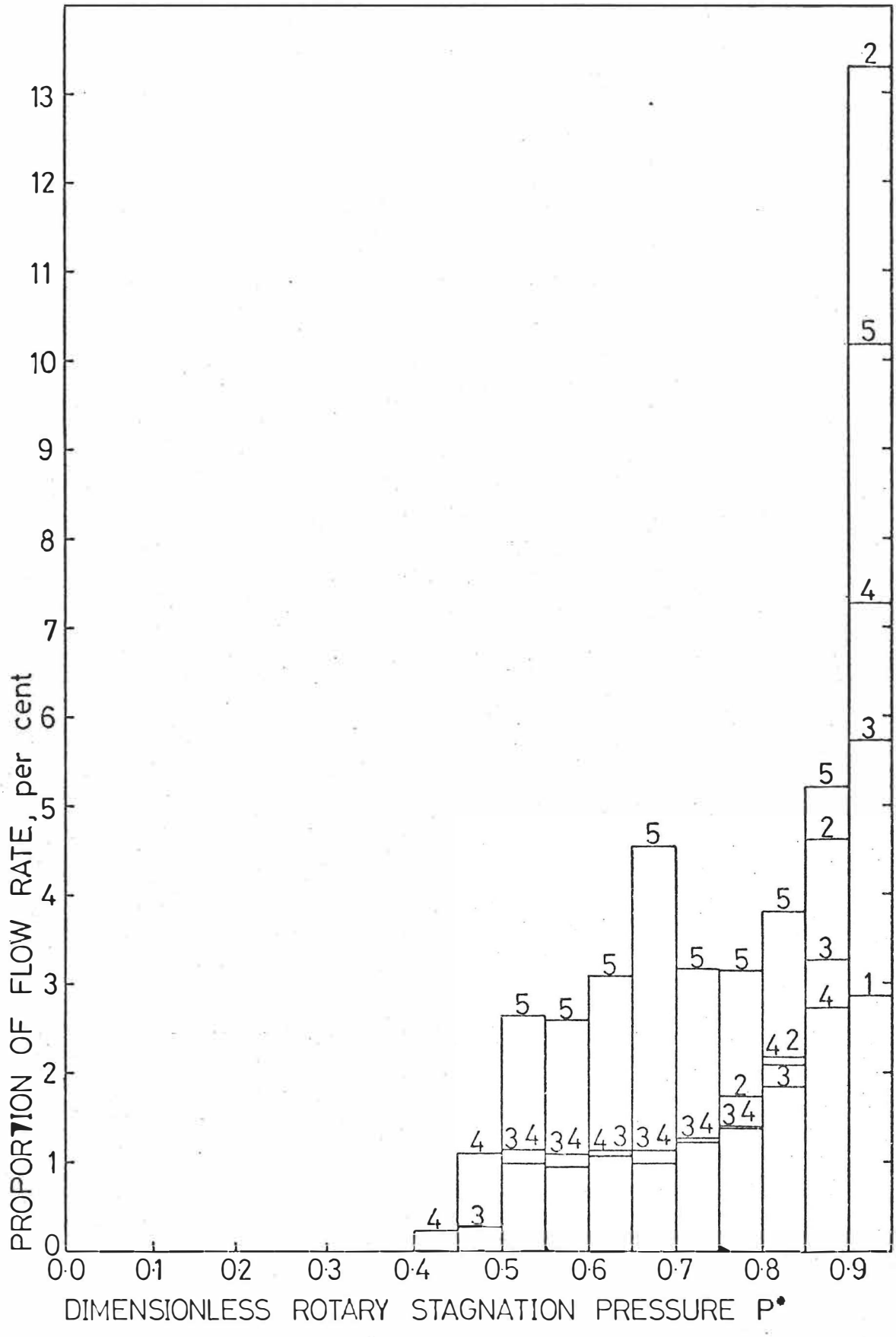

Figure 4.37 'Above design' flow. Distribution of dimensionless rotary stagnation pressure P*.

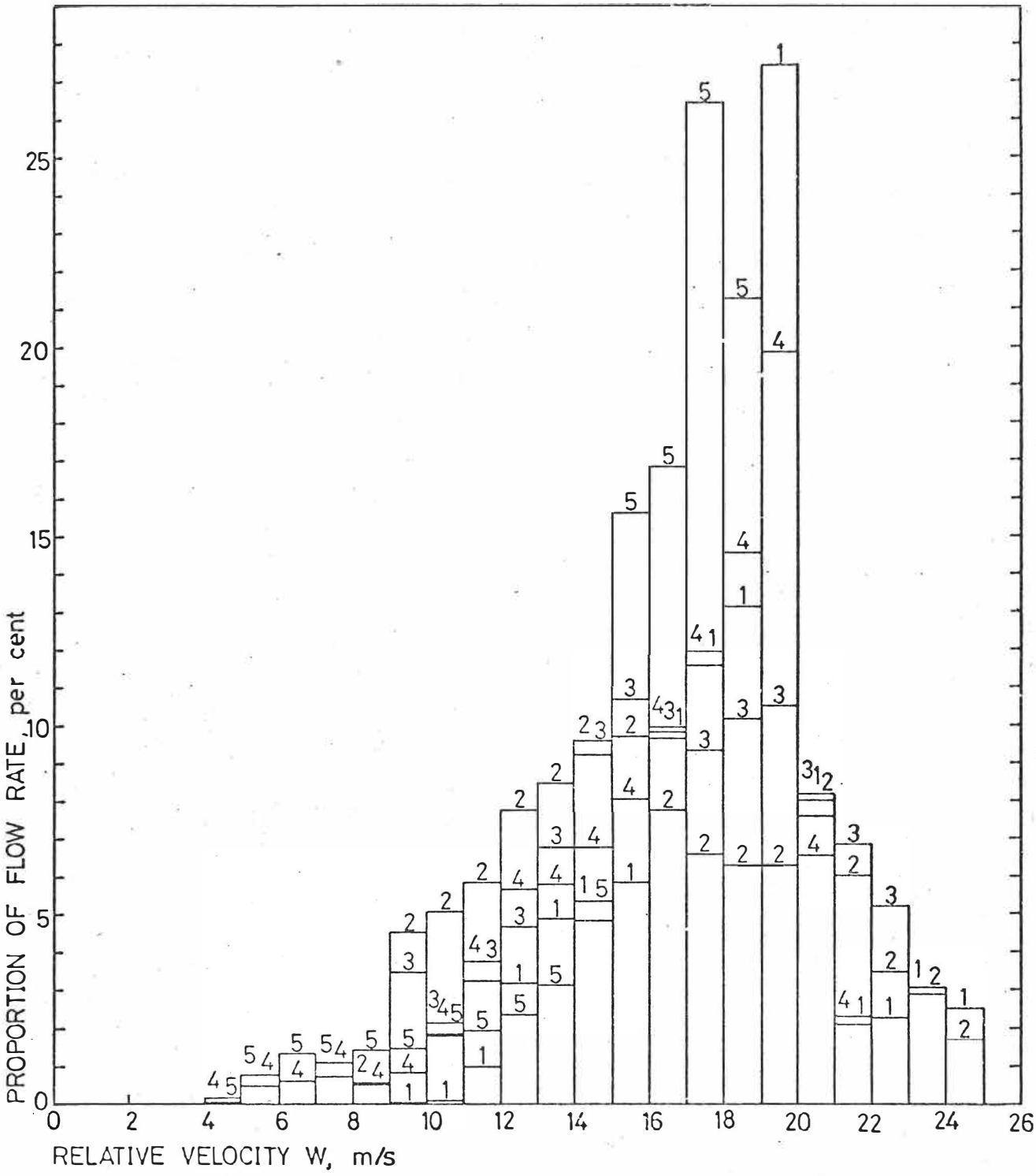

Figure 4.38 'Above design' flow. Distribution of relative velocity.

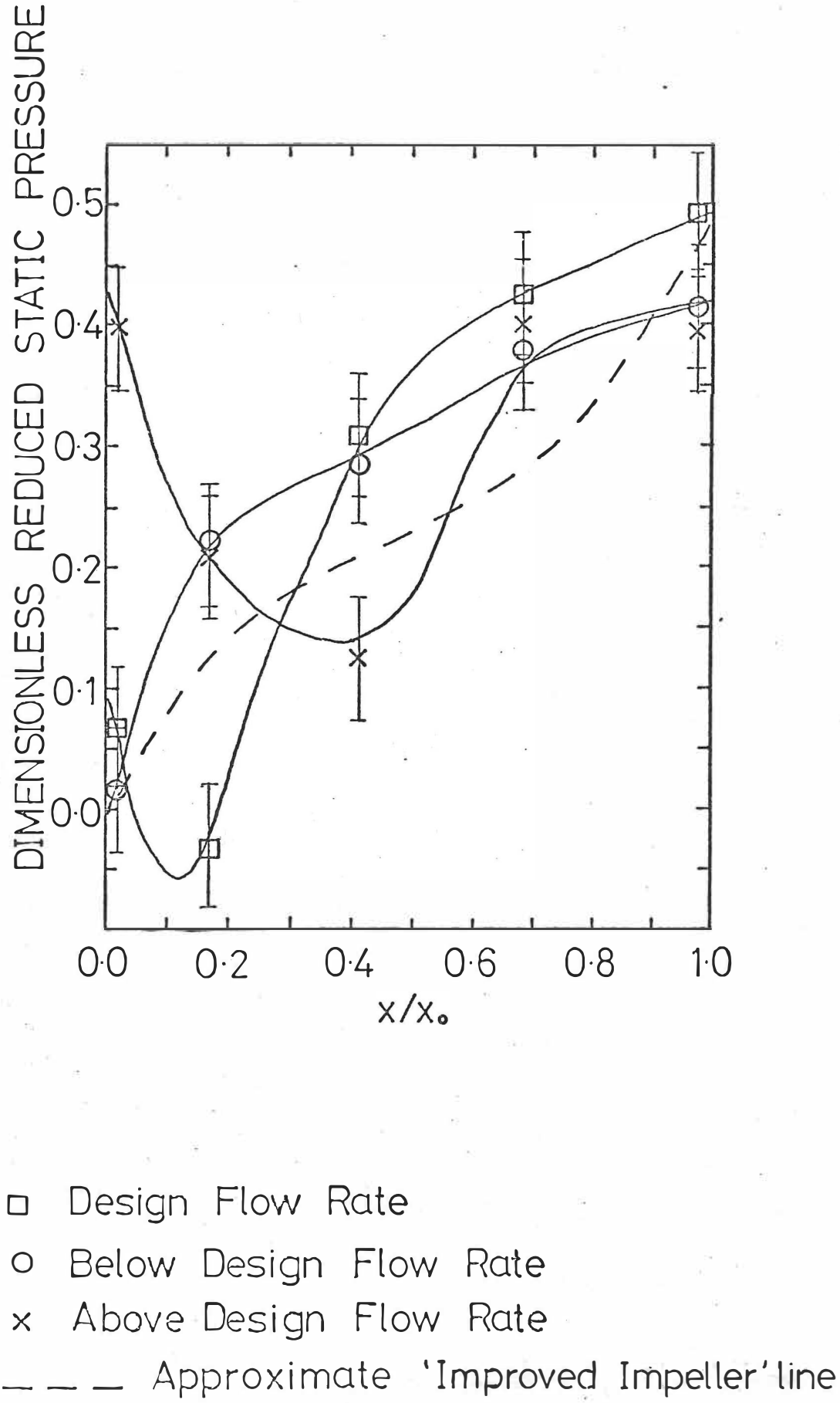

Figure 5.1 Dimensionless reduced static pressure in the suction-side/shroud corner region (y/y_o=0.9; z/z_o=0.9).

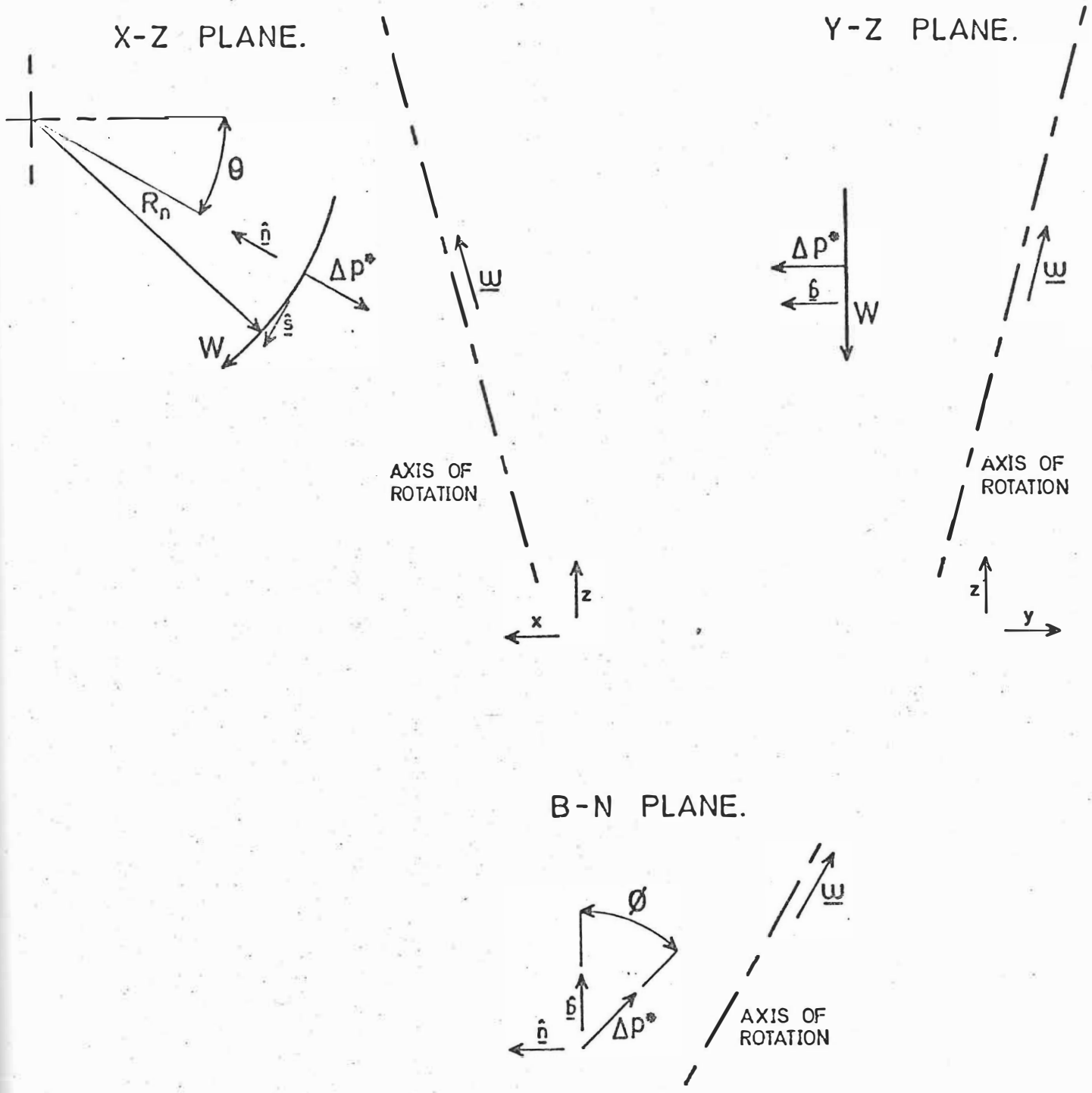

Figure 6.1 Notation for rotating streamtube.

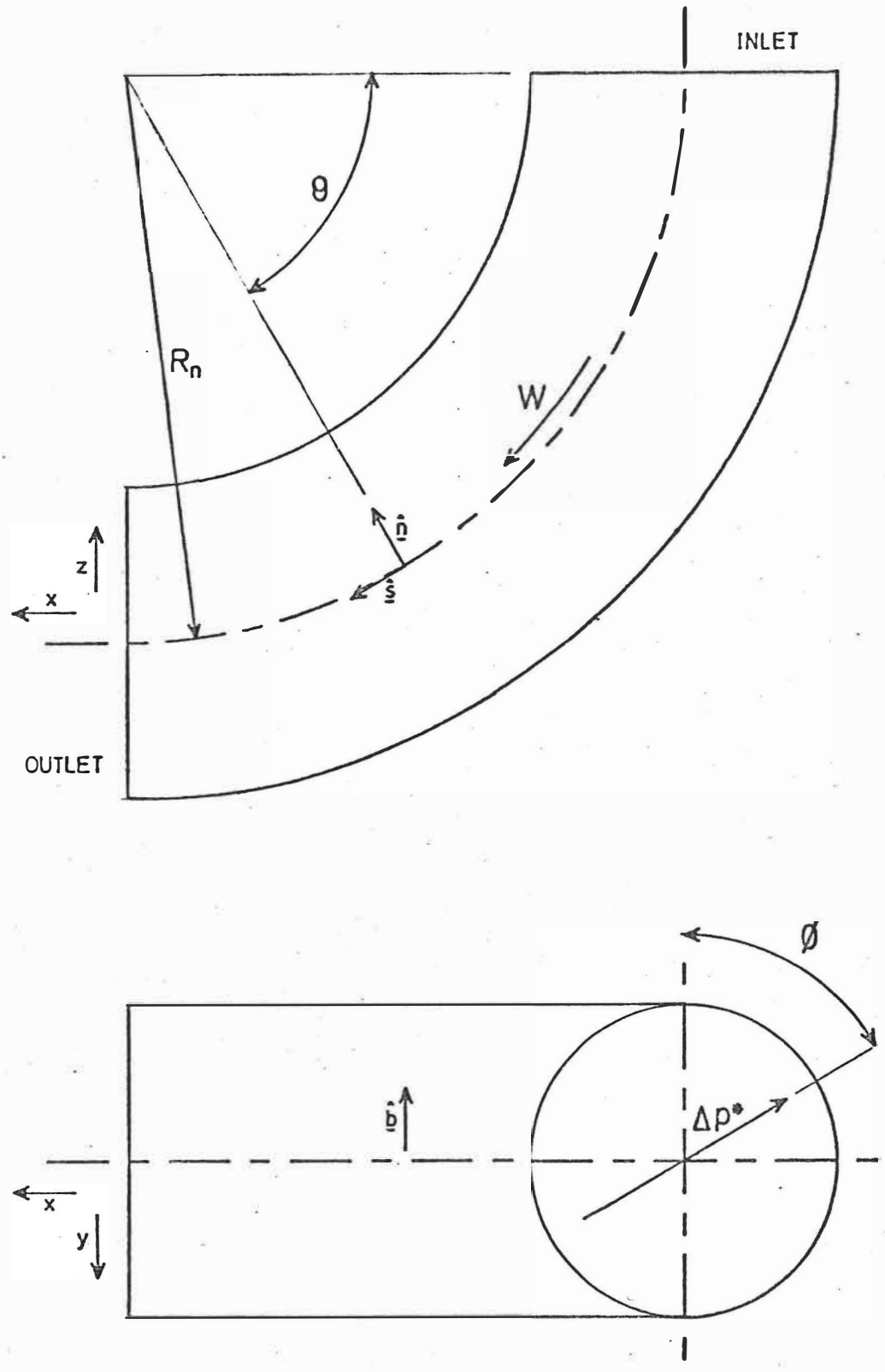

Figure 6.2 Stationary Pipe Bend.

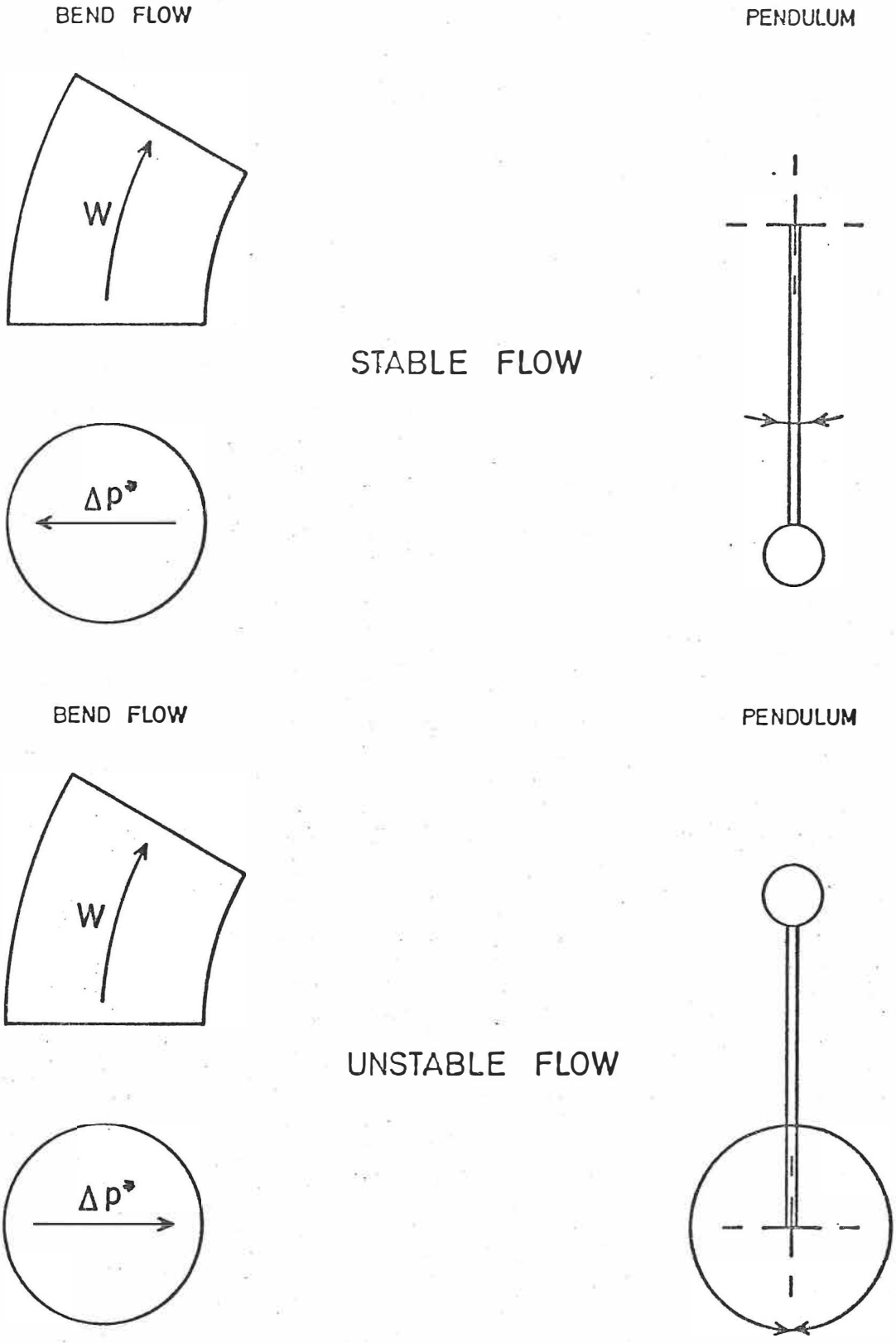

Figure 6.3 Stability of Pipe Bend flow.

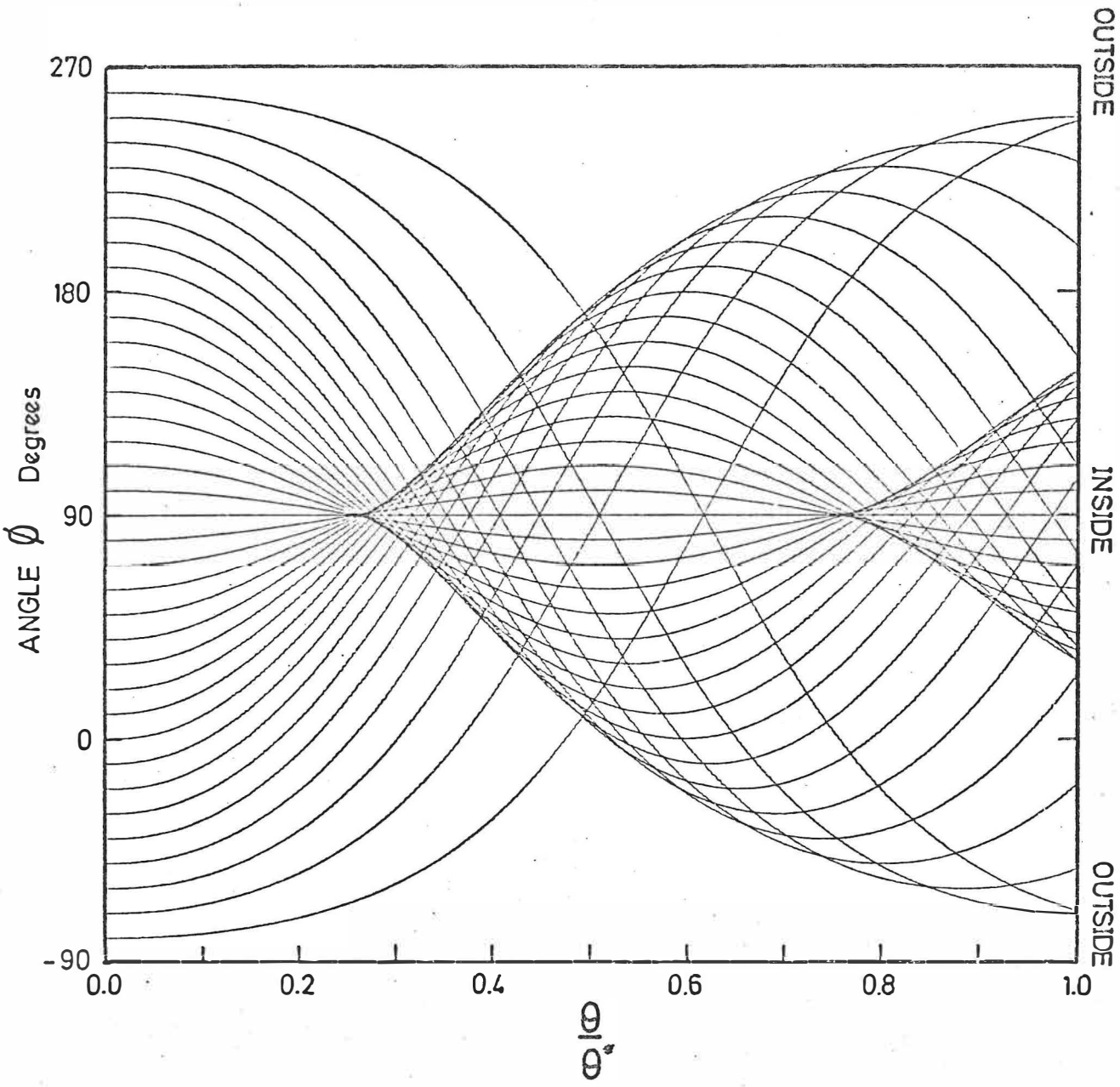

Figure 6.4 Stationary Pipe Bend solution.

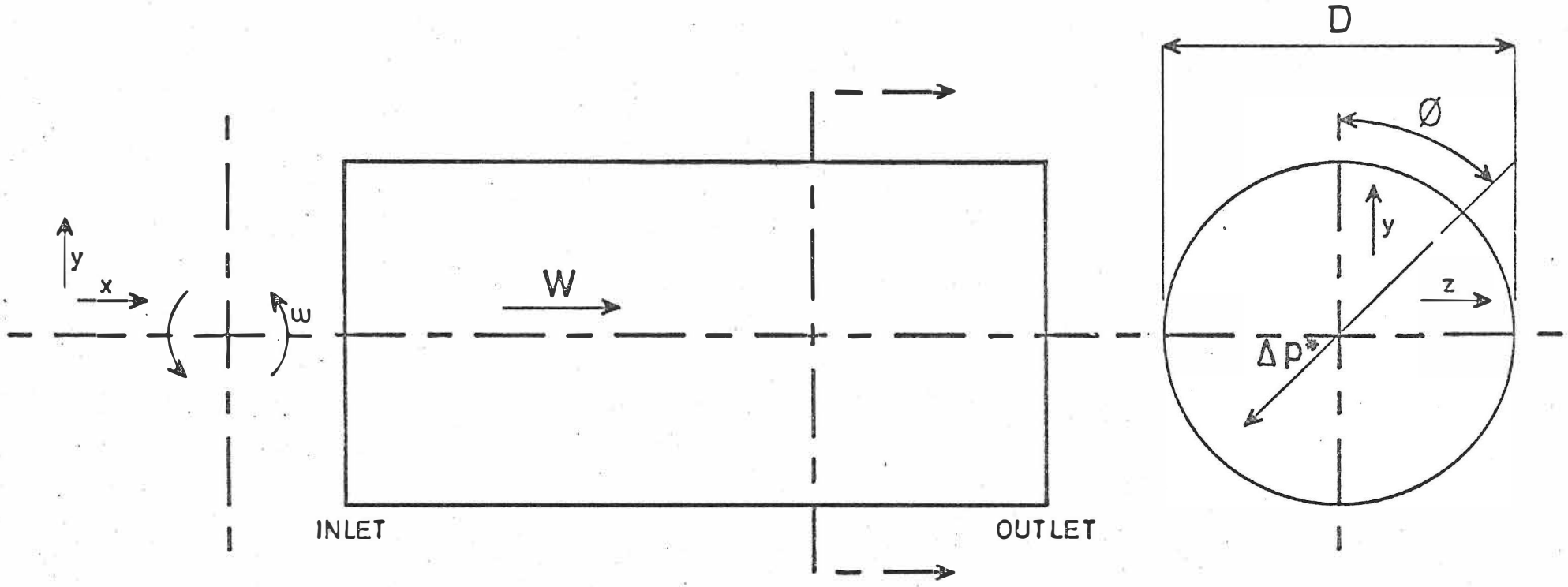

Figure 6.5 Straight rotating Pipe.

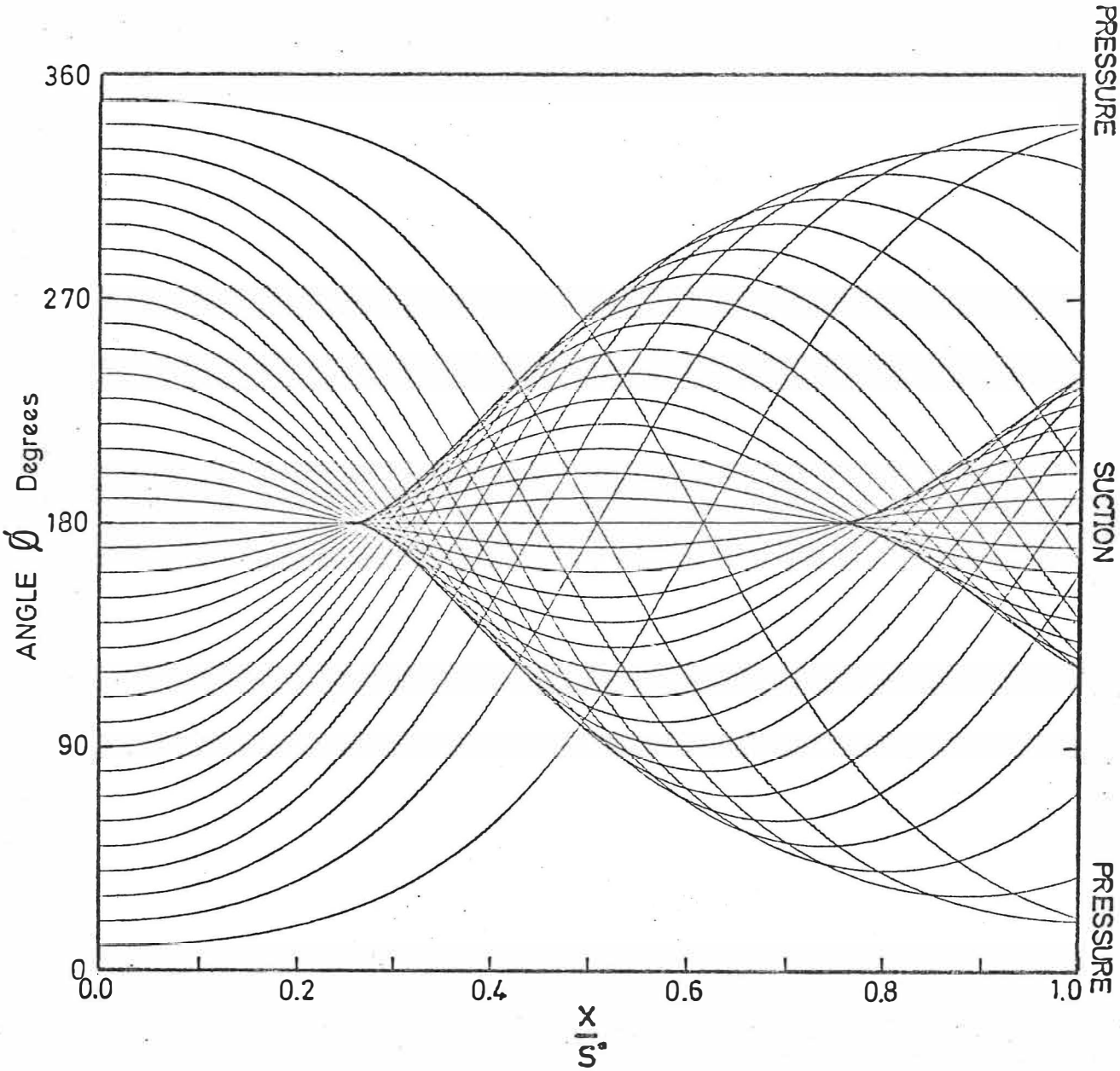

Figure 6.6 Straight rotating Pipe solution.

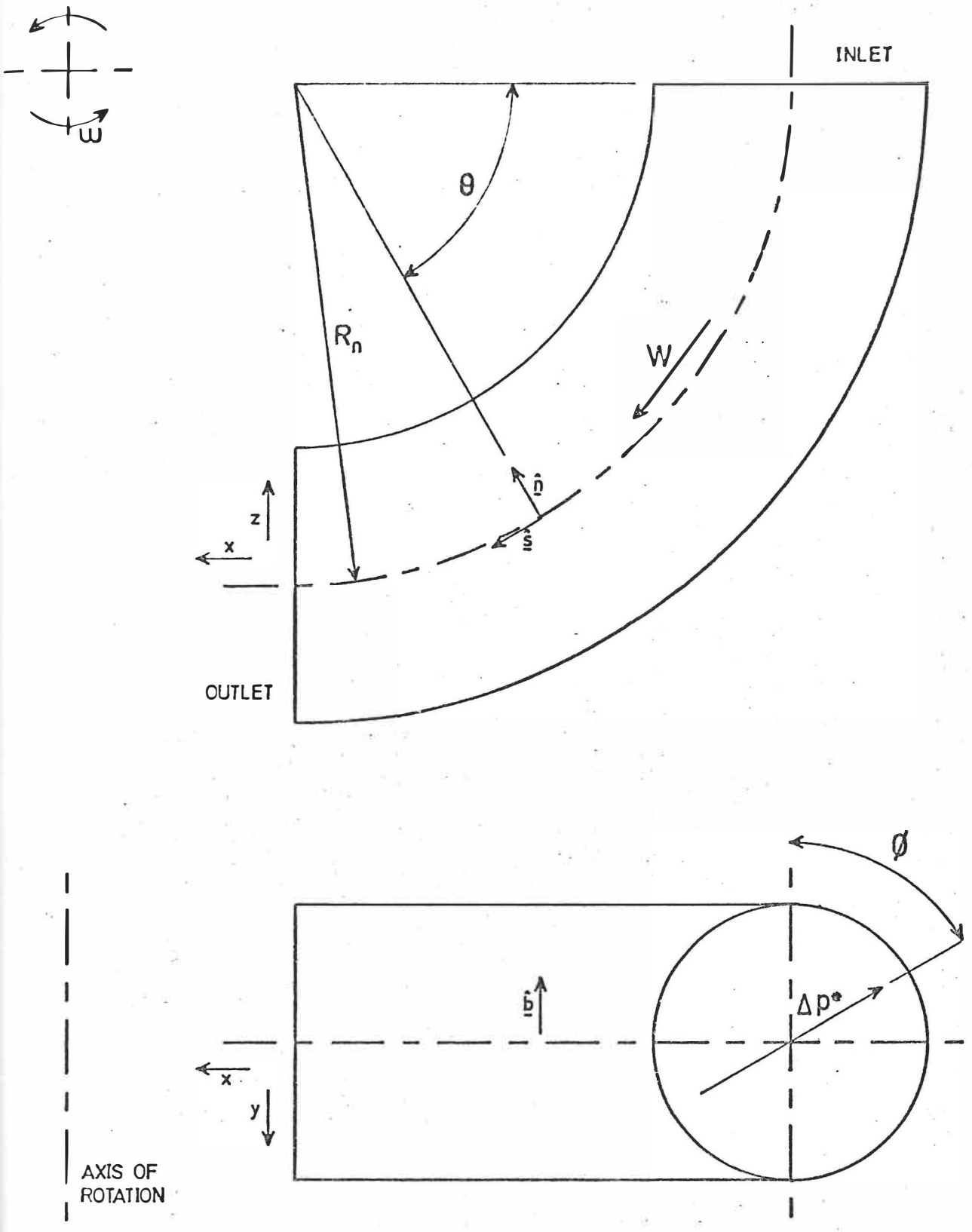

Figure 6.7 Rotating Bend.

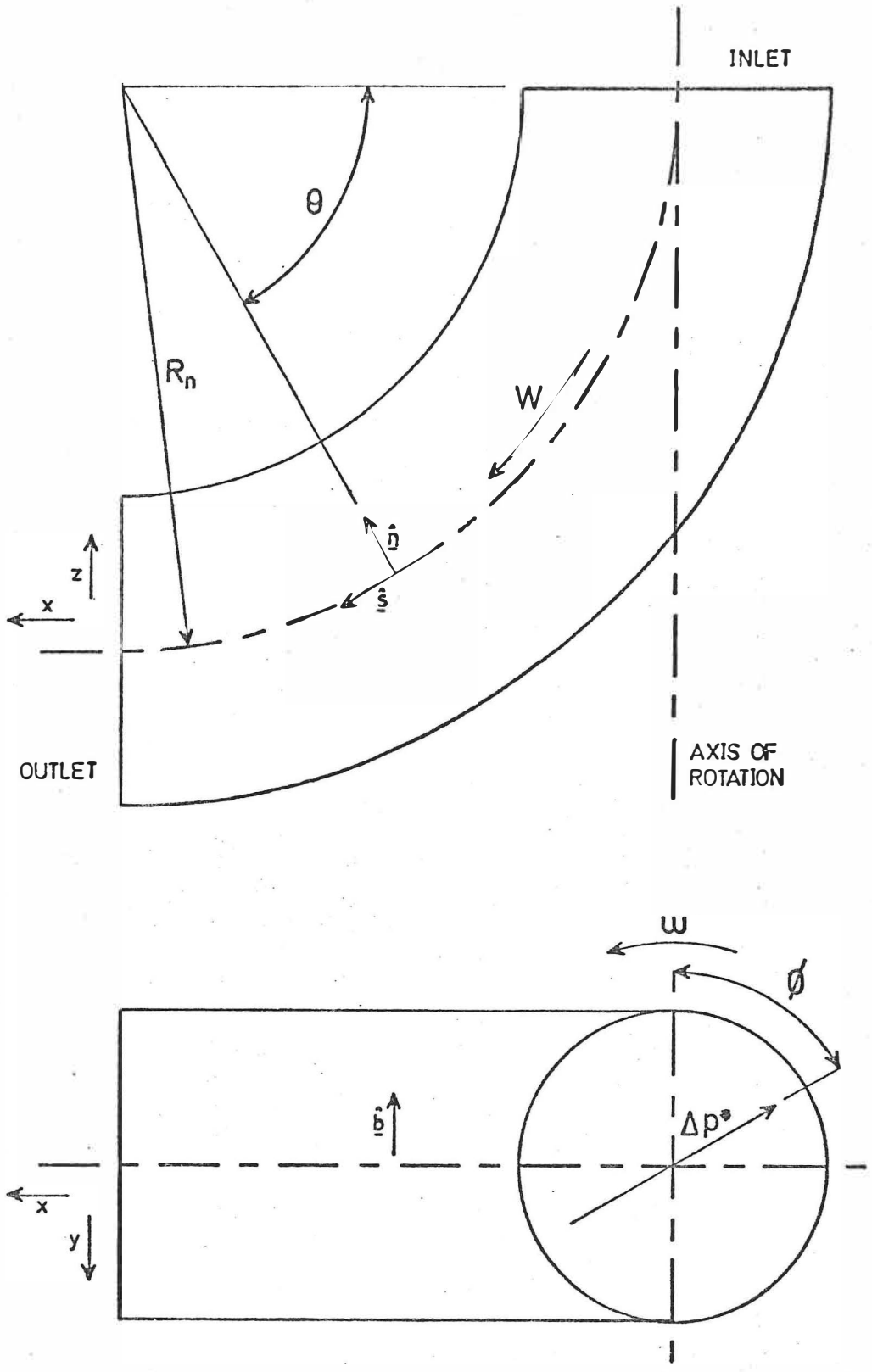

Figure 6.8 Rotating axial-to-radial Bend.

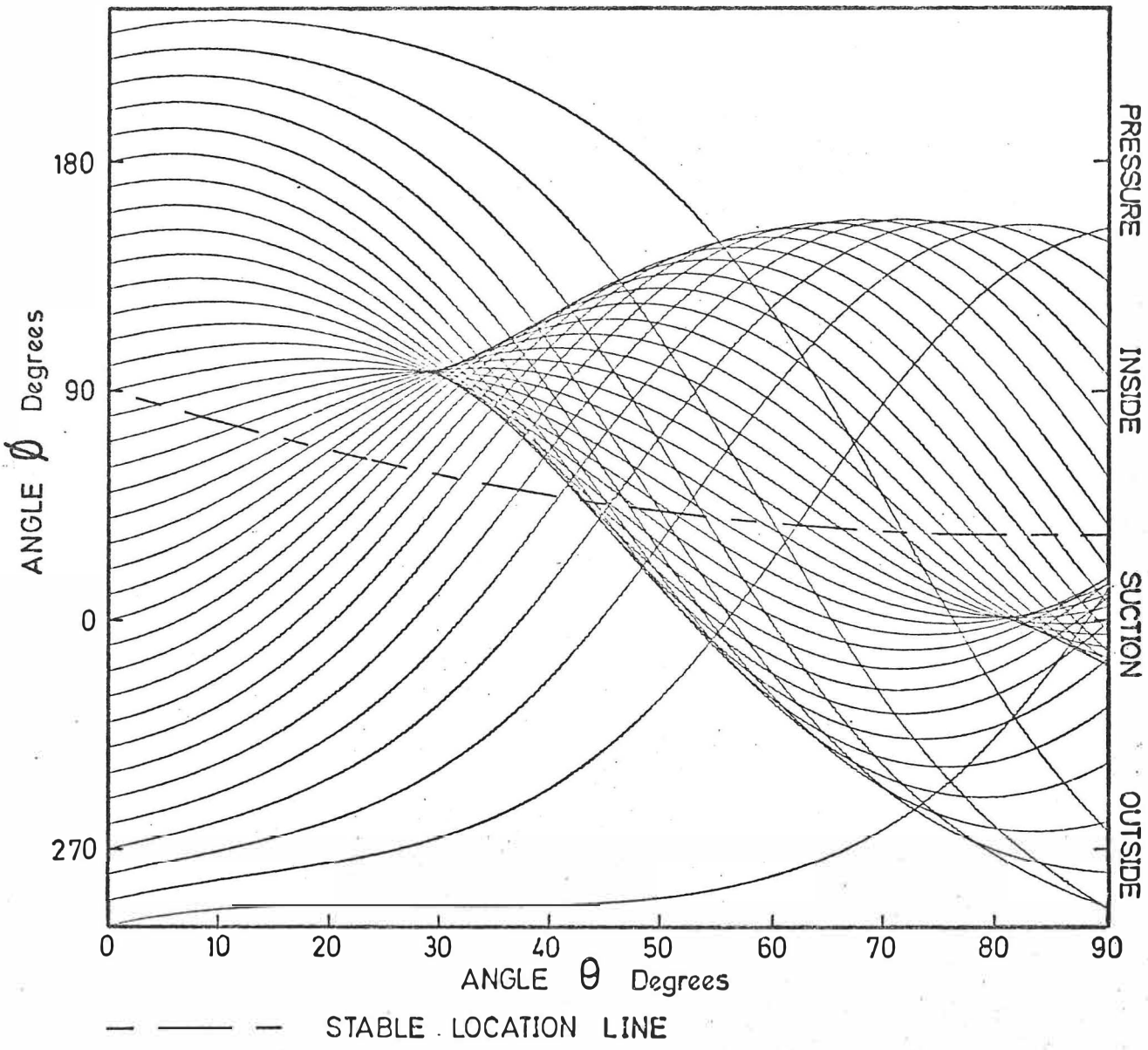

Figure 6.9 Axial-to-radial Bend solution.

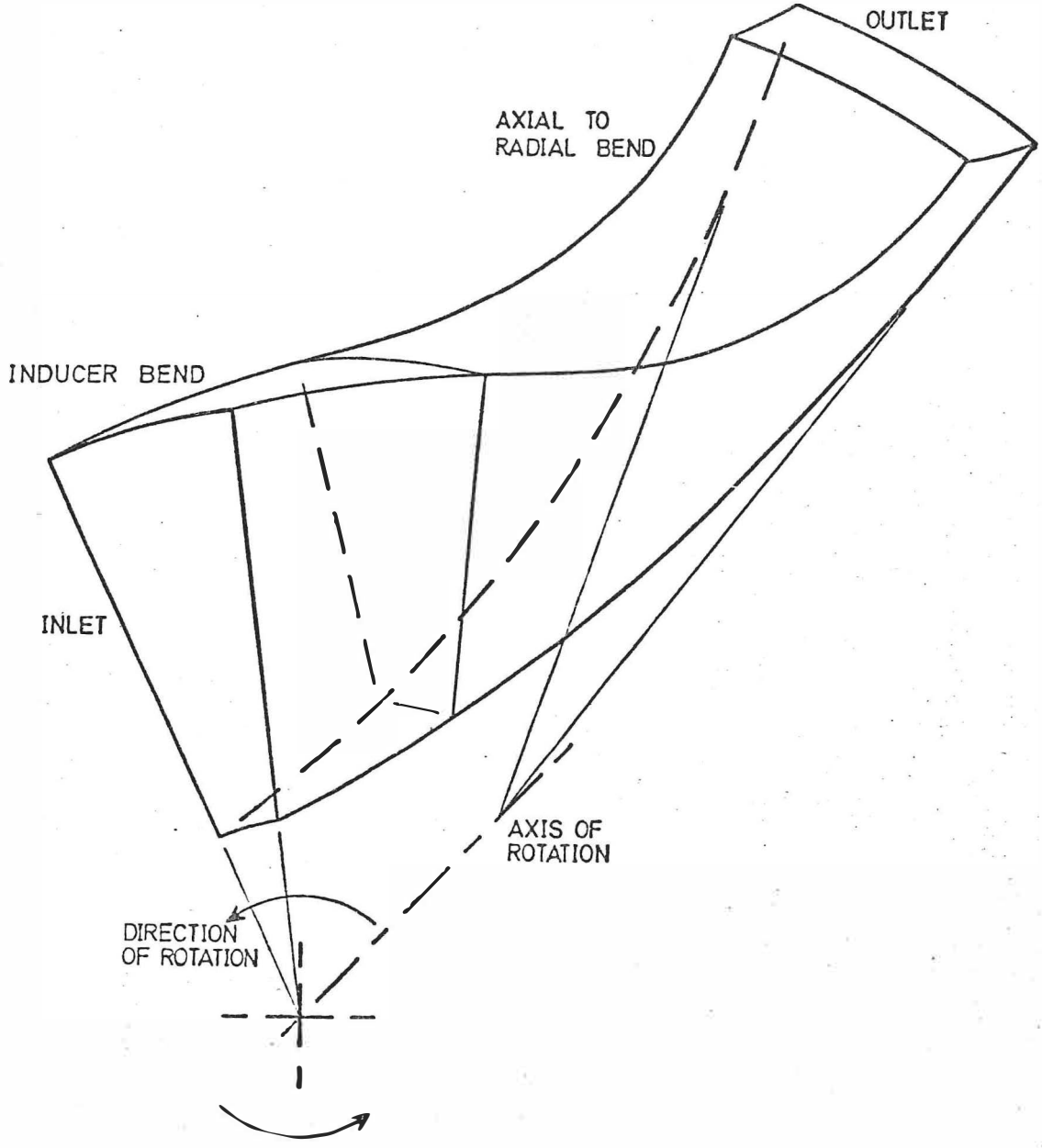

Figure 6.10 Eckardt's impeller Passage.

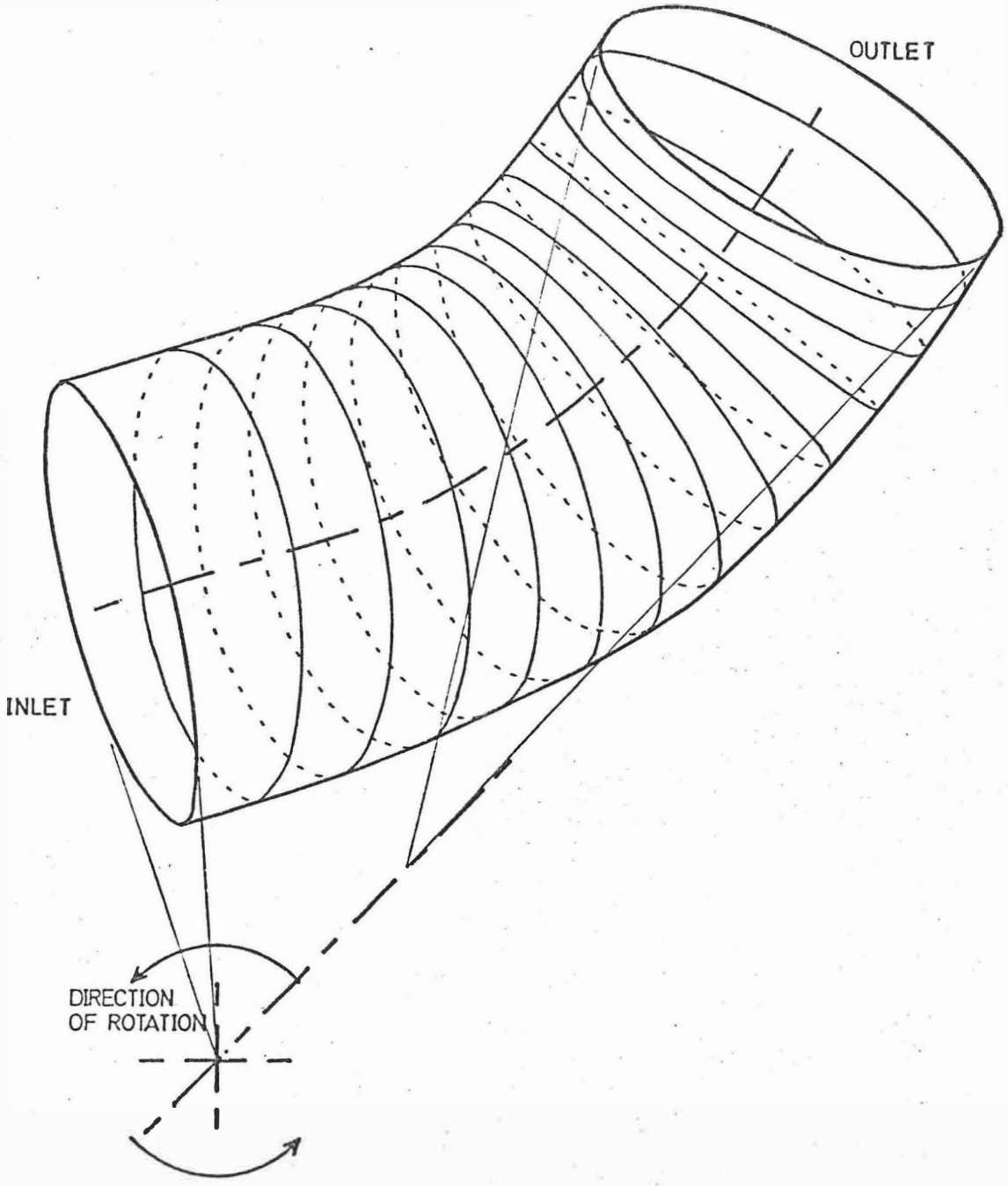

Figure 6.11 Eckardt's impeller Passage representation.

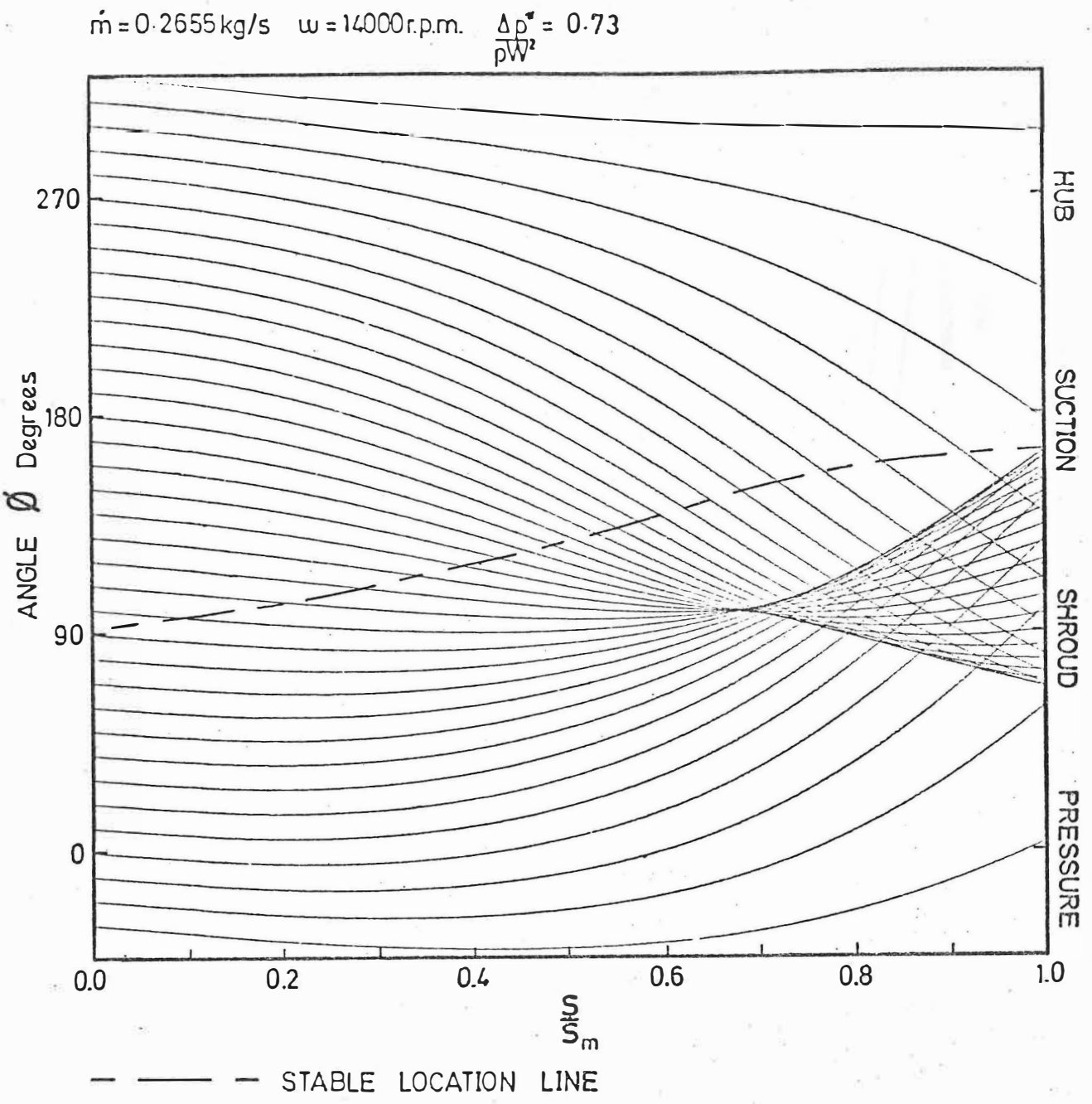

Figure 6.12 Eckardt's impeller Passage solution.

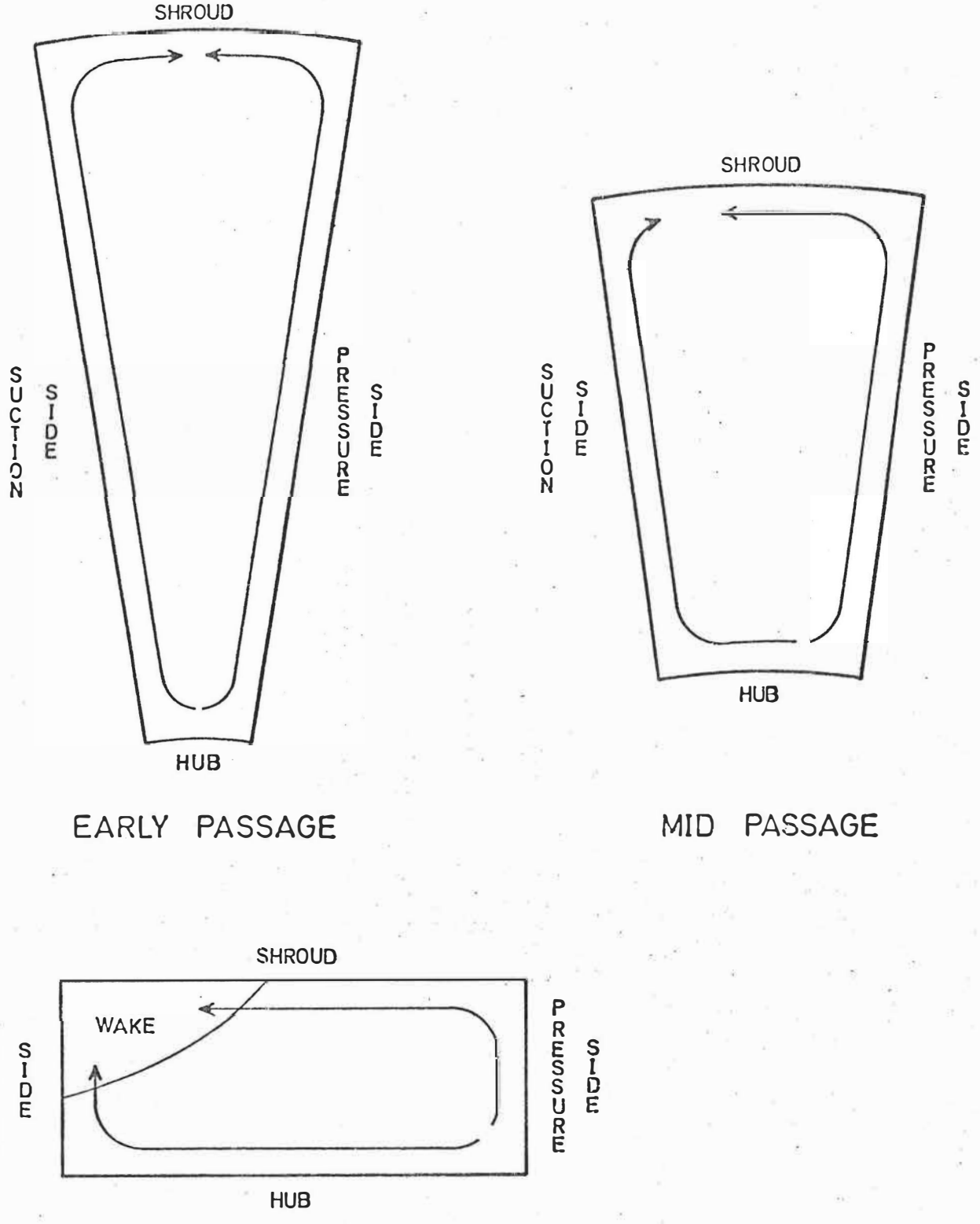

Figure 6.13 Low p* fluid movement in an impeller passage.

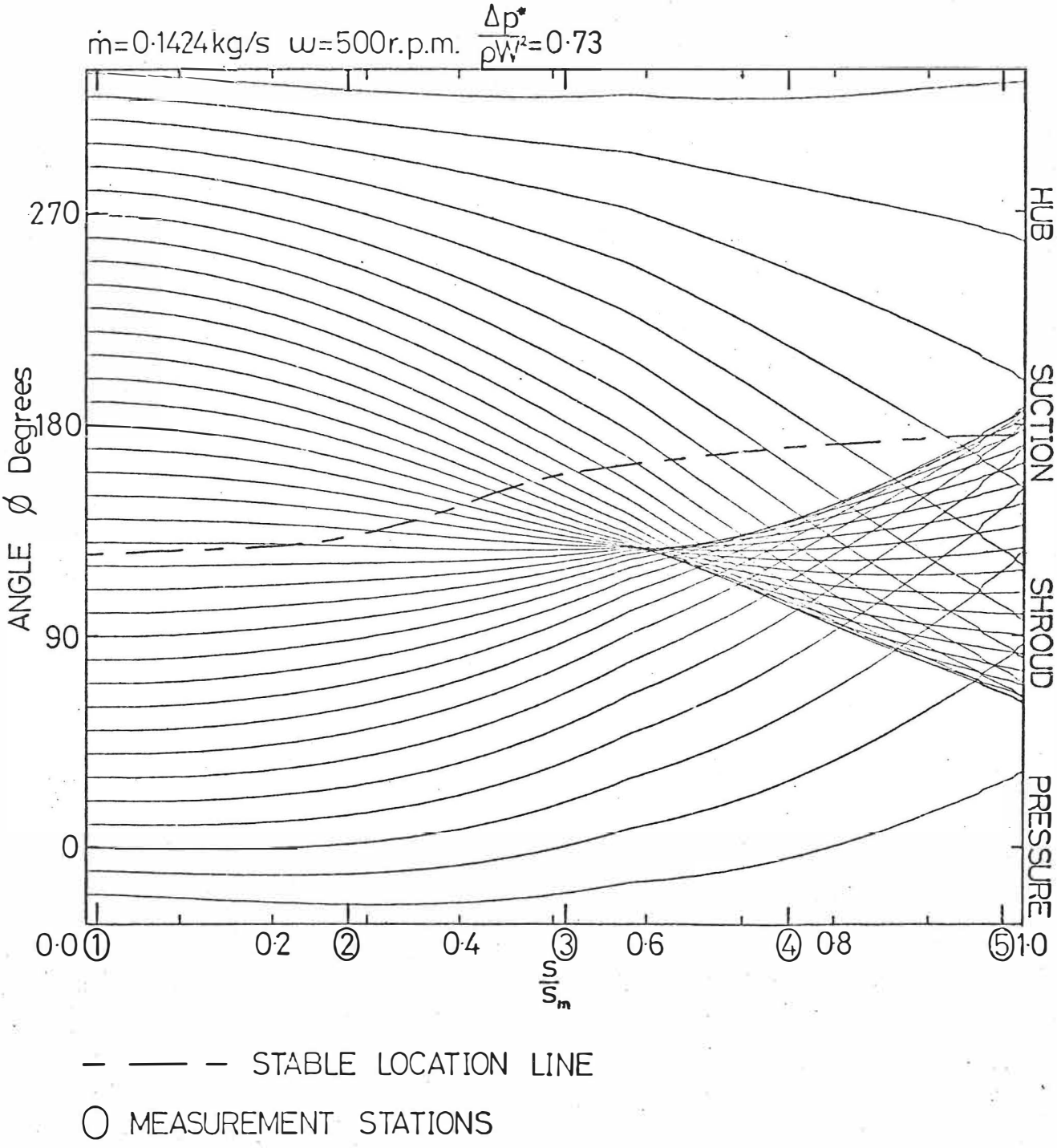

Figure 6.14 Ghost impeller Passage solution. 'Design' flow.

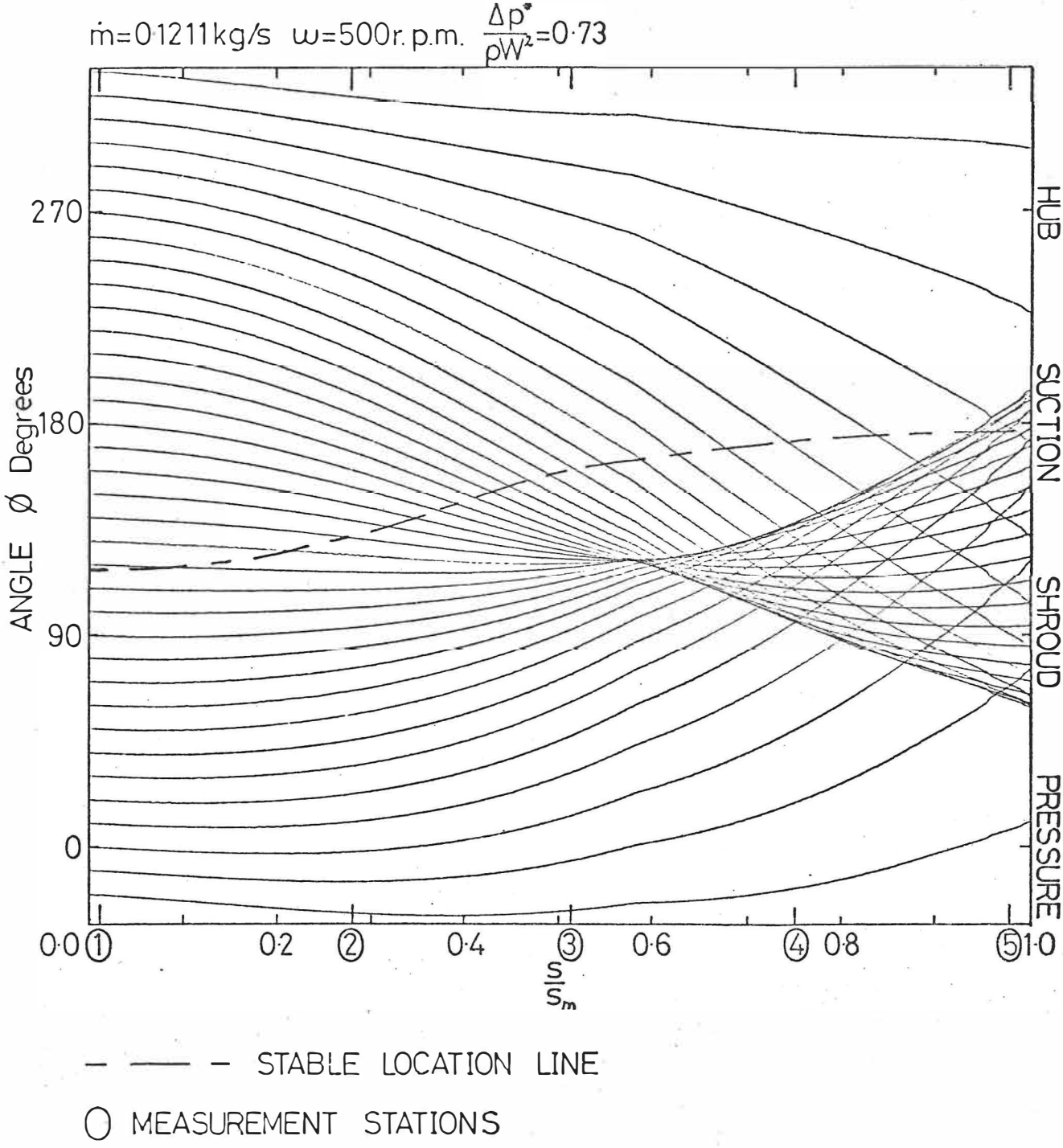

Figure 6.15 Ghost impeller Passage solution. 'Below design' flow.

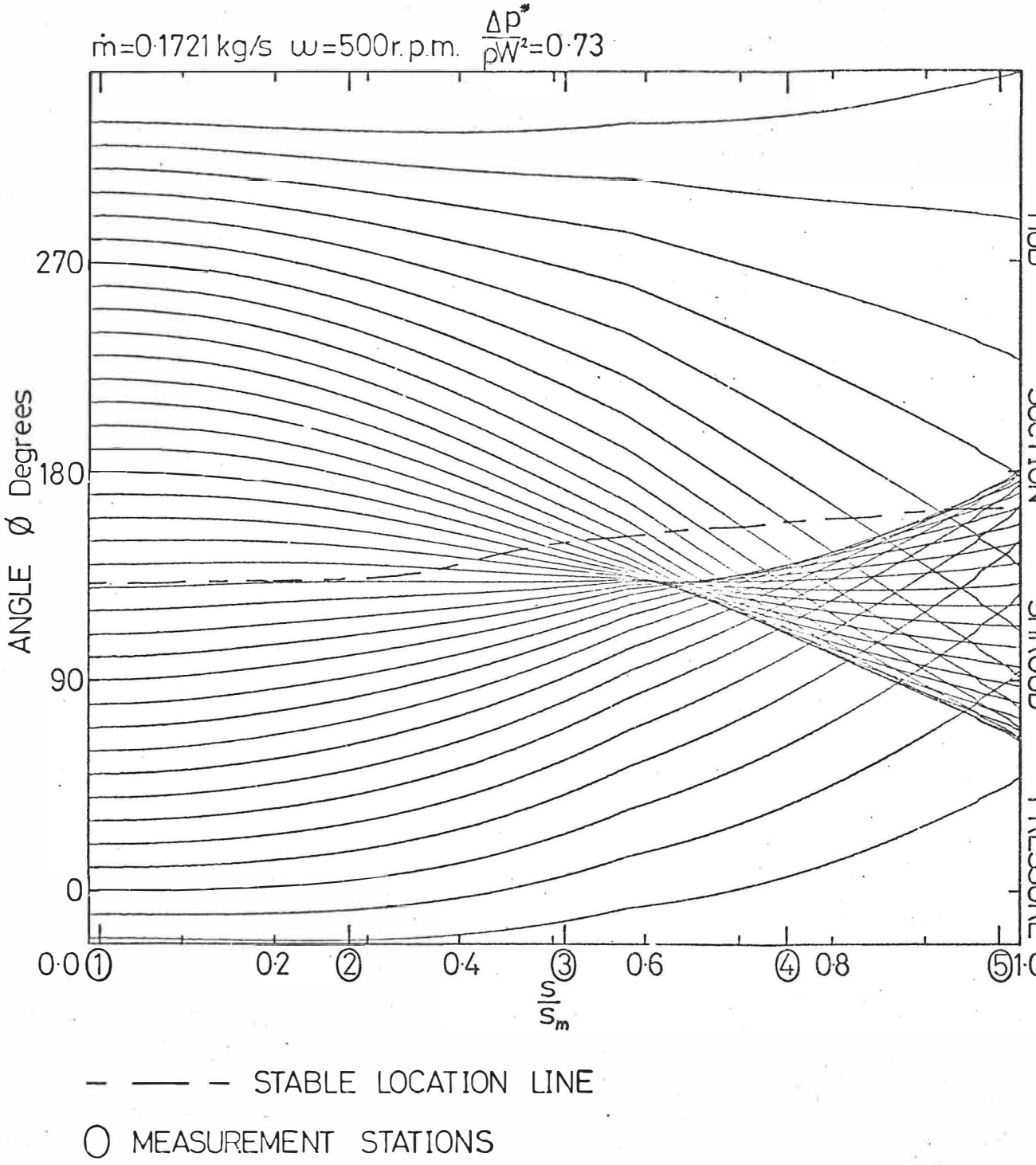

Figure 6.16 Ghost impeller Passage solution. 'Above design' flow.

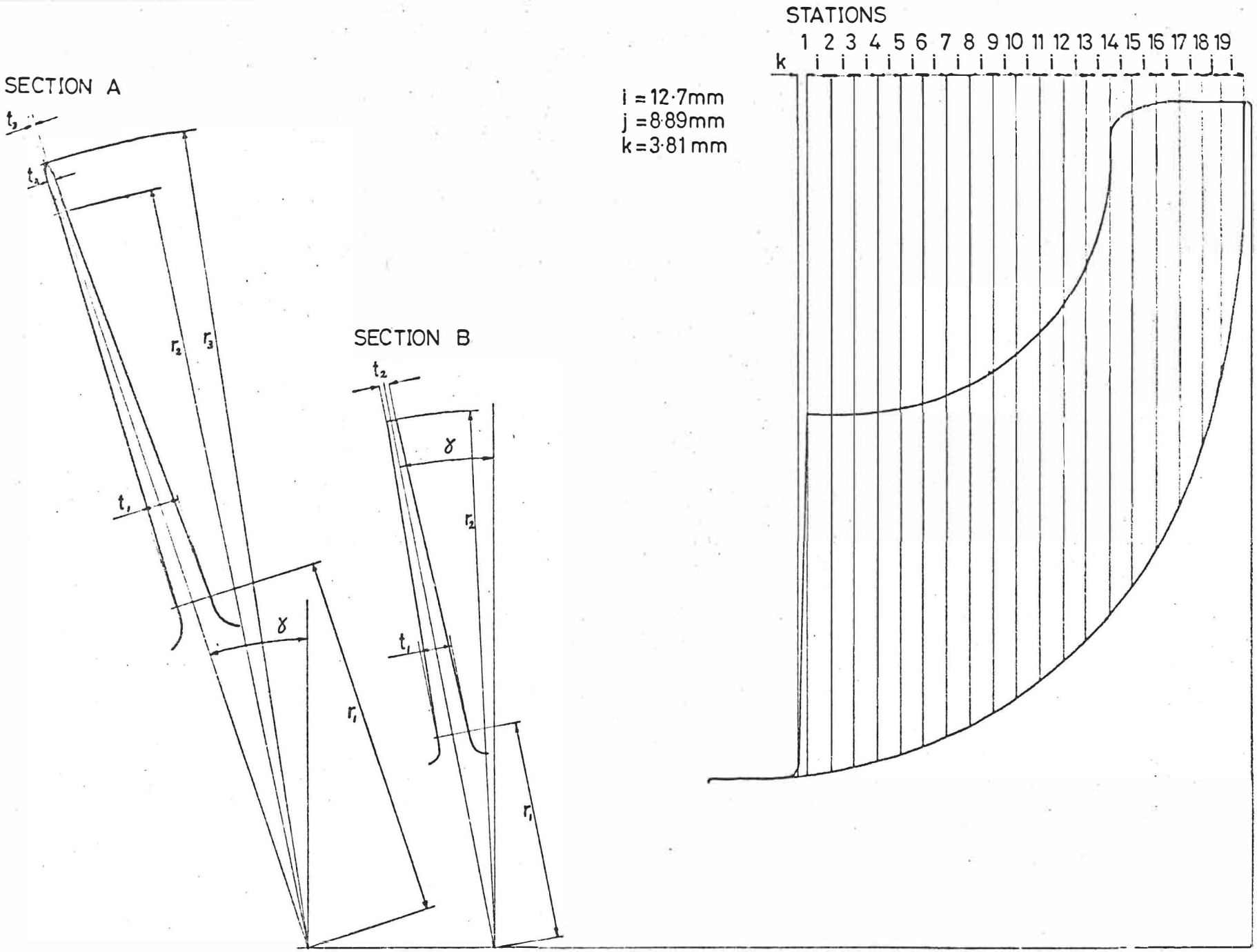

Figure A1 Ghost impeller Blade thickness.

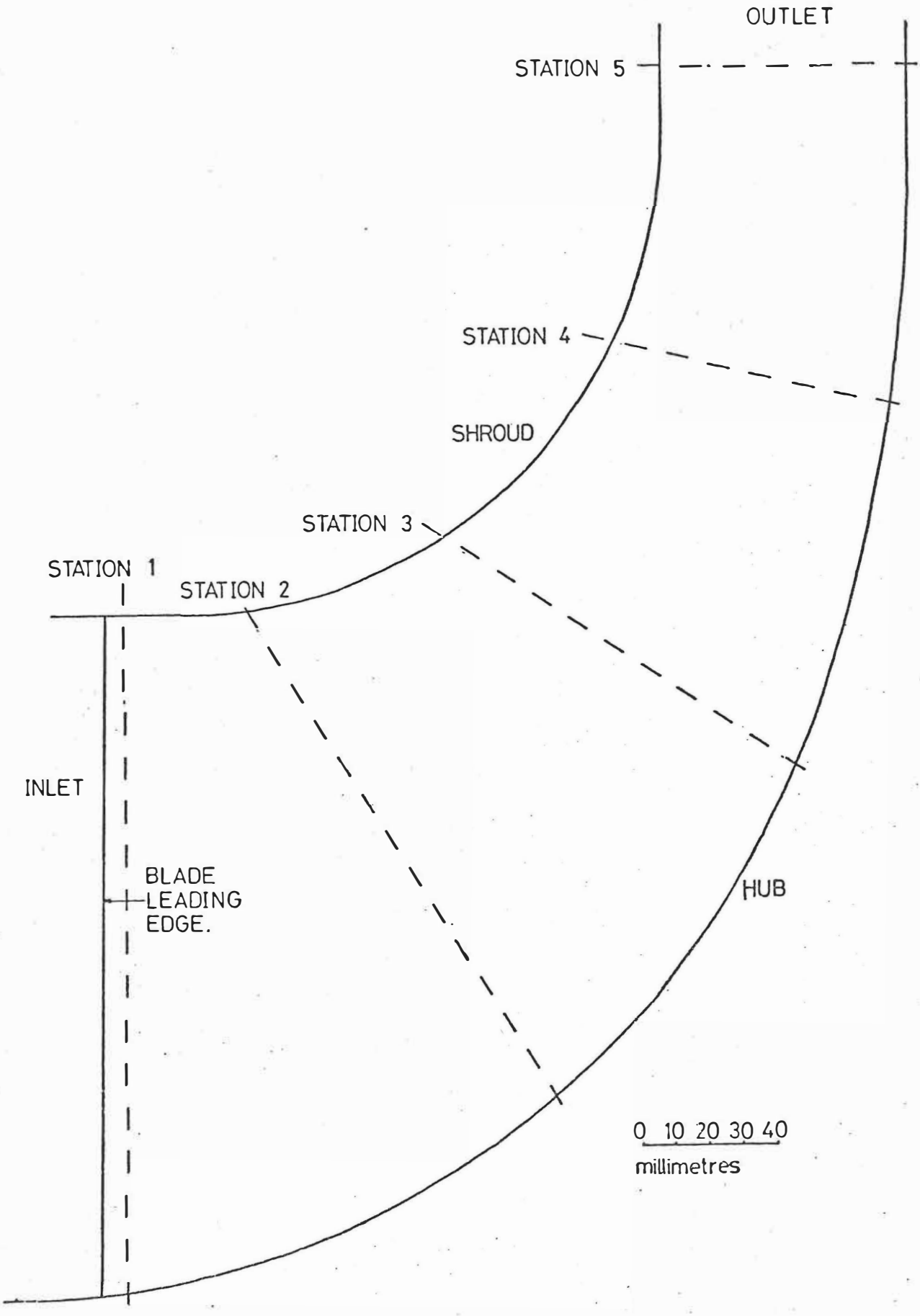

Figure A2. Meridional cross-section of impeller with the locations of the measurement planes.

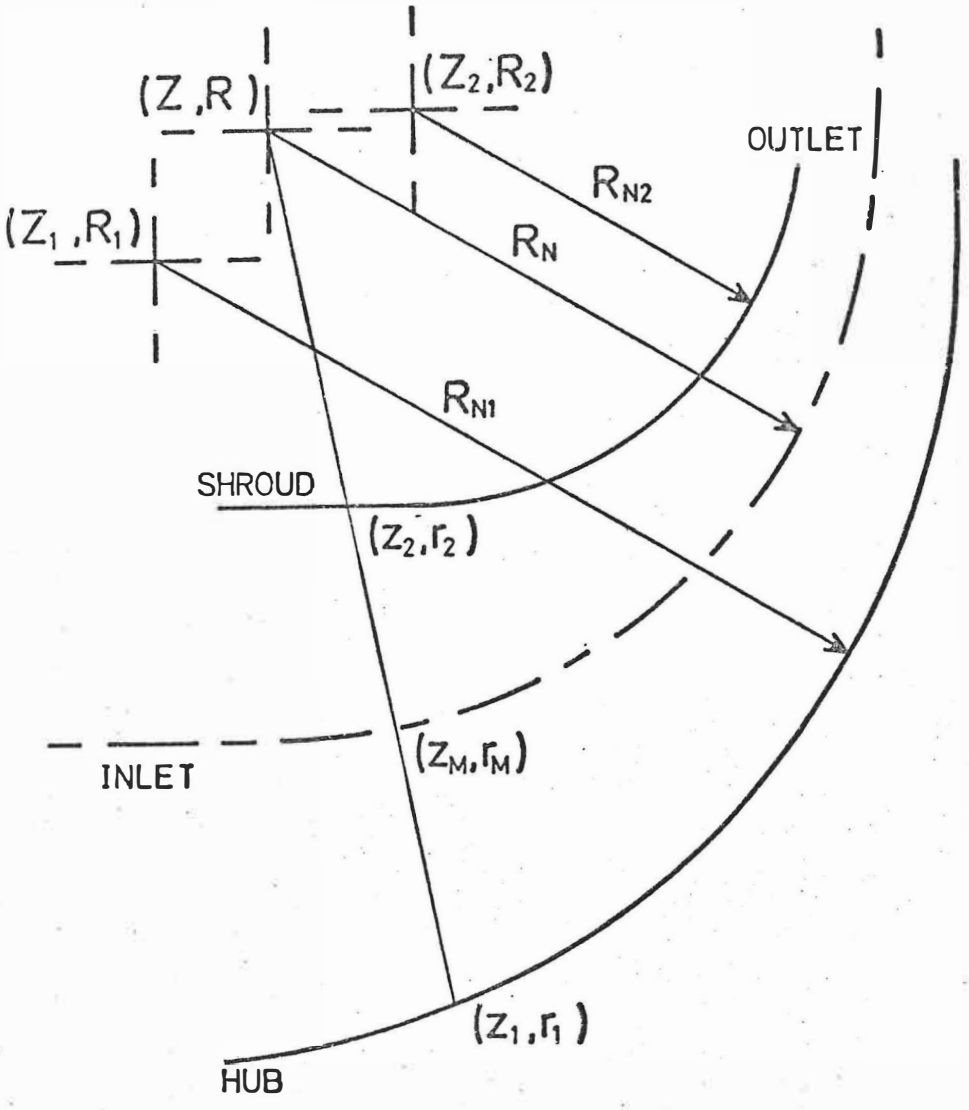

Figure A3 Centre of area of the impeller passage.